

Department of Mechanical Engineering

**Numerical Analysis for Piezoelectric Unimorph Beam Power
Harvesting Applications**

Eziwarman

**This thesis is presented for the Degree of
Doctor of Philosophy
of
Curtin University**

June 2015

Declaration

To the best of my knowledge and belief this thesis contains no material previously published by any other person except where due acknowledgment has been made.

This thesis contains no material which has been accepted for the award of any other degree or diploma in any university.

Signature :.....

Date:.....

Abstract

This thesis focusses on modelling of power harvesting from piezoelectric unimorph beams under base excitation using finite element methods. The harvested power can be extracted from ambient vibration environments and this power can be used for powering small devices such as wireless sensors for health condition monitoring of machinery or structures. Development of piezoelectric power harvesting devices has been given attention from numerous researchers because these devices are expected to show strong benefit for low power demand applications. In addition, piezoelectric devices can also be applied in micro-scale system design with high sensitivity to low amplitude mechanical vibration.

This research presents the derivation of the electromechanical dynamic equations of motion for the unimorph beam using finite element methods. A single coupled piezoelectric unimorph beam element with total of four degrees of freedom was developed in order to construct fundamental understanding of the electromechanical dynamic equations and to show the power harvesting frequency response. Here, a new novel solution using the direct method with non-orthonormalisation is introduced to derive the frequency response function (FRF) for voltage, current and power output. The generalised electromechanical dynamic equations were formulated based on Hamilton's principle and the subsequent linear constitutive equations. In the multi-elements case study, another technique of deriving the global electromechanical coupled transformation matrices was given in order to form the global matrices of the electromechanical dynamic equation. The resulting multi-element case studies were compared with the previously published research in order to validate the resulting equations from the proposed method.

Design optimisation of the unimorph beam with an additional tip mass added at the end of the beam is presented to show the power harvesting frequency responses. Here, the approach of tip mass offset is explored based on the location of the tip mass attached onto the top of the substructure. The challenge of design optimisation is explored by investigating varying lengths of piezoelectric material attached to the

substructure with the tip mass attached to the end of the unimorph beam. Comparing the resulting power harvesting frequency responses shows that the unimorph beam with piezoelectric material covering the whole length on top of the substructure gives much more power than other designs.

The developed research also investigates the segmented unimorph beam with different angles of orientation under base excitation. The coupled equations of motion for each element now included the axial degrees of freedom requiring six degrees of freedom per element. A case study is presented where the modelled piezoelectric unimorph beam was bent in the middle having symmetrical segmented design where the piezoelectric material has the same length either side of the bend. The two piezoelectric elements were connected in parallel and the subsequent voltage, current and power behaviour explored for different angles of orientation. Comparison of the numerical and experimental system behaviour shows the validation of the coupled axial-transverse-electromechanical numerical model.

Acknowledgement

I would like to express my gratitude to my supervisor A/Prof. Ian Howard for his excellent support, patience, and continuous encouragement throughout my doctoral study.

Thanks are given to Dr. Mikail Lumentut for sharing knowledge. His comments and discussion have been a great help to the author.

Grateful acknowledgment is given to the Education Department (DIKTI) Indonesia for the sponsorship that was provided for 3.5 years and also to the University of Bung Hatta for their great support.

Thanks to my family especially to my mother, *Erlina*, mother in law *Akirma* and in memory of my father Drs. *M. Tamin*, who receive my deepest gratitude and love for their dedication and support during my study.

Finally, but most importantly, I would like to thank my wife *Rafina* and son *Danish Abqary* for their thoughtfulness and love during the course of this study. Their support and encouragement made this dissertation possible.

Table of contents

Declaration	ii
Abstract	iii
Acknowledgement.....	v
Table of contents	vi
List of Figure.....	xii
List of Tables.....	xx
Chapter 1	1
General Introduction	1
1.1 Introduction	1
1.2 Objective of the Dissertation.....	3
1.3 Significance and Innovation.....	5
1.4 Research Method of the Dissertation	5
1.5 Layout of the Dissertation	6
Chapter 2	9
Literature Review	9
2.1 Piezoelectric Energy Harvesting	9
2.1.1 History of Piezoelectricity.....	9
2.1.2 Piezoelectric Effect	9
2.1.3 Power Harvesting Through Piezoelectric Materials.....	10
2.1.4 Implantable and wearable system	11
2.1.5 Energy Harvesting using Fluid Motion	14
2.1.6 Cantilever-based Piezoelectric Generator and MEMS.....	16
2.2 Summary	28

Chapter 3	30
Finite Element Formulation for a Single Element Piezoelectric Beam Power Harvester	30
3.1 Electromechanical Single Finite Element Formulation for a Cantilevered Unimorph Piezoelectric Power Harvester	32
3.1.1 Single Finite Element Modelling	32
3.1.2 Electromechanical Coupled Field Piezoelectric Equations.....	35
3.2 Governing Dynamic Equation for Single Element Unimorph Cantilevered Piezoelectric Beam.....	38
3.2.1 The use of Extended Hamilton’s Principle for Deriving the General Electromechanical Dynamic Equation	38
3.2.2 Global Electromechanical Dynamic Matrix Equation Based on Electromechanical Vector Transformation	42
3.2.3 Frequency response function of the Direct Non-Orthonormalised Electromechanical Dynamic Equation	44
3.3 Finite Element Case Study for Single Unimorph Piezoelectric Element....	46
3.3.1 Properties and Geometry of the Unimorph Piezoelectric Element	46
3.3.2 Frequency Response of Electrical Voltage Output	48
3.3.3 Frequency response of Electrical Current Output	49
3.3.4 Frequency response of Electrical Power Output	50
3.4 Summary	51
Chapter 4	54
Finite Element Formulation for Multi Element Piezoelectric Unimorph Beam Power Harvester	54
4.1 Numerical Multi Element Distributed Cantilever Piezoelectric Unimorph Beam	54
4.1.1 Multi Finite Element Modelling.....	54
4.1.2 Local Electromechanical Dynamic Matrix Equation for Multi Element Cantilever Piezoelectric Unimorph Beam.....	55

4.1.3 Global Electromechanical Dynamic Matrix Equation for Multi Element Based on Electromechanical Vector Transformation	56
4.2 Validation of Multi-Element Piezoelectric Unimorph with the Analytical Method Published by (Alper Erturk & Inman, 2008a)	61
4.2.1 Convergence Study	61
4.2.2 Frequency Response of Electrical Voltage Output	63
4.2.3 Frequency Response of Electrical Current Output	65
4.2.4 Frequency Response of Electrical Power Output.....	67
4.3 Multi-Element Comparison of the Distributed Piezoelectric Unimorph Using Orthonormalised Method Published by (M. Lumentut & Howard, 2014)	70
4.3.1 Orthonormalised Finite Element Method.....	70
4.3.2 Material Properties and Geometry	74
4.3.3 Convergence, Mode Shape and FRF Displacement.....	74
4.3.4 Frequency Response of Electrical Voltage Output	77
4.3.5 Frequency Response of Electrical Current Output.....	79
4.3.6 Frequency Response of Electrical Power Output.....	80
4.3.7 Convergence Study Number of Elements with the Electrical Voltage, Current and Power Output at the First Resonance	81
4.5 Summary	83
Chapter 5	86
Modelling the Effect of Tip Mass Offset with Numerical Parametric Study	86
5.1 Electromechanical Finite Element model for the Unimorph with Tip Mass Offset.....	86
5.1.1 Modelling of the Unimorph Beam with Tip Mass Offset	86
5.1.2 Developing the Tip Mass equations for the Unimorph Cantilever Beam under Base Excitation.....	87
5.1.3 The Electromechanical Coupled Equation for the Unimorph Beam under Base Excitation with the Tip Mass.....	89

5.2 Configuration of the Dynamic Electromechanical Equations.....	92
5.2.1 Generalized Element Matrices for the Electromechanical Dynamic System with Tip Mass.....	92
5.2.2 Equation for Voltage, Current and Power Frequency Responses.....	93
5.3 Case study of the Dynamic Response of the Unimorph Beam with Tip Mass	94
5.3.1 Unimorph Beam Parameter Dimensions and Material Property Details .	94
5.3.2 Unimorph Beam with Tip Mass Voltage, Current and Power FRFs.....	95
5.3.3 The Absolute Dynamic Displacement FRFs of the Unimorph tip.....	101
5.4 Case Study of the Unimorph Beam with Tip Mass under Varying Piezoelectric Element Length	103
5.4.1 Electrical Voltage, Current and Power Output Frequency Response under Varying Piezoelectric Element Length	103
5.4.2 Comparison of Voltage, Current Dynamic Response of the Unimorph Beam with Varying Piezoelectric Element Length for Short and Open Circuit Resistances 680 Ω and 20.5 M Ω	111
5.4.3 The Unimorph Beam Power Output Dynamic Response with Varying Parametric Piezoelectric Element Length and Load Resistance	117
5.5 Summary	134
Chapter 6.....	135
Unimorph Beam Power Harvester with Different Orientations.....	135
6.1 Electromechanical Finite Element for Unimorph Beam with Different Orientation with Three Degrees of Freedom per Node.....	135
6.1.1 Finite Element Modelling with Different Orientation.....	135
6.1.2 Piezoelectric Coupled Field Mechanical and Electrical Equations.....	137
6.2 Global Electromechanical Finite Element Equation for the Distributed Piezoelectric Unimorph Beam with Different Orientations.....	145
6.2.1 Case Study without Tip Mass.....	149
6.2.2 Displacement Frequency Response with $\theta = 0^\circ$ Angle of orientation....	150

6.2.3 Voltage, Current and Power Output Frequency Response with $\theta = 0^\circ$	
Angle of orientation	151
6.2.4 Comparison of Voltage and Current Response as a Function of Angle of Orientation.....	153
6.2.5 Power Output Frequency Response Comparison with Varying Orientation Angle	156
6.3 Comparison between Axial Deformation and Non-Axial Deformation ...	162
6.4 Comparison Study Considering the Shifting Neutral Axis	165
6.5 Summary	168
Chapter 7	171
Experimental Power Harvesting of the Piezoelectric Unimorph Beam with Different Angle of orientation.....	171
7.1 Material Properties of the Unimorph Beam and Experimental Set up.....	171
7.2 Unimorph Frequency Response with 0° Angle of orientation	174
7.2.1 Validation of First Mode Electrical Voltage Frequency Response.....	174
7.2.2 Validation of First Mode Electrical Current Frequency Response	176
7.2.3 Validation of First Mode Electrical Power Output Frequency Response	177
7.3 Piezoelectric Unimorph Frequency Response with 30° Angle of orientation	178
7.3.1 Validation of First Mode Electrical Voltage Frequency Response.....	178
7.3.2 Validation of First Mode Electrical Current Frequency Response	179
7.3.3 Validation of First Mode Electrical Power Output Frequency Response	180
7.4 Piezoelectric Unimorph Frequency Response with 90° Angle of orientations	182
7.4.1 Validation of First Mode Electrical Voltage Frequency Response.....	182
7.4.2 Validation of First Mode Electrical Current Frequency Response	183

7.4.3 Validation of First Mode Electrical Power Output Frequency Response	184
7.5 Summary	186
Chapter 8	188
Summary, Conclusion and Future Work	188
References	192
Appendixes	202

List of Figure

Figure 2.1 Piezoelectric composite actuator, (Henry A Sodano et al., 2006).	11
Figure 2.2 Insole shoe mounted (Kymissis et al., 1998).	12
Figure 2.3 The piezoelectric array adapted from (Hobeck & Inman, 2012).	15
Figure 2.4 Self-powered wireless sensor for temperature and humidity (Arms et al., 2005).	19
Figure 2.5 Concept of piezoelectric design adapted from (Chen et al., 2006).	19
Figure 2.6 Different shape of cantilever adopted from (Goldschmidtboeing & Woias, 2008).	21
Figure 3.1 Single beam element with a total of four degrees of freedom.	33
Figure 3.2 Detail of unimorph beam with mode (3-1).	35
Figure 3.3 Modelling single finite element cantilevered piezoelectric unimorph under transverse base excitation.	47
Figure 3.4 FRFs single element electrical voltages output with varying load resistance.	48
Figure 3.5 FRFs single element electrical current output with varying load resistances.	50
Figure 3.6 FRFs single element power output with varying load resistances.	50
Figure 4.1 Electromechanical discretisation of piezoelectric unimorph adapted from (M. Lumentut & Howard, 2014).	55
Figure 4.2 Convergence study of coupled system resonance versus number of elements.	63
Figure 4.3 (a) FRFs electrical voltage using 20 discretised elements (b) First Mode (c) Second Mode.	64
Figure 4.4 Variation of voltage output and load resistance under base excitations at short and open circuit resonance frequencies for the first mode.	65
Figure 4.5 (a) FRF's electrical current using 20 discretised elements (b) First Mode (c) Second mode.	66
Figure 4.6 Variation of current output and load resistance under base excitations at the short and open circuit resonance frequencies of the first mode.	67
Figure 4.7 (a) FRFs of power electrical response with 20 discretised elements (b) First mode (c) Second mode.	68

Figure 4.8 (a) Variation in power output versus load resistance under base excitations at the short and open circuit resonance frequencies of the first mode (b) second mode (c) third mode.	70
Figure 4.9 Convergence study of the coupled system resonance versus number of element.	75
Figure 4.10 Modes shape of the first four unimorph beam modes with 50 discretised elements.	76
Figure 4.11 (a) FRFs of tip displacement with 50 discretised elements (b) The first Mode (c) The second Mode.	77
Figure 4.12 Electrical voltage FRFs with 50 discretised elements: solid line (proposed model) and round dot FE model; (Warman et al., 2014).	78
Figure 4.13 Variation of voltage output with load resistance for base excitation at the short circuit and at the open circuit resonance frequencies of the first vibration mode.	78
Figure 4.14 Electrical current FRFs with 50 discretised elements: solid line (proposed model) and round dot FE model; (Warman et al., 2014).	79
Figure 4.15 Variation of current output with load resistance for base excitations at the short circuit and at the open circuit first mode.	80
Figure 4.16 Electrical power FRFs with 50 discretised element: solid line (proposed model) and round dot FE model; (Warman et al., 2014).	80
Figure 4.17 Variation of power output with load resistance for base excitations at the short circuit and at the open circuit first mode.	81
Figure 4.18 Convergence of voltage resonance frequencies as a function of number of elements.	82
Figure 4.19 Convergence of electrical current resonance frequency under varying load resistance with number of elements.	82
Figure 4.20 Convergence of power output resonance frequencies with varying load resistance and number of elements.	83
Figure 5.1 (a) Piezoelectric unimorph beams with tip mass offset (b) Local element with arbitrary tip mass.	87
Figure 5.2 The voltage frequency response for the unimorph beam with tip mass (a) first three modes, (b) The first mode (c) The second mode.	96
Figure 5.3 Variation of voltage output and load resistance under base excitation at the short and open circuit resonance frequency for the first mode.	97

Figure 5.4 Unimorph beam electrical current FRFs with tip mass offset (a) FRFs first three modes, (b) First mode resonance, (c) Second mode resonance.	98
Figure 5.5 Variation of electrical current output against load resistance under base excitation for the first mode short and open circuit conditions.....	99
Figure 5.6 Power frequency response for unimorph beam with tip mass (a) first three modes, (b) The first mode (c) The second mode.	100
Figure 5.7 Variation of first mode power output with varying load resistance under base excitation for short and open circuit conditions.....	101
Figure 5.8 Tip displacement of the unimorph beam under varying load resistances in the range 680Ω to $100 \text{ M}\Omega$ under base excitation of 1 m/s^2 (a) The first three modes (b) The first mode (c) The second mode.	102
Figure 5.9 Variation of tip displacement output with varying load resistance under base excitation at the short and open circuit resonance conditions for the first mode.....	103
Figure 5.10 Piezoelectric unimorph beam with varying piezoelectric element length attached onto the substructure with tip mass.....	104
Figure 5.11 Electrical voltage FRFs using parametric piezoelectric length of 10 mm.	105
Figure 5.12 Electrical current FRF using parametric piezoelectric length 10 mm.	105
Figure 5.13 Electrical power FRF using parametric piezoelectric length 10 mm.	105
Figure 5.14 Electrical voltages FRF using parametric piezoelectric length 20 mm.	106
Figure 5.15 Electrical current FRF using parametric piezoelectric length 20 mm.	106
Figure 5.16 Electrical power FRF using parametric piezoelectric length 20 mm.	107
Figure 5.17 Electrical voltage FRFs with parametric piezoelectric length 30 mm.	108
Figure 5.18 Electrical current FRF with parametric piezoelectric length 30 mm.	108
Figure 5.19 Electrical power FRF with parametric piezoelectric length 30 mm.	108

Figure 5.20 Electrical voltages FRF using parametric piezoelectric length 40 mm.	109
Figure 5.21 Electrical current FRF using parametric piezoelectric length 40 mm.	109
Figure 5.22 Electrical power FRF using parametric piezoelectric length 40 mm.	110
Figure 5.23 Electrical voltage FRF using parametric piezoelectric length 50 mm.	110
Figure 5.24 Electrical current FRF using parametric piezoelectric length 50 mm.	111
Figure 5.25 Electrical power FRF using parametric piezoelectric length 50 mm.	111
Figure 5.26 Voltage frequency responses with varying length at short circuit resistance of 680 Ω : a) First two modes, b) Enlarged view for first mode, c) Enlarged view for second mode.	113
Figure 5.27 Voltage frequency responses with varying length at open circuit resistance of 20.5 M Ω : a) First two modes, b) Enlarged view for first mode, c) Enlarged view for second mode.	114
Figure 5.28 Short circuit current frequency responses with varying piezoelectric element length for 680 ohms resistance: a) First two modes, b) Enlarged view for first mode, c) Enlarged view for second mode.	116
Figure 5.29 Current frequency responses with varying length at open circuit resistance 20.5 M Ω : a) First two modes, b) Enlarged view for first mode, c) Enlarged view for second mode.	117
Figure 5.30 (a) Power harvesting FRF's for varying piezoelectric element length with load resistance 680 Ω . (b) First mode resonance frequency. (c) Second mode resonance frequency.	119
Figure 5.31 (a) Power harvesting FRF's of varying piezoelectric element length with load resistance 6 k Ω . (b) First mode resonance. (c) Second mode resonance.	121
Figure 5.32 (a) Power harvesting FRF's for varying piezoelectric element length with load resistance 18 k Ω . (b) First mode resonance. (c) Second mode resonance.	122

Figure 5.33 (a) Power harvesting FRF's of varying length piezoelectric element with load resistance 120 k Ω . (b) First mode resonance. (c) Second mode resonance.....	124
Figure 5.34 (a) Power harvesting FRF's of varying length piezoelectric element with load resistance 650 k Ω . (b) First mode resonance. (c) Second mode resonance.....	126
Figure 5.35 (a) Power harvesting FRF's of varying length piezoelectric element with load resistance 1.54 M Ω . (b) First mode resonance. (c) Second mode resonance.....	127
Figure 5.36 (a) Power harvesting FRF's of varying length piezoelectric element with load resistance 3.2 M Ω . (b) First mode resonance. (c) Second mode resonance.....	129
Figure 5.37 (a) Power harvesting FRF's of varying length piezoelectric element with load resistance 3.2 M Ω . (b) First mode resonance. (c) Second mode resonance.....	131
Figure 5.38 Result of changing resonance frequency under varying load impedances as a function of varying piezoelectric length for first mode.	131
Figure 5.39 Result of changing electrical power output under varying load impedances as a function of varying piezoelectric length for first mode.	132
Figure 5.40 Result of changing resonance frequency under varying load impedances as a function of varying piezoelectric length for second mode.....	133
Figure 5.41 Result of changing electrical power output under varying load impedances as a function of varying piezoelectric length for the second mode.	133
Figure 6.1 Piezoelectric unimorph beam with 6 degrees of freedom.	136
Figure 6.2 Bent segmented piezoelectric unimorph beam.	150
Figure 6.3 Segmented piezoelectric beam tip displacement frequency response of with 0 $^{\circ}$ angle of orientation.	150
Figure 6.4 Segmented piezoelectric voltage frequency response of 0 $^{\circ}$ angle of orientation.	151
Figure 6.5 Segmented piezoelectric current frequency response with 0 $^{\circ}$ angle of orientation.	152
Figure 6.6 Segmented piezoelectric power output frequency response with 0 $^{\circ}$ angle of orientation.	152

Figure 6.7 (a) Segmented FRFs voltage comparison for orientation angles from 0° to 90° (b) The first mode (c) The second mode.	154
Figure 6.8 (a) Segmented current FRFs comparison as a function of orientation angle (b) The first mode (c) The second mode.	156
Figure 6.9 (a) Segmented power output FRFs comparison as a function of orientation angle (b) The first mode (c) Second mode.	157
Figure 6.10 First mode FRF variation of the segmented piezoelectric system as a function of orientation angle from 0° to 90° with load resistances.	159
Figure 6.11 First mode comparison of power output FRFs of the segmented piezoelectric for varying angle of orientation from 0° to 90° with load resistance.	160
Figure 6.12 Power output at short and open circuit conditions for varying angles of orientation.	160
Figure 6.13 Power output of the segmented piezoelectric system with different angle of orientation at the first mode resonance.	162
Figure 6.14 Influence of axial deformation and axial electromechanical coupling with 0° angle of orientation for electrical voltage.	163
Figure 6.15 Influence of axial deformation and axial electromechanical coupling with 0° angle of orientation for power harvesting.	163
Figure 6.16 Influence of axial deformation and axial electromechanical coupling with 45° angle of orientation for electrical voltage.	164
Figure 6.17 Influence of axial deformation and axial electromechanical coupling with 45° angle of orientation for electrical power.	165
Figure 6.18 (a) Generalized neutral axis (b) Shifting neutral axis.	165
Figure 6.19 Electrical voltage frequency response comparison for generalized neutral axis and shifting neutral axis for 0° angle of orientation.	166
Figure 6.20 Electrical power output frequency response comparison for generalized neutral axis and shifting neutral axis 0° angle of orientation.	167
Figure 6.21 Electrical voltage frequency response comparison for generalized neutral axis and shifting neutral for axis 45° angle of orientation.	167
Figure 6.22 Comparison electrical power output frequency response for generalized neutral axis and shifting neutral axis of 45° angle of orientation. ...	168
Figure 7.1 Segmented unimorph beam configuration with varying angle of orientation.	173

Figure 7.2 (a) Experimental test set up (b) piezoelectric unimorph samples with 0°, 30° and 90° orientations.	174
Figure 7.3 (a) Voltage frequency response comparison between numerical (solid line) and experimental analysis (round dot) for 0° angle (flat) orientation (b) The first mode resonant voltage peak amplitude under the base excitation with the short circuit and open circuit resistances (c) 3-D plot.	175
Figure 7.4 (a) Electrical current frequency response comparison between numerical (solid line) and experimental analysis (round dot) for 0° angle (flat) orientation (b) Current under base excitation at short and open circuit (c) 3-D plot.	177
Figure 7.5 (a) Power output frequency response comparison between numerical (solid line) and experimental analysis (round dot) for 0° angle (flat) orientation (b) Variable power under base excitation at short and open circuit resonance (c) 3-D plot.	178
Figure 7.6 (a) FRFs voltage comparison between numerical (solid line) and experimental analysis (round dot) for 30° angle of orientation (b) Voltage and load resistance under short and open circuit frequency excitation (c) 3-D plot.	179
Figure 7.7 (a) FRFs current comparison between numerical (solid line) and experimental analysis (round dot) for 30° angle of orientation (b) Current and load resistance under base short and open circuit frequency excitation (c) 3-D plot.	180
Figure 7.8 FRFs of power output comparison between numerical (solid line) and experimental analysis (round dot) for 30° angle of orientation (b) current and load resistance under short and open circuit base excitation (c) 3-D plot.	181
Figure 7.9 (a) Voltage frequency response comparison between numerical (solid line) and experimental analysis (round dot) for 90° angle of orientation (b) Voltage and load resistance under short and open circuit base excitation (c) 3-D plot.	183
Figure 7.10 Electrical current frequency response comparison between numerical (solid line) and experimental analysis (round dot) for piezoelectric with 90° angle of orientation (b) Current and load resistance response under short and open circuit base excitation (c) 3-D plot.	184
Figure 7.11 Power output frequency response comparison between numerical (solid line) and experimental analysis (round dot) for 90° angle of orientation (b)	

Power output and load resistance under short and open circuit base excitation (c)	
3-D plot.	186
Figure A.1 Unimorph beam with section a-a view	202

List of Tables

Table 3.1 Geometrical and material properties of the piezoelectric unimorph beam.	47
Table 4.1 Number of element and the frequencies of the first six modes.....	62
Table 4.2 Properties of piezoelectric unimorph beam material.	74
Table 5.1 Piezoelectric unimorph beam properties and geometry details.	95
Table 5.2 Frequency and voltage magnitude for first two resonance modes with load resistance 680Ω and varying piezoelectric element length.	112
Table 5.3 Varying frequency and voltage magnitude for the first two modes with load resistance $20.5 \text{ M}\Omega$ and varying piezoelectric element length.	114
Table 5.4 Frequency and electrical current magnitude for the first two modes with load resistance 680Ω and varying piezoelectric element length.	115
Table 5.5 Frequency and electrical current magnitude for the first two modes with load resistance $20.5 \text{ M}\Omega$ with varying piezoelectric element length.	117
Table 5.6 Electrical power outputs for the first two resonant modes with load resistance 680Ω and varying piezoelectric element length.....	118
Table 5.7 Detail frequency and electrical power outputs for first two resonance modes with load resistance $6 \text{ k}\Omega$ and varying piezoelectric element length.	120
Table 5.8 Detail frequencies and electrical power outputs for the first two resonance modes with load resistance $18 \text{ k}\Omega$ and varying piezoelectric element length.....	121
Table 5.9 Detail frequencies and electrical power outputs for the first two resonance modes with load resistance $120 \text{ k}\Omega$ and varying piezoelectric length.	123
Table 5.10 Detailed frequencies and electrical power outputs for the first two resonance modes with load resistance of $650 \text{ k}\Omega$ for varying piezoelectric length.	125
Table 5.11 Detailed frequencies and electrical power outputs for the first two resonance modes with load resistance of $1.54 \text{ M}\Omega$ and varying piezoelectric length.....	126

Table 5.12 Detailed frequencies and electrical power outputs for first two resonance modes with load resistance 3.2 M Ω and varying piezoelectric length.	128
Table 5.13 Detailed frequencies and electrical power outputs for first two resonance modes with load resistance 20.5 M Ω and varying piezoelectric length.	130
Table 6.1 Comparison of first two modes electrical voltage responses with resistance 100 Ω	154
Table 6.2 Comparison of first two modes electrical current responses with resistance 100 Ω	155
Table 6.3 Comparison of modes one and two electrical power responses with resistance 100 Ω	157
Table 6.4 Comparison of modes one and two electrical power responses with resistance 1 k Ω	158
Table 6.5 Comparison of modes one and two electrical power responses with resistance 10 k Ω	158
Table 6.6 Comparison of modes one and two electrical power responses with resistance 100 k Ω	158
Table 6.7 Comparison of modes one and two electrical power responses with resistance 1 M Ω	159
Table 6.8 Maximum power output and resistances under base excitation for short and open circuit resonances conditions.	161
Table 6.9 Maximum power output and crossover resistances under base excitation for the first mode.	161
Table 7.1 Properties and geometries of the piezoelectric unimorph beam.	173

Chapter 1

General Introduction

1.1 Introduction

In the last decade, energy harvesting using smart structures has attracted the attention of many researchers and principally this energy is harvested from the waste energy from the surrounding environment sources. The waste energy can be extracted from vibrating devices and structures and it can be utilised to power electronic devices, supplying direct current into rechargeable batteries. Presently, smart structures using piezoelectricity have received a great deal of interest and promising technologies are being developed which can be used in future applications. One of many applications being considered is for powering smart wireless sensors for health condition monitoring of structures or machines. Since the wireless technology requires continuous energy consumption, batteries are one of the most usable tools to provide the power. In real life, battery technology has shown significant advancement of features, but in the end the batteries still face the limitation of capacity which has a life time for supplying the energy.

Smart structure power harvesting and related technology shows great potential for providing support for wireless systems. The use of piezoelectric material has potential benefits for the development of lifetime energy generators and it also gives a reasonable prospect for microelectromechanical design having compact configuration and is very sensitive to the vibration even for very low input motion. In addition, research into the use of piezoelectric elements in the application of energy conversion requires specialist knowledge of the theoretical methods of solid mechanics material properties and geometrical structures.

Smart piezoelectric material often functions as an actuator or sensor as a result of the interaction of linear electromechanical coupling between mechanical and electrical states. The reverse piezoelectric effect exhibits the generation of mechanical strain from the applied electrical field and mostly this method is applied for control of structural vibration. On the other hand the direct piezoelectric effect results from the

applied mechanical force and produces electrical charge from the piezoelectric materials and has given rise to a wide range of uses of the piezoelectric material as sensors as well as power generators in application.

Literature survey about the piezoelectric generator has been given by (Henry A Sodano, Inman, & Park, 2004) . Other published works reviewing the piezoelectric literature is given again by (Anton & Sodano, 2007) and (Priya, 2007b). The contribution of the previous research literature provides the development overview of piezoelectric energy harvesting research including different prototype design applications and represents very useful information for developing future power harvesting applications. Extraction of waste energy from the environment to electrical power can be optimised by the addition of electronic systems that are capable of recharging the batteries for wireless sensor systems (Roundy & Wright, 2004) and (Henry A Sodano, Inman, & Park, 2005b).

There has been numerous research into power harvesting modelling with the following discussion focusing on the use of analytical and finite element methods. Analytical investigation of piezoelectric materials attached to the structure was earlier presented by (Wang, Ehlers, & Neitzel, 1997), however this research was limited to show the analytical investigation on the static model. Analytical power harvesting that utilised Hamilton's principle with approaching Rayleigh-Ritz solution for unimorph and bimorph beam energy harvester were presented in (M. F. Lumentut & Howard, 2009), (Noël E Dutoit, Wardle, & Kim, 2005) and (H. A. Sodano, Park, & Inman, 2004). A research paper that discussed the distributed parameter modelling of the piezoelectric unimorph beam with the solution using the Euler–Bernoulli beam assumption is given by (Alper Erturk & Inman, 2008a).

In addition, for the power harvesting area the concept of finite element methods have been shown to provide another alternative solution technique for investigating self-powered devices. Some beginning research using finite elements for modelling the piezoelectric vibration response was explored by (Allik & Hughes, 1970). In the power harvesting research development in recent years, the finite element method has been developed by utilising the concept of Hamilton's principle and the solution of

Rayleigh-Ritz equations (M. F. Lumentut, Teh, & Howard, 2008), (Elvin & Elvin, 2009b), (Junior, Erturk, & Inman, 2009) and (M. Lumentut & Howard, 2014).

This research investigates the application of smart structures with coupled piezoelectric material and brass metal substructure known as a unimorph beam. The research shows the development of the mathematical electromechanical finite element equations with different types of design. The electromechanical finite element model for the piezoelectric unimorph beam is developed with a solution using a direct non-orthonormalised method whereas most other published research papers promote the use of the orthonormalised method. Exploration research using the proposed method is firstly applied to a single finite element beam and is then followed by the discussion of more complex designs such as attaching tip masses to the unimorph beam, varying the geometry of the piezoelectric component and then considering a segmented design with different angles of orientation of the piezoelectric unimorph beam.

1.2 Objective of the Dissertation

This thesis addresses the application of numerical methods solution for the piezoelectric unimorph beam. The purpose of the methods presents the dynamic behaviour of the piezoelectric unimorph beam for generation of the electricity from the ambient mechanical vibration. The methods are carried out by implementing Hamilton's principle, electromechanical coupling equation and frequency response functions (FRFs) using non-orthonormalise solution.

The main objective of the research is to develop the analysis of numerical methods for power harvesting of the piezoelectric unimorph beam. The resulting solution for FRFs are used to investigate the generating electricity of different models piezoelectric unimorph beam.

This dissertation contains a number of chapters and each chapter presents the development of the general aim of the research for understanding the concept of the coupled electromechanical system.

Chapter 1 purposes to present the introduction, objective research, innovation research, research method and layout of the thesis.

Chapter 2 aims to present the literature study and to show the developing power harvesting research in recent years and research gap.

Chapter 3 aims to show the step by step derivation of the electromechanical coupling equation based on developing the energy equation and the corresponding linear constitutive equation to find the governing dynamic electromechanical equations. The dynamic electromechanical equations were defined using the direct non-orthonormalisation method to find the frequency response functions for voltage, current and power output.

Further discussion in chapter 4, extends the application of the previous electromechanical finite element using multi-element discretisation. The purpose of chapter 4 is to check the frequency response function using non-orthonormalised methods against other methods such as the analytical and finite element methods using orthonormalised approaches.

Chapter 5 discusses the modelling of the piezoelectric system with additional tip mass and parametric study of the length of the piezoelectric element attached to the substructure.

The purpose of chapter 6 is presented to show the electromechanical derivation of the piezoelectric unimorph with different angle of orientations using six degrees of freedom per element and the effect of changing the angle of orientation of the unimorph beam.

Chapter 7 presents the comparison study between simulation and experimental tests. The investigation of the piezoelectric unimorph beam is given using angle of 0° , 30° and 90° orientations.

Chapter 8 presents the research conclusion found in the thesis and provides a discussion on future research opportunities.

1.3 Significance and Innovation

The significant innovation of this research shows the numerical derivation using finite element methods to show the frequency response function for the electrical voltage, current, power harvesting under contribution of axial, non-axial deformation and shifted neutral axis. In addition, a new solution of the frequency response function using direct methods with non-orthonormalisation is proposed in this dissertation as no other researcher discussed this method previously.

Discussion of a single element with four degrees of freedom (non-axial contribution) shows the step by step process governing the electromechanical dynamic equation that is easily adapted into the multi-element discretisation structure. A new design is investigated for the piezoelectric segmented unimorph beam with different angle of orientation having six degrees of freedom (axial contribution). The effect of the neutral axis position for asymmetrical and non-attached piezoelectric elements is shown to provide crucial contribution in the resulting response of electrical voltage, current and power.

1.4 Research Method of the Dissertation

This research investigates the energy harvesting for piezoelectric unimorph beams using different models. The solution of the electromechanical dynamic equation is derived by finite element analysis. The numerical analysis is developed based on having four and six degrees of freedom for each element. The analytical equations are explored by adapting the energy equation based on Hamilton's principle. Exploration of the electromechanical coupled equation is based on the linear constitutive relationship of the substructure and for the piezoelectric material. The resulting linear constitutive equation can be adapted into energy equations, including the contributions of mechanical and electrical energy equations. Derivation of the energy equation results in the electromechanical dynamic equation in the form of local matrix functions. The governing local matrix of the electromechanical dynamic equation can be extended into the generalised global matrix form. It should be noted that changing the electromechanical coupled equation of the local matrix into global matrices can be formulated using the electromechanical coupled discretisation based on vector

transformation. The governing global electromechanical dynamic equation can be solved using harmonic steady state base input motion. The process of finding the frequency response function can use the direct method with non-orthonormalised solution. The dynamic frequency responses for voltage, current, power and dynamic displacement can be explored after transforming the frequency response function into the program for the software simulation. In this research, MATLAB software was used to transform the FRFs equations and a program has been written to present the solution. In order to confirm that the program presents the correct solution, the resulting research has been validated using previous published research.

1.5 Layout of the Dissertation

This dissertation is presented in 8 chapters and each chapter discusses different aspects for example, background of research, literature review and detailing of the analysis numerical analysis for the solution of the piezoelectric unimorph power harvesting beam. Verification of the simulation research is explored using the available published papers and also experimental tests. The detailed outline of each chapter is given below.

Chapter 1 gives the detailed general introduction of the energy harvesting research using different model applications. This section shows the main objective of research, the significant innovation of research such as developing the method and formulating the proposed model and the general outline of each chapter.

Chapter 2 presents the previous related work of the energy harvester research using smart structure material. The literature review shows the earliest published research through to the recent years until 2015. The previous research is presented into different classifications of the various types of research based on the applications.

Chapter 3 shows the mathematical finite element solution for a single element with a total of four degrees of freedom. Here, the single element solution shows the derivation of the local matrix equations and the electromechanical coupling equation as they will be substituted into the energy equation based on Hamilton's principle. The global electromechanical dynamic matrices are derived based on Hamilton's equation with the addition of Rayleigh damping. The general solution of the global

electromechanical dynamic equation can be formulated using the steady state harmonic base acceleration and the resulting derivation gives the frequency response functions (FRFs) for voltage, current and power output.

Chapter 4 presents the multi-element investigation of the power harvesting piezoelectric unimorph beam using finite elements. Here, the same method is used to derive the FRFs equations but in this case the problem uses multi-element discretisation. Electromechanical coupling equations based on element discretisation and coupled vector transformation are presented in detail to show the processing of the local transformation to the global matrix. The simulation results from the multi-element model is verified by those using the previous published research.

Chapter 5 shows the investigation of the power harvesting response using multi elements with the addition of a tip mass attached to the end of the piezoelectric unimorph beam. The energy harvester analysis is also investigated using the parametric case study with varying length of the piezoelectric element attached to the substructure. The varying length of the piezoelectric element caused the shifting of the neutral axis between the attached and non-attached piezoelectric areas as discussed in this research. In addition, another advantage of varying the piezoelectric length can show optimisation in design of the energy harvester.

Chapter 6 presents a new proposed design of the segmented unimorph beam with different angles of orientations. In this chapter, the segmented piezoelectric unimorph beam with different angle of orientations such as 0° , 10° , 20° , 30° , 40° , 50° , 60° , 70° , 80° and 90° are explored to show the resulting dynamic frequency response of voltage, current and power. The mathematical finite element model including the contribution from the axial response is also presented, followed by the transformation of the electromechanical coupling matrices for the segmented piezoelectric elements. The segmented piezoelectric system can give a different form of frequency response function depending on the electrical connection changes. However, this research is only limited to parallel connection, though serial connection can be considered in future research.

Chapter 7 presents the comparison of results between the numerical and the experimental tests for the piezoelectric unimorph beam with angle of orientations of 0° , 30° and 90° . The comparison of results are presented for the frequency responses of electrical voltage, current and power output.

Chapter 8 presents the major conclusions of the research. References are also given to show the major research literature that is most relevant to the research. The appendix provides some additional information that were not explained clearly in the contents of the thesis chapters.

Chapter 2

Literature Review

2.1 Piezoelectric Energy Harvesting

This chapter presents a literature review of energy harvesting research development for various types of power harvesting applications through to the recent years. Generally, three different types of power harvester generators utilise mechanical motion such as electrostatic, electromagnetic and piezoelectric device. The next section focuses on energy harvesting research using the piezoelectric device in different applications.

2.1.1 History of Piezoelectricity

Piezoelectric materials have been used for many years and provide a convenient means of measuring response signals from various sensors. The piezoelectric effect was demonstrated the first time by two Brothers (Curie & Curie, 1880). That breakthrough was the beginning of the development of the theory of piezoelectricity. The theory was continuously developed and idealized by the further work of (Lippmann, 1881) and (Voigt, 1908) at the beginning of the 20th century. For many decades many research works continued into the properties and characteristics of piezoelectric materials.

Piezoelectric components are made from natural crystals such as Quartz, Rochelle Salt and Tourmaline as well as from manufactured ceramics such as Barium Titanate and Lead Zirconate Titanates (PZT). In recent years, the piezoelectric technologies have been developed to utilise the ability of piezoelectric material to be used for example as actuator, sensor and generator.

2.1.2 Piezoelectric Effect

The piezoelectric effect contributes to the development of significant engineering applications especially in relation to vibration matters. The piezoelectric effects can be used in two different formations either as sensors or as actuators. The sensor application represents the direct effect which transforms the external mechanical field

into the electrical field to give the electric charge. In this mode, the applied stress acts onto the surface of the piezoelectric material, which gains the electric charge depending on the polarity direction of the field.

On the other hand, the actuator application represents the converse effect where the piezoelectric material transforms the electrical energy into the induced strain. In this case, the applied voltage generates an electric field and induces the material deformation due to the polarisation direction.

The derivation of the electromechanical dynamic equation of a coupled piezoelectric beam was introduced the first time by (Hagood, Chung, & Von Flotow, 1990) . The research focused on the active control of structural vibration.

2.1.3 Power Harvesting Through Piezoelectric Materials

The research literature review on energy harvesting using piezoelectric material has been presented in several recent research papers (Henry A Sodano et al., 2004), (Anton & Sodano, 2007), (Beeby, Tudor, & White, 2006) and (Priya, 2007a). Those papers reviewed the significant information of vibration energy harvesting research.

According to (Roundy, Wright, & Rabaey, 2003) resonance frequency of the piezoelectric material with mode-31 is lower than that with the mode-33 when the piezoelectric material was excited under the natural vibration environment. Even though the piezoelectric mode-31 results in lower frequency but it was able to provide high power.

(Richards, Anderson, Bahr, & Richards, 2004) presented the optimisation of the coupling coefficient for cantilever beam applications. The resulting model showed that the coupling coefficient of piezoelectricity changed as the electrode size changed. They found that the maximum power could be obtained when the electrode covered at least 42% of the top surface area. Another way the piezoelectric coefficient could be increased was by changing the passive elastic layer to give the optimal piezoelectric layer thickness. The result showed that the residual stress has given the greatest effect on the coupling coefficient among all the design parameters.

(Henry A Sodano, Inman, & Park, 2005a) compared piezoelectric devices to identify the feasibility using piezoelectric material in practical applications. The piezoelectric materials of Lead-Zirconate-Titanate (PZT), Quick Pack (QP) and Macro-fibre Composite (MFC) were experimented to explore the abilities of the piezoelectric materials to be used to transform the mechanical ambient vibration into electricity which recharged a battery. The required recharging time was analysed. The specimens were tested under the natural resonance condition with frequencies ranging from 0-500 Hz. The frequency of excitation was taken based on random vibration from the air compressor of a passenger vehicle. The results showed the comparison of the three types of piezoelectric devices where the PZT material gave the highest efficiency for charging the battery rather than the other two materials.

Experiments of the use of composite piezoelectric materials for generating power was studied by (Henry A Sodano, Lloyd, & Inman, 2006) to find the effectiveness of using the fibre composites of Quick Pack, MFC and Quick Pack IDE piezoelectric devices as shown in figure 2.1. The result from the experimental study showed that over the first three modes of resonance excitation, the Quick Pack presented better power output rather than the MFC and Quick Pack IDE devices.

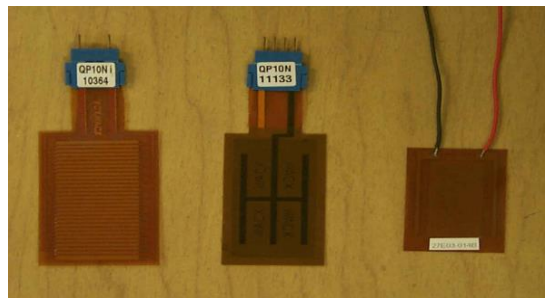


Figure 2.1 Piezoelectric composite actuator, (Henry A Sodano et al., 2006).

2.1.4 Implantable and wearable system

The development of human wearable power harvesting devices has become an interesting research area showing promising developments to meet several future needs. The early study of wearable energy power harvesting devices was inspired using animals and this research was studied by (Häsler, Stein, & Harbauer, 1984) for low frequency vibration. A PVDF piezoelectric system was attached to a Mongrel dog rib cage to generate electrical power from a dog weighing 25 kg, while breathing. The

experimental research showed 18 V of peak potential where the maximum power output reached 17 μ W. Continuing research into human wearable power harvesting systems has been shown by (Starner, 1996), where the paper showed other possible sources for generating electrical power from daily human activities in terms of body movements. Simple mathematical explanations were given in the paper including the calculation of the power from body heat, human breath, upper limb motion, blood pressure and human walking. Further research of human wearable systems were developed by some other researchers (González, Rubio, & Moll, 2002), (Starner & Paradiso, 2004), (Mitcheson, Yeatman, Rao, Holmes, & Green, 2008) and presented the possibility to use the electrical power to operate low power electronic equipment.

Utilising the energy harvester from the inside and outside of the soles of shoes was developed by (Kymissis, Kendall, Paradiso, & Gershenfeld, 1998) with the proposed design as shown in figure 2.2. The research has shown three different methods for generating power using the unimorph concept. First, the unimorph was employed directly in the soles of shoes using a PVDF piezoelectric device. A very thin PVDF piezoelectric element was attached as a flat structure directly into the shoe sole. Secondly, the unimorph power harvester was bent as the sheet of PVDF was deformed into a curved shape so that the electrical power can be generated by the contraction and expansion. Thirdly, the heel strike pressure was used where the piezoelectric element was squeezed during walking.

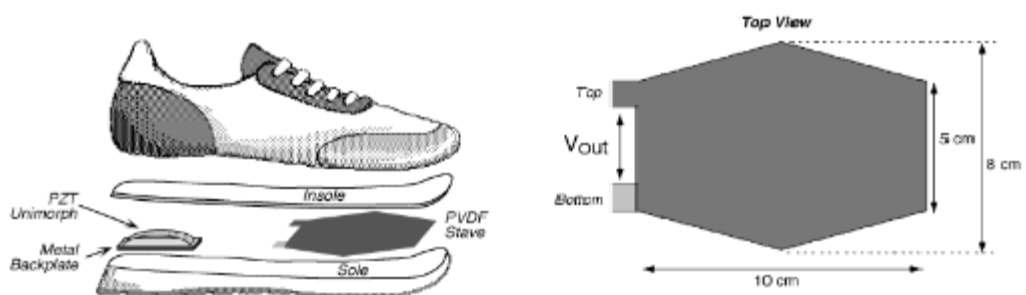


Figure 2.2 Insole shoe mounted (Kymissis et al., 1998).

Further implementation of wearable systems was shown by (Kymissis et al., 1998) who introduced the adapted electromagnetic machine system onto shoes. The advantage was found to be that the electrical response provided higher efficiency of

power conversion. However, this method was shown to be very difficult to be integrated into the shoe and was very uncomfortable during walking whereas placing the PVDV material inside the shoe soles was found to be more easily adapted.

Early research using low vibration for powering wireless sensors was given by (Roundy et al., 2003). The research showed the numerous possibilities of using low vibration sources that can be used in many different applications. Review of the energy power harvester using low vibration from human activities was further published by (Paradiso & Starner, 2005) with more applications of human wearable systems for generating power. Investigation of low and high input force power harvesting was shown by (Platt, Farritor, & Haider, 2005). The research demonstrated the possibility of power harvesting for biomedical applications. Here, the electric power was used to promote bone growth where this method was applied for the human implantation of piezoelectric materials within the total knee replacement. Based on the experiments, it was shown that the low input force could generate power of 225 μW whereas in high input force situations the power output of 4 mW was obtained.

Optimization design of the unimorph piezoelectric device using PZT inserted into the shoe sole was modelled with different constructions. The system was designed by changing the shape of the unimorph device into a curved shape to increase the charge generation as shown by (Yoon, Washington, & Danak, 2005). The unimorph design using different dimensions was also investigated by (Mateu & Moll, 2005).

Investigation of the energy available from a backpack strap during the human walking using PVDF was presented by (Granstrom, Feenstra, Sodano, & Farinholt, 2007). The electrical power was generated when the PVDF was strained. The fatigue test of the PVDF was investigated during use in the outdoor environment undergoing cyclic loading. The simulation and experiments of the PVDF materials were performed using different thicknesses of 28 and 52 μm . The wires were connected into serial and parallel connection where the loading was set at 444 N. The resulting research showed good agreement between the simulation and the experimental tests with the average power of 45.6 mW being harvested for the strap using thickness of 52 μm .

The mechanical amplified stack actuator for backpack energy harvesting from human motion was again proposed by (Feenstra, Granstrom, & Sodano, 2008). The amplified stack actuator was found to be useful to reduce the stiffness of the system to achieve the appropriate level of energy harvesting where the amplified stack actuator system was designed and fabricated using a CAD and CNC milling machine. The electrical voltage was measured using a SPACE data acquisition system with 10X probe. The 10X probes enabled the experiments to achieve increased accuracy in higher levels of impedance. The results showed that the power output of 0.175 mW can be achieved using the stack actuator in simulation whereas in the experiment 0.176 mW was obtained.

2.1.5 Energy Harvesting using Fluid Motion

Energy harvesting research using fluid motion was undertaken by some researchers to investigate the feasibility of using fluid motion to extract electrical energy from waves. Employing piezoelectric components to windmill structures was also investigated by (Schmidt, 1992) using a compressed piezoelectric PVDF. Theoretically, the research showed the power output could generate around 100 W/cm³. The results showed that at a rotating rotor frequency of 1000 Hz, the power output obtained was 91 W/cm³ with efficiency of 72 % whereas for 60 Hz rotating frequency the power output of 5.1 W/cm³ with efficiency of 67% was obtained.

A research paper on energy harvesting using submerged piezoelectric materials underwater was developed by (Taylor, Burns, Kammann, Powers, & Wel, 2001). The development technology was called the energy harvesting eel and the generator was made using a polymer strip of piezoelectric material. Here, the piezoelectric material was placed upstream to make enough force to vibrate the piezoelectric material by the fluid motion. The eel prototype was tested in a flow tank with eel dimension length of 9.5 μm, width 3 μm and thickness 150 μm. The voltage generation by using the eel was measured and recorded for water velocity of 5 ms⁻¹ with peak voltage recorded of 3 V.

Piezoelectric grass was proposed by (Hobeck & Inman, 2012) where the novel application of this research was to develop an application of piezoelectric materials in

grass situated in highly turbulent fluid flow environments. The figure 2.3 below shows the proposed piezoelectric research grass application. The resulting research showed that the piezoelectric element with a steel PZT wafer gave the maximum power output of 1 mW per cantilever whereas the piezoelectric element with Mylar piezo film gave the maximum power of 1.40 μ W.

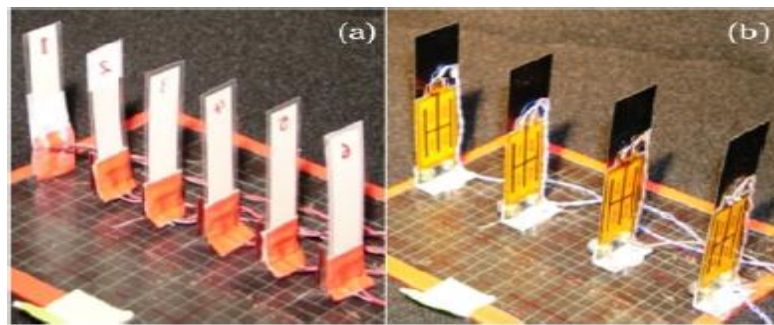


Figure 2.3 The piezoelectric array adapted from (Hobeck & Inman, 2012).

(Allen & Smits, 2001) researched the possibility of placing a piezoelectric EEL membrane under an unsteady flow field. The application of the Von Karman Vortex was applied to get a bluff body to induce the oscillation to the membrane under unsteady flow. Here, the investigation showed that the coupling coefficient under the hydrodynamic vibration test can be optimized to maximise the strain energy and mechanical power under unsteady flow.

A further potential energy source for power harvesting is with the use of wind currents. The concept of energy harvesting using wind was applied by giving a strain to the piezoelectric element. A design of a piezoelectric energy harvesting windmill using a conventional fan was given by (Priya, 2005). The experiment showed the effect when the wind developed by the fan impacted the piezoelectric bimorph beam. Research showed that under a wind speed of 16 km/hr, the windmill gave a power output of 7.5 mW with load resistance of 6.7 k Ω . In addition, (Akaydin, Elvin, & Andreopoulos, 2010) researched the application of piezoelectric energy harvesting in highly unsteady turbulent fluid flow. The voltage was generated using a flexible piezoelectric beam inside the tube under turbulent flow at high Reynold numbers where the tube was also vibrated. The coupled response was also simulated by three different transformations from the aerodynamic field to the structural vibration, then into the electrical response.

The energy harvesting using wind energy was continuously developed in the last decade, (Bibo, Li, & Daqaq, 2011) approached wind power harvesting using a piezoelectric unimorph by developing an aero elastic micro-power generator. (Q. Zhu, 2011) introduced wind energy harvesting using a flapping foil propeller, and (Sirohi & Mahadik, 2011) introduced a wind energy harvester that utilised a galloping beam concept. The galloping concept was also applied by (L. Zhao, Tang, Yang, & Asme, 2012), (A Abdelkefi, Hajj, & Nayfeh, 2012) and (Abdessattar Abdelkefi, Yan, & Hajj, 2013).

Recently, (H. Kim et al., 2015) propose a practical way of designing piezoelectric power harvesting which was based on the hose vibration of an outdoor condenser unit of an air conditioning system. The piezoelectric power harvesting system was used to operate five wireless sensor units. Here, the attachment location of the piezoelectric power harvesting device was targeted on the operating deflection of the mechanical system. The piezoelectric material was cut into segments and attached onto the areas of the maximum deflection. The advantages of the proposed practical approach is not only to find the best location of attaching the piezoelectric material but also in reducing the apparent voltage cancellation effect. Based on the investigation, the resulting power harvesting device could provide enough power to operate a five wireless sensor network.

2.1.6 Cantilever-based Piezoelectric Generator and MEMS

Power harvesting using unimorph, bimorph and microelectromechanical systems have been of great interest for many researchers because of the compatibility and ease of application. In addition, MEMS application using piezoelectric elements as power generators was investigated by (Lu, Lee, & Lim, 2003). In the research the frequencies of vibration were shown to give a very important influence on the power performance as increasing the frequency of vibration could increase the power output. The research compared the feasibility of two piezoelectric materials PZN8% -PT and PZT-PIC 255. The results of the PZN8%-PT gave the maximum power of 0.66 mW at load resistance of 65 k Ω whereas the PZT-PIC255 gave the maximum power of 0.571 mW at a load resistance of 215 k Ω with the piezoelectric length of 5 mm, 1 mm width and thickness 0.1 mm covers all the surface piezoelectric beam with the thickness of 0.4 mm. Their

research showed that the PZT-PIC 255 was highly sensitive to load resistance and the PZN8%-PT was highly sensitive to the excitation frequency.

Research investigation of small cantilever piezoelectric power harvesting systems for powering wireless sensor operations was performed by (Roundy & Wright, 2004). The generator was designed as a two layer bender and a total volume of 1 cm^3 . A mass was placed on the free end of the cantilever beam and the chosen source of vibration has amplitude of 2.5 ms^{-2} with frequency of 120 Hz. The result showed that the transferred power from varying resistive load could reach to $375 \text{ } \mu\text{W cm}^{-3}$.

Design of a MEMS power generating device was performed by (Jeon, Sood, Jeong, & Kim, 2005) where the device was to resonate under particular frequencies from the vibration source. The thin film was added as the tip mass at the end of the structure and the cantilever power harvester was designed to be a flat structure. The novel application used a combination of the generator modes d_{31} and d_{33} to obtain higher voltage under operation. The experiment showed that the first three resonance modes were 13.9 Hz, 21.9 Hz and 48.5 Hz. The experimental result for the first resonant mode response showed that the charge coefficient was $4.14 \text{ pC}/\mu\text{m}$ with respect to the relative tip displacement. The dimension of the PZT was given by length of $170 \text{ } \mu\text{m}$ and width of $260 \text{ } \mu\text{m}$ whereas the resulting power was $1 \text{ } \mu\text{W}$ under load resistance of $5.2 \text{ M}\Omega$.

An earlier study for MEMS device design consideration was introduced by (Noël E Dutoit et al., 2005). The research tried to characterise the ambient energy sources and concluded the significant power based on peak selection from the previous research covered the frequency excitation range from 100 to 300 Hz. The information provided very useful consideration for their next MEMS design. Moreover, (Noel E Dutoit & Wardle, 2006) presented the MEMS prototype which was called the MPVEH for low vibration harvester. The model and design of the power harvester were based on the required power consumption of the wireless sensor during operation. Here, the research targeted that the model was designed for operation at an acceleration amplitude of 2.5 m/s^2 with frequency of 150 Hz and power density of $313 \text{ } \mu\text{W}/\text{cm}^3$. This test was conducted using PZT-5A and PZT-5H. As the fabrication model was set for a specific operating point, 3 variables of the geometry were optimised in a single

device to reach the target model. The research found that the performance of the device was directed to the maximum allowable strain and the optimization design was based on the quality factor and the vibration input.

Investigation of the unimorph beam based on storage device type has been presented by (Henry A Sodano et al., 2005b). This research introduced the attachment of piezoelectric elements to an aluminium substructure. Two types of storage devices were introduced in this research. The first type was using the capacitor and the second was using a nickel metal hydride battery. The piezoelectric material was a PZT PSI-5H4E ceramic and the excitation source was taken from a random signal generator with frequency range from 1-1000 Hz. The results showed that when using the capacitor, it appeared to be better to use low-frequency and low impedance. It was found that when using high frequency, the capacitor discharges and the charging became so fast that the capacitor provide only very low storage of the energy. In addition, the result from the battery test showed that it appears the battery responds better at low frequency for effective recharging and discharging. In performing the test, the battery was charged during 0.5 hours using the excitation signal. The excitation signal used was similar to the vibration of the automobile compressor.

A self-powered wireless sensor for temperature and humidity measurement was designed and fabricated by (Arms, Townsend, Churchill, Galbreath, & Mundell, 2005). The design used the cantilever beam to harvest the mechanical energy vibration for powering the sensor and the wireless data transmission. The device was designed to be used in operation under low input vibration of the order of 1 m/s^2 . The integrated system is given in figure 2.4.

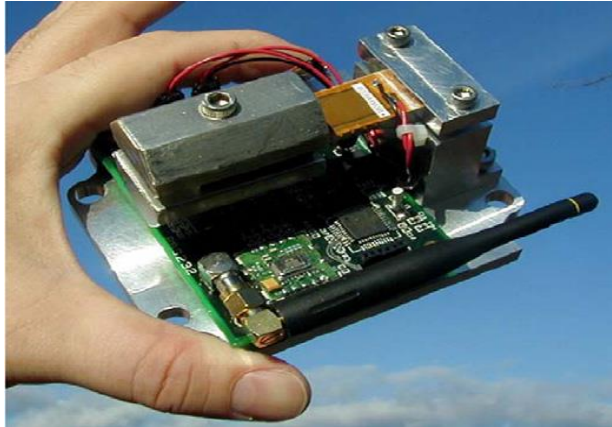


Figure 2.4 Self-powered wireless sensor for temperature and humidity (Arms et al., 2005).

Power harvesting using a vibration-induced micro power generator has been researched by (Chen, Wang, & Chien, 2006). The design was modelled using the Euler-Bernoulli beam and Rayleigh-Ritz solution. The design of the power generator was based on vibration induced from the base acceleration. The design used the MEMS concept approached and is shown in figure 2.5 below. The analysis included the validation based on the theoretical result, finite element analysis using ANSYS software and the experimental result. The voltage output was found to increase or reduce based on the excitation frequency, and was inversely proportional to the length of the cantilever beam and the damping factor. An energy harvester using the same models was also shown by (Fang, Liu, Xu, Dong, Chen, et al., 2006) and (Fang, Liu, Xu, Dong, Wang, et al., 2006). The design optimisation using an array method was also presented again by (Liu et al., 2008).

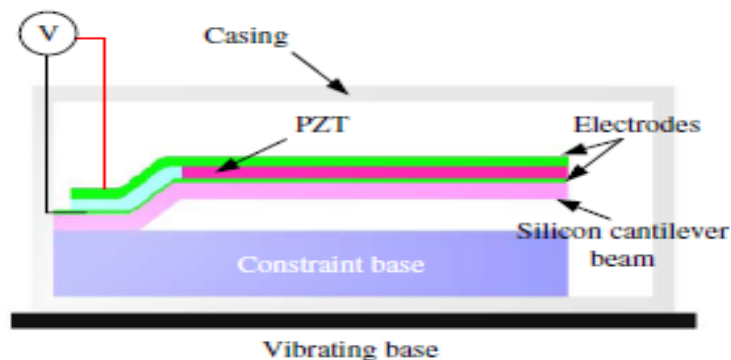


Figure 2.5 Concept of piezoelectric design adapted from (Chen et al., 2006).

(Ferrari, Ferrari, Marioli, & Taroni, 2006) showed techniques for modelling and fabrication of a piezoelectric harvester. Here, the technique of manufacturing the piezoelectric element was presented where the main structure was made by steel, with the piezoelectric element having the form of a thick element placed close to the clamped end. The piezoelectric compound was prepared from powder with 67% PZT powder and epoxy 33%. The PZT film was cured at a temperature of about 180°C and poled in the thickness direction. The PZT film was designed to have the length of 25 mm, width of 15 mm and thickness of 500 µm. Comparison of the simulation and the experimental test showed good agreement indicating that the piezoelectric generator should be categorised as a micro-power generator.

Analysis of a piezoelectric bimorph system was investigated by (Ajitsaria, Choe, Shen, & Kim, 2007) where this device was found to be quite easy to be applied in the real condition. The research focused on the development of the analytical electromechanical equation based on derivation using Euler-Bernoulli and Timoshenko beam equations to find the FRFs voltage and power output. Both derivations were compared to show the validation of the research and the modelling of the piezoelectric system was taken from the previous models that used the methods of electrical equivalence and the energy method. Simulation was investigated by using Matlab/Simulink/Simpower software with AC/DC power conversion circuit.

The further mathematical mechanical model of power harvesting was given by (Alper Erturk & Inman, 2008b) for the cantilever beam. Their research proposed the correction factor for the common model of energy harvesting using single-degree-of-freedom SDOF in relation to harmonic base motion. Based on their research, they found that for the transverse excitation, the common SDOF model gave inaccurate results for predicting the motion, though the SDOF model gave correct results when it had a high tip mass to beam mass ratio. Therefore, their research suggested that the SDOF model using low tip mass to beam mass ratios must apply appropriate correction factors. The distributed parameters of the electromechanical equation for the piezoelectric harvester was presented again by (Alper Erturk & Inman, 2008a). The research developed the electromechanical modelling for cantilevered piezoelectric unimorph beam based on Euler-Bernoulli beam theory, the linear constitutive equation

and the Rayleigh-Ritz solution. They also introduced air damping and base motion that included a small rotation.

(Goldschmidtboeing & Woias, 2008) researched energy harvesting with different shapes of beams as shown in figure 2.6. This research showed the possibility of using different shapes for the piezoelectric power harvester. The proposed research used the triangular shaped beam to investigate the voltage and power response where the result was compared with the rectangular shaped power generator. The advantages of the triangular shape was that it appeared to show enough ability to perform in high amplitude so that it has increased ability to produce higher power output. The shape of the tip mass of the triangular piezoelectric shape could be adjusted in a way to optimize the resonance frequency. The following research investigation of variable-shaped piezoelectric energy harvester was also investigated by (Ayed, Abdelkefi, Najar, & Hajj, 2013) where at this stage the investigator used the piezoelectric material and metallic layers.

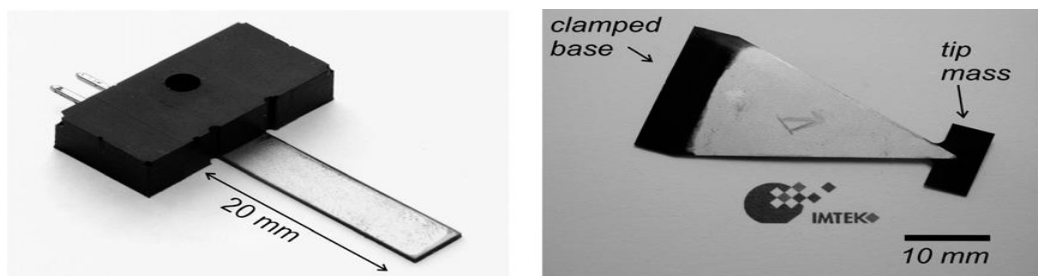


Figure 2.6 Different shape of cantilever adopted from (Goldschmidtboeing & Woias, 2008).

Theoretical analysis of an electromechanical coupled finite element plate was proposed by (Junior et al., 2009). The research investigated the plate application to UAVs (Unmanned Aerial Vehicles and MAVs (Micro Air Vehicle). The mathematical finite element formulation for the plate model was derived based on Kirchhoff plate theory. The electromechanical model was verified using the analytical close-form under base excitation and the bimorph model was reported by (Alper Erturk & Inman, 2008a). However, for UAV applications, the study seems to ignore the air flow that should exist in real conditions. Besides, embedding the piezoceramic element to the wing resulted in increasing weight of the aircraft as the density of piezoceramic

materials is heavier than aircraft material resulting in additional mass to the whole design.

An analytical bimorph cantilever beam configured with serial and parallel connection between the two piezoelectric layers was investigated by (A Erturk & Inman, 2009). The research assumed the bimorph beam was excited under transverse displacement and small rotation. The frequency response function was formulated by assuming the piezoelectric bimorph was subject to steady state harmonic excitation. The single-mode FRFs were validated with the experimental test. Results showed that the solution using closed-form techniques predicts the voltage output very accurately.

The effect of the strain node for the various resonance modes was investigated by (Alper Erturk, Tarazaga, Farmer, & Inman, 2009). The cancellation due to the strain node results in changing of the sign of the dynamic strain with respect to the direction of the piezoelectric length. The theoretical and experimental investigation showed that the electrical output can be strongly cancelled due to the continuous electrode coverage of the material. The research introduced the concept of using the segmented piezoelectric component in order to avoid the cancellation problem.

(Elvin & Elvin, 2009b) developed the equivalent model of the cantilevered piezoelectric system in terms of an electrical circuit model where in application most previous circuits connected to the piezoelectric harvester have been simplified as single resistors connected to the electrode layers. This research introduced SPICE software to show the circuit connection. The advantage in using the simulation software was that it can easily capture the model behaviour of each of the vibration mode shapes. In addition, the equivalent generator model presents a very similar result to the piezoelectric generator having the same boundary condition, material properties and geometry. The resulting research showed that the frequency response from the electrical equivalent system have good agreement with the previous work (Alper Erturk & Inman, 2008a) for the first three vibration modes.

Focused research on the use of a coupled equivalent energy harvester for cantilever beam applications using a finite element method was given by (Elvin & Elvin, 2009a). This paper described the steps in derivation of the electromechanical coupled system

equation for the piezoelectric cantilever beam using finite element software package, combined with simulation of electrical circuit using SPICE software.

(Yang & Tang, 2009) presented the resulting dynamic behaviour for power harvesting using ANSYS finite element software package and equivalent circuit analysis using SPICE software. The finite element procedure was proposed to find the static capacitance of the coupled structure, short-circuit resonance, charge response for each mode and used all parameters found in the FEA software package for the SPICE circuit modelling.

A bimorph cantilever beam using two input base motion was investigated by (M. Lumentut & Howard, 2010) where the combined input excitation in the transverse and the longitudinal direction was investigated to predict the harvested energy and power. Research focused on the direction of base motion because the polarity was found to affect the generating power. The research showed the analytical derivation of the electromechanical coupled equation under input base motion to find the transfer function. The dynamic equation was formulated from the extended weak form of the Hamilton's principle and the Laplace transformation to show the multi-mode frequency response. Continuing research of (M. Lumentut & Howard, 2011) presented the further analytical modelling of a self-powered sensor using a cantilevered bimorph in multi-directional base excitation. This research focused on the analytical model for predicting power under simultaneous longitudinal and transverse input base motion utilizing the same approach method as previously published. Parametric case study with changing parametric length, width and thickness of the piezoelectric layer was also given by (M. Zhu, Worthington, & Tiwari, 2010). (Patel, McWilliam, & Popov, 2011) showed the parametric case study under changing shape of piezoelectric length and piezoelectric layer thickness on the performance of the cantilevered unimorph beam.

Application of an array of piezoelectric harvesters has been presented by some researchers as a way to find increased power that can be harvested by the piezoelectric device. In addition, the array application can result in the difficulties in finding the equivalent impedance to be applied to the device. Research investigation by (Lien &

Shu, 2012) proposed to use the equivalent impedance to investigate the electrical response of a piezoelectric array.

The effect of piezoelectric patch placement on the loss factor was investigated by (Liao & Sodano, 2012). The purpose of this research was to find an optimal location of patching small piezoelectric elements on to the substructure. The results showed that for small size of the piezoelectric cantilever harvester device, the highest strain appeared to occur near the root of the structure but this location might change as the size of the structure changed. The resulting research also found that the small size of the piezoelectric patch could give better performance compared to the larger size of the patch because at the higher modes the highest strain substructure and piezoelectric exists over the smaller area.

Research to widen the frequency bandwidth in power harvesting has become of interest (Ou et al., 2012). The research utilised two masses at different locations in order to increase the bandwidth of the vibration response. The research also showed the piezoelectric response optimisation using two masses at different locations and the derivation of equations was also presented for any model using any number of masses.

Other methods of improving broadband energy harvesting utilising magnets was presented by (Tang, Yang, & Soh, 2012). The research introduced the use of magnets to explore the nonlinearities that occur between two magnets as a function of distance. The study of the nonlinearities was investigated to improve the performance of energy harvesting. A monostable-to-bistable configuration in terms of distance between magnets was investigated under sinusoidal and random vibration. The results showed that the monostable-to-bistable nonlinear configuration can significantly outperform the linear harvester near the transition. Other conductive research for using magnets to improve the power generation was also recently proposed by (Abdessattar Abdelkefi & Barsallo, 2014).

Improving the strain distribution in a cantilever energy harvesting using a H-shaped device was investigated by (Guan, Ju, Xu, Liu, & Feng, 2013). Here, the piezoelectric system had additional mass comprised of two metal segments and two tip mass blocks. The proposed design can provide a large rotary inertia to increase the coupling

coefficient. A prototype of the H-shape device was designed, fabricated and tested. The results showed that when the two masses were detached from the structure, it appears that the proposed device has a uniform strain distribution in the direction of extension. Figure 2.7 gives the representation of the H-shaped prototype.

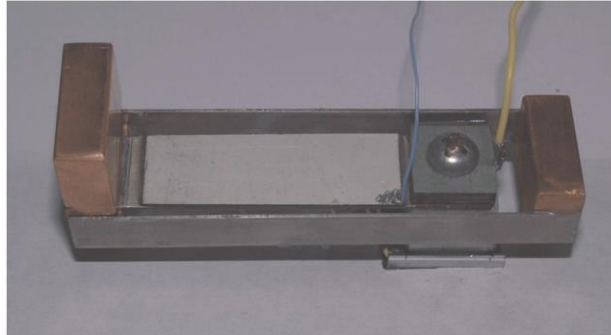


Figure 2.7 Piezoelectric beam with H-shaped tip mass (Guan et al., 2013).

(Park & Park, 2013) researched the piezoelectric bimorph with an asymmetrical inertial mass which was located at the edge of the bimorph beam as shown in figure 2.8. In order to harvest the energy from the multi-dimensional vibration, the inertial mass was designed with adjustment of the centre of mass. Here the asymmetrical mass contributed to the generation of power from the vibration in the direction of length and the thickness of the PZT bender. The PZT bender was set to $36 \times 10 \times 0.72 \text{ mm}^3$ and capacitance 7.5 nF . Based on the excitation for two input axes, in the z-axis the resulting bimorph can produce power output about 7.5 mW and in the x-axis the power generated was approximately 1.4 mW with 10 m/s^2 acceleration.

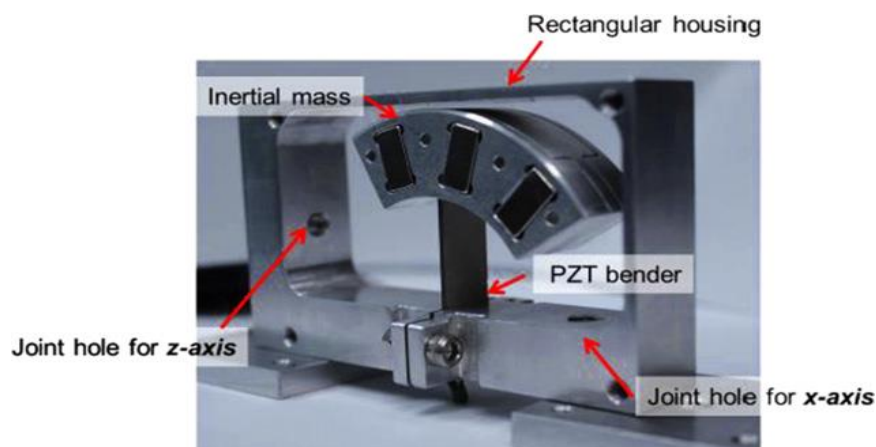


Figure 2.8 Asymmetrical PZT power harvester (Park & Park, 2013).

Energy harvesting from broadband random vibration was also investigated by (S. Zhao & Erturk, 2012). The research employed the result of distributed parameter electroelastic formulation by (A Erturk & Inman, 2009). In this case, the research proposed to find the result of power harvesting under shunted vibration response. The force vibration was taken in terms of power spectral density (PSD) or time history of random vibration input. The result showed the analytical solution of the frequency response based on the input power spectral density (PSD) to have good agreement with the experimental measurements taken. Here, the numerical solution was found using two different solution methods being deterministic and stochastic. The deterministic method utilised the ordinary differential equation (ODE) solver and the stochastic method used the stochastic differential equation (SDEs) solver.

Analytical parametric study considering the modal electromechanical coupling and mechanical behaviour as a function of geometry was presented by (Xiong & Oyadiji, 2013) for the rectangular, convergent, divergent cantilevered beams and for the effect of a tip mass. The modal electromechanical response was presented to find the effect of the electromechanical coupling coefficient and damping ratio on the maximum resulting power. The research suggested that the investigations of modal electromechanical coupling effect and the mass ratio effect should be separated in order to optimise the performance of the vibration energy harvesting. The resulting research for the rectangular cantilever beam in the first mode has the electromechanical coefficient higher than the second and third modes. Then, changing geometries of the piezoelectric cantilevered beam to be wider at the base clamp or shorten the system design was found to possibly enhance electromechanical coupling coefficient by 10% while partly covering the substrate could increase the electromechanical coupling coefficient by 10% to 20%. Divergent cantilevered beams were able to generate acceptable electromechanical coupling coefficients with much smaller coverage of the piezoelectric material than the rectangular and convergent cantilevered beam. Application of tip mass to the covered piezoelectric system increased the electromechanical coupling coefficient by 10% and moving the tip mass to the centre of the beam was able to increase the electromechanical coupling coefficient by 25%. Lately, research on the optimisation of the piezoelectric energy harvester involving the electromechanical coupling coefficient parameter was presented (Deng, Wen, Jiang, Zhao, & She, 2015). Here, the resulting research showed the conflict of the resulting

power output with respect to the effect of electromechanical coupling coefficient where under lower damping ratio it does not always give high power output.

Piezoelectric performance under low frequency situations was recently researched by (Abdessattar Abdelkefi, Barsallo, Tang, Yang, & Hajj, 2014), where the researchers used analytical and finite element models and then verified the resulting models with experiments. The analytical results showed the correct estimation of the result when the piezoelectric material does not cover the surface of the structure. In addition, the finite element analysis was developed using the ANSYS software package where it appears the resulting FEA solution shows a small discrepancy in the global frequency response and a slight overestimation of the value of power. Investigation of the unimorph beam power harvester with tip mass offset using the finite element method was shown recently by (M. Lumentut & Howard, 2014). Here, the investigation focused on the explanation in detail about the mathematical processing of the electromechanical discretisation, kinematic equation, coupled field equations, Lagrangian electromechanical dynamic equation and orthonormalised electromechanical dynamic equation.

Optimisation of the energy harvesting efficiency for the piezoelectric vibration energy harvesting was presented recently by (Kim, Dugundji, & Wardle, 2015). The analytical solution of harvesting efficiency was evaluated based on finding the ratio of electrical power output and mechanical power input. Here, the mechanical input power was quantified based on the dimensions, property of material and frequency input, followed by the damping value and load resistances. The two stages of coupling were included in the evaluation of the electrical and mechanical power output. Firstly, the coupling of the mechanical to mechanical system was considered due to the connection of the base support to the piezoelectric device. Secondly, the coupling of the mechanical to the electrical system was considered as this is commonly discussed by many researchers.

Optimisation of the design by configuring the shape of the piezoelectric cantilever for rectangular and truncated beams was presented by (Muthalif & Nordin, 2015). This research used the multiphysics software MATLAB and COMSOL to study the variation in length and the shape on the output voltage generation and the resulting

simulation was also compared with the experimental work. This research also proposed the use of the rectangular piezoelectric cantilever comb-shaped beam.

Investigation of power harvesting with splitting the width of the piezoelectric harvesting device was presented by (Sang, Dayou, & Liew, 2013). The research showed that the power output using two splitting widths has given the highest power output compared to the single split or without splitting the width of the harvester device. This research investigated the optimum power output at load resistance of 2 M Ω for the piezo bender without splitting, in single even splitting and for two even splitting configurations. The resonance frequencies of the three systems were identified to be 25 Hz, 26.6 Hz and 27.1 Hz, respectively. The maximum power output increased by a factor of 6 for the single even split and by a factor of 7.62 for two even splits as compared to the original design. Further research of width reduction was presented recently by (Dayou et al., 2015) and the investigation showed the resulting damping ratio of cantilever beams with respect to the splitting width of the cantilever beam. It confirmed the increasing electrical energy due to decreasing the damping ratio and the piezoelectric width. The smaller width of the piezoelectric component was found to give high voltage amplitude therefore providing increased power output. Based on the resulting research, the power output of the piezoelectric beam used in the experiment and the harvested power under load resistance of 100 k Ω showed the resulting power of 6 nW for the original system without the split, 7.3 nW for the even single split, and 11.6 nW for two even splits and 38.2 nW for three even splits, respectively.

2.2 Summary

The literature review has been given to show the development of energy harvesting from its beginning until now. Discussion in the literature review was given based on the application of piezoelectric materials in the real applications. This research presented the numerical analysis of power harvesting for piezoelectric unimorph beam. The research described the derivation of a single element of the electromechanical coupling system for the cantilevered unimorph beam with four degrees of freedom. The single element concept was used to explore the piezoelectric unimorph beam using multi elements in different models. For example, the cantilevered unimorph beam

without and with tip mass, the cantilevered unimorph beam with different length geometries and the cantilevered unimorph beam with different angles of orientation with segmented piezoelectric elements.

Chapter 3

Finite Element Formulation for a Single Element Piezoelectric Beam Power Harvester

Analytical and finite element piezoelectric equations have been presented by many researchers. The finite element piezoelectric equations were introduced the first time by (Allik & Hughes, 1970). This research concerns the development of finite element analysis of a piezoelectric beam focusing on the correlation between the electrical and mechanical discretisation effect for modelling the electromechanical equations.

In this chapter, the mathematical finite element method is explored to solve the cantilevered piezoelectric unimorph beam under base excitation in the transverse direction. The piezoelectric unimorph is considered to undergo transverse and rotational deformations associated with the electromechanical coupling. A further case study with the axial deformation coupled with the axial electromechanical response will be discussed in chapter 6. Here, the exploration of the cantilevered beam is simplified into a single element beam in order to construct the basic mathematical finite element model for the energy harvester. The reason for choosing a single element for this approach is that the resulting model can be very useful for obtaining the understanding of the fundamental concepts so as to reduce the complexity and difficulty with the derivation process, especially in formulating the electromechanical dynamic equations. The resulting mathematical dynamic equations for the frequency response functions are then explored using the MATLAB programme language. The software programme is constructed based on the mathematical equations derived from the simplified model using the finite element approaches. In addition, the extension of the single element formulation to the multi-discretised elements will be explored in chapter 5. The extension to multi-element modelling will be verified by comparison with the analytical and finite element results from the previous published research in (Alper Erturk & Inman, 2008a) and (M. Lumentut & Howard, 2014). Both references have introduced the electrical frequency response functions with an orthonormalisation method while the present research approach is developed by solving the direct matrix equations using the non-orthonormalised methods.

The prediction of the electrical response of the piezoelectric element is based on the Euler-Bernoulli bending beam theory. A review of the derivation of the cubic polynomial displacement derived using the Euler-Bernoulli approach will be presented in order to form the shape function and to obtain the matrix equations of motion which are reduced from the energy equations. It is known that the cantilevered piezoelectric unimorph consists of two different material layers representing the substructure and piezoceramic layers. This requires the development of coupled mechanical and electrical equations for modelling the system behaviour. The electromechanical system response due to input base excitation requires the modelling of the transverse strain of the cantilevered unimorph piezoelectric structure based on the Euler-Bernoulli beam theory. The dynamic response shape of the coupled unimorph piezoelectric beam creates dynamic changes in the elemental length. The piezoelectric material has polarisation creating dynamic charge in the z -(thickness) direction along the entire length of the piezoelectric material. In addition, the electromechanical phenomenon is modelled here using linear constitutive piezoelectric equations in 2-D plane-stress form. The piezoelectric constitutive equations will be accounted for by deriving the potential energy term using Hamilton's Principle.

The use of cubic polynomial displacement functions gives first order and second order displacement shape function terms to form the matrix mechanical vector response. The mechanical matrix vector response equation can be formulated by substituting the shape function to achieve the matrix formation. Generally, the first order shape function can be substituted into the kinetic energy equation to give the mass matrix form. The second order shape function is used to form the stiffness matrices using the potential energy equation. The electrical shape functions can be derived from the electrical field function as the negative gradient operator which is poled in the thickness direction. The piezoelectric unimorph element will be analysed using the variational principle by including the input base excitation and the electrical charges into Hamilton's principle equation. The resulting set of equations can be separated to represent the two general formations of the mechanical and electrical coupled equations where Rayleigh damping factor is then included. Finally, the frequency responses for voltage, current and power output responses are derived by using a direct method after transforming the local element matrices into global element matrices form. Therefore, this chapter proposes the development of a mathematical finite

element formulation of a single element of the cantilever piezoelectric unimorph beam energy harvester. For clear explanation of the main points of this chapter, three areas will be discussed as follows,

1. Review the conceptual derivation of the shape function for a single beam element using the Euler-Bernoulli formulation to represent the mass and stiffness components of the substructure and piezoelectric element matrix formations under base excitation.
2. Model the mathematical and physical representation of the electrical shape function, including the correlation between the mechanical and electrical equations and electrical charge for the piezoelectric unimorph beam.
3. The direct finite element application method is solved to obtain multimode expressions for the voltage, current and power frequency responses.

3.1 Electromechanical Single Finite Element Formulation for a Cantilevered Unimorph Piezoelectric Power Harvester

3.1.1 Single Finite Element Modelling

The finite element formulation of the piezoelectric unimorph beam for one element is performed here only for the local element by assuming that the unimorph beam has two nodes. The nodal displacement includes both transverse and rotational directions with a total of four degrees of freedom. As previously stated, developing the general degree of freedom expression requires a cubic polynomial displacement equation. The polynomial form can be used to formulate the general shape function. The polynomial function having four coefficients can be solved by substituting the polynomial shape function into the four boundary conditions of the element at node 1 and node 2 positions as shown in figure 3.1. The explanation of the steps is shown below to achieve the first and the second order shape function. The second order shape function is based on the Euler-Bernoulli strain displacement for the elemental beam with respect to the horizontal axis motion. The piezoelectric unimorph cantilevered beam is assumed under base motion as displayed in figure 3.1 with two nodes having transverse and rotational displacement direction. In figure 3.1, it should be noted that the finite element is separated from the base excitation to give the displacement direction for each node. In actual condition, they are connected together where the elemental beam is clamped to the rigid base support. This separation is also very useful to show the

location of the local node for an elemental beam. Each node has two degrees of freedom in the two directions of transverse and rotational displacements representing u_1 and u_2 , respectively. The other node represents u_3 and u_4 .

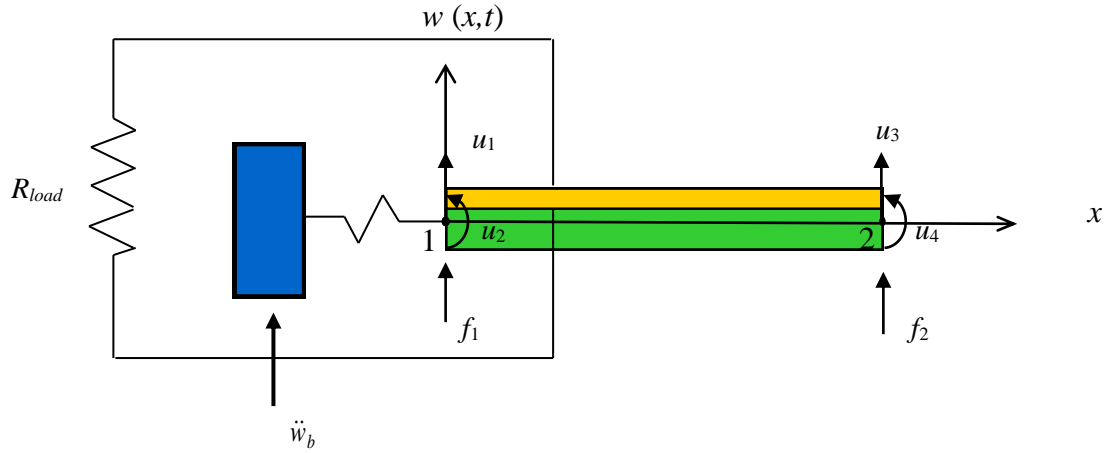


Figure 3.1 Single beam element with a total of four degrees of freedom.

The displacement function of the element can be represented by a cubic polynomial with four constant coefficients namely,

$$w(x,t) = c_1 + c_2x + c_3x^2 + c_4x^3. \quad (3.1)$$

Equation (3.1) represents the nodal vector displacement equation in terms of the transverse and rotational motion with four unknown coefficients. The boundary condition terms for each end of the element need to be specified with respect to nodal values as shown in figure 3.1. This can be shown from equation 3.1 to give for node 1, the vertical displacement at $x=0$, gives $u_1(t) = c_1 = u_1$. The slope at $x=0$, gives $du/dx|_{x=0} = \theta_1(t) = c_2 = u_2$. Node 2, the vertical displacement at $x=L$, gives $u_3(t) = c_1 + c_2L + c_3L^2 + c_4L^3 = u_3$. The slope at $x=L$, gives $du/dx|_{x=L} = u_4(t) = c_2 + 2c_3L + 3c_4L^2 = u_4$.

Solving coefficient of C_1 , C_2 , C_3 and C_4 , the displacement function can be reduced in terms of the shape function and the nodal displacements of the single element. Substituting the above result into the cubic polynomial equation, the result can be modified into a matrix equation with the following form,

$$\underline{w}(x,t) = \Phi_1 u_1 + \Phi_2 u_2 + \Phi_3 u_3 + \Phi_4 u_4. \quad (3.2)$$

The equation (3.2) can then be simplified as the following matrix form,

$$\underline{w}(x,t) = \underline{\Phi}(x) \underline{u}(t). \quad (3.3)$$

As reduced from the Hermite shape function, the continuous first derivative shape function associated with nodal displacement can be expressed as,

$$\begin{aligned} \underline{\Phi}(x) &= [\Phi_1(x) \quad \Phi_2(x) \quad \Phi_3(x) \quad \Phi_4(x)] \\ \underline{u}(t) &= [u_1 \quad u_2 \quad u_3 \quad u_4]^T, \end{aligned} \quad (3.4)$$

where the shape functions are given by,

$$\begin{aligned} \Phi_1(x) &= 1 - \frac{x^2}{L^2} + \frac{2x^3}{L^3}, & \Phi_2(x) &= x - \frac{2x^2}{L} + \frac{x^3}{L^2}, \\ \Phi_3(x) &= \frac{3x^2}{L^2} - \frac{2x^3}{L^3}, & \Phi_4(x) &= \frac{x^3}{L^2} - \frac{x^2}{L}. \end{aligned} \quad (3.5)$$

In terms of the corresponding strain of the elemental Euler-Bernoulli beam with respect to the x axis, this can be given as,

$$\underline{S}_{-1} = -z \frac{\partial^2 w(x,t)}{\partial x^2} \quad \text{or} \quad \underline{S}(x,t) = -z \frac{d^2 \underline{\Phi}(x)}{dx} \underline{u}(t) = -z \underline{\Psi}(x) \underline{u}(t). \quad (3.6)$$

The second derivative of the shape function of the strain displacement relationship can also be formulated as,

$$\underline{\Psi}(x) = \frac{d^2 \underline{\Phi}(x)}{dx^2} = [\Psi_1(x) \quad \Psi_2(x) \quad \Psi_3(x) \quad \Psi_4(x)], \quad (3.7)$$

where

$$\begin{aligned}\Psi_1(x) &= \frac{d^2 \Phi_1(x)}{dx^2} = -\frac{2}{L^2} + \frac{12x}{L^3}, \quad \Psi_2(x) = \frac{d^2 \Phi_2(x)}{dx^2} = -\frac{4}{L} + \frac{6x}{L^2}, \\ \Psi_3(x) &= \frac{d^2 \Phi_3(x)}{dx^2} = \frac{6}{L^2} - \frac{12x}{L^3}, \quad \Psi_4(x) = \frac{d^2 \Phi_4(x)}{dx^2} = \frac{6x}{L^2} - \frac{2}{L}.\end{aligned}\quad (3.8)$$

As previously shown above, equation (3.5) represents the first order shape function and the second order derivative is shown in (3.8). The two expressions can be substituted into the kinetic and potential energy equations to give the mass and stiffness matrices where more detailed discussion can be found in literatures (Reddy, 1993) and (Moaveni, 2003). It should be noted that the cantilevered piezoelectric unimorph beam is formed by two different layers consisting of the substructure and piezoelectric layers indicating continuous uniform composite materials as shown in figure 3.1. The nodal vector displacement structure does not occur about the neutral axis for each material layer as it must occur about the neutral axis of the combined structure. Here, the neutral axis for the combined structure can be found from balancing the resultant cross-sectional area of the unimorph. In addition, finding the neutral axis is a subtle task due to the asymmetrical characteristic of the composite materials. The precise location of the neutral axis affects the total mechanical potential energy and the resulting superimposed potential energy of the piezoelectric and substructure layers.

3.1.2 Electromechanical Coupled Field Piezoelectric Equations

The constitutive equations of linear piezoelectricity can be found in (Meitzler et al., 1988) with the standardized equations for materials made from Lead Zirconate Titanate (PZT). The utilising mode (3-1) can be reduced from the plane-stress matrix or initial polarised state and the poled direction can be referred to figure 3.2 below.

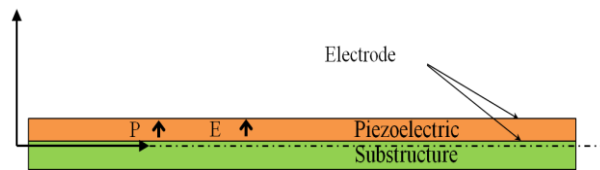


Figure 3.2 Detail of unimorph beam with mode (3-1).

P is stated as the polarisation direction in the vertical direction and E is the electric charge due to the polarisation action. Based on the plane-stress 3-D form assumption as given in Appendix D, the constitutive equation for piezoelectric beam can be described as the following form after simplifying the stress tensor as $\underline{S}_{\underline{3}} = \underline{S}_{\underline{4}} = \underline{S}_{\underline{5}} = 0$

$$\begin{Bmatrix} \underline{T}_{\underline{1}} \\ \underline{T}_{\underline{2}} \\ \underline{T}_{\underline{6}} \\ \underline{D}_{\underline{3}} \end{Bmatrix} = \begin{bmatrix} c_{11}^E & c_{12}^E & 0 & -e_{31} \\ c_{21}^E & c_{22}^E & 0 & -e_{31} \\ 0 & 0 & c_{66}^E & 0 \\ e_{31} & e_{32} & 0 & \varepsilon_{33}^S \end{bmatrix} \begin{Bmatrix} \underline{S}_{\underline{1}} \\ \underline{S}_{\underline{2}} \\ \underline{S}_{\underline{6}} \\ \underline{E}_{\underline{3}} \end{Bmatrix}. \quad (3.9)$$

In the particular case that the beam only bends in the transverse direction, the constitutive equation can be reduced into 1-D form as shown in equation (3.10), assuming the parameters $\underline{S}_{\underline{2}} = \underline{S}_{\underline{3}} = \underline{S}_{\underline{4}} = \underline{S}_{\underline{5}} = \underline{S}_{\underline{6}} = 0$. It should be noted that equation (3.9) was derived by using Voigt's notation and Einstein's summation convention. The matrix equation formation for piezoelectric beams is presented in terms of constant electric field and constant strain which is given by,

$$\begin{Bmatrix} \underline{T}_{\underline{1}} \\ \underline{D}_{\underline{3}} \end{Bmatrix} = \begin{bmatrix} c_{11}^E & -e_{31} \\ e_{31} & \varepsilon_{33}^S \end{bmatrix} \begin{Bmatrix} \underline{S}_{\underline{1}} \\ \underline{E}_{\underline{3}} \end{Bmatrix}. \quad (3.10)$$

Here, the parameters c_{11}^E , e_{31} , ε_{33}^S , $\underline{T}_{\underline{1}}$, $\underline{S}_{\underline{1}}$, $\underline{D}_{\underline{3}}$ and $\underline{E}_{\underline{3}}$ represent the piezoelectric elastic stiffness at constant electric field, piezoelectric coefficient, permittivity at constant strain field, stress, strain, electric displacement and electric field, respectively.

The piezoelectric elastic stiffness can be given as $c_{11}^E = 1/s_{11}^E$ and permittivity at constant strain could be achieved by $\varepsilon_{33}^S = \varepsilon_{33}^T - e_{31}d_{31}$ or $\varepsilon_{33}^S = \varepsilon_{33}^T - d_{31}^2 c_{11}^E$ where s_{11}^E is the elastic compliance at constant electric field, ε_{33}^T is the permittivity at constant stress and d_{31} is the piezoelectric constant. The constitutive piezoelectric constant d_{31} can be modified using equation $e_{31} = d_{31}c_{11}^E$. The unimorph beam has two layers which are commonly known as the active and inactive layers. The active layer refers

to the piezoelectric element and the inactive layer is the substructure. Therefore, the plane stress field for the piezoelectric layer equation can be calculated by using equation (3.10) and the substructure layer can be formulated by removing the electricity variable or by using equation (3.11) below. However, due to the use of the same symbols for stress, strain and elastic stiffness, the use of subscript and superscript notations is used to avoid confusion. The forthcoming symbol is also used for notation of density and volume. It should be noted that the superscript notations $(\cdot)^{(1)}$ and $(\cdot)^{(2)}$ refer to the substructure and piezoelectric layer respectively while the subscript notation symbol refers to the Voigt notation. Equation (3.11) represents the symbolic representation of the substructure plane-stress field equation which is formulated as,

$$\underline{\mathbf{T}}_{-1}^{(1)} = c_{11}^{(1)} \underline{\mathbf{S}}_{-1}^{(1)}. \quad (3.11)$$

Rewriting equation (3.10a), the plane-stress piezoelectric field equation becomes,

$$\underline{\mathbf{T}}_{-1}^{(2)} = c_{11}^{-(2)} \underline{\mathbf{S}}_{-1}^{(2)} - e_{31} \underline{\mathbf{E}}_3. \quad (3.12)$$

The imposed strain field due to the base excitation develops the polarization of the piezoelectric material in the z -direction along the thickness of the piezoelectric material and the electric potential energy which varies from 0 to +1, referring to figure 3.2. Since the piezoelectric material is poled in the thickness or z direction, the non-zero electric field component as a function of the electrical potential which has negative gradient operator can be represented as,

$$\underline{\mathbf{E}}_3 = -\nabla \underline{\boldsymbol{\varphi}}(z, t), \quad (3.13)$$

where ∇ is a gradient operator for the first derivative of the shape function with respect to the thickness direction and it can be expressed as, $\underline{\boldsymbol{\Omega}}(z) = \frac{d\boldsymbol{\varphi}(z)}{dz} = \frac{1}{h_p}$, and the electrical potential is assumed to be linear as, $\underline{\boldsymbol{\varphi}}(z, t) = \underline{\boldsymbol{\vartheta}}(z) \underline{\mathbf{v}}_{-p}(t)$, where the shape function of the electrical potential energy can be found as,

$\mathcal{G}(z) = (z - z_n + h_p)/h_p$ from the interval $z_n - h_p < z < z_n$ (see Appendix A). The parameters h_p and z_n refer to the thickness of the piezoelectric material and the distance from the asymmetrical neutral axis to the top layer of the unimorph beam. Therefore, the electric field equation can be rewritten in terms of the first derivative of the shape function and the electrical potential as,

$$\underline{\mathbf{E}}_3 = -\underline{\mathcal{Q}}(z)\underline{\mathbf{v}}_{-p}(t). \quad (3.14)$$

In addition, the equations representing the plane-stress field for the substructure and piezoelectric element can be obtained by substituting equation (3.6) and (3.14) into equation (3.10) or (3.12) and (3.11) to give,

$$\underline{\mathbf{T}}_{-1}^{(1)} = -z c_{11}^{(1)} \underline{\Psi}(x) \underline{\mathbf{u}}(t), \quad (3.15)$$

and

$$\underline{\mathbf{T}}_{-1}^{(2)} = c_{11} \underline{\Psi}(x) \underline{\mathbf{u}}(t) + e_{31} \underline{\mathcal{Q}}(z) \underline{\mathbf{v}}_{-p}(t). \quad (3.16)$$

Finally the electric displacement direct mode equation of the piezoelectric material can also be formulated by substituting equation (3.6) and (3.14) into equation (3.10) to give,

$$\underline{\mathbf{D}}_3 = z e_{31} \underline{\Psi}(x) \underline{\mathbf{u}}(t) - \epsilon_{33}^S \underline{\mathcal{Q}}(z) \underline{\mathbf{v}}_{-p}(t). \quad (3.17)$$

3.2 Governing Dynamic Equation for Single Element Unimorph Cantilevered Piezoelectric Beam

3.2.1 The use of Extended Hamilton's Principle for Deriving the General Electromechanical Dynamic Equation

The extended Hamilton's principle equation is used here to formulate the cantilevered piezoelectric unimorph beam using functional energy forms of the kinetic energy KE ,

the potential energy PE , the electrical energy WE and the external work WF . The generalized Hamilton's principle can be written as,

$$\int_{t_1}^{t_2} [\delta(KE - PE + WE) + \delta WF] dt = 0, \quad (3.18)$$

where each of the individual variable terms are defined as,

$$KE = \frac{1}{2} \int_{V^{(1)}} \rho^{(1)} \underline{\dot{\mathbf{w}}}^T \underline{\dot{\mathbf{w}}} dV^{(1)} + \frac{1}{2} \int_{V^{(2)}} \rho^{(2)} \underline{\dot{\mathbf{w}}}^T \underline{\dot{\mathbf{w}}} dV^{(2)}, \quad (3.19)$$

$$PE = \frac{1}{2} \int_{V^{(1)}} \underline{\mathbf{S}}_{-1}^{(1)T} \underline{\mathbf{T}}_{-1}^{(1)} dV^{(1)} + \frac{1}{2} \int_{V^{(2)}} \underline{\mathbf{S}}_{-1}^{(2)T} \underline{\mathbf{T}}_{-1}^{(2)} dV^{(2)}, \quad WE = \frac{1}{2} \int_{V^{(2)}} \underline{\mathbf{E}}^T \underline{\mathbf{D}} dV^{(2)}, \quad (3.20)$$

and

$$WF = -\delta \underline{\mathbf{w}} \underline{\mathbf{f}} + \delta \underline{\mathbf{v}}_{-p} \underline{\mathbf{q}}_{-p}. \quad (3.21)$$

As shown from the above equations, the term ρ refers to the mass density, $\underline{\dot{\mathbf{w}}}$ is the first derivative of displacement, V is the volume, $\underline{\mathbf{S}}$ is the strain, $\underline{\mathbf{T}}$ is the stress, $\underline{\mathbf{E}}$ is the electric field, $\underline{\mathbf{D}}$ is the electric displacement, $\underline{\mathbf{w}}$ is the displacement, $\underline{\mathbf{f}}$ is the applied force, $\underline{\mathbf{v}}_{-p}$ is the applied voltage, $\underline{\mathbf{q}}$ is the electric charge and superscript $(\cdot)^{(1)}$ and $(\cdot)^{(2)}$ represent the material substructure and the piezoelectric element, respectively. The equations (3.19), (3.20) and (3.21) can be substituted into equation (3.18). The sub-terms of energy for the substructure and piezoelectric layers have already been explained in the previous section as can be seen from equation (3.1) to (3.17).

By substituting the plane-stress field for the substructure and piezoelectric element equations (3.11) and (3.12) into equation (3.20), the total potential energy of the system can be developed to give,

$$\begin{aligned}
PE &= \frac{1}{2} \int_{V^{(1)}} \underline{\mathbf{S}}_{-1}^{(1)T} c_{11}^{(1)} \underline{\mathbf{S}}_{-1}^{(1)} dV^{(1)} + \frac{1}{2} \int_{V^{(2)}} \underline{\mathbf{S}}_{-1}^{(2)T} c_{11}^{(2)} \underline{\mathbf{S}}_{-1}^{(2)} dV^{(2)} - \frac{1}{2} \int_{V^{(2)}} \underline{\mathbf{S}}_{-1}^{(2)T} e_{31} \underline{\mathbf{E}} dV^{(2)} \\
WE &= \frac{1}{2} \int_{V^{(2)}} \underline{\mathbf{E}}^T e_{31} \underline{\mathbf{S}}_{-1}^{(2)} dV^{(2)} + \frac{1}{2} \int_{V^{(2)}} \underline{\mathbf{E}}^T \varepsilon_{33}^S \underline{\mathbf{E}} dV^{(2)}
\end{aligned} \quad (3.22)$$

Taking the expression of the kinetic energy from equation (3.19) and incorporating it with equation (3.18) the general equation for the first variation of the kinetic energy can be expressed as,

$$\delta KE = \int_{V^{(1)}} \rho^{(1)} \delta \underline{\dot{\mathbf{w}}}^T \underline{\dot{\mathbf{w}}} dV^{(1)} + \int_{V^{(2)}} \rho^{(2)} \delta \underline{\dot{\mathbf{w}}}^T \underline{\dot{\mathbf{w}}} dV^{(2)}. \quad (3.23)$$

Incorporating equation (3.22) with equation (3.18), first variation of the total potential energy can be written as,

$$\begin{aligned}
\delta PE &= \int_{V^{(1)}} \delta \underline{\mathbf{S}}_{-1}^{(1)T} c_{11}^{(1)} \underline{\mathbf{S}}_{-1}^{(1)} dV^{(1)} + \int_{V^{(2)}} \delta \underline{\mathbf{S}}_{-1}^{(2)T} c_{11}^{(2)} \underline{\mathbf{S}}_{-1}^{(2)} dV^{(2)} - \int_{V^{(2)}} \delta \underline{\mathbf{S}}_{-1}^{(2)T} e_{31} \underline{\mathbf{E}}_3 dV^{(2)} \\
\delta WE &= \int_{V_p} \delta \underline{\mathbf{E}}_{-3}^T e_{31} \underline{\mathbf{S}}_{-1}^{(2)} dV^{(2)} + \int_{V_p} \delta \underline{\mathbf{E}}_{-3}^T \varepsilon_{33}^S \underline{\mathbf{E}}_3 dV^{(2)}
\end{aligned} \quad (3.24)$$

The energy terms in equations (3.23), (3.24) and the non-conservative or external work in equation (3.21) can be substituted into equation (3.18) and the resulting expression in variational form can be given as,

$$\int_{t_1}^{t_2} \left[\begin{aligned} & \int_{V^{(1)}} \rho^{(1)} \delta \underline{\dot{\mathbf{w}}}^T \underline{\dot{\mathbf{w}}} dV^{(1)} + \int_{V^{(2)}} \rho^{(2)} \delta \underline{\dot{\mathbf{w}}}^T \underline{\dot{\mathbf{w}}} dV^{(2)} \\ & - \int_{V^{(1)}} \delta \underline{\mathbf{S}}_{-1}^{(1)T} c_{11}^{(1)} \underline{\mathbf{S}}_{-1}^{(1)} dV^{(1)} - \int_{V^{(2)}} \delta \underline{\mathbf{S}}_{-1}^{(2)T} c_{11}^{(2)} \underline{\mathbf{S}}_{-1}^{(2)} dV^{(2)} + \int_{V^{(2)}} \delta \underline{\mathbf{S}}_{-1}^{(2)T} e_{31} \underline{\mathbf{E}}_3 dV^{(2)} \\ & + \int_{V^{(2)}} \delta \underline{\mathbf{E}}_{-3}^T e_{31} \underline{\mathbf{S}}_{-1}^{(2)} dV^{(2)} + \int_{V^{(2)}} \delta \underline{\mathbf{E}}_{-3}^T \varepsilon_{33}^S \underline{\mathbf{E}}_3 dV^{(2)} \\ & - \delta \underline{\mathbf{w}}_{-p} \underline{\mathbf{f}} + \delta \underline{\mathbf{v}}_{-p} \underline{\mathbf{q}}_{-p} \end{aligned} \right] dt = 0 \quad (3.25)$$

Substituting the first derivative from equation (3.3) to (3.5) and (3.15) to (3.17) into equation (3.25) gives,

$$\int_{t_1}^{t_2} \left(\begin{aligned} & \int_{V^{(1)}} \rho^{(1)} \delta \underline{\dot{\mathbf{u}}}(t)^T \underline{\Phi}(x)^T \underline{\Phi}(x) \underline{\dot{\mathbf{u}}}(t) dV^{(1)} + \int_{V^{(2)}} \rho^{(2)} \delta \underline{\dot{\mathbf{u}}}(t)^T \underline{\Phi}(x)^T \underline{\Phi}(x) \underline{\dot{\mathbf{u}}}(t) dV^{(2)} \\ & - \int_{V^{(1)}} z^2 \delta \underline{\mathbf{u}}(t)^T \underline{\Psi}(x)^T c_{11}^{(1)} \underline{\Psi}(x) \underline{\mathbf{u}}(t) dV^{(1)} - \int_{V^{(2)}} z^2 \delta \underline{\mathbf{u}}(t)^T \underline{\Psi}(x)^T c_{11}^{(2)} \underline{\Psi}(x) \underline{\mathbf{u}}(t) dV^{(2)} \\ & \quad - \int_{V^{(1)}} z \delta \underline{\mathbf{u}}(t)^T \underline{\Psi}(x)^T e_{31} \underline{\Omega}(z) \underline{\mathbf{v}}_p(t) dV^{(2)} \\ & + \int_{V^{(2)}} z \delta \underline{\mathbf{v}}_p(t)^T \underline{\Omega}(z)^T e_{31} \underline{\Psi}(x) \underline{\mathbf{u}}(t) dV^{(2)} + \int_{V^{(2)}} \delta \underline{\mathbf{v}}_p(t)^T \underline{\Omega}(z)^T \epsilon_{33}^S \underline{\Omega}(z) \underline{\mathbf{v}}_p(t) dV^{(2)} \\ & \quad - \delta \underline{\mathbf{w}} \underline{\mathbf{f}} + \delta \underline{\mathbf{v}}_{-p} \underline{\mathbf{q}}_{-p} \end{aligned} \right) dt = 0. \quad (3.26)$$

After applying the variational principle, equation (3.26) can be written as two general expressions where the first term represents the electromechanical dynamic equation for the piezoelectric unimorph as,

$$\begin{aligned} & \int_{V^{(1)}} \rho^{(1)} \underline{\Phi}(x)^T \underline{\Phi}(x) \underline{\ddot{\mathbf{u}}}(t) dV^{(1)} + \int_{V^{(2)}} \rho^{(2)} \underline{\Phi}(x)^T \underline{\Phi}(x) \underline{\ddot{\mathbf{u}}}(t) dV^{(2)} \\ & \quad + \int_{V^{(1)}} z^2 \underline{\Psi}(x)^T c_{11}^{(1)} \underline{\Psi}(x) \underline{\mathbf{u}}(t) dV^{(1)} \quad . \quad (3.27) \\ & + \int_{V^{(2)}} z^2 \underline{\Psi}(x)^T c_{11}^{(2)} \underline{\Psi}(x) \underline{\mathbf{u}}(t) dV^{(2)} - \int_{V^{(2)}} z \underline{\Psi}(x)^T e_{31} \underline{\Omega}(z) \underline{\mathbf{v}}_p(t) dV^{(2)} = -\underline{\Phi}(x)^T \underline{\mathbf{f}}(t) \end{aligned}$$

The second term of the electromechanical dynamic equation can be expressed as the formation of the electrical charge component as,

$$- \int_{V^{(2)}} z \underline{\Omega}(z)^T e_{31} \underline{\Psi}(x) \underline{\mathbf{u}}(t) dV^{(2)} - \int_{V^{(2)}} \underline{\Omega}(z)^T \epsilon_{33}^S \underline{\Omega}(z) \underline{\mathbf{v}}_p(t) dV^{(2)} = \underline{\mathbf{q}}_p. \quad (3.28)$$

Altering the formation of the electric charge expression into a current formulation can be achieved by differentiating the electrical charge with respect to time to give the internal single element current. Rewriting the electrical charge equation gives the current formulation,

$$- \int_{V^{(2)}} z \underline{\Omega}(z)^T e_{31} \underline{\Psi}(x) \underline{\dot{\mathbf{u}}}(t) dV^{(2)} - \int_{V^{(2)}} \underline{\Omega}(z)^T \epsilon_{33}^S \underline{\Omega}(z) \underline{\dot{\mathbf{v}}}_p(t) dV^{(2)} = \underline{\mathbf{i}}_{-p}(t). \quad (3.29)$$

Accounting for the Rayleigh damping term, the new expression for a local single finite element electromechanical dynamic equation can be further described as,

$$\begin{bmatrix} \mathbf{M}^{(e)} & 0 \\ \mathbf{C}^{(e)} & 0 \\ \mathbf{0} & \mathbf{0} \end{bmatrix} \begin{Bmatrix} \ddot{\underline{\mathbf{u}}} \\ \dot{\underline{\mathbf{v}}}_p \\ \underline{\mathbf{v}}_p \end{Bmatrix} + \begin{bmatrix} \mathbf{C}^{(e)} & 0 \\ \mathbf{P}_{sr}^{(e)} & \mathbf{P}_D^{(e)} \end{bmatrix} \begin{Bmatrix} \dot{\underline{\mathbf{u}}} \\ \dot{\underline{\mathbf{v}}}_p \end{Bmatrix} + \begin{bmatrix} \mathbf{K}^{(e)} & \mathbf{P}_{rs}^{(e)} \\ 0 & 0 \end{bmatrix} \begin{Bmatrix} \underline{\mathbf{u}} \\ \underline{\mathbf{v}}_p \end{Bmatrix} = \begin{Bmatrix} \underline{\mathbf{F}}^{(e)} \\ \underline{\mathbf{i}}_p^{(e)} \end{Bmatrix}, \quad (3.30)$$

where,

$$\begin{aligned} \mathbf{M}^{(e)} &= \int_{V^{(1)}} \rho^{(1)} \underline{\boldsymbol{\Phi}}(x)^T \underline{\boldsymbol{\Phi}}(x) dV^{(1)} + \int_{V^{(2)}} \rho^{(2)} \underline{\boldsymbol{\Phi}}(x)^T \underline{\boldsymbol{\Phi}}(x) dV^{(2)}, \\ \mathbf{K}^{(e)} &= \int_{V^{(1)}} z^2 \underline{\boldsymbol{\Psi}}(x)^T c_{11}^{(1)} \underline{\boldsymbol{\Psi}}(x) dV^{(1)} + \int_{V^{(2)}} z^2 \underline{\boldsymbol{\Psi}}(x)^T c_{11}^{(2)} \underline{\boldsymbol{\Psi}}(x) dV^{(2)}, \\ \mathbf{C}^{(e)} &= \alpha \mathbf{M} + \beta \mathbf{K}, \quad \mathbf{P}_{rs}^{(e)} = \int_{V^{(2)}} z \underline{\boldsymbol{\Psi}}(x)^T e_{31} \underline{\boldsymbol{\Omega}}(z) dV^{(2)}, \\ \mathbf{P}_{sr}^{(e)} &= -\int_{V^{(2)}} z \underline{\boldsymbol{\Omega}}(z)^T e_{31} \underline{\boldsymbol{\Psi}}(x) dV^{(2)}, \quad \mathbf{P}_D^{(e)} = -\int_{V^{(2)}} \underline{\boldsymbol{\Omega}}(z)^T \varepsilon_{33}^S \underline{\boldsymbol{\Omega}}(z) dV^{(2)}, \\ \underline{\mathbf{F}}^{(e)} &= -\delta \underline{\mathbf{w}}(x) \underline{\mathbf{f}}(x) = -\underline{\mathbf{Q}} \ddot{\underline{\mathbf{w}}}_{base}(t), \quad \underline{\mathbf{Q}} = \int_{V^{(1)}} \rho^{(1)} \underline{\boldsymbol{\Phi}}(x)^T dV^{(1)} + \int_{V^{(2)}} \rho^{(2)} \underline{\boldsymbol{\Phi}}(x)^T dV^{(2)}. \end{aligned}$$

3.2.2 Global Electromechanical Dynamic Matrix Equation Based on Electromechanical Vector Transformation

The generalised global dynamic equation of one element has the same formation as that of the local element since the global coordinate axis is located in the same place. In addition, the formation of the generalised local element in equation (3.30) can be formulated into global matrix form to give,

$$\begin{aligned} \mathbf{M} \ddot{\underline{\mathbf{u}}}(t) + \mathbf{C} \dot{\underline{\mathbf{u}}}(t) + \mathbf{K} \underline{\mathbf{u}}(t) + \mathbf{P}_{rs} \underline{\mathbf{v}}_p(t) &= \underline{\mathbf{F}}(t), \\ \mathbf{P}_{sr} \dot{\underline{\mathbf{u}}}(t) + \mathbf{P}_D \dot{\underline{\mathbf{v}}}_p(t) &= \underline{\mathbf{i}}_p(t), \end{aligned} \quad (3.31)$$

where \mathbf{M} is the global mass matrix, \mathbf{C} is the global Rayleigh damping matrix, \mathbf{K} is the global stiffness matrix, \mathbf{P}_{rs} and \mathbf{P}_{sr} are the global electromechanical coupling, \mathbf{P}_D is global capacitance matrix, $\underline{\mathbf{F}}$ and $\underline{\mathbf{i}}_p$ are the global mechanical forces and global current output, $\underline{\mathbf{u}}$ is the global mechanical coordinate and $\underline{\mathbf{v}}_p$ is the global voltage output.

In addition, the electrodes of the piezoelectric layer are connected with two wires and result in the one single value of voltage output. Since the beam only has one finite element in the resulting formulation, the calculation of the generalised output electrical current is equal to $(i_{p_1} = i = i_p)$ where this should be calculated as $(i_p = \mathcal{G}i)$ and the single voltage value will be $(v_1 = v = v_p)$, which can be written as $v_p = (1)^T v$, $(v_p = \mathcal{G}^T v)$. The modification of the generalised voltage output term can be substituted into the electromechanical coupling equation in the fourth term of the first expression in equation (3.31), where this operation can be expressed as,

$$\mathbf{P}_{rs} \mathcal{G}^T v = \mathbf{\Theta} v . \quad (3.32)$$

$\begin{matrix} (4 \times 1) & & (4 \times 1) \end{matrix}$

The second term of the global matrix expression in equation (3.31) must also be modified by multiplying the transformed electromechanical vector \mathcal{G} on both sides of the equation (3.31b) and introducing the electrical vector transformation followed by altering the current function expression $i = v/R_{load}$, the results of which can be formulated as,

$$\mathcal{G}\mathbf{P}_{sr} \dot{\mathbf{u}} + \mathcal{G}\mathbf{P}_D \mathcal{G}^T \dot{v} = \frac{\mathcal{G}\mathcal{G}^T v}{R_{load}} . \quad (3.33)$$

$\begin{matrix} (1 \times 4) & & (1 \times 1) & & (1 \times 1) \end{matrix}$

Reformulating the modified equation (3.31) to represent the global dynamic equation for the single finite element and altering the global force vector into base acceleration $\mathbf{F}(t) = -\mathbf{Q}\ddot{\mathbf{w}}_{base}$, the new formation of the electromechanical finite element equation can be written as,

$$\mathbf{M} \ddot{\mathbf{u}} + \mathbf{C} \dot{\mathbf{u}} + \mathbf{K} \mathbf{u} + \mathbf{\Theta} v = -\mathbf{Q} \ddot{\mathbf{w}}_{base}$$

$$\mathbf{\Theta}^T \dot{\mathbf{u}} - \frac{v}{R_{load}} + \mathbf{C}_p \dot{v} = 0$$

(3.34)

$\begin{matrix} (4 \times 4) & (4 \times 4) & (4 \times 4) & (4 \times 1) & (4 \times 1) \\ (1 \times 4) & & (1 \times 1) & & (1 \times 1) \end{matrix}$

It should be noted that the modified electromechanical coupling \mathcal{P}_{sr} is equivalent to the transformed electromechanical coupling Θ^T and the capacitance matrix $\mathcal{P}_D \mathcal{P}^T$ is equivalent to the trace of the global capacitance matrix C_p .

3.2.3 Frequency response function of the Direct Non-Orthonormalised Electromechanical Dynamic Equation

The electromechanical matrix dynamic equations shown in equation (3.34) can be solved by assuming that the piezoelectric system response is linear under harmonic base excitation where the beam is excited in the transverse direction. Therefore the solution for the resulting displacement and voltage response can be formulated as $\mathbf{u} = \mathbf{a} e^{i\omega t}$ and $v = b e^{i\omega t}$, where \mathbf{a} is the amplitude of the base translation, b is the amplitude of the harmonic voltage across the resistive load and ω is the driving frequency. Then, rewriting the global dynamic equation, the first term of the matrix equation becomes,

$$\left[\begin{array}{c} -\mathbf{M} \omega^2 + \mathbf{C} i \omega + \mathbf{K} \\ (4 \times 4) \quad (4 \times 4) \quad (4 \times 4) \end{array} \right] \mathbf{a} e^{i\omega t} + \Theta b e^{i\omega t} = \mathbf{Q} \omega^2 w_{base} e^{i\omega t}. \quad (3.35)$$

Cancelling the function $e^{i\omega t}$, and rearranging the displacement onto the left side and another equation onto the right side, the matrix equation becomes,

$$\mathbf{a} = \left[\begin{array}{c} -\mathbf{M} \omega^2 + \mathbf{C} i \omega + \mathbf{K} \\ (4 \times 4) \quad (4 \times 4) \quad (4 \times 4) \end{array} \right]^{-1} \left[\begin{array}{c} \mathbf{Q} \omega^2 w_{base} - \Theta b \\ (4 \times 1) \quad (4 \times 1) \end{array} \right]. \quad (3.36)$$

The second term from equation (3.34) can be manipulated in the same way by substituting the harmonic voltage input to give,

$$\Theta^T i \omega \mathbf{a} e^{i\omega t} - \frac{b e^{i\omega t}}{R_{load}} + C_p i \omega b e^{i\omega t} = 0. \quad (3.37)$$

Substituting equation (3.36) into equation (3.37) after cancelling the $e^{i\omega t}$ term and noting the parameter $R_l = -1/R_{load}$ gives,

$$\begin{aligned} & \begin{bmatrix} \boldsymbol{\Theta}_{(1 \times 4)}^T i\omega \left[-\mathbf{M}_{(4 \times 4)} \omega^2 + \mathbf{C}_{(4 \times 4)} i\omega + \mathbf{K}_{(4 \times 4)} \right]^{-1} \mathbf{Q}_{(4 \times 1)} \omega^2 w_{base} \\ -\boldsymbol{\Theta}_{(1 \times 4)}^T i\omega \left[-\mathbf{M}_{(4 \times 4)} \omega^2 + \mathbf{C}_{(4 \times 4)} i\omega + \mathbf{K}_{(4 \times 4)} \right]^{-1} \boldsymbol{\Theta}_{(4 \times 1)} b \end{bmatrix} \\ & + \begin{bmatrix} C_p i\omega + R_l \\ (1 \times 1) \quad (1 \times 1) \end{bmatrix} b = 0 \end{aligned} \quad (3.38)$$

Rearranging the equation (3.38) and equating the two different terms on the left and right side, the equation can be rewritten in the following form,

$$\begin{aligned} & \begin{bmatrix} -\boldsymbol{\Theta}_{(1 \times 4)}^T i\omega \left[-\mathbf{M}_{(4 \times 4)} \omega^2 + \mathbf{C}_{(4 \times 4)} i\omega + \mathbf{K}_{(4 \times 4)} \right]^{-1} \boldsymbol{\Theta}_{(4 \times 1)} + C_p i\omega + R_l \\ (1 \times 1) \quad (1 \times 1) \end{bmatrix} b \\ & = - \begin{bmatrix} \boldsymbol{\Theta}_{(1 \times 4)}^T i\omega \left[-\mathbf{M}_{(4 \times 4)} \omega^2 + \mathbf{C}_{(4 \times 4)} i\omega + \mathbf{K}_{(4 \times 4)} \right]^{-1} \left[\mathbf{Q}_{(4 \times 1)} \omega^2 w_{base} \right] \end{bmatrix} \end{aligned} \quad (3.39)$$

The amplitude voltage response function can be represented in matrix form as,

$$\begin{aligned} \frac{b}{-\omega^2 w_{base}} &= \begin{bmatrix} C_p i\omega + R_l - \boldsymbol{\Theta}_{(1 \times 4)}^T i\omega \left[-\mathbf{M}_{(4 \times 4)} \omega^2 + \mathbf{C}_{(4 \times 4)} i\omega + \mathbf{K}_{(4 \times 4)} \right]^{-1} \boldsymbol{\Theta}_{(4 \times 1)} \\ (1 \times 1) \quad (1 \times 1) \end{bmatrix}^{-1} \\ & \times \boldsymbol{\Theta}_{(1 \times 4)}^T i\omega \left[-\mathbf{M}_{(4 \times 4)} \omega^2 + \mathbf{C}_{(4 \times 4)} i\omega + \mathbf{K}_{(4 \times 4)} \right]^{-1} \mathbf{Q}_{(4 \times 1)} \end{aligned} \quad (3.40)$$

The multi-mode voltage frequency response can be solved by substituting equation (3.40) into the general voltage solution $v = b e^{i\omega t}$ to obtain the voltage response frequency response function as,

$$\frac{v}{-\omega^2 w_{base} e^{i\omega t}} = \left[\begin{array}{c} i\omega C_p + R_l - i\omega \Theta^T \left[\begin{array}{c} \mathbf{K} - \omega^2 \mathbf{M} + i\omega \mathbf{C} \\ (4 \times 4) \quad (4 \times 4) \quad (4 \times 4) \end{array} \right]^{-1} \Theta \\ (1 \times 1) \quad (1 \times 1) \quad (1 \times 4) \quad (4 \times 4) \quad (4 \times 4) \quad (4 \times 1) \end{array} \right]^{-1} \Theta \quad (3.41)$$

$$\times i\omega \Theta^T \left[\begin{array}{c} \mathbf{K} - \omega^2 \mathbf{M} + i\omega \mathbf{C} \\ (4 \times 4) \quad (4 \times 4) \quad (4 \times 4) \end{array} \right]^{-1} \mathbf{Q} \quad (4 \times 1)$$

The multi-mode FRFs of electric current output can be formulated in terms of Kirchhoff's Current Law where electric current is the fractional voltage over the load resistance ($i = v/R_{load}$). The current frequency response function can be formulated as,

$$\frac{i_p}{-\omega^2 w_{base} e^{i\omega t}} = \frac{1}{R_{load} \quad (1 \times 1)} \left\{ \begin{array}{c} \left[\begin{array}{c} i\omega C_p + R_l - i\omega \Theta^T \left[\begin{array}{c} \mathbf{K} - \omega^2 \mathbf{M} + i\omega \mathbf{C} \\ (4 \times 4) \quad (4 \times 4) \quad (4 \times 4) \end{array} \right]^{-1} \Theta \\ (1 \times 1) \quad (1 \times 1) \quad (1 \times 4) \quad (4 \times 4) \quad (4 \times 4) \quad (4 \times 1) \end{array} \right]^{-1} \\ \times i\omega \Theta^T \left[\begin{array}{c} \mathbf{K} - \omega^2 \mathbf{M} + i\omega \mathbf{C} \\ (4 \times 4) \quad (4 \times 4) \quad (4 \times 4) \end{array} \right]^{-1} \mathbf{Q} \quad (4 \times 1) \end{array} \right\} \quad (3.42)$$

The multi-mode FRFs of electrical power output can be formulated by using the fraction of voltage squared over the load resistance ($P = v^2/R_{load}$). The electrical power output frequency response function can then be given as,

$$\frac{P}{(-\omega^2 w_{base} e^{i\omega t})^2} = \frac{1}{R_{load} \quad (1 \times 1)} \left\{ \begin{array}{c} \left[\begin{array}{c} i\omega C_p + R_l - i\omega \Theta^T \left[\begin{array}{c} \mathbf{K} - \omega^2 \mathbf{M} + i\omega \mathbf{C} \\ (4 \times 4) \quad (4 \times 4) \quad (4 \times 4) \end{array} \right]^{-1} \Theta \\ (1 \times 1) \quad (1 \times 1) \quad (1 \times 4) \quad (4 \times 4) \quad (4 \times 4) \quad (4 \times 1) \end{array} \right]^{-1} \\ \times i\omega \Theta^T \left[\begin{array}{c} -\omega^2 \mathbf{M} + i\omega \mathbf{C} + \mathbf{K} \\ (4 \times 4) \quad (4 \times 4) \quad (4 \times 4) \end{array} \right]^{-1} \mathbf{Q} \quad (4 \times 1) \end{array} \right\}^2 \quad (3.43)$$

3.3 Finite Element Case Study for Single Unimorph Piezoelectric Element

3.3.1 Properties and Geometry of the Unimorph Piezoelectric Element

This section presents a case study of the dynamic frequency response for a one-element piezoelectric unimorph system under base excitation. Here, the presented results only include the first two modes of frequency responses as shown previously in the final derivations of the voltage, current and power FRFs equations (3.41, 3.42 and 3.43). In the case study, the geometrical arrangement for the substructure and the PZT material was taken from the previous analytical research (Alper Erturk & Inman, 2008a) . The

main reason here is to validate the trend behaviour from the proposed non-orthonormalised finite element method. The orthonormalised solution technique can be powerful to simplify a set of large function matrices however the orthogonality forms must be calculated using the eigenvectors. The process of orthogonality can be removed by using the non-orthonormalised finite element method but the operation of large matrix functions can no longer be avoided. It should be noted that the result from the single element model compared with the analytical formulations may have high percentage errors especially for the second to fourth modes. The multi-discretised element formulation will be further considered in the next chapter. The summary of the geometries and the material properties is given in table 3.1. Figure 3.3 shows the set up model of the unimorph power harvester for the single element under harmonic base excitation.

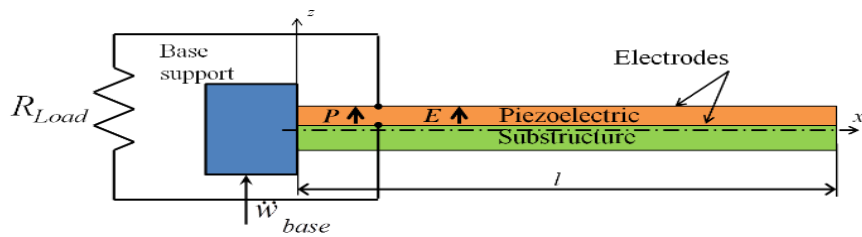


Figure 3.3 Modelling single finite element cantilevered piezoelectric unimorph under transverse base excitation.

Table 3.1 Geometrical and material properties of the piezoelectric unimorph beam.

Dimensional	Parameter
Length of the beam, l (mm)	100
Width of the beam, b (mm)	20
Thickness of the substructure, h_s (mm)	0.5
Thickness of the PZT, h_p (mm)	0.4
Young's Modulus of the substructure, E_s (GPa)	100
Young's Modulus of the PZT, E_p (GPa)	66
Mass Density of the substructure layer, ρ_s (kg/m ³)	7165
Mass Density of the PZT layer, ρ_p (kg/m ³)	7800
Piezoelectric constant, d_{31} (pm/V)	-190
Permittivity, ϵ^s (nF/m)	15.93

Here, the x and z terms show the axis coordinate directions and the horizontal dot dash line shows that the location of the neutral axis coincides with the x axis direction. The

piezoelectric material is polarised in the initial state, in the z -axis direction as seen with the arrow P . The rectangle in blue colour represents the base support of the unimorph cantilevered beam, where as in real condition the unimorph will be clamped to a rigid structure. Two wires are connected in parallel to the load resistances and the two wires are connected to the top and bottom electrode surface layers.

3.3.2 Frequency Response of Electrical Voltage Output

The PZT material model is assumed to be bonded perfectly and covers the entire substructure. Here, the piezoelectric unimorph is considered without the tip mass as clearly shown in figure 3.3. The piezoelectric unimorph is excited under translation motion without rotational motion at the base. The excitation for the simulation model is harmonic and for the current simulation, the base excitation was set to be 1 m/s^2 or 0.101g . The multi-mode voltage FRF is described as the ratio of the voltage output with respect to the base acceleration. Therefore, the FRFs of the electrical voltage can be used from the formulation equation (3.41). In the simulation, the frequency range of interest can be in terms of various modes of resonance. However in this particular case study, only the first two modes were considered. Figure 3.4 shows the simulation result for the first two modes.

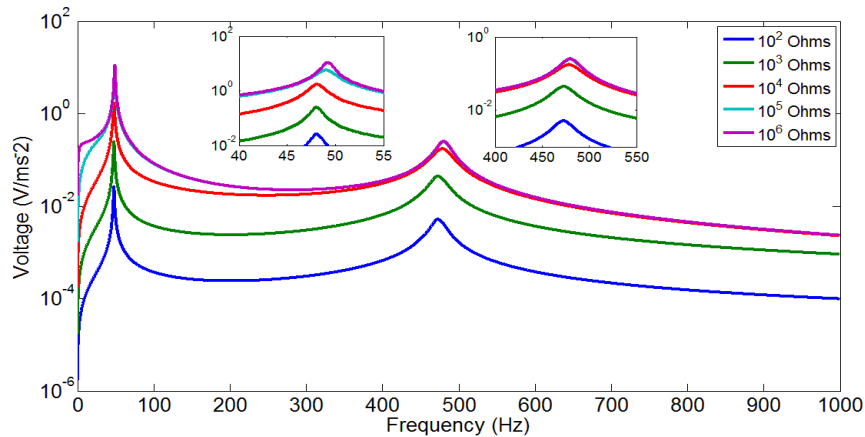


Figure 3.4 FRFs single element electrical voltages output with varying load resistance.

The resistance values R_l were set to cover from 100Ω to $1 \text{ M}\Omega$ to explore the short circuit and open circuit behaviour. The voltage FRFs for the first two short circuit modes show the resonance frequencies of 48.06 Hz and 473.2 Hz while the two

resonance frequencies for open circuit were at 49.18 Hz and 480.3 Hz. The enlarged figure 3.4 showed the peak points of the first and second resonance frequencies. Obviously from figure 3.4, the enlarged pictures give a clear depiction of the behaviour of the first two resonance frequencies with respect to the variable load resistances ranging from 100 Ω to 1 M Ω . The expected result shows the same trend as the previous work (Alper Erturk & Inman, 2008a). The results also show numerical errors of 1% at the first resonance and around 58% for the second resonance at the short circuit condition. This is due to a very coarse finite element model, with just a single element presented in the case study. Therefore, convergence of the number of elements is a very important step to be performed as discussed in the next chapter. Based on the expected result, the varying load resistances showed the monotonic increasing frequency response from the short to open circuits as shown in the two enlarged pictures.

3.3.3 Frequency response of Electrical Current Output

Previously, the FRF of electrical current was formulated using the electrical Kirchhoff Law as the ratio of voltage over the resistance value. The previous multi-mode FRF of electrical current can be shown in the equation (3.42). Figure 3.5 shows the response of the electrical current with the varying load resistances from $R_l=100 \Omega$ to 1 M Ω . As expected, the system response seems to have the opposite trend with the voltage responses. The electrical current FRF shows the decreasing amplitude from the short to open circuits. Obviously, increasing the load resistance reduces the magnitude of the electrical current followed by the shifting resonance frequency at the first mode from 48.06 Hz at short circuit to 49.18 Hz at open circuit resistances as shown in the two enlarged plots from figure 3.5. Moreover, the shifting resonance frequencies also appear for the second mode responses indicating 473.2 Hz at short circuit and 480.3 Hz at open circuit, respectively. Again, all depicted electrical current response behaviours in figure 3.5 have the same trend as those of the previous research references.

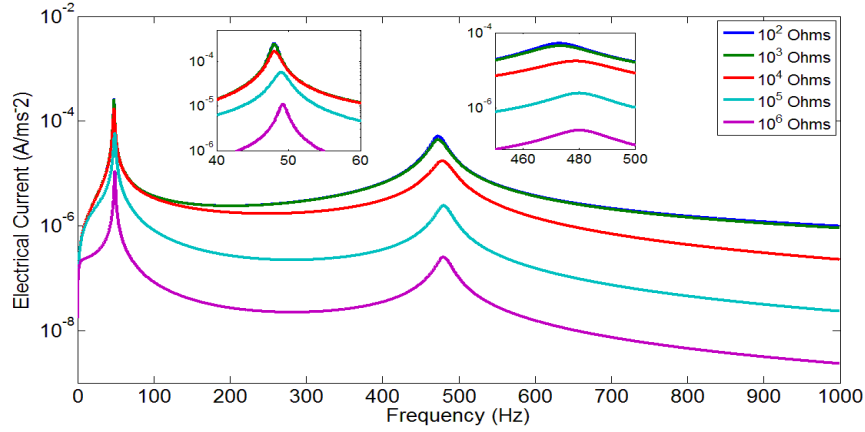


Figure 3.5 FRFs single element electrical current output with varying load resistances.

3.3.4 Frequency response of Electrical Power Output

The expression for multi-mode power FRF can be shown previously in the equation (3.43). Based on Kirchoff's Law the electrical power output can be expressed as $P = v^2 / R_{load}$ for pure resistive load. The electrical power output P is proportional to the square of the voltage output. As the electrical power output is the product of the two voltage and current functions, the trend of the power output response gives the combined results from the voltage and current responses where this can be shown in figure 3.6.

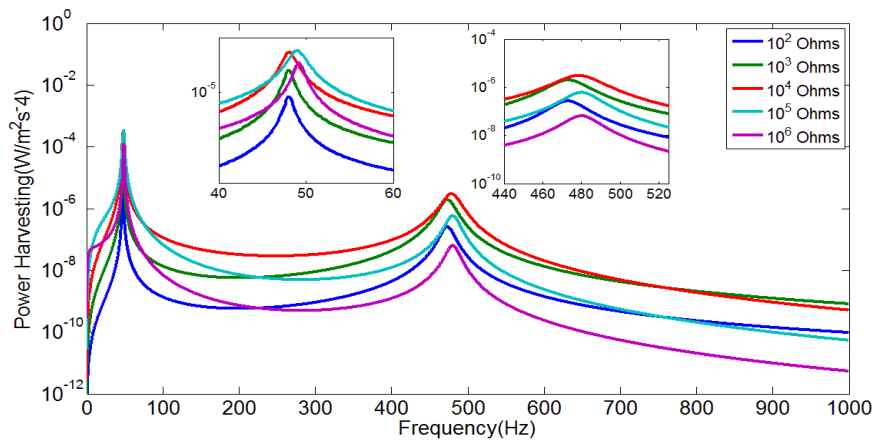


Figure 3.6 FRFs single element power output with varying load resistances.

As previously shown, the voltage response had a monotonic increasing voltage magnitude with increasing load resistances whereas the electrical current had a

monotonic decreasing current magnitude with decreasing load resistances. However, when the electrical power outputs is plotted against the varying load resistances as shown in figure 3.6, increasing power magnitude occurs with load resistances ranging from 100 Ω to 1 k Ω . Moreover, electrical power output reduces with load resistance ranging from 100 k Ω to 1 M Ω . The shifting behaviour also occurs for the power output resonance frequencies. It should be noted that figure 3.6 shows the response of the electrical power output FRF as shown in equation (3.43). Accordingly, the results based on the varying load resistances show that the maximum power value of the first resonance mode occurs at the load resistance of 100 k Ω , as shown in the enlarged view of figure 3.6 with peak resonance frequency around 49.02 Hz. The electrical power magnitude with load resistance of 100 k Ω shows higher value than other load resistances however the power magnitude does not refer to the maximum power output. The load resistance of 100 k Ω is presumed at the open-circuit range as the existing load is relatively located at shifting resonance frequency region. Further investigation needs to be performed to obtain the maximum power output value.

Considering the second mode, the maximum power output response appeared at the load resistance of 10 k Ω where the resonance frequency was at 478.9 Hz (see the enlarged view in figure 3.6). For the load chosen resistance, at 10 k Ω at the second mode the highest power output approaches short circuit load resistance. All samples of the load resistance values used in the analysis are taken arbitrarily in order to show the behaviour of the frequency responses. In addition, the lines in between the first and second resonance frequencies appear to overlap when the load resistances approach 100 Ω and 1 M Ω . Following another crossing line occurs for load resistances of 1 k Ω and 100 k Ω . Mid-range load resistance of 10 k Ω seems to have the highest magnitude power at the second resonance frequency. Resulting observation in figure 3.6 seems to have a similar trend with previous research published by (Alper Erturk & Inman, 2008a).

3.4 Summary

This chapter aimed to show the mathematical derivation of the finite element method for a single piezoelectric beam electromechanical power harvester. A single element was investigated to simplify the model and to reduce the severity of derivation of the

dynamic equation. The fundamental concept was developed using a single element method and will be adapted for developing more complicated structures with different models as discussed in the next few chapters. Here, the dynamic equations for the electrical vibration responses such as voltage, current and power output were obtained using the non-orthonormalised finite element equations.

The extended Hamilton's principle gave the representation of all the energy equations. The kinetic energy equation derived the mass matrices and the potential energy expression reduced from the constitutive linear plane-stress field for the substructure and piezoelectric material developed the stiffness matrices. The electro mechanical potential energy was also derived and developed using the linear-constitutive piezoelectric equation based on the (Meitzler et al., 1988) publication. The development of the linear-constitutive piezoelectric equation was used for formulating the total potential energy including both mechanical and electrical components of the piezoelectric material as this can be substituted into the Hamiltonian equation. It should be noted that the piezoelectric unimorph beam was modelled with the asymmetric thickness dimension. Therefore, the calculation of stiffness matrices gave a very important contribution for calculating the neutral axis and the second moment of inertia for the piezoelectric unimorph. The second moment of inertia can be formulated using summation of internal force balance as presented in the Appendix A. Therefore, these two variables are very important to obtain a correct calculation for identifying the mechanical stiffness behaviour of the structure. Other considerations including the effect of the piezoelectric patch onto the substructure must be correctly modelled. Since the electrodes of the piezoelectric layer are connected with two wires this produced only one single value of voltage or identical voltage output across the entire piezoelectric element. Therefore, a modification of the transformation electromechanical coupling must be performed in order to find the correct voltage.

The direct non-orthonormalised matrix equations were developed using the extended Hamilton's principle to formulate matrix equations of voltage, current and power frequency response functions. The piezoelectric unimorph beam was assumed to be excited under harmonic base acceleration of 1 m/s^2 . The voltage response found from figure 3.4 gave a monotonic increasing voltage magnitude with increasing load resistance from short to open circuit followed by a shift in resonance of around 1 Hz.

The monotonic decreasing current magnitude with increasing load resistance was found to give the opposite trend to that of voltage response from open to short circuit. The power output response represented different trend with the voltage and current behaviours. Observing figure 3.6, the magnitude of power output increased gradually until the load resistance reached the mid-range from $100\ \Omega$ to $10\ \text{k}\Omega$. The power magnitude decreased when the load resistance further increased further from $100\ \text{k}\Omega$ to $1\ \text{M}\Omega$. Again the shifting resonance frequency was also observed with increasing load resistance.

Chapter 4

Finite Element Formulation for Multi Element Piezoelectric Unimorph Beam Power Harvester

As discussed in chapter 3, the derivation of the single finite element electromechanical piezoelectric beam has been shown in detail to achieve a better understanding of finite element power harvester. However, the analysis gives less accurate results since the single element application is only limited to the fundamental frequency and gives a very coarse mode shape. Therefore, the development of the multi-element system is very important to achieve an accurate result using the electromechanical finite element techniques. The purpose of this chapter is to explore the validation and the convergent study using discretised elements to model the piezoelectric unimorph beam. The previous numerical study in chapter 3 presented the foundation for broadening the new frequency response equation using the electromechanical discretised finite element method. In addition, in this chapter, the derivation of the electromechanical dynamic equation and the frequency response function will be explored in detail demonstrating the accuracy of the system response using the direct method with non-orthonormality where no other researcher has investigated this technique. This method will be clarified using the established orthonormalised analytical and finite element response technique introduced by (Alper Erturk & Inman, 2008a) and (M. Lumentut & Howard, 2014). In this chapter, the parametric case study will also be discussed in detail. First, the convergence study based on the number of elements will be given in terms of the eigenvalues and the mode shapes. Second, the voltage, current and power frequency response functions will be discussed in detail.

4.1 Numerical Multi Element Distributed Cantilever Piezoelectric Unimorph Beam

4.1.1 Multi Finite Element Modelling

Figure 4.1 shows the development of the extension of the single finite element model from one element to multi element. It is known that the cantilevered piezoelectric unimorph beam is formed by two different substructure and piezoelectric material layers. The model here assumes that the electrode layers are distributed evenly on the

piezoelectric surfaces. The extension to the multi element formulation can be obtained by making the assumption of identical generated voltage in the parallel connection for each discretised element. The notation P and E with arrow illustrate the polarization and electrical field in the z -(thickness) direction as shown in figure 4.1.

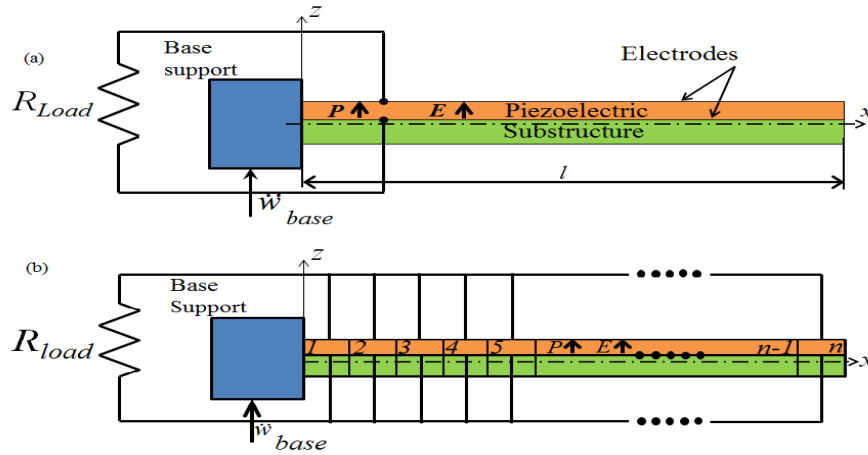


Figure 4.1 Electromechanical discretisation of piezoelectric unimorph adapted from (M. Lumentut & Howard, 2014).

In addition, the multi-element discretisation in figure 4.1b can be assumed using the number of divisions of the single element as shown in figure 4.1a. It should be noted that the piezoelectric element has the same vector polarisation across its length resulting in single voltage output (M. Lumentut & Howard, 2014). Although the piezoelectric element seems to be connected in parallel by multiple wires for each element as shown figure 4.1b, in the physical system only two wires are connected onto the two electrode layers. The two wires are also connected in parallel via the single load resistance.

4.1.2 Local Electromechanical Dynamic Matrix Equation for Multi Element Cantilever Piezoelectric Unimorph Beam

Development of the electromechanical discretised elements equations of motion can be extended from the previous formula using the single element model. Derivation of the local element matrix can be referred to section 3.1 and 3.2 in Chapter 3. Rewriting the general electromechanical dynamic equation of the local element based on Hamilton's principle in equation (3.30), Chapter 3, gives,

$$\begin{bmatrix} \mathbf{M}^{(e)} & \mathbf{0} \\ \mathbf{0} & \mathbf{0} \end{bmatrix} \begin{Bmatrix} \ddot{\mathbf{u}} \\ \dot{\mathbf{v}}_p \end{Bmatrix} + \begin{bmatrix} \mathbf{C}^{(e)} & \mathbf{0} \\ \mathbf{P}_{sr}^{(e)} & \mathbf{P}_D^{(e)} \end{bmatrix} \begin{Bmatrix} \dot{\mathbf{u}} \\ \mathbf{v}_p \end{Bmatrix} + \begin{bmatrix} \mathbf{K}^{(e)} & \mathbf{P}_{rs}^{(e)} \\ \mathbf{0} & \mathbf{0} \end{bmatrix} \begin{Bmatrix} \mathbf{u} \\ \mathbf{v}_p \end{Bmatrix} = \begin{Bmatrix} \mathbf{F}^{(e)} \\ \mathbf{i}_p \end{Bmatrix}, \quad (4.1)$$

where,

$$\begin{aligned} \mathbf{M}^{(e)} &= \int_{V^{(1)}} \rho^{(1)} \underline{\Phi}(x)^T \underline{\Phi}(x) dV^{(1)} + \int_{V^{(2)}} \rho^{(2)} \underline{\Phi}(x)^T \underline{\Phi}(x) dV^{(2)}, \\ \mathbf{K}^{(e)} &= \int_{V^{(1)}} z^2 \underline{\Psi}(x)^T c_{11}^{(1)} \underline{\Psi}(x) dV^{(1)} + \int_{V^{(2)}} z^2 \underline{\Psi}(x)^T c_{11}^{(2)} \underline{\Psi}(x) dV^{(2)}, \\ \mathbf{C}^{(e)} &= \alpha \mathbf{M} + \beta \mathbf{K}, \quad \mathbf{P}_{rs}^{(e)} = \int_{V^{(2)}} z \underline{\Psi}(x)^T e_{31} \underline{\Omega}(z) dV^{(2)}, \\ \mathbf{P}_{sr}^{(e)} &= -\int_{V^{(2)}} z \underline{\Omega}(z)^T e_{31} \underline{\Psi}(x) dV^{(2)}, \quad \mathbf{P}_D^{(e)} = -\int_{V^{(2)}} \underline{\Omega}(z)^T \varepsilon_{33}^S \underline{\Omega}(z) dV^{(2)}, \\ \mathbf{F}^{(e)} &= -\delta \underline{\mathbf{w}}(x) \underline{\mathbf{f}}(x) = -\mathbf{Q} \ddot{\mathbf{w}}_{base}(t), \quad \mathbf{Q} = \int_{V^{(1)}} \rho^{(1)} \underline{\Phi}(x)^T dV^{(1)} + \int_{V^{(2)}} \rho^{(2)} \underline{\Phi}(x)^T dV^{(2)}. \end{aligned}$$

The expression symbols have been explained previously in chapter 3.

4.1.3 Global Electromechanical Dynamic Matrix Equation for Multi Element Based on Electromechanical Vector Transformation

The global electromechanical dynamic equation of the single element can be adapted from equation (3.31) to give the global dynamic matrix equation for the multi element model as,

$$\begin{aligned} \begin{matrix} \mathbf{M} \\ (n_m \times n_m) \end{matrix} \begin{matrix} \ddot{\mathbf{u}} \\ (n_m \times 1) \end{matrix} (t) + \begin{matrix} \mathbf{C} \\ (n_m \times n_m) \end{matrix} \begin{matrix} \dot{\mathbf{u}} \\ (n_m \times 1) \end{matrix} (t) + \begin{matrix} \mathbf{K} \\ (n_m \times n_m) \end{matrix} \begin{matrix} \mathbf{u} \\ (n_m \times 1) \end{matrix} (t) + \begin{matrix} \mathbf{P}_{rs} \\ (n_m \times n_e) \end{matrix} \begin{matrix} \mathbf{v}_p \\ (n_e \times 1) \end{matrix} = \begin{matrix} \mathbf{F} \\ (n_m \times 1) \end{matrix} (t), \\ \begin{matrix} \mathbf{P}_{sr} \\ (n_e \times n_m) \end{matrix} \begin{matrix} \dot{\mathbf{u}} \\ (n_m \times 1) \end{matrix} (t) + \begin{matrix} \mathbf{P}_D \\ (n_e \times n_e) \end{matrix} \begin{matrix} \dot{\mathbf{v}}_p \\ (n_e \times 1) \end{matrix} = \begin{matrix} \mathbf{i}_p \\ (n_e \times 1) \end{matrix} (t), \end{aligned} \quad (4.2)$$

where \mathbf{M} is the global mass matrix, \mathbf{C} is the global Rayleigh damping matrix, \mathbf{K} is the global stiffness matrix, \mathbf{P}_{rs} and \mathbf{P}_{sr} are the global electromechanical coupling, \mathbf{P}_D is global capacitance matrix, \mathbf{F} and \mathbf{i}_p are the global mechanical forces and global current output, \mathbf{u} is the global mechanical coordinate and \mathbf{v}_p is the global voltage output. Here, the notation of subscription under matrix notation is $(\cdot)_{n_m}$ for the

$$i_{p_1} + i_{p_2} + \dots + i_{p_{n_e}} = i = \underset{(1 \times n_e)}{\mathcal{G}} \mathbf{i}_p. \quad (4.6)$$

The notation symbol \mathcal{G} represents the electromechanical vector transformation parameter that can be used to generalise the electromechanical coupling matrix expression \mathbf{P}_{rs} in equation (4.2). To simplify the distinct elemental voltage output in the global coordinate, the electromechanical vector transformation \mathcal{G} from equation (4.5) can be used to multiply with the electromechanical coupling matrices taken from the fourth term of the first expression in equation (4.2). The operational form can be formulated as,

$$\underset{(n_m \times n_e)}{\mathbf{P}_{rs}} \underset{(n_e \times 1)}{\mathcal{G}^T} v = \underset{(n_m \times 1)}{\Theta} v. \quad (4.7)$$

In addition, the second expression of the global matrices from equation (4.2) must also be modified by multiplying the electromechanical vector transformation \mathcal{G} on both sides of equation (4.2) and introducing the electrical vector transformation at the second mode term of equation (4.2), the result of which can be formulated as,

$$\underset{(1 \times n_e)}{\mathcal{G}} \underset{(n_e \times n_m)}{\mathbf{P}_{sr}} \dot{\mathbf{u}} + \underset{(1 \times n_e)}{\mathcal{G}} \underset{(n_e \times n_e)}{\mathbf{P}_D} \underset{(n_e \times 1)}{\mathcal{G}^T} \dot{v} = \underset{(1 \times n_e)}{\mathcal{G}} \mathbf{i}_p. \quad (4.8)$$

Reformulating equation (4.2) using equation (4.7) and altering equation (4.8) using equation (4.6) and the current expression $i = v/R_{load}$ and altering the global force vector as $\mathbf{F} = -\mathbf{Q} \ddot{\mathbf{w}}_{base}(t)$, the new formation of the electromechanical finite element equation for the first and the second terms can be written as,

$$\begin{aligned} \underset{(n_m \times n_m)}{\mathbf{M}} \ddot{\mathbf{u}} + \underset{(n_m \times n_m)}{\mathbf{C}} \dot{\mathbf{u}} + \underset{(n_m \times n_m)}{\mathbf{K}} \mathbf{u} + \underset{(n_m \times 1)}{\Theta} v &= - \underset{(n_m \times 1)}{\mathbf{Q}} \ddot{\mathbf{w}}_{base}, \\ \underset{(1 \times n_m)}{\Theta}^T \dot{\mathbf{u}} - \frac{v}{\underset{(1 \times 1)}{R_{load}}} + \underset{(1 \times 1)}{C_p} \dot{v} &= 0. \end{aligned} \quad (4.9)$$

The generalisation of equation (4.9) can be formulated in the same way as previously discussed in chapter 3. Assuming the unimorph piezoelectric beam behaves linearly under harmonic base excitation, the general solution for the resulting displacement and voltage responses can be formulated as $\mathbf{u} = \mathbf{a} e^{i\omega t}$ and $v = b e^{i\omega t}$, where \mathbf{a} is the amplitude of the base translation, b is the amplitude of the harmonic voltage across the resistive load and ω is the driving frequency. Then, rewriting the global dynamic equation, the first matrix equation becomes,

$$\left[\begin{matrix} -\mathbf{M} \omega^2 + \mathbf{C} i \omega + \mathbf{K} \\ (n_m \times n_m) & (n_m \times n_m) & (n_m \times n_m) \end{matrix} \right] \mathbf{a} e^{i\omega t} + \begin{matrix} \boldsymbol{\Theta} \mathbf{b} e^{i\omega t} \\ (n_m \times 1) \end{matrix} = \begin{matrix} \mathbf{Q} \omega^2 w_{base} e^{i\omega t} \\ (n_m \times 1) \end{matrix}. \quad (4.10)$$

Cancelling the function $e^{i\omega t}$, and rearranging the displacement onto the left side and the voltage term to the right side, the matrix equation becomes,

$$\mathbf{a} = \left[\begin{matrix} -\mathbf{M} \omega^2 + \mathbf{C} i \omega + \mathbf{K} \\ (n_m \times n_m) & (n_m \times n_m) & (n_m \times n_m) \end{matrix} \right]^{-1} \left[\begin{matrix} \mathbf{Q} \omega^2 w_{base} - \boldsymbol{\Theta} \mathbf{b} \\ (n_m \times 1) & (n_m \times 1) \end{matrix} \right]. \quad (4.11)$$

The second term equation (4.9) can be manipulated by substituting the harmonic voltage input to give,

$$\begin{matrix} \boldsymbol{\Theta}^T i \omega \mathbf{a} e^{i\omega t} \\ (1 \times n_m) \end{matrix} - \frac{b e^{i\omega t}}{\begin{matrix} R_{load} \\ (1 \times 1) \end{matrix}} + C_p i \omega b e^{i\omega t} = 0. \quad (4.12)$$

Rearranging equation (4.12) in the same manner by cancelling the function $e^{i\omega t}$ and altering the parameter for load resistance $R_l = -1/R_{load}$, equation (4.12) can be written as,

$$\begin{matrix} \boldsymbol{\Theta}^T i \omega \mathbf{a} \\ (1 \times n_m) \end{matrix} + \left[\begin{matrix} C_p i \omega + R_l \\ (1 \times 1) & (1 \times 1) \end{matrix} \right] b = 0. \quad (4.13)$$

Rewriting equation (4.13) and (4.11) by multiplying the amplitude matrix equation (4.11) with equation (4.13), the resulting expression becomes,

$$\begin{aligned} & \begin{bmatrix} \Theta_{(1 \times n_m)}^T i\omega \left[-\mathbf{M}_{(n_m \times n_m)} \omega^2 + \mathbf{C}_{(n_m \times n_m)} i\omega + \mathbf{K}_{(n_m \times n_m)} \right]^{-1} \mathbf{Q}_{(n_m \times 1)} \omega^2 w_{base} \\ -\Theta_{(1 \times n_m)}^T i\omega \left[-\mathbf{M}_{(n_m \times n_m)} \omega^2 + \mathbf{C}_{(n_m \times n_m)} i\omega + \mathbf{K}_{(n_m \times n_m)} \right]^{-1} \Theta_{(n_m \times 1)} b \end{bmatrix} \\ & + \begin{bmatrix} \mathbf{C}_p i\omega + \mathbf{R}_l \\ (1 \times 1) \quad (1 \times 1) \end{bmatrix} b = 0 \end{aligned} \quad (4.14)$$

Separating two different terms of function equation (4.14) to the left hand side and the right hand side becomes,

$$\begin{aligned} & \begin{bmatrix} \mathbf{C}_p i\omega + \mathbf{R}_l - \Theta_{(1 \times n_m)}^T i\omega \left[-\mathbf{M}_{(n_m \times n_m)} \omega^2 + \mathbf{C}_{(n_m \times n_m)} i\omega + \mathbf{K}_{(n_m \times n_m)} \right]^{-1} \Theta_{(n_m \times 1)} \end{bmatrix} b \\ & = -\Theta_{(1 \times n_m)}^T i\omega \left[-\mathbf{M}_{(n_m \times n_m)} \omega^2 + \mathbf{C}_{(n_m \times n_m)} i\omega + \mathbf{K}_{(n_m \times n_m)} \right]^{-1} \mathbf{Q}_{(n_m \times 1)} \omega^2 w_{base} \end{aligned} \quad (4.15)$$

Formulating equation (4.15) to find the voltage amplitude ratio with respect to the base acceleration gives,

$$\begin{aligned} \frac{b}{-\omega^2 w_{base}} & = \left[\begin{bmatrix} \mathbf{C}_p i\omega + \mathbf{R}_l \\ (1 \times 1) \quad (1 \times 1) \end{bmatrix} - \Theta_{(1 \times n_m)}^T i\omega \left[-\mathbf{M}_{(n_m \times n_m)} \omega^2 + \mathbf{C}_{(n_m \times n_m)} i\omega + \mathbf{K}_{(n_m \times n_m)} \right]^{-1} \Theta_{(n_m \times 1)} \right]^{-1} \\ & \times \Theta_{(1 \times n_m)}^T i\omega \left[-\mathbf{M}_{(n_m \times n_m)} \omega^2 + \mathbf{C}_{(n_m \times n_m)} i\omega + \mathbf{K}_{(n_m \times n_m)} \right]^{-1} \mathbf{Q}_{(n_m \times 1)} \end{aligned} \quad (4.16)$$

The voltage FRF function can be derived by substituting equation (4.16) onto the general voltage output solution $v = b e^{i\omega t}$ to find the voltage frequency response function as,

$$\frac{v}{-\omega^2 w_{base} e^{i\omega t}} = \left[\begin{array}{c} i\omega C_p + R_l - i\omega \Theta^T \left[\begin{array}{c} \mathbf{K} \\ \omega^2 \mathbf{M} + i\omega \mathbf{C} \end{array} \right]^{-1} \Theta \\ (1 \times 1) \quad (1 \times 1) \quad (1 \times n_m) \quad \left(\begin{array}{c} n_m \times n_m \\ n_m \times n_m \\ n_m \times n_m \end{array} \right) \quad (n_m \times 1) \end{array} \right]^{-1} \cdot \quad (4.17)$$

$$\times i\omega \Theta^T \left[\begin{array}{c} \mathbf{K} \\ \omega^2 \mathbf{M} + i\omega \mathbf{C} \end{array} \right]^{-1} \mathbf{Q} \\ (1 \times n_m) \quad \left(\begin{array}{c} n_m \times n_m \\ n_m \times n_m \\ n_m \times n_m \end{array} \right) \quad (n_m \times 1)$$

The multi-mode FRFs of electric current can be formulated in terms of Kirchhoff's Current Law where the current is the fractional voltage over the load resistance value or $i = v/R_{load}$. The current frequency response function can be presented as,

$$\frac{i}{-\omega^2 w_{base} e^{i\omega t}} = \frac{1}{R_{load}} \left\{ \begin{array}{c} \left[\begin{array}{c} i\omega C_p + R_l - i\omega \Theta^T \left[\begin{array}{c} \mathbf{K} \\ \omega^2 \mathbf{M} + i\omega \mathbf{C} \end{array} \right]^{-1} \Theta \\ (1 \times 1) \quad (1 \times 1) \quad (1 \times n_m) \quad \left(\begin{array}{c} n_m \times n_m \\ n_m \times n_m \\ n_m \times n_m \end{array} \right) \quad (n_m \times 1) \end{array} \right]^{-1} \\ \times i\omega \Theta^T \left[\begin{array}{c} \mathbf{K} \\ \omega^2 \mathbf{M} + i\omega \mathbf{C} \end{array} \right]^{-1} \mathbf{Q} \\ (1 \times n_m) \quad \left(\begin{array}{c} n_m \times n_m \\ n_m \times n_m \\ n_m \times n_m \end{array} \right) \quad (n_m \times 1) \end{array} \right\}^{-1} \cdot \quad (4.18)$$

The multi-mode FRFs of power output for the purely resistive load can be formulated using the correlation of the fractional voltage squared over the load resistance value or $P = v^2/R_{load}$. The power frequency response function can then be given by,

$$\frac{P}{(-\omega^2 w_{base} e^{i\omega t})^2} = \frac{1}{R_{load}} \left\{ \begin{array}{c} \left[\begin{array}{c} i\omega C_p + R_l - i\omega \Theta^T \left[\begin{array}{c} \mathbf{K} \\ \omega^2 \mathbf{M} + i\omega \mathbf{C} \end{array} \right]^{-1} \Theta \\ (1 \times 1) \quad (1 \times 1) \quad (1 \times n_m) \quad \left(\begin{array}{c} n_m \times n_m \\ n_m \times n_m \\ n_m \times n_m \end{array} \right) \quad (n_m \times 1) \end{array} \right]^{-1} \\ \times i\omega \Theta^T \left[\begin{array}{c} \mathbf{K} \\ \omega^2 \mathbf{M} + i\omega \mathbf{C} \end{array} \right]^{-1} \mathbf{Q} \\ (1 \times n_m) \quad \left(\begin{array}{c} n_m \times n_m \\ n_m \times n_m \\ n_m \times n_m \end{array} \right) \quad (n_m \times 1) \end{array} \right\}^{-1} \cdot \quad (4.19)$$

4.2 Validation of Multi-Element Piezoelectric Unimorph with the Analytical Method Published by (Alper Erturk & Inman, 2008a)

4.2.1 Convergence Study

In this section, the multimode frequency response is investigated based on the convergence study approach. The study focuses on behaviour of the resonance frequency of the coupled piezoelectric unimorph system with respect to the increasing number of elements. The resonance frequency here is taken purely as the mechanical

response without load resistance to simulate the piezoelectric system. The resonance frequencies were calculated using eigenvalue methods at the first six modes with number of element from 1 to 30 elements. The results of the convergent study are shown in table 4.1 and the graphical representation of the resonant frequency versus the number of elements is shown in figure 4.2. It should be noted that the case study uses the same geometry and material properties in table 3.1 of chapter 3.

Table 4.1 Number of element and the frequencies of the first six modes.

Number of elements	Frequencies (Hz)					
	Mode 1	Mode 2	Mode 3	Mode 4	Mode 5	Mode 6
1	48.04	473.29	-	-	-	-
2	47.83	302.16	1021.95	2966.14	-	-
3	47.81	300.60	849.38	1912.78	3599.86	7176.74
4	47.81	299.97	845.43	1667.84	3102.11	4982.00
5	47.81	299.76	841.94	1663.25	2760.58	4586.08
10	47.81	299.63	839.14	1645.54	2724.42	4081.54
15	47.81	299.62	838.97	1644.26	2719.03	4064.28
20	47.81	299.62	838.94	1644.07	2718.06	4061.15
25	47.81	299.62	838.94	1644.01	2717.79	4060.26
30	47.81	299.62	838.94	1643.99	2717.69	4059.93

The resonance frequency results shown in the table 4.1 and figure 4.2, indicate that the first six resonance frequencies have identical values after the number of elements is increased. The first mode of resonance reaches the converged result after increasing to 3 elements. The second mode of resonance reaches the converged frequency for 10 elements while third mode of resonance frequency converges using 20 elements. The 4th, 5th and 6th modes still show the changes of resonance until reaching convergence with 30 elements. It should be noted here that the convergence results with the fraction lower than 0.1 Hz is generally not considered in the physical situation where it can be difficult to achieve the required geometrical tolerances. The consideration here based on the use of two decimal numbers as shown above is helpful to compare with the result shown by (Alper Erturk & Inman, 2008a). Moreover, the published research by (Alper Erturk & Inman, 2008a), only shows the first three modes of the resonance frequency. According to table 4.1 and figure 4.2, 20 discretised finite elements provide resonance results with very similar values as the published research. If the analysis of

the model only requires the first mode resonance, 3 discretised finite elements will be sufficient to show the correct resonance frequency value. Moreover, the second resonance frequency will require 15 elements and the third resonance frequency will require 20 elements. Therefore, 20 discretised elements were chosen here to validate the simulation research for the first three modes of coupled resonance behaviour.

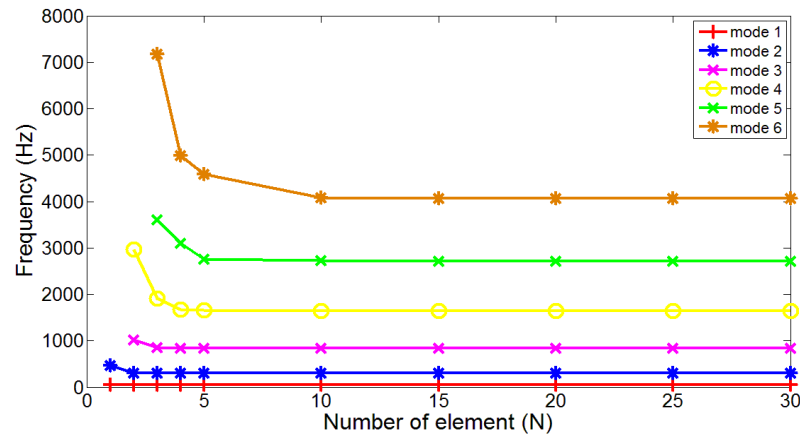


Figure 4.2 Convergence study of coupled system resonance versus number of elements.

4.2.2 Frequency Response of Electrical Voltage Output

This section aims to describe the dynamic response of electrical voltage of the piezoelectric unimorph with the asymmetrical neutral axis. As previously mentioned, the case study will be compared with the analytical method proposed by (Alper Erturk & Inman, 2008a). Since the voltage FRFs has been formulated in equation (4.12), the corresponding response can be simulated using the MATLAB program. The resulting simulation shows the dynamic response of the piezoelectric unimorph using the non-orthonormalised finite element method having a very similar pattern with the analytical orthonormalised method. The results are shown in figure 4.3.

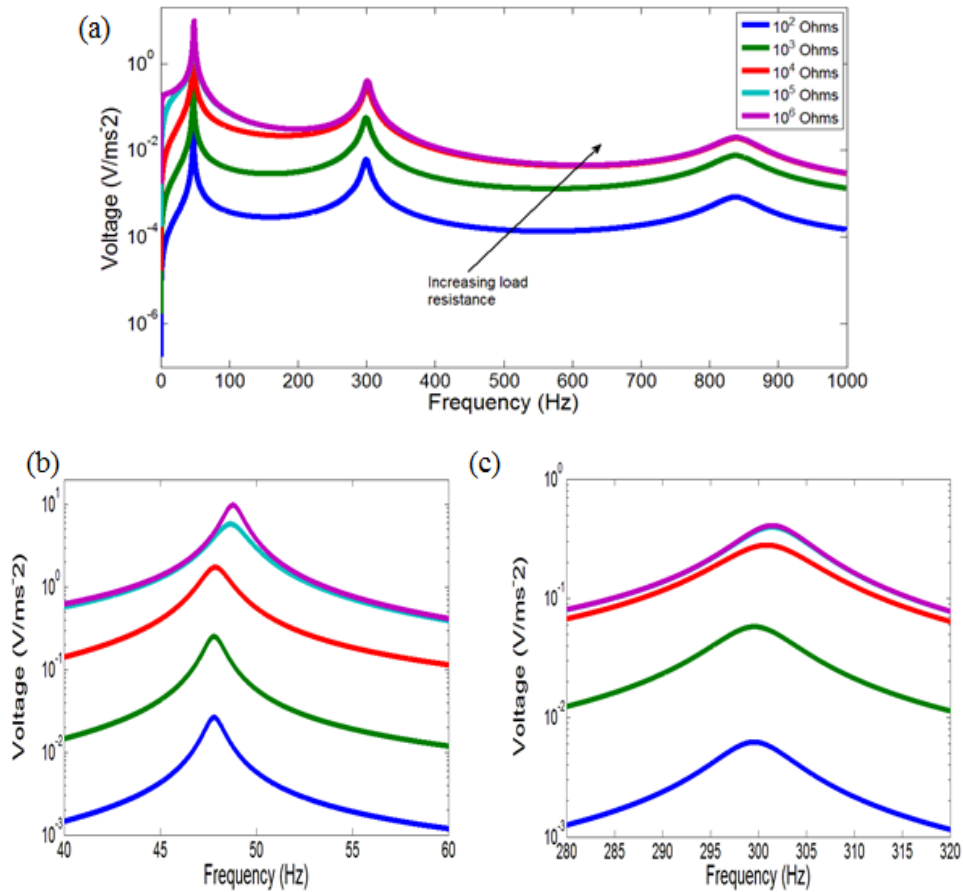


Figure 4.3 (a) FRFs electrical voltage using 20 discretised elements (b) First Mode (c) Second Mode.

Figure 4.3a-c shows that the electrical voltage frequency responses increase monotonically with increasing load resistances from 100 Ω to 1 M Ω . The resonance frequency shifts for the first two modes with varying load resistance from the short to open circuits. The two enlarged figures of 4.3b and 4.3c with 20 discretised elements confirm the resulting simulation behaviour to be very similar with the published research.

Further investigation of figure 4.3b shows the frequency shifts about 1 Hz with the applied load resistances. The resonance frequency with load resistance of 100 Ω (or short circuit) approximately gives 47.8 Hz. Meanwhile, when the load resistance is altered to about 1 M Ω (or open circuit), the resonance frequency changes to 48.8 Hz. Figure 4.3c shows the second mode with the shift of resonance frequencies from 299.5 Hz at short circuit to 301.4 Hz at open circuit. The resonance frequency at the third mode shifts from 838.2 Hz to 839.2 Hz representing the short and open circuits,

respectively. Generally, the resulting electrical voltage FRFs are shown in figure 4.3 having a good agreement with the research published by (Alper Erturk & Inman, 2008a).

The system response at the first resonance frequency at the short and open circuit conditions shows the voltage magnitude with variable load resistance as shown in figure 4.4. As expected, the voltage output at the short circuit has higher amplitude than the open circuit resonance frequency excitation for lower load resistances. The behaviour of voltage magnitude changes after the two resonances overlap at load resistance of 39.8 k Ω . It means that when voltage passes the overlapped point, the open circuit resonance frequency gives higher amplitude than the short circuit resonance frequency at higher load resistances.

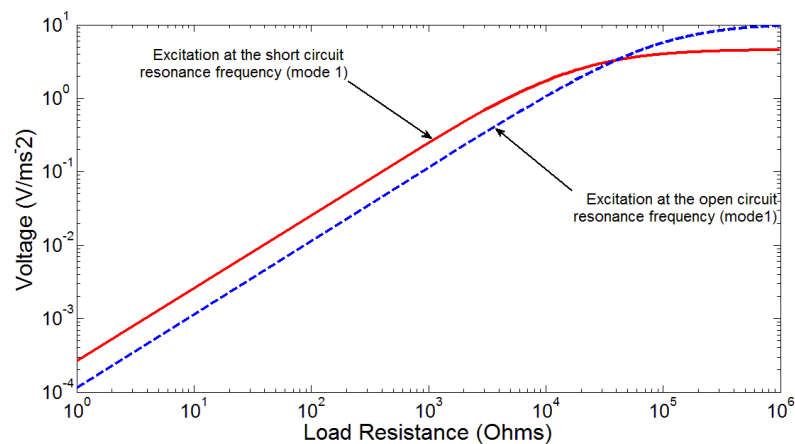


Figure 4.4 Variation of voltage output and load resistance under base excitations at short and open circuit resonance frequencies for the first mode.

4.2.3 Frequency Response of Electrical Current Output

The current FRFs is shown in figure 4.5, where the frequency response function can be obtained by dividing the voltage output with the load resistance. Here, when the current FRF is plotted against the load resistance, the reverse trend of current response occur. Unlike the voltage response, the current magnitude FRFs decrease monotonically with increasing load resistance values. The highest current magnitude stays constant until reaching the short circuit resonance frequency which is opposite to that of the voltage output. Comparing the result obtained from the current response,

the finite element method and the analytical results published by (Alper Erturk & Inman, 2008a), again the finite element study is found to give good agreement.

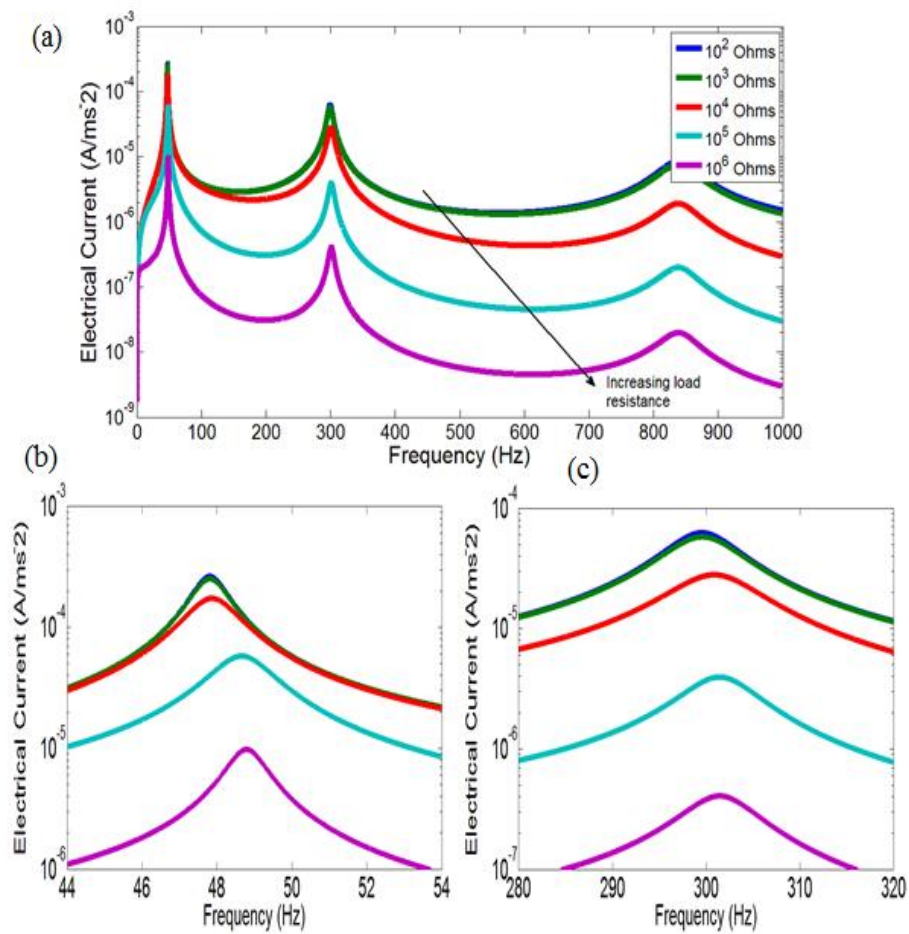


Figure 4.5 (a) FRF's electrical current using 20 discretised elements (b) First Mode (c) Second mode.

Figure 4.6 shows the current output versus load resistance under base excitation at the short and open circuit resonance frequency condition. A similar trend appears in figure 4.6 with the graphical voltage magnitude verse load resistance in figure 4.4. Here, the magnitude of the electrical current output gives higher amplitude at the short circuit than the open circuit resonance for relatively low ranges of load resistances. As shown in figure 4.6, when the system is close to the short circuit conditions, the current output at the short and open circuit do not change with the variation of the load resistance at the lower range resistances. Therefore, the current output stays flat and then decreases linearly for higher load resistances as shown in figure 4.6. Both magnitude lines intersect at the load resistance of 39.8 kΩ and the position lines show the opposite

pattern after the intersection point which is higher at open circuit resonance frequency excitation than short circuit resonance frequency excitation.

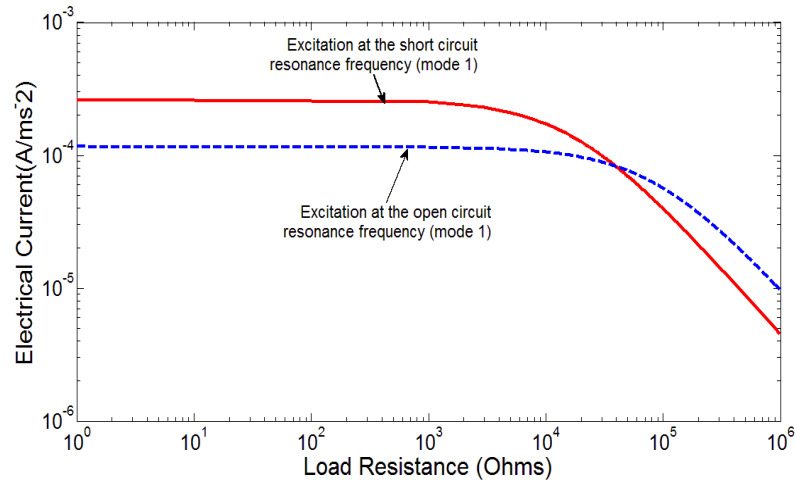


Figure 4.6 Variation of current output and load resistance under base excitations at the short and open circuit resonance frequencies of the first mode.

4.2.4 Frequency Response of Electrical Power Output

The power output FRFs versus the load resistances are shown in figure 4.7 and provide some interesting results. The power output response shifts with varying load resistance ranging from 100 Ω to 1 M Ω . As previously shown, the magnitude of the electrical voltage and current output behave in opposite trend with increasing load resistance. Figure 4.7b the first resonance frequency, the maximum power output occurs at the load resistance of 100 k Ω where the resonance frequency attains 48.7 Hz giving very close to open circuit conditions. Meanwhile, the maximum power of the second mode appears at the resonance frequency of 300.9 Hz with load resistance close to 10 k Ω . It should be noted that the load resistance of 10 k Ω is in the middle of the short and open circuit resistance range. In addition, for the third mode resonance frequency shown in figure 4.7a, the maximum power at 838.3 Hz occurs at the resistance approaching short circuit condition. The resulting voltage, current and power output response have a very similar result with the previous published literature.

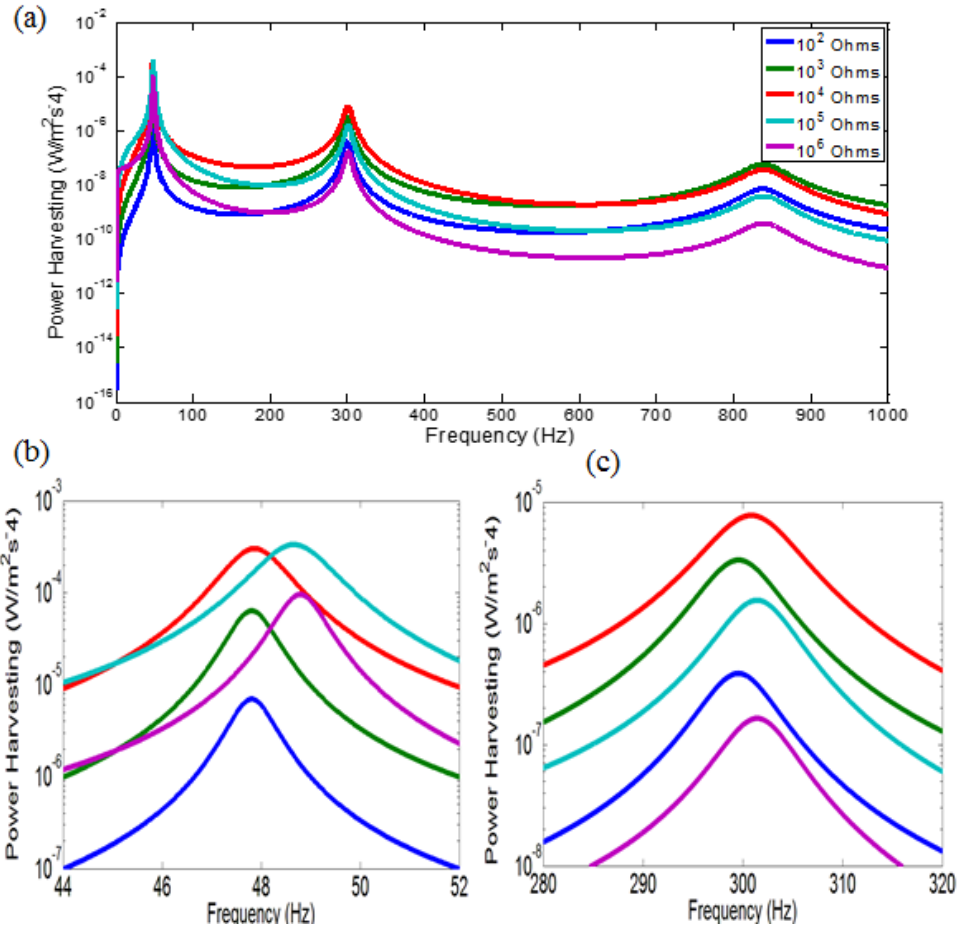
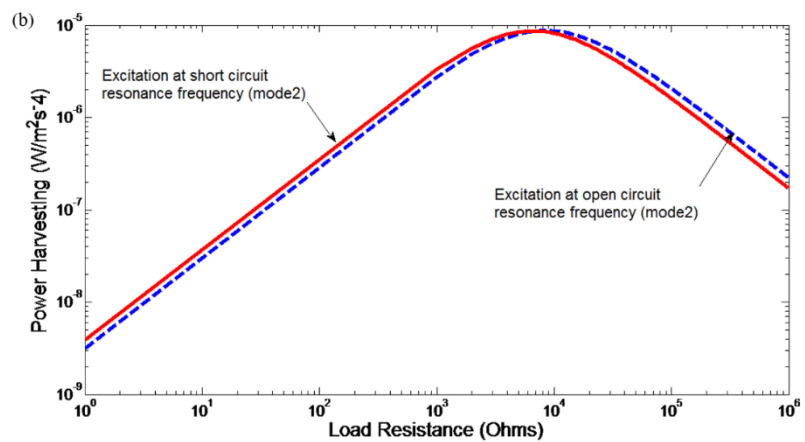
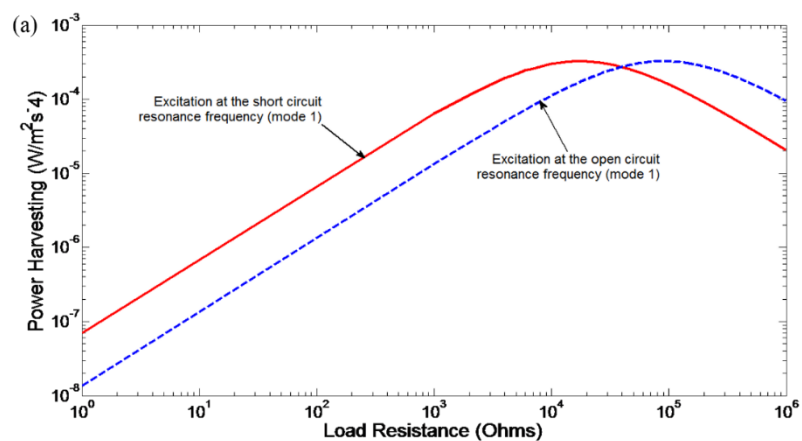


Figure 4.7 (a) FRFs of power electrical response with 20 discretised elements (b) First mode (c) Second mode.

Moreover, figure 4.8a shows the power output versus variable load resistances, when the system is excited under short and open circuit resonance frequencies. Previously, the voltage and current responses in figure 4.4 and 5.6 showed higher amplitude at the short circuit base excitation at lower resistances and behave in the opposite way after passing the overlapped point. The trend is also valid for the power output with respect to variable load resistances because it is known that the power output is simply a function of voltage and current. Even the overlapped point occurs at the similar load resistance of 39.8 k Ω . The power at the open circuit base excitation at high load resistances becomes higher amplitude than the short circuit base excitation after passing the junction point. The trends of power at lower load resistances show a similar pattern with short and open circuit base excitation as the power amplitude increases linearly with varying load resistance. Figure 4.8a shows the piezoelectric beam response under the short and open circuit resonances. The two maximum peaks show

the same power amplitude for short and open circuit load resistances. Obviously, if the load resistance at both peaks are applied in the frequency response, both of them yield the same amount of power. The resistance between the two peaks shows optimum value with the maximum power. The resulting power output versus varying load resistances can be seen in figure 4.8a where the trend of the result very similar with the research published by (Alper Erturk & Inman, 2008a). Power outputs for the second and third modes can be seen in figure 4.8b-c. The maximum power amplitude peak for the second variable load resistance versus short and open circuit resonance frequencies seem to be close to each other. In figure 4.8b, the power amplitude at the second mode changes where the short and open circuit lines tend to be close to each other as shown in figure 4.8c, where the power amplitude in the third mode coincides for both lines under short and open circuit resonance frequencies.



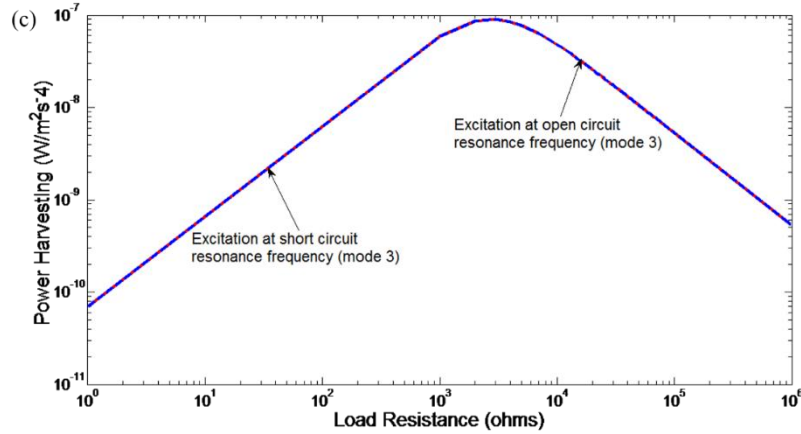


Figure 4.8 (a) Variation in power output versus load resistance under base excitations at the short and open circuit resonance frequencies of the first mode (b) second mode (c) third mode.

The validation between the finite element with direct non-orthonormalised method and the analytical orthonormalised method introduced by (Alper Erturk & Inman, 2008a) shows very good agreement. Utilising the convergence study as given in table 4.1 informs the choice of the number of elements to give results close to the analytical orthonormalised method. Based on table 4.1, discretisation with 20 elements shows very similar resonance frequencies for the first three modes.

4.3 Multi-Element Comparison of the Distributed Piezoelectric Unimorph Using Orthonormalised Method Published by (M. Lumentut & Howard, 2014)

4.3.1 Orthonormalised Finite Element Method

Recently, new methods for modelling the electromechanical finite element equations were developed by (M. Lumentut & Howard, 2014) for the cantilever unimorph beam under tip mass offset. The comparison study using the same method was published in the conference paper by (Warman, Lumentut, & Howard, 2014) without tip mass contribution. This section illustrates the technical review and comparison of results using the different solution techniques. In this case the piezoelectric unimorph beam is considered here without tip mass to the structure. The solution form of equation (4.2) can be written using time-dependent displacements in terms of the normalised modal vector and the time-dependent displacement generalised coordinate as,

$$\mathbf{u}(t) = \varphi_1 \mathbf{a}_1(t) + \varphi_2 \mathbf{a}_2(t) + \dots + \varphi_{m-1} \mathbf{a}_{m-1}(t) + \varphi_m \mathbf{a}_m(t) = \boldsymbol{\varphi} \mathbf{a}(t), \quad (4.20)$$

and the normalised modal matrix is given as,

$$\boldsymbol{\varphi} = \mathbf{U} (\mathbf{U}^T \mathbf{M} \mathbf{U})^{-\frac{1}{2}}. \quad (4.21)$$

Parameters $\boldsymbol{\varphi}$ and \mathbf{U} represent the normalised modal matrix and generalised eigenvector, respectively. The orthogonality can be calculated using the eigenvector which is reduced from the undamped mechanical dynamic equation. The eigenvector is also recognised as a mechanical shape of the natural mode and includes the contribution of mechanical properties such as stiffness and mass matrices.

In order to diagonalise the mass, stiffness and damping matrices for simplifying the numerical technique, equation (4.20) are substituted into equation (4.2), pre-multiplying with $\boldsymbol{\varphi}^T$, to give,

$$\begin{aligned} \boldsymbol{\varphi}^T \mathbf{M} \boldsymbol{\varphi} \ddot{\mathbf{a}}(t) + \boldsymbol{\varphi}^T \mathbf{C} \boldsymbol{\varphi} \dot{\mathbf{a}}(t) + \boldsymbol{\varphi}^T \mathbf{K} \boldsymbol{\varphi} \mathbf{a}(t) + \boldsymbol{\varphi}^T \mathbf{P}_\theta \mathbf{v}(t) &= \boldsymbol{\varphi}^T \mathbf{F} \\ \mathbf{P}_\theta^T \boldsymbol{\varphi} \dot{\mathbf{a}}(t) + \mathbf{P}_D \dot{\mathbf{v}}(t) &= \mathbf{i}_p(t). \end{aligned} \quad (4.22)$$

After simplifying, equation (4.22) becomes,

$$\begin{aligned} \ddot{\mathbf{a}}(t) + 2\zeta \boldsymbol{\omega} \dot{\mathbf{a}}(t) + \boldsymbol{\omega}^2 \mathbf{a}(t) + \hat{\mathbf{P}}_\theta \mathbf{v}(t) &= -\hat{\mathbf{Q}} \ddot{\mathbf{w}}_{base}(t), \\ \hat{\mathbf{P}}_\theta^T \dot{\mathbf{a}}(t) + \mathbf{P}_D \dot{\mathbf{v}}(t) &= \mathbf{i}_p(t). \end{aligned} \quad (4.23)$$

The orthonormalised parameters in equation (4.23) can be represented by the following form,

$$\begin{aligned} \boldsymbol{\varphi}^T \mathbf{M} \boldsymbol{\varphi} = \mathbf{I}, \boldsymbol{\varphi}^T \mathbf{K} \boldsymbol{\varphi} = \boldsymbol{\omega}^2, \boldsymbol{\varphi}^T \mathbf{C} \boldsymbol{\varphi} = \alpha (\boldsymbol{\varphi}^T \mathbf{M} \boldsymbol{\varphi}) + \beta (\boldsymbol{\varphi}^T \mathbf{K} \boldsymbol{\varphi}) = \alpha \mathbf{I} + \beta \boldsymbol{\omega}^2 = 2\zeta \boldsymbol{\omega}, \\ \hat{\mathbf{P}}_\theta = \boldsymbol{\varphi}^T \mathbf{P}_\theta, \hat{\mathbf{P}}_\theta^T = \mathbf{P}_\theta^T \boldsymbol{\varphi}, \hat{\mathbf{Q}} = \boldsymbol{\varphi}^T \mathbf{Q}. \end{aligned} \quad (4.24)$$

The orthonormality property of the mechanical dynamic equations as given by equation (4.24a) results in diagonal matrices that can be further simplified into the global scalar form of the electromechanical dynamic equations. The process of changing the electromechanical dynamic equations into global scalar form provides a very useful method to formulate the series form of the multimode frequency response functions. Based on the formulation given in equation (4.23), the first scalar form of the discretised electromechanical piezoelectric dynamic equation can be formulated for the multi degree of freedom (multimode) system $r = 1, 2, 3, \dots, NDOF$ and in terms of the number of normalised piezoelectric elements $s = 1, 2, 3, \dots, NELP$ as,

$$\ddot{a}_r(t) + 2\zeta_r \omega_r \dot{a}_r(t) + \omega_r^2 a_r(t) + \sum_{s=1}^{NELP} \hat{P}_{rs} v_s(t) = -\hat{Q}_r \ddot{w}_{base}(t),$$

$$r = 1, 2, \dots, NDOF. \quad (4.25)$$

The $NDOF$ and $NELP$ represent the number of degrees of freedom and number of piezoelectric elements. The second form of the discretised electromechanical piezoelectric dynamic equation can be formulated as,

$$\sum_{r=1}^{NDOF} \hat{P}_{sr} \dot{a}_r(t) + P_{Ds} \dot{v}_s(t) = i_{Ps}(t),$$

$$s = 1, 2, 3, \dots, NELP. \quad (4.26)$$

The electromechanical equation can be formulated by using the terms of the electromechanical discretisation as shown in figure 4.1. As stated previously, the piezoelectric surface is covered evenly by the electrode layers and results in only a single output. The terms of voltage and current in the global scalar formation equation (4.25) and (4.26) can be solved by using electrical voltage and current discretisation. Therefore, internal parallel connection in terms of the electrical discretised response using the Kirchhoff's voltage law (KVL) and Kirchhoff's current law (KCL) must be formulated in the scalar form as,

$$v_1(t) = v_2(t) = \dots = v_s(t) = v(t),$$

$$i_{p1}(t) + i_{p2}(t) + \dots + i_{ps}(t) = i_p(t). \quad (4.27)$$

Voltage output related to the external load resistance can be formulated as,

$$v(t) = i_p(t)R_{load} . \quad (4.28)$$

Mathematical operation to formulate the multimode frequency response functions of the unimorph beam can be done in a few steps. First, modifying the first term of equation (4.26) algebraically corresponding with the number of the normalised piezoelectric elements. Second, the obtained result in the first step is substituted using equations (4.27) and (4.28). Third, substituting equation (4.27) into equation (4.25). Finally, using Laplace transforms to solve the obtained result from the second and third steps and the resulting step to obtain the superposition matrix form. The first superposition form of the voltage multimode FRFs series can be given as,

$$\frac{v(j\omega)}{-\omega^2 w_b e^{j\omega t}} = \frac{\sum_{r=1}^{NDOF} \frac{\hat{Q}_r j\omega \sum_{s=1}^{NELP} \hat{P}_{sr}}{\omega_r^2 - \omega^2 + j2\zeta_r \omega_r \omega}}{\sum_{s=1}^{NELP} j\omega P_{Ds} - \frac{1}{R_{load}} - \sum_{r=1}^{NDOF} \frac{j\omega \sum_{s=1}^{NELP} \hat{P}_{sr} \sum_{s=1}^{NELP} \hat{P}_{rs}}{\omega_r^2 - \omega^2 + j2\zeta_r \omega_r \omega}} . \quad (4.29)$$

The series form of the multimode FRF for the electric current output is given as,

$$\frac{i_p(j\omega)}{-\omega^2 w_b e^{j\omega t}} = \frac{\frac{1}{R_{load}} \sum_{r=1}^{NDOF} \frac{\hat{Q}_r j\omega \sum_{s=1}^{NELP} \hat{P}_{sr}}{\omega_r^2 - \omega^2 + j2\zeta_r \omega_r \omega}}{\sum_{s=1}^{NELP} j\omega P_{Ds} - \frac{1}{R_{load}} - \sum_{r=1}^{NDOF} \frac{j\omega \sum_{s=1}^{NELP} \hat{P}_{sr} \sum_{s=1}^{NELP} \hat{P}_{rs}}{\omega_r^2 - \omega^2 + j2\zeta_r \omega_r \omega}} . \quad (4.30)$$

The power harvesting multimode FRF related to the input transverse acceleration can be formulated as,

$$\frac{P_p(j\omega)}{-\omega^2 w_b e^{j\omega t}} = \left[\frac{\frac{1}{\sqrt{R_{load}}} \sum_{r=1}^{NDOF} \frac{\hat{Q}_r j\omega \sum_{s=1}^{NELP} \hat{P}_{sr}}{\omega_r^2 - \omega^2 + j2\zeta_r \omega_r \omega}}{\sum_{s=1}^{NELP} j\omega P_{Ds} - \frac{1}{R_{load}} - \sum_{r=1}^{NDOF} \frac{j\omega \sum_{s=1}^{NELP} \hat{P}_{sr} \sum_{s=1}^{NELP} \hat{P}_{rs}}{\omega_r^2 - \omega^2 + j2\zeta_r \omega_r \omega}} \right]^2 \quad (4.31)$$

4.3.2 Material Properties and Geometry

The investigation of the numerical method can involve comparison between the finite element non-orthonormalised and orthonormalised solution technique (M. Lumentut & Howard, 2014) but the piezoelectric unimorph is used without the tip mass attached to the structure. Here, the entire voltage, current and power output response will be validated. However, the validation of the case study is only limited to the first two modes of resonance frequency behaviour. In the case study, the geometry and material properties of the piezoelectric unimorph beam are given in table 4.2. Note that the input base excitation onto the structure is set to be 1 m/s².

Table 4.2 Properties of piezoelectric unimorph beam material.

Dimensional	Parameter
Length of the beam, l (mm)	60
Width of the beam, b (mm)	6
Thickness of the substructure, h_s (mm)	0.5
Thickness of the PZT, h_p (mm)	0.127
Young's Modulus of the substructure, E_s (GPa)	105
Young's Modulus of the PZT, E_p (GPa)	66
Mass Density of the substructure layer, ρ_s (kg/m ³)	9000
Mass Density of the PZT layer, ρ_p (kg/m ³)	7800
Piezoelectric constant, d_{31} (pm/V)	-190
Permittivity, ϵ^s (nF/m)	15.93

4.3.3 Convergence, Mode Shape and FRF Displacement

The previous convergent study showed the convenient methods for simulating the numerical method. Figure 4.9 shows the numerical convergence of the number of

elements with respect to the calculated resonance frequency. A very small error in the resonance frequency is shown when the element numbers increase especially for the first three modes. 50 discretised elements were used for the simulation here in order to give very accurate frequency result and smooth mode shapes as shown in the previous numerical study.

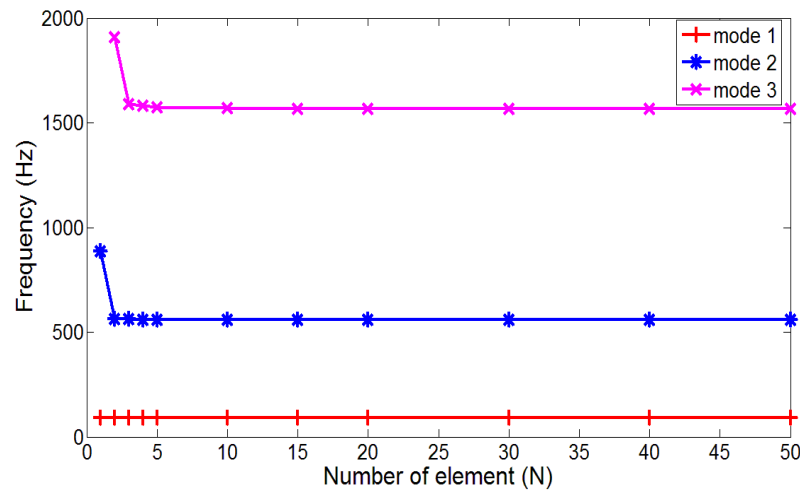


Figure 4.9 Convergence study of the coupled system resonance versus number of element.

Typically, decreasing numbers of discrete elements will result in coarse mode shapes while increasing number of discrete elements will create smooth mode shape curves. However if the number of finite elements increase too high it can result in longer computation time for the calculations. Figure 4.10 shows the eigenvector of the first four modes of the coupled piezoelectric system plotted against the number of discretised elements with piezoelectric length of 60 mm. The resonance frequencies of the first, second, third and fourth modes give 89.38 Hz, 599.9 Hz, 1568.41 Hz and 3073.46 Hz.

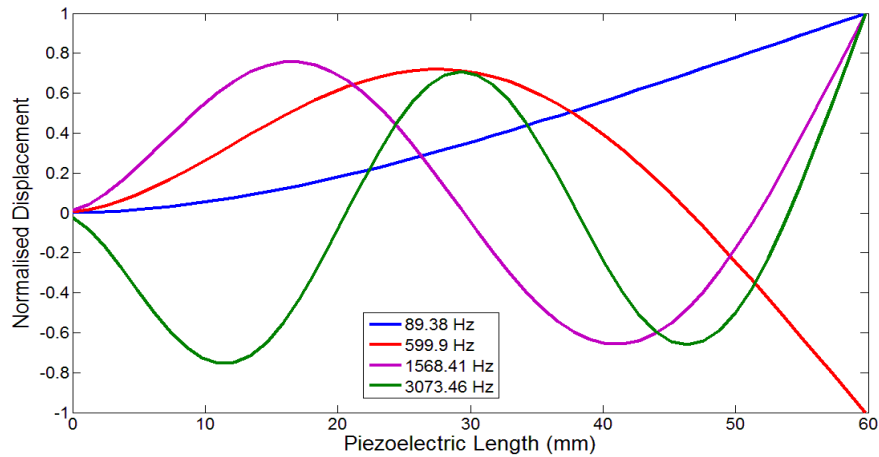
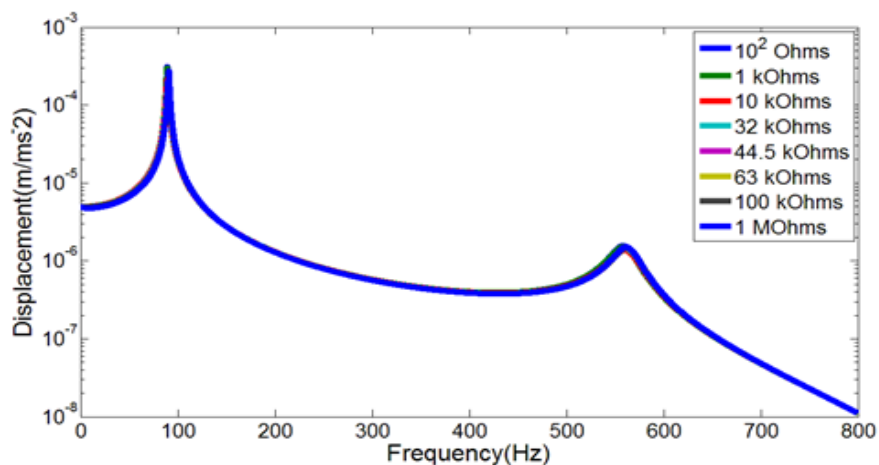


Figure 4.10 Modes shape of the first four unimorph beam modes with 50 discretised elements.

Figure 4.11 shows the FRF of the tip displacement of the cantilever piezoelectric unimorph beam as a function of load resistance. Figure 4.11b shows the first mode resonance of the tip displacement. The highest amplitude of tip displacement occurs at the load resistance 100Ω and the amplitude of tip displacements continuously reduces to the lowest value at load resistance of $44.5 \text{ k}\Omega$. The tip amplitude response again increases as the load resistance reaches $1 \text{ M}\Omega$. Figure 4.11b-c show the resonance frequency shifts between the short and open circuit load resistance conditions. Here the resonance shifts from 89.38 Hz at the short circuit to 90.94 Hz at the open circuit load resistance. Both of the load resistances result in amplitude displacements of $0.3135 \text{ mm/ms}^{-2}$ and $0.2749 \text{ mm/ms}^{-2}$, respectively. The second mode (see figure 4.11c) showed similar behaviour with the first mode resonance, but the lowest amplitude occurred with the load resistance value of $44.5 \text{ k}\Omega$.



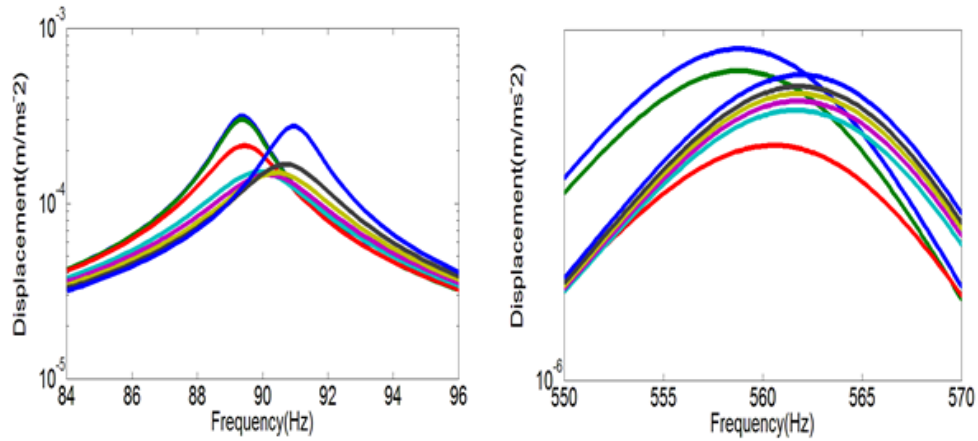


Figure 4.11 (a) FRFs of tip displacement with 50 discretised elements (b) The first Mode (c) The second Mode.

4.3.4 Frequency Response of Electrical Voltage Output

The resulting behaviour of electrical voltage output under base input excitation of 1 m/s^2 acceleration is shown in figure 4.12. As previously mentioned, the proposed non-orthonormality direct method is compared with the orthonormalised finite element response technique. The results show that the electromechanical frequency responses are identical between the two different methods as expected. The electrical voltage FRF is shown in figure 4.12, where the trends of the two numerical methods for the electrical voltage under variable load resistance show agreement and the amplitudes increase from short to open circuit load resistances, followed by the frequency shift. This occurs especially at the first mode where the second mode frequency response seems to stay at a constant frequency with increasing amplitude. According to the two enlarged views from figure 4.12, the first mode of the electrical voltage FRF with short circuit resonance frequency shows 89.38 Hz and the frequency shifts to 90.94 Hz for the open circuit resonance frequency. The second mode of the electrical voltage FRF shows 559.9 Hz at short circuit and the frequency shifts to 562.7 Hz at the open circuit condition. It should be noted that for the finite element simulation the electrical voltage FRFs have similarities of response behaviour with the previous analytical method research study.

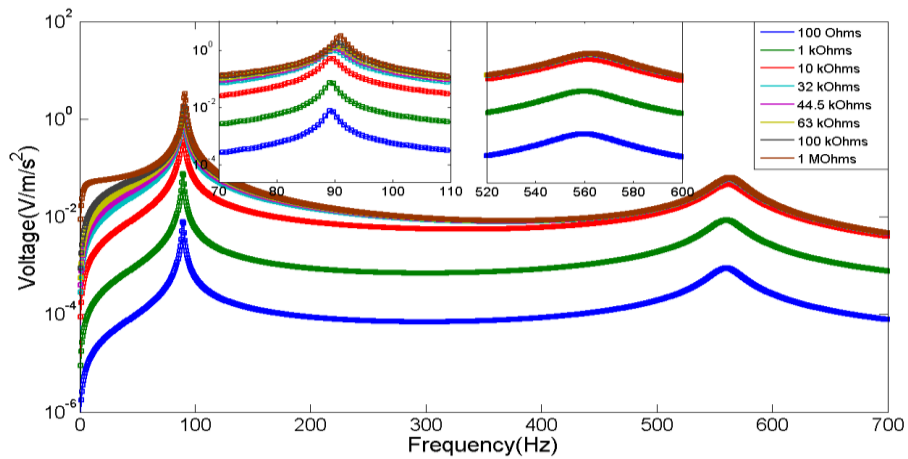


Figure 4.12 Electrical voltage FRFs with 50 discretised elements: solid line (proposed model) and round dot FE model; (Warman et al., 2014).

In addition, figure 4.13 shows the voltage magnitude versus the load resistance under base excitation for short and open circuit conditions for the first resonance. This shows that the magnitude response of the electrical voltage under variable load resistance has the same behaviour as presented in section 5.2. The trends of the electrical voltage response under short circuit excitation give higher amplitude at resistance of 1 k Ω than open circuit excitation. The opposite behaviour appears after passing the intersection point. By inspecting figure 4.13, the electrical voltage response increased under variable load resistance from 1 k Ω to 1 M Ω .

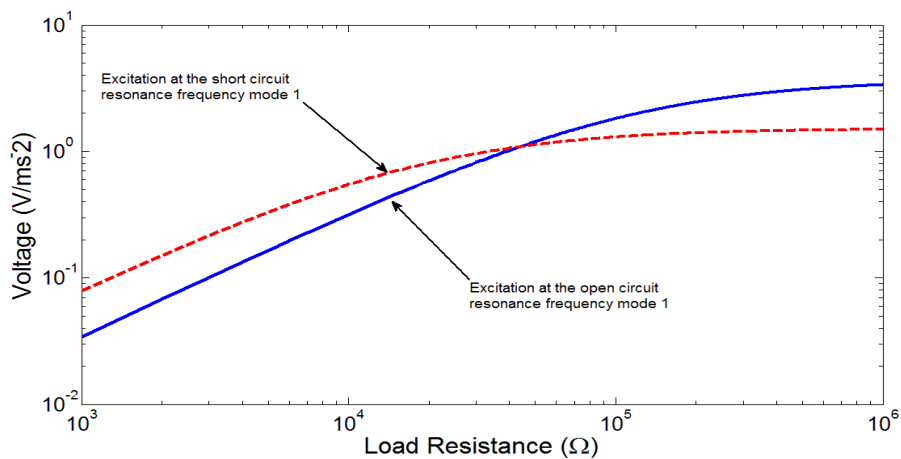


Figure 4.13 Variation of voltage output with load resistance for base excitation at the short circuit and at the open circuit resonance frequencies of the first vibration mode.

4.3.5 Frequency Response of Electrical Current Output

Figure 4.14 also shows the reducing trend of the electrical current with increasing load resistances. The appearance of electrical current is shown to have the opposite trend with the electrical voltage magnitude, followed with a consistently similar result for the two different methods. The two enlarged sections as shown in figure 4.14, indicate the electrical current resonance frequency shows 89.38 Hz and shifts to 90.94 Hz at short and open circuit resonance frequency for the first mode. The second mode of electrical current shows resonance at 559.9 Hz at the short circuit, shifting to 562.7 Hz for the open circuit condition.

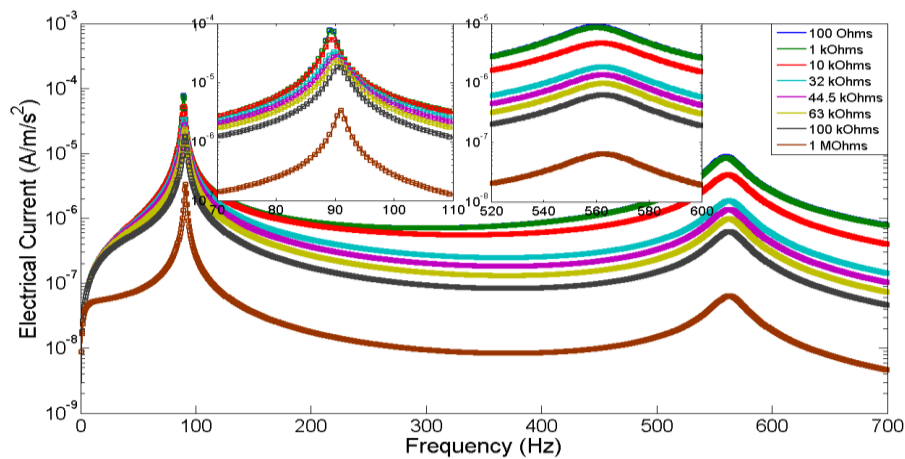


Figure 4.14 Electrical current FRFs with 50 discretised elements: solid line (proposed model) and round dot FE model; (Warman et al., 2014).

Figure 4.15 shows the electrical current short and open circuit response under base excitation of the first mode resonance. For relatively low load resistance values, the electrical current gives higher amplitude at the short circuit than open circuit under base excitation. Both curves of electrical current response also decrease in magnitude followed by further increasing load resistance. The two curves again intersect at a certain resistance value, after approaching higher resistance, where the amplitude for the open circuit response becomes higher than the short circuit response.

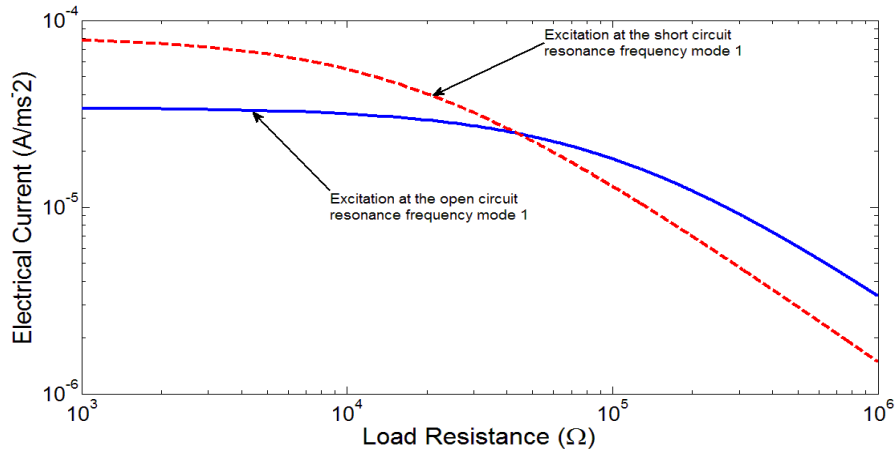


Figure 4.15 Variation of current output with load resistance for base excitations at the short circuit and at the open circuit first mode.

4.3.6 Frequency Response of Electrical Power Output

The power output FRFs has the very same trend with the previous case study as presented in section 4.2.4. Figure 4.16 shows that the maximum power output occurs at load resistance of 44.5 kΩ with resonance frequency of 90.16 Hz. The load resistance of 1 MΩ is assumed to approach the open circuit frequency response behaviour (see enlarged figure 4.16) with the resonance frequency 90.94 Hz. The short circuit condition shows the load resistance of 100 Ω (see figure 4.16) giving the lowest power output with the resonance frequency of 89.38 Hz. Similar behaviour also occurs for the short circuit load resistance, only giving minimum power output.

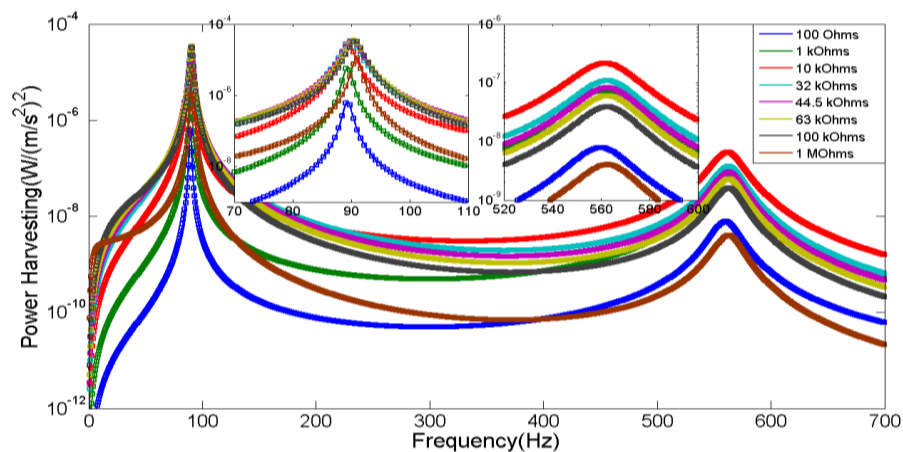


Figure 4.16 Electrical power FRFs with 50 discretised element: solid line (proposed model) and round dot FE model; (Warman et al., 2014).

Figure 4.17 shows the variation of power output with load resistance for excitation at the short circuit and open circuit resonance for the first vibration mode. Previously, the voltage and current output showed that the electrical voltage and current give higher amplitude at the short circuit rather than open circuit resonance conditions. The observation is also valid for the power output with variable load resistance. It is known that the monotonic behaviour does not appear in the power output under variable load resistance. The power output for short and open circuit resonances can give the same amplitude at the intersection point indicating the load resistance close to 44.5 k Ω .

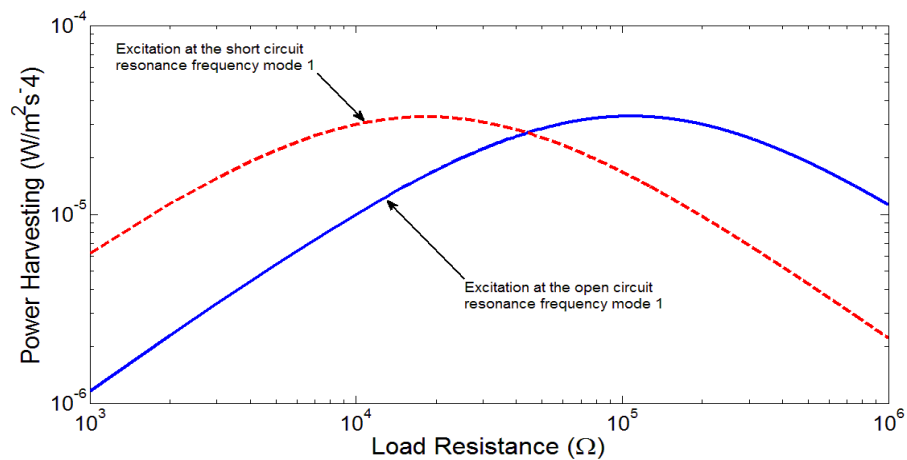


Figure 4.17 Variation of power output with load resistance for base excitations at the short circuit and at the open circuit first mode.

4.3.7 Convergence Study Number of Elements with the Electrical Voltage, Current and Power Output at the First Resonance

In this section, the first mode voltage, current and power output FRFs are investigated under variable load resistance based on the convergence of the number of elements. The study shows the behaviour of the resonance frequency of the piezoelectric system with respect to increasing number of elements with different load resistances. Unlike the convergence case study in section 4.3.3, the first mode resonance frequency was used here with varying load resistances from 100 Ω to 1 M Ω . The result of convergence study is shown in figures 4.18, 4.19 and 4.20 for voltage, current and power response, respectively.

Figure 4.18 presents the effect of varying number of elements on the corresponding first mode voltage response. The voltage resonance frequency is shown as the number

of elements goes from 1 to 50 elements under variable load resistance. The system response shows the significant change as the number of elements increases from 1 to 2 and then the voltage resonance frequency remains constant for all the different values of load resistance. The results shown in figures 4.19 and 4.20 for the current and power resonant frequency under varying load resistances show very similar behaviour.

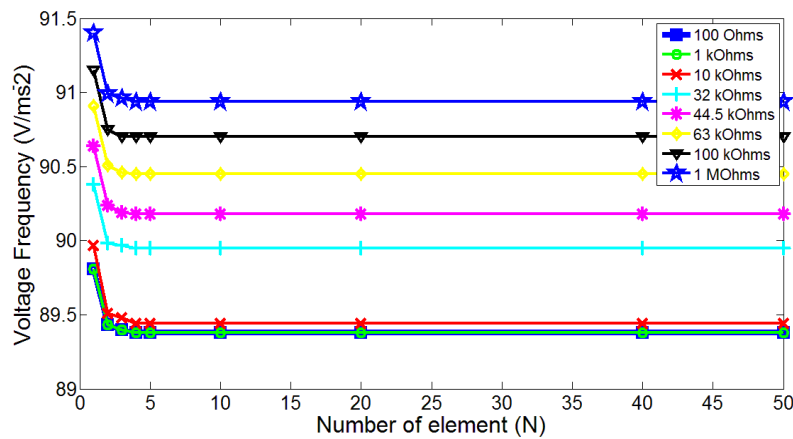


Figure 4.18 Convergence of voltage resonance frequencies as a function of number of elements.

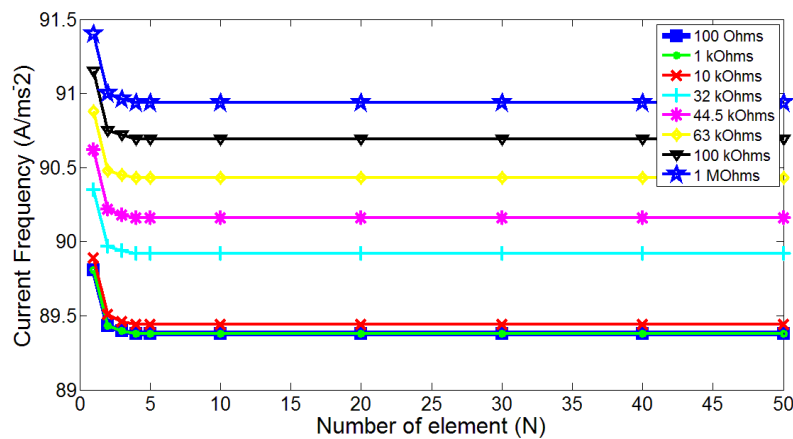


Figure 4.19 Convergence of electrical current resonance frequency under varying load resistance with number of elements.

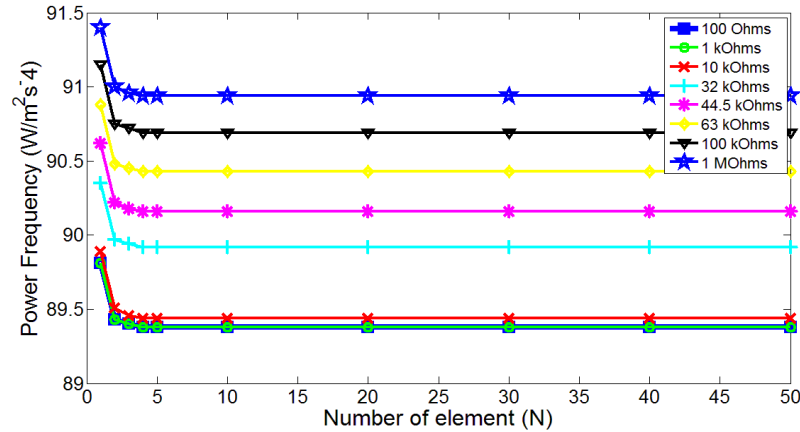


Figure 4.20 Convergence of power output resonance frequencies with varying load resistance and number of elements.

In addition, summarising the comparison of the two proposed solution methods using simulation work between direct non-orthonormalised and the orthonormalised (Warman et al., 2014) based on the resulting frequency response function of voltage, current and power output, good agreement can be seen for all the frequency responses. Here, the two methods were simulated by using the same analysis software MATLAB. Investigation of the eigenvalue results for the first three modes considered with the number of elements increasing from 1 to 50 elements. The non-orthonormalised method has shown constant lines of the first resonance frequency after using more than 5 discretisation elements. This result is also confirmed by plotting the eigenvector values to show the mode shapes with 50 number of elements with piezoelectric length 60 mm. A very smooth representation of the first four mode shapes can also be noted as seen in figure 4.10. The convergence study of number elements versus the electrical voltage, current and power resonance frequencies appear to give the flat line with the number of elements above 5 as below 3 elements are not enough to show the first natural frequency.

4.5 Summary

This chapter shows the comparison of studies using the direct non-orthonormalised finite element method and the analytical orthonormalised methods of previous publication of (Alper Erturk & Inman, 2008a) and also of the finite element orthonormalised methods published by (M. Lumentut & Howard, 2014) with the comparison study presented by (Warman et al., 2014). A multi-element discretisation

with parallel connection for the unimorph beam was applied to show the dynamic responses. The research emphasis here was to develop the vector transformation method for formulating the electromechanical coupling equation in the vector matrix form where no other researchers have used this method. In addition, the frequency response functions were derived by using the direct method of application from the general electromechanical dynamic equation.

In the two case studies, the resulting research shows the similarities of voltage, current and power FRFs with the previous published research that were based on the use of orthonormalised methods. The convergence study was used to determine the correct number of elements to find the voltage, current and power responses. The convergence study not only shows the required number of elements to achieve the required accuracy of calculation but it was also very useful to show the smoothness of the mode shape behaviour of the piezoelectric unimorph beam during vibration.

The comparison study of the direct non-orthonormalised and analytical orthonormalised finite element methods was based on the use of the first three modes of resonance. The result showed the first resonance frequency at the short circuit condition to be 47.8 Hz that shifts to 48.8 Hz for the open circuit condition. The second mode of the short circuit condition occurred at 299.5 where the frequency shifts to 301.4 Hz for the open circuit condition. The third mode resonance goes from the short circuit result of 838.2 Hz to the 839.2 Hz open circuit resonance. The observation of voltage, current and power output with variable load resistances showed that the magnitude of the short circuit response was higher than the open circuit response under relatively low load resistance which behaves in the opposite sense after crossing a certain point of load resistance. Two similar values of maximum power were shown by the short circuit and open circuit line considered to be the region of optimum load resistance.

In addition, a further comparison study of the finite element direct non-orthonormalised and orthonormalised methods was shown by the first two modes of resonance behaviour. Again, the similarities in results of the two methods were found for the voltage, current and power output FRFs where identical results were obtained for the first mode resonance frequency of 89.38 Hz at the short circuit condition that

then alters to 90.94 at the open circuit condition. The second mode resonance frequency shifted from 559.9 Hz to 562.7 Hz for the short circuit and open circuit conditions respectively. The close analysis of voltage, current and power response under short and open circuit excitation with variable load resistances shows the same behaviour with the previous case study where the magnitude of voltage, current and power at the short circuit are higher than at the open circuit resonance frequency at low level resistances and behave in the opposite sense after passing the intersection point. The results from the two case studies give very close agreement in trend and values with the previous published research, providing clear validation of the direct finite element non-orthonormalised method and the implementation methods used for the simulation.

Chapter 5

Modelling the Effect of Tip Mass Offset with Numerical Parametric Study

In this chapter, numerical parametric modelling of the unimorph power harvester with tip mass offset will be discussed in detail. This study investigates the dynamic response behaviour of the electrical voltage, current and power output FRFs using design optimisation with varying length of the piezoelectric segment. The study can improve the standard of power harvesting device because adding tip mass away from direct contact with piezoelectric material can provide a practical and effective design, as it is known that piezoelectric material has a brittle nature. The review of previous research literature provided in chapter 2 illustrated that the addition of the tip mass to the unimorph beam enhances the generated electrical power followed by shift of resonance because the motion of the tip mass with respect to the neutral axis and base support increases the resulting strain of the piezoelectric element of the substructure. It should be noted that previous work of electromechanical discretisation of piezoelectric beam with tip mass offset (M. Lumentut & Howard, 2014) will be extended here using non-orthonormalised finite element equations.

5.1 Electromechanical Finite Element model for the Unimorph with Tip Mass Offset

This section presents the formulation of the electromechanical finite element of the unimorph with the addition of the tip mass at the end of the beam. The theoretical method is developed using the same approach as introduced in previous chapters 3 and 4. However, the additional section explains the basic theoretical calculation of the tip mass variables, which is then combined with previous formulations from chapters 3 and 4.

5.1.1 Modelling of the Unimorph Beam with Tip Mass Offset

In figure 5.1, the tip mass located at the end of the unimorph beam lies on top of an extra substructure dimension and the dimension of the tip mass has the same length and width as the extra substructure element.

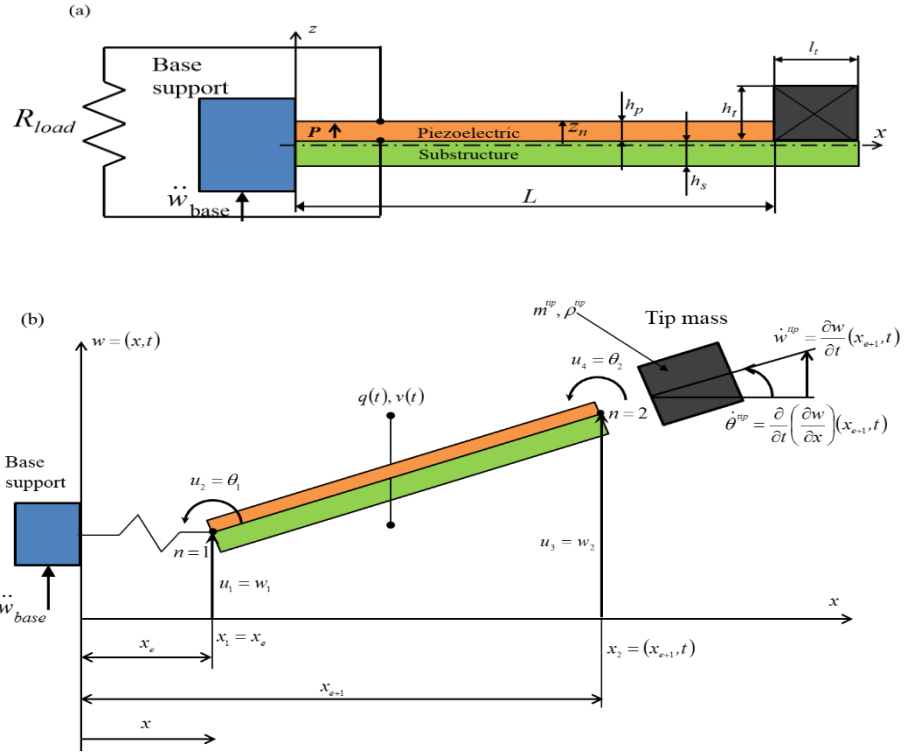


Figure 5.1 (a) Piezoelectric unimorph beams with tip mass offset (b) Local element with arbitrary tip mass.

5.1.2 Developing the Tip Mass equations for the Unimorph Cantilever Beam under Base Excitation

Development of the electromechanical discretised finite element equations has been provided in previous formulas in chapters 3 and 4. Figure 5.1 presents the illustration of the unimorph beam with the attached tip mass. The contribution of the tip mass along with the piezoelectric beam can be developed using kinetic energy formulations based on the density of the piezoelectric unimorph beam and the tip mass. The total kinetic energy of the system can then be formulated as,

$$KE = KE^{unimorph} + KE^{tip} , \quad (5.1)$$

where,

$$KE^{unimorph} = \frac{1}{2} \int_{V^{(1)}} \rho^{(1)} \underline{\dot{w}}(x)^T \underline{\dot{w}}(x) dV^{(1)} + \frac{1}{2} \int_{V^{(2)}} \rho^{(2)} \underline{\dot{w}}(x)^T \underline{\dot{w}}(x) dV^{(2)} ,$$

$$KE^{tip} = I_0^{tip} x_c \underline{\dot{w}}(x_{e+1})^T \underline{\dot{\theta}}(x_{e+1}) + \frac{1}{2} I_0^{tip} \underline{\dot{w}}(x_{e+1})^T \underline{\dot{w}}(x_{e+1}) + \frac{1}{2} I_2^{tip} \underline{\dot{\theta}}(x_{e+1})^T \underline{\dot{\theta}}(x_{e+1}) .$$

Note that equation 5.1 can be found in detail in (M. Lumentut & Howard, 2014). The kinetic energy equation 5.1 can be rewritten as the following form below,

$$KE = \frac{1}{2} \int_{V^{(1)}} \rho^{(1)} \dot{\underline{\mathbf{w}}}(x)^T \dot{\underline{\mathbf{w}}}(x) dV^{(1)} + \frac{1}{2} \int_{V^{(2)}} \rho^{(2)} \dot{\underline{\mathbf{w}}}(x)^T \dot{\underline{\mathbf{w}}}(x) dV^{(2)} + I_0^{tip} x_c \dot{\underline{\mathbf{w}}}(x_{e+1})^T \dot{\underline{\boldsymbol{\theta}}}(x_{e+1}) + \frac{1}{2} I_0^{tip} \dot{\underline{\mathbf{w}}}(x_{e+1})^T \dot{\underline{\mathbf{w}}}(x_{e+1}) + \frac{1}{2} I_2^{tip} \dot{\underline{\boldsymbol{\theta}}}(x_{e+1})^T \dot{\underline{\boldsymbol{\theta}}}(x_{e+1}) \quad (5.2)$$

Note that the derivation of the potential energy equation for the piezoelectric unimorph with tip mass is assumed to have the same form as the previous equations in chapter 3. Only the kinetic energy and non-conservative work equations are modified since the tip mass of the piezoelectric unimorph is located offset at the end of the unimorph beam. The non-conservative energy equation can then be formulated as,

$$\delta WF = -\delta \underline{\mathbf{w}}(x) \underline{\mathbf{f}}(t) - I_0^{tip} x_c \delta \underline{\boldsymbol{\theta}}(x_{e+1})^T - I_0^{tip} \delta \underline{\mathbf{w}}(x_{e+1})^T + \delta \underline{\mathbf{v}}_{-p} \underline{\mathbf{q}}_{-p} \quad (5.3)$$

Here the new notations represent the zeroth and second mass moment of inertias of the tip mass where this can be formulated by using the equation,

$$I_0^{tip} = \int_{V^{(tip)}} \rho^{tip} dV, \quad I_2^{tip} = \left(I_c^{(tip)} + m^{(tip)} d_s^2 \right) + \left(I_c^{(1)} + m^{(1)} d_{tip}^2 \right) \quad (5.4)$$

Normally, superscript (1) and (2) represent the substructure and piezoelectric layer, respectively. Equation (5.4) can be extended to find the geometrical calculation of the zeroth and second mass moment of inertia as,

$$I_0^{tip} = \rho^{tip} b l_t h_t + \rho^{(1)} b l_s h_s = m^{(tip)} + m^{(1)} \quad (5.5)$$

The mass moment of inertias about the centroid of the tip mass and the substructure element can be stated as,

$$I_c^{tip} = \frac{1}{12} m^{tip} (l_t^2 + h_t^2) = \rho^{tip} b l_t h_t \left(\frac{l_t^2 + h_t^2}{12} \right), \quad (5.6)$$

$$I_c^{(1)} = \frac{1}{12} m^{(1)} (l_t^2 + h_s^2) = \rho^{(1)} b l_t h_s \left(\frac{l_t^2 + h_s^2}{12} \right). \quad (5.7)$$

The distance of the centroid of the tip mass and the substructure element to the end of the tip mass offset point are found as,

$$d_{tip} = \left(z_n - h_p + \frac{h_t}{2} \right)^2 + \left(\frac{l_t}{2} \right)^2, \quad (5.8)$$

$$d_s = \left(\frac{h_s}{2} - z_n - h_p \right)^2 + \left(\frac{l_t}{2} \right)^2. \quad (5.9)$$

Combining equations 5.4-5.9, the second mass moment of inertia for the total tip mass can be stated as,

$$I_2^{tip} = \left(\rho^{tip} b l_t h_t \left(\frac{l_t^2 + h_t^2}{12} \right) + \rho^{tip} b l_t h_t \left(z_n - h_p + \frac{h_t}{2} \right)^2 + \left(\frac{l_t}{2} \right)^2 \right) + \left(\rho^{(1)} b l_t h_s \left(\frac{l_t^2 + h_s^2}{12} \right) + \rho^{(1)} b l_t h_s \left(\frac{h_s}{2} - z_n - h_p \right)^2 + \left(\frac{l_t}{2} \right)^2 \right). \quad (5.10)$$

5.1.3 The Electromechanical Coupled Equation for the Unimorph Beam under Base Excitation with the Tip Mass

The section describes the development of the dynamic equations for a cantilever unimorph beam with tip mass using the extended Hamiltonian formulation. Applying the total kinetic energy from equation (5.1-5.2) into Hamilton's equation, the kinetic energy equation can be written as,

$$\begin{aligned} \delta KE = & \int_{V^{(1)}} \rho^{(1)} \delta \underline{\dot{w}}(x)^T \underline{\dot{w}}(x) dV^{(1)} + \int_{V^{(2)}} \rho^{(2)} \delta \underline{\dot{w}}(x)^T \underline{\dot{w}}(x) dV^{(2)} \\ & + I_0^{tip} \left(x_c \delta \underline{\dot{w}}(x_{e+1})^T \underline{\dot{\theta}}(x_{e+1}) + \underline{\dot{w}}(x_{e+1})^T \delta \underline{\dot{\theta}}(x_{e+1}) \right) + I_0^{tip} \delta \underline{\dot{w}}(x_{e+1})^T \underline{\dot{w}}(x_{e+1}) + I_2^{tip} \delta \underline{\dot{\theta}}(x_{e+1})^T \underline{\dot{\theta}}(x_{e+1}). \end{aligned} \quad (5.11)$$

The virtual work equation can be adapted from equation (5.3) and the corresponding potential energy can be formulated as,

$$\begin{aligned} \delta PE &= \int_{V^{(1)}} \delta \underline{\mathbf{S}}_{-1}^{(1)T} c_{11}^{(1)} \underline{\mathbf{S}}_{-1}^{(1)} dV^{(1)} + \int_{V^{(2)}} \delta \underline{\mathbf{S}}_{-1}^{(2)T} c_{11}^{(2)} \underline{\mathbf{S}}_{-1}^{(2)} dV^{(2)} - \int_{V^{(2)}} \delta \underline{\mathbf{S}}_{-1}^{(2)T} e_{31} \underline{\mathbf{E}}_3 dV^{(2)} \\ \delta WE &= \int_{V_p} \delta \underline{\mathbf{E}}_3^T e_{31} \underline{\mathbf{S}}_{-1}^{(2)} dV^{(2)} + \int_{V_p} \delta \underline{\mathbf{E}}_3^T \varepsilon_{33}^S \underline{\mathbf{E}}_3 dV^{(2)} \end{aligned} \quad (5.12)$$

Adapting the general dynamic equation (3.26) in chapter 3 with the additional tip mass effect gives the new form of the equation that can be represented as,

$$\int_{t_1}^{t_2} \left[\begin{aligned} &\int_{V^{(1)}} \rho^{(1)} \delta \underline{\dot{\mathbf{w}}}(x)^T \underline{\dot{\mathbf{w}}}(x) dV^{(1)} + \int_{V^{(2)}} \rho^{(2)} \delta \underline{\dot{\mathbf{w}}}(x)^T \underline{\dot{\mathbf{w}}}(x) dV^{(2)} \\ &+ I_0^{tip} x_c \left(\delta \underline{\dot{\mathbf{w}}}(x_{e+1})^T \underline{\dot{\theta}}(x_{e+1}) + \underline{\dot{\mathbf{w}}}(x_{e+1})^T \delta \underline{\dot{\theta}}(x_{e+1}) \right) + I_0^{tip} \delta \underline{\dot{\mathbf{w}}}(x_{e+1})^T \underline{\dot{\mathbf{w}}}(x_{e+1}) + I_2^{tip} \delta \underline{\dot{\theta}}(x_{e+1})^T \underline{\dot{\theta}}(x_{e+1}) \\ &- \int_{V^{(1)}} \delta \underline{\mathbf{S}}_{-1}^{(1)T} c_{11}^{(1)} \underline{\mathbf{S}}_{-1}^{(1)} dV^{(1)} - \int_{V^{(2)}} \delta \underline{\mathbf{S}}_{-1}^{(2)T} c_{11}^{(2)} \underline{\mathbf{S}}_{-1}^{(2)} dV^{(2)} + \int_{V^{(2)}} \delta \underline{\mathbf{S}}_{-1}^{(2)T} e_{31} \underline{\mathbf{E}}_3 dV^{(2)} \\ &+ \int_{V^{(2)}} \delta \underline{\mathbf{E}}_3^T e_{31} \underline{\mathbf{S}}_{-1}^{(2)} dV^{(2)} + \int_{V^{(2)}} \delta \underline{\mathbf{E}}_3^T \varepsilon_{33}^S \underline{\mathbf{E}}_3 dV^{(2)} \\ &- \delta \underline{\mathbf{w}}(x) \underline{\mathbf{f}} - I_0^{tip} x_c \delta \underline{\theta}(x_{e+1})^T - I_0^{tip} \delta \underline{\mathbf{w}}(x_{e+1})^T + \delta \underline{\mathbf{v}}_{-p} \underline{\mathbf{q}}_{-p} \end{aligned} \right] dt = 0. \quad (5.13)$$

The variational electromechanical equation can be derived by substituting the relative displacement function from equation (3.3) in chapter 3. Then, based on Euler-Bernoulli beam theory, the axial strain can be expressed in terms of the second derivative of the shape function and the generalised electrical shape function as shown in equations (3.6) and (3.14), respectively. Utilising the functions as given in chapter 3 allows these to be written as,

$$\begin{aligned} \underline{\mathbf{w}}(x, t) &= \underline{\Phi}(x) \underline{\mathbf{u}}(t), \\ \underline{\mathbf{S}} &= -z \frac{\partial^2 \underline{\mathbf{w}}(x, t)}{\partial x^2} = -z \frac{d^2 \underline{\Phi}(x)}{dx^2} \underline{\mathbf{u}}(t) = -z \underline{\Psi}(x) \underline{\mathbf{u}}(t), \\ \underline{\mathbf{E}} &= -\underline{\Omega}(z) \underline{\mathbf{v}}_{-p}(t). \end{aligned} \quad (5.14)$$

Considering the tip mass to be attached to the end of the unimorph beam, the angular velocity of the tip mass can be transformed into the local position of the element (x) to be expressed as,

$$\dot{\theta}(x,t) = \frac{d\Phi(x)}{dx} \dot{\underline{u}}(t), \quad (5.15)$$

and substituting into the general dynamic equation gives,

$$\int_{t_1}^{t_2} \left(\int_{V^{(1)}} \rho^{(1)} \delta \dot{\underline{u}}(t)^T \underline{\Phi}(x)^T \underline{\Phi}(x) \dot{\underline{u}}(t) dV^{(1)} + \int_{V^{(2)}} \rho^{(2)} \delta \dot{\underline{u}}(t)^T \underline{\Phi}(x)^T \underline{\Phi}(x) \dot{\underline{u}}(t) dV^{(2)} \right. \\ \left. + 2I_0^{tip} x_c \delta \dot{\underline{u}}(t)^T \underline{\Phi}(x_{e+1})^T \frac{d\underline{\Phi}(x_{e+1})}{dx} \dot{\underline{u}}(t) + I_0^{tip} \delta \dot{\underline{u}}(t)^T \underline{\Phi}(x_{e+1})^T \underline{\Phi}(x_{e+1}) \dot{\underline{u}}(t) \right. \\ \left. + I_2^{tip} \frac{d\underline{\Phi}(x_{e+1})^T}{dx} \delta \dot{\underline{u}}(t)^T \frac{d\underline{\Phi}(x_{e+1})}{dx} \dot{\underline{u}}(t) - \int_{V^{(1)}} z^2 \delta \underline{u}(t)^T \underline{\Psi}(x)^T c_{11}^{(1)} \underline{\Psi}(x) \underline{u}(t) dV^{(1)} \right. \\ \left. - \int_{V^{(2)}} z^2 \delta \underline{u}(t)^T \underline{\Psi}(x)^T c_{11}^{(2)} \underline{\Psi}(x) \underline{u}(t) dV^{(2)} + \int_{V^{(1)}} z \delta \underline{u}(t)^T \underline{\Psi}(x)^T e_{31} \underline{\Omega}(z) \underline{v}_{-p}(t) dV^{(1)} \right. \\ \left. + \int_{V^{(2)}} z \delta \underline{v}_{-p}(t)^T \underline{\Omega}(z)^T e_{31} \underline{\Psi}(x) \underline{u}(t) dV^{(2)} + \int_{V^{(2)}} \delta \underline{v}_{-p}(t)^T \underline{\Omega}(z)^T \varepsilon_{33}^S \underline{\Omega}(z) \underline{v}_{-p}(t) dV^{(2)} \right. \\ \left. - \delta \underline{u}(t)^T \underline{\Phi}(x)^T \underline{f} - I_0^{tip} x_c \frac{d\underline{\Phi}(L_e)^T}{dx} \underline{u}(t) - I_0^{tip} \underline{\Phi}(L_e)^T \underline{u}(t) + \delta \underline{v}_{-p}(t)^T \underline{q}_{-p} \right) dt = 0. \quad (5.16)$$

The expression in equation (5.16) can be separated into two electromechanical dynamic equations in which the first term formation can be written as,

$$\int_{V^{(1)}} \rho^{(1)} \underline{\Phi}(x)^T \underline{\Phi}(x) \ddot{\underline{u}}(t) dV^{(1)} + \int_{V^{(2)}} \rho^{(2)} \underline{\Phi}(x)^T \underline{\Phi}(x) \ddot{\underline{u}}(t) dV^{(2)} \\ + 2I_0^{tip} x_c \underline{\Phi}(x_{e+1})^T \frac{d\underline{\Phi}(x_{e+1})}{dx} \ddot{\underline{u}}(t) + I_0^{tip} \underline{\Phi}(x_{e+1})^T \underline{\Phi}(x_{e+1}) \ddot{\underline{u}}(t) \\ + I_2^{tip} \frac{d\underline{\Phi}(x_{e+1})^T}{dx} \frac{d\underline{\Phi}(x_{e+1})}{dx} \ddot{\underline{u}}(t) + \int_{V^{(1)}} z^2 \underline{\Psi}(x)^T c_{11}^{(1)} \underline{\Psi}(x) \underline{u}(t) dV^{(1)} \quad (5.17) \\ + \int_{V^{(2)}} z^2 \underline{\Psi}(x)^T c_{11}^{(2)} \underline{\Psi}(x) \underline{u}(t) dV^{(2)} - \int_{V^{(2)}} z \underline{\Psi}(x)^T e_{31} \underline{\Omega}(z) \underline{v}_{-p}(t) dV^{(2)} \\ = -\underline{\Phi}(x)^T \underline{f}(t) - I_0^{tip} x_c \frac{d\underline{\Phi}(L_e)^T}{dx} \underline{u}(t) - I_0^{tip} \underline{\Phi}(L_e)^T \underline{u}(t)$$

The second term of the electromechanical dynamic equation, due to the electricity effect, can be expressed as,

$$- \int_{V^{(2)}} z \underline{\Omega}(z)^T e_{31} \underline{\Psi}(x) \underline{u}(t) dV^{(2)} - \int_{V^{(2)}} \underline{\Omega}(z)^T \varepsilon_{33}^S \underline{\Omega}(z) \underline{v}_{-p}(t) dV^{(2)} = \underline{q}_{-p}. \quad (5.18)$$

Altering the electric charge into current form can be achieved by differentiating the electrical charge with respect to time as,

$$-\int_{V^{(2)}} z \underline{\underline{\Omega}}(z)^T e_{31} \underline{\underline{\Psi}}(x) \dot{\underline{\underline{u}}}(t) dV^{(2)} - \int_{V^{(2)}} \underline{\underline{\Omega}}(z)^T \epsilon_{33}^S \underline{\underline{\Omega}}(z) \dot{\underline{\underline{v}}}_p(t) dV^{(2)} = \underline{\underline{i}}_p(t) . \quad (5.19)$$

5.2 Configuration of the Dynamic Electromechanical Equations

5.2.1 Generalized Element Matrices for the Electromechanical Dynamic System with Tip Mass

The constitutive equations (5.17) and (5.19) can be rearranged by adding the Rayleigh damping matrix. This local matrix equation can be written as the following form,

$$\begin{bmatrix} \mathbf{M}^{(e)} & \mathbf{0} \\ \mathbf{0} & \mathbf{0} \end{bmatrix} \begin{Bmatrix} \ddot{\underline{\underline{u}}} \\ \dot{\underline{\underline{v}}}_p \end{Bmatrix} + \begin{bmatrix} \mathbf{C}^{(e)} & \mathbf{0} \\ \mathbf{P}_{sr}^{(e)} & \mathbf{P}_D^{(e)} \end{bmatrix} \begin{Bmatrix} \dot{\underline{\underline{u}}} \\ \dot{\underline{\underline{v}}}_p \end{Bmatrix} + \begin{bmatrix} \mathbf{K}^{(e)} & \mathbf{P}_{rs}^{(e)} \\ \mathbf{0} & \mathbf{0} \end{bmatrix} \begin{Bmatrix} \underline{\underline{u}} \\ \underline{\underline{v}}_p \end{Bmatrix} = \begin{Bmatrix} \underline{\underline{F}}^{(e)} \\ \underline{\underline{i}}_p \end{Bmatrix}, \quad (5.20)$$

where:

$$\begin{aligned} \mathbf{M}^{(e)} &= \int_{V^{(1)}} \rho^{(1)} \underline{\underline{\Phi}}(x)^T \underline{\underline{\Phi}}(x) dV^{(1)} + \int_{V^{(2)}} \rho^{(2)} \underline{\underline{\Phi}}(x)^T \underline{\underline{\Phi}}(x) dV^{(2)} \\ &+ 2I_0^{tip} x_c \underline{\underline{\Phi}}(x_{e+1})^T \frac{d\underline{\underline{\Phi}}(x_{e+1})}{dx} + I_0^{tip} \underline{\underline{\Phi}}(x_{e+1})^T \underline{\underline{\Phi}}(x_{e+1}) + I_2^{tip} \frac{d\underline{\underline{\Phi}}(x_{e+1})^T}{dx} \frac{d\underline{\underline{\Phi}}(x_{e+1})}{dx}, \\ \mathbf{K}^{(e)} &= \int_{V^{(1)}} z^2 \underline{\underline{\Psi}}(x)^T c_{11}^{(1)} \underline{\underline{\Psi}}(x) dV^{(1)} + \int_{V^{(2)}} z^2 \underline{\underline{\Psi}}(x)^T c_{11}^{(2)} \underline{\underline{\Psi}}(x) dV^{(2)}, \quad \mathbf{C}^{(e)} = \alpha \mathbf{M} + \beta \mathbf{K}, \\ \mathbf{P}_{rs}^{(e)} &= \int_{V^{(2)}} z \underline{\underline{\Psi}}(x)^T e_{31} \underline{\underline{\Omega}}(z) dV^{(2)}, \quad \mathbf{P}_{sr}^{(e)} = -\int_{V^{(2)}} z \underline{\underline{\Omega}}(z)^T e_{31} \underline{\underline{\Psi}}(x) dV^{(2)}, \\ \mathbf{P}_D^{(e)} &= -\int_{V^{(2)}} \underline{\underline{\Omega}}(z)^T \epsilon_{33}^S \underline{\underline{\Omega}}(z) dV^{(2)}, \\ \underline{\underline{F}}^{(e)} &= -\underline{\underline{\Phi}}(x)^T \underline{\underline{f}}(t) - I_0^{tip} x_c \frac{d\underline{\underline{\Phi}}(L_e)^T}{dx} - I_0^{tip} \underline{\underline{\Phi}}(L_e)^T = -\underline{\underline{Q}} \ddot{\underline{\underline{w}}}_{base}(t), \\ \underline{\underline{Q}} &= \int_{V^{(1)}} \rho^{(1)} \underline{\underline{\Phi}}(x)^T dV^{(1)} + \int_{V^{(2)}} \rho^{(2)} \underline{\underline{\Phi}}(x)^T dV^{(2)} - I_0^{tip} x_c \frac{d\underline{\underline{\Phi}}(L_e)^T}{dx} - I_0^{tip} \underline{\underline{\Phi}}(L_e)^T. \end{aligned} \quad (5.21)$$

The representations of symbols and notations have the same meaning with those given in chapters 3 and 4. However, contribution of the tip mass offset can be seen in local

mass and force matrix equations. The formation of the local matrix terms can be seen in appendix B.

Generalised formation of the local matrix into the global matrices can be written by the following form but transforming to the global matrix equations must follow the continuity of element requirements. The generalised global matrices can be given by,

$$\begin{aligned} \underset{(n_m \times n_m)}{\mathbf{M}} \underset{(n_m \times 1)}{\ddot{\mathbf{u}}}(t) + \underset{(n_m \times n_m)}{\mathbf{C}} \underset{(n_m \times 1)}{\dot{\mathbf{u}}}(t) + \underset{(n_m \times n_m)}{\mathbf{K}} \underset{(n_m \times 1)}{\mathbf{u}}(t) + \underset{(n_m \times n_e)}{\mathbf{P}_{rs}} \underset{(n_e \times 1)}{\mathbf{v}_p} = \underset{(n_m \times 1)}{\mathbf{F}}(t) \\ \underset{(n_e \times n_m)}{\mathbf{P}_{sr}} \underset{(n_m \times 1)}{\dot{\mathbf{u}}}(t) + \underset{(n_e \times n_e)}{\mathbf{P}_D} \underset{(n_e \times 1)}{\dot{\mathbf{v}}_p} = \underset{(n_e \times 1)}{\mathbf{i}_p}(t) \end{aligned} \quad (5.22)$$

The entire symbols in equation (5.22) have the same meaning with the previous equations in chapters 3 and 4.

5.2.2 Equation for Voltage, Current and Power Frequency Responses

It should be noted that the global dynamic electromechanical equation with tip mass in section 5.2.1 has the same form with the global dynamic equation in Chapter 4. However, the only difference between the two chapters is that the global mass matrices and global force matrices consist of elements of the substructure, piezoelectric component and tip mass. The resulting electromechanical coupled voltage response along the length of the unimorph is assumed to be identical. Therefore, the generalised electrodynamic equation (5.22) can be formulated in terms of the transformation of the electromechanical vector transformation as formulated in previous equations (4.3)-(4.7). Rewriting the electromechanical dynamic equation gives,

$$\begin{aligned} \underset{(n_m \times n_m)}{\mathbf{M}} \ddot{\mathbf{u}} + \underset{(n_m \times n_m)}{\mathbf{C}} \dot{\mathbf{u}} + \underset{(n_m \times n_m)}{\mathbf{K}} \mathbf{u} + \underset{(n_m \times 1)}{\boldsymbol{\Theta}} \mathbf{v} = - \underset{(n_m \times 1)}{\mathbf{Q}} \ddot{\mathbf{w}}_{base} \\ \underset{(1 \times n_m)}{\boldsymbol{\Theta}^T} \dot{\mathbf{u}} - \underset{(1 \times 1)}{R_{load}} \frac{\mathbf{v}}{(1 \times 1)} + \underset{(1 \times 1)}{C_p} \dot{\mathbf{v}} = 0 \end{aligned} \quad (5.23)$$

The solution form of equation (5.23) can be reformulated into frequency functions for electrical voltage as,

$$\frac{v}{-\omega^2 w_{base} e^{i\omega t}} = \left[\begin{array}{c} i\omega C_p + R_l - i\omega \Theta^T \\ (1 \times 1) \quad (1 \times 1) \quad (1 \times n_m) \end{array} \left[\begin{array}{c} \mathbf{K} - \omega^2 \mathbf{M} + i\omega \mathbf{C} \\ (n_m \times n_m) \quad (n_m \times n_m) \quad (n_m \times n_m) \end{array} \right]^{-1} \begin{array}{c} \Theta \\ (n_m \times 1) \end{array} \right]^{-1} \quad (5.24)$$

$$\times i\omega \Theta^T \left[\begin{array}{c} \mathbf{K} - \omega^2 \mathbf{M} + \mathbf{C} i\omega \\ (n_m \times n_m) \quad (n_m \times n_m) \quad (n_m \times n_m) \end{array} \right]^{-1} \begin{array}{c} \mathbf{Q} \\ (n_m \times 1) \end{array}$$

The electrical current response equation can be given as,

$$\frac{i}{-\omega^2 w_{base} e^{i\omega t}} = \frac{1}{R_{load} (1 \times 1)} \left\{ \begin{array}{c} \left[\begin{array}{c} i\omega C_p + R_l - i\omega \Theta^T \\ (1 \times 1) \quad (1 \times 1) \quad (1 \times n_m) \end{array} \left[\begin{array}{c} \mathbf{K} - \omega^2 \mathbf{M} + i\omega \mathbf{C} \\ (n_m \times n_m) \quad (n_m \times n_m) \quad (n_m \times n_m) \end{array} \right]^{-1} \begin{array}{c} \Theta \\ (n_m \times 1) \end{array} \right]^{-1} \\ \times i\omega \Theta^T \left[\begin{array}{c} \mathbf{K} - \omega^2 \mathbf{M} + i\omega \mathbf{C} \\ (n_m \times n_m) \quad (n_m \times n_m) \quad (n_m \times n_m) \end{array} \right]^{-1} \begin{array}{c} \mathbf{Q} \\ (n_m \times 1) \end{array} \end{array} \right\}. \quad (5.25)$$

The power output electrical response is given by,

$$\frac{P(t)}{(-\omega^2 w_{base} e^{i\omega t})^2} = \frac{1}{R_{load} (1 \times 1)} \left\{ \begin{array}{c} \left[\begin{array}{c} i\omega C_p + R_l - i\omega \Theta^T \\ (1 \times 1) \quad (1 \times 1) \quad (1 \times n_m) \end{array} \left(\begin{array}{c} \mathbf{K} - \omega^2 \mathbf{M} + i\omega \mathbf{C} \\ (n_m \times n_m) \quad (n_m \times n_m) \quad (n_m \times n_m) \end{array} \right)^{-1} \begin{array}{c} \Theta \\ (n_m \times 1) \end{array} \right]^{-1} \\ \times i\omega \Theta^T \left[\begin{array}{c} \mathbf{K} - \omega^2 \mathbf{M} + \mathbf{C} i\omega \\ (n_m \times n_m) \quad (n_m \times n_m) \quad (n_m \times n_m) \end{array} \right]^{-1} \begin{array}{c} \mathbf{Q} \\ (n_m \times 1) \end{array} \end{array} \right\}^2. \quad (5.26)$$

5.3 Case study of the Dynamic Response of the Unimorph Beam with Tip Mass

5.3.1 Unimorph Beam Parameter Dimensions and Material Property Details

A cube-shaped rectangular tip mass is modelled as glued onto the substructure located at the end of the cantilever piezoelectric unimorph beam. The details of the property and geometry for the piezoelectric unimorph beam are presented in table 5.1. In addition, the tip mass dimension was set with the same length and width as the extra length of substructure and also had the same material made from brass. Dimension of the tip mass has length $l_t = 15$ mm, height $h_t = 10$ mm and width $b = 6$ mm. The tip mass density is $\rho = 9000$ kg/m³.

Table 5.1 Piezoelectric unimorph beam properties and geometry details.

Dimensional	Piezoceramic PSI-5A4E	Substructure (Brass)
Length, l (mm)	50	65
Width, b (mm)	6	6
Thickness, h_p, h_s (mm)	0.190	0.5
Young's Modulus, E_p, E_s (GPa)	66	105
Density, ρ_p, ρ_s (kg/m ³)	7800	9000
Piezoelectric constant, d_{31} (pm/V)	-190	-
Permittivity, ϵ^s (nF/m)	1800 ϵ_0	-
Permittivity free space ϵ_0 (pF/m)	8.854	-

5.3.2 Unimorph Beam with Tip Mass Voltage, Current and Power FRFs

The simulated voltage FRFs is given by figure 5.2 obtained by using the frequency response function given by equation (5.24). The diagram shows the detail of the voltage frequency response with varying load resistances over the range of 680 Ω to 100 M Ω . The unimorph beam with tip mass is under base excitation set at 1 m/s². In simulation, varying load resistances of 680 Ω , 6 k Ω , 18 k Ω , 120 k Ω , 265 k Ω , 660 k Ω , 4.8 M Ω , 12.5 M Ω and 100 M Ω were chosen to connect each of them in parallel connection with the piezoelectric element.

Figure 5.2 shows the first three modes of voltage frequency response spanning from 0-1200 Hz with enlargement of the first two resonance modes. In addition, figure 5.3 shows the variation of voltage output with load resistance when the unimorph beam is excited at the short and open circuit resonance frequencies.

From the enlarged figure 5.2b and 5.2c, the FRFs depict a similar increasing voltage monotonic behaviour response for the first and second modes. The first mode voltage resonance frequency is now given by 26.68 Hz where this resonance frequency is assumed at the short circuit condition with load resistance of 680 Ω . The first mode resonance frequency then increases to be 28.1 Hz at the open circuit condition with load resistance of 100 M Ω . Therefore, the first mode resonance frequency shifts by 1.42 Hz between the short and open circuit conditions. In addition, the second mode voltage resonance frequency is given by 214.2 Hz for short circuit load resistance and

increases to be 216.4 Hz for the open circuit load resistance, a change in frequency of 2.2 Hz.

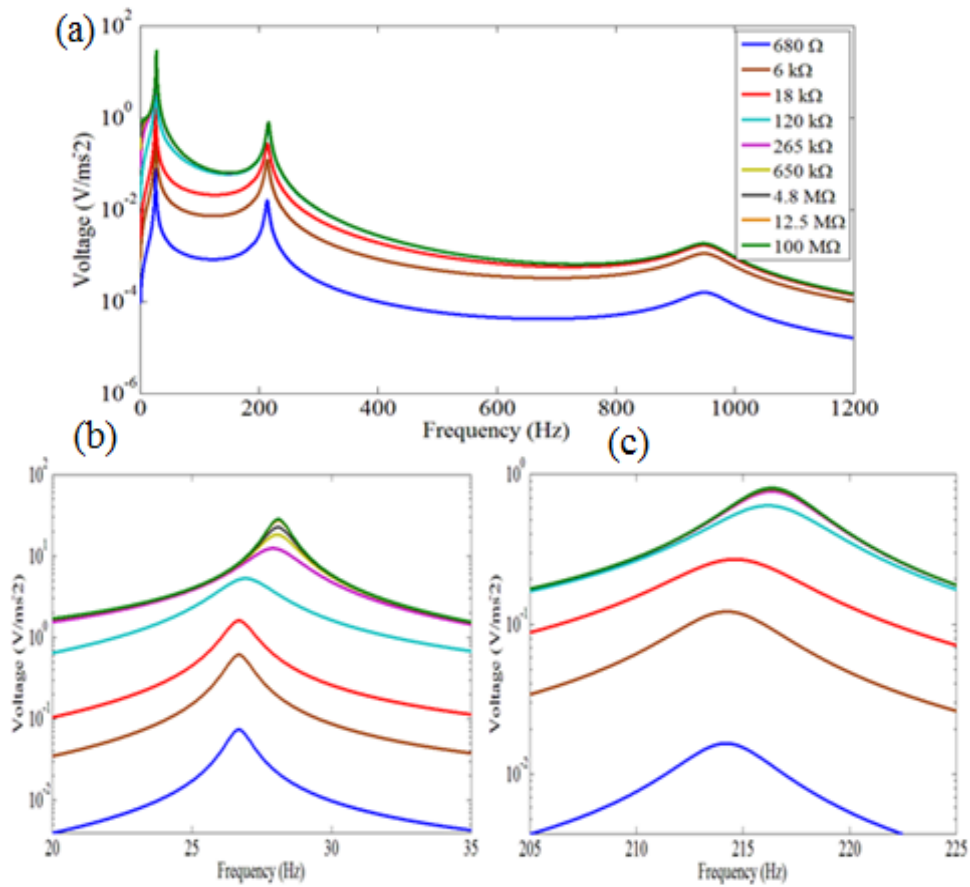


Figure 5.2 The voltage frequency response for the unimorph beam with tip mass (a) first three modes, (b) The first mode (c) The second mode.

Figure 5.3 describes the voltage output relationship with respect to the varying load resistance when the unimorph beam is excited under short and open circuit resonance frequency conditions. The result shows that the behaviour of electrical voltage magnitude under short circuit resonance frequency base excitation at low resistance is higher than the electrical voltage magnitude under open circuit base excitation. However, the opposite behaviour occurs after both curves cross over at a certain point, where the electrical voltage magnitude under open circuit resonance increases higher than the electrical voltage under short circuit resonance. A crossing point or transition point occurs when the short and open circuit resonances overlapped each other giving the load resistance of 257 kΩ. It should be noted the transition point gives the same

amplitude of electrical voltage in the parallel connection at short and open circuit resonances.

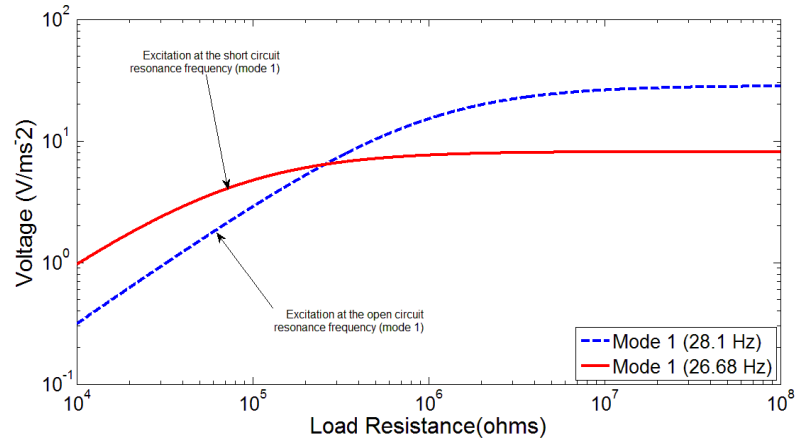


Figure 5.3 Variation of voltage output and load resistance under base excitation at the short and open circuit resonance frequency for the first mode.

The electrical current amplitude behaviour reduces monotonically in opposite direction from short to open circuit load resistances followed by a shift, showing opposite trend with the voltage response. Figure 5.4a shows the electrical current magnitude against the varying load resistances for the first three resonance modes. The result shows that the amplitude of electrical current continuously reduces with increasing frequency. Zooming into the first resonance frequency as shown by figure 5.4b, the electrical current response has peak amplitude of 0.108 mA/ms^{-2} with the resonance frequency of 26.68 Hz and load resistance (short circuit resistance) of $680 \text{ }\Omega$. The lowest value of electrical current magnitude shows $0.282 \text{ }\mu\text{A/ms}^{-2}$ with the resonance frequency of 28.1 Hz under load resistance value of $100 \text{ M}\Omega$ (open circuit resistance). From enlarging figure 5.4b, the first mode resonance frequency presents monotonically decreasing electrical current amplitude with increasing load resistances. Moreover, the monotonic behaviour can also be seen for the second mode where the current magnitude at short circuit is given by $23.43 \text{ }\mu\text{A/ms}^{-2}$ with resonance of 214.2 Hz . The electrical current amplitude at open circuit resistance is shown by 8.1 nA/ms^{-2} and resonance frequency of 216.4 Hz .

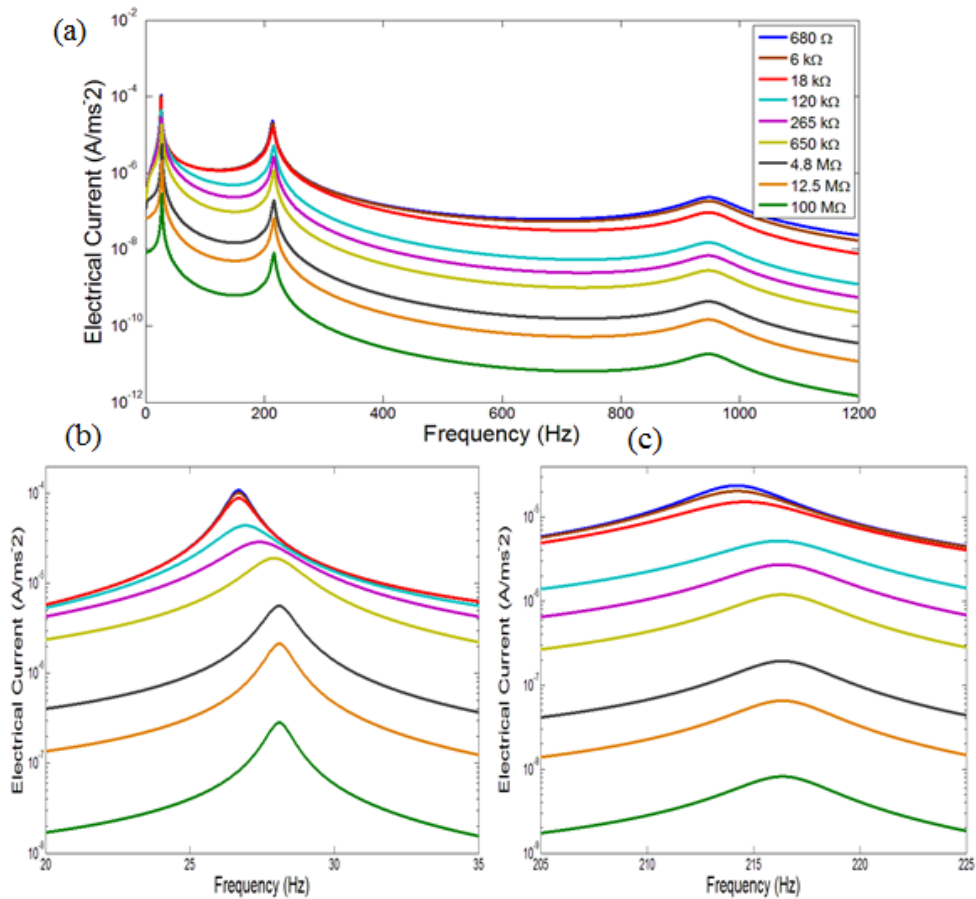


Figure 5.4 Unimorph beam electrical current FRFs with tip mass offset (a) FRFs first three modes, (b) First mode resonance, (c) Second mode resonance.

Figure 5.5 shows the varying load resistance against electrical current output under short and open circuit resonance frequencies. The result shows that the electrical current amplitude at low resistances for excitation at short circuit resonance is higher than the open circuit resonance response. However, the performance at the short circuit resonance declines after crossing over the open circuit resonance response. Again, the transition point of the overlapping electrical current amplitude is shown by figure 5.5 with the load resistance of 257 kΩ. The illustration in figure 5.5 confirms that the performance of electrical current amplitude decreases as the load resistance increases. Other evidence is also shown by the monotonic decreasing amplitude in figure 5.4a-c. In addition, the intersection at point in figure 5.5 can be seen in the transition point when the electrical current amplitude from the short to open circuit region overlaps each other.

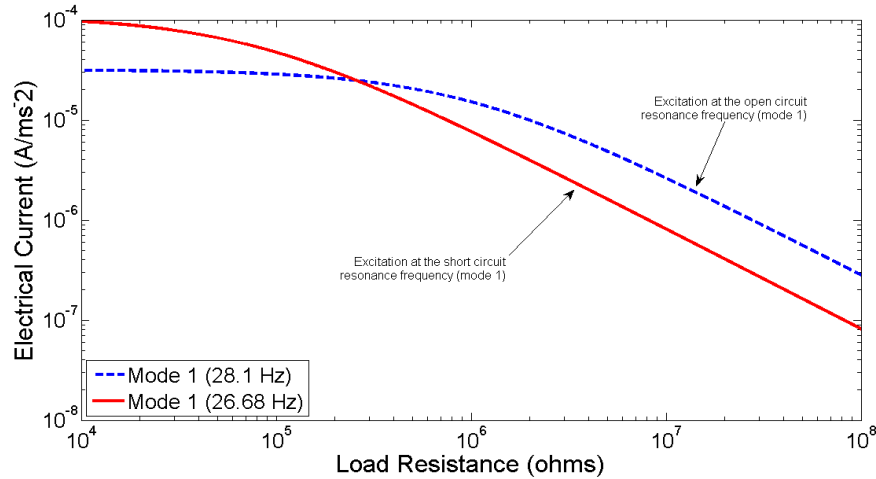


Figure 5.5 Variation of electrical current output against load resistance under base excitation for the first mode short and open circuit conditions.

Figure 5.6a illustrates the power output FRFs for the first three resonance modes. It can be noted that in general, figure 5.6a shows decreasing power output as the frequency increases. Exploring figure 5.6a by enlarging the first mode behaviour in figure 5.6b shows that a shift of the resonance frequency is clearly indicated with varying load resistances ranging from 680 Ω to 100 M Ω . Figure 5.6b describes the enlarged first mode FRFs power output. The generated power amplitude increases with increasing load resistances from the short circuit condition, then stays constant in a transition region until reaching the open circuit load resistance. The power output response then drops with increasing load resistance values. Figure 5.6b illustrates the regions of low resistance and high resistance effect with respect to the generated power amplitude and resonance frequencies. The first mode resonance maximum power region can be observed across a range of frequencies and load resistances. This phenomenon can be seen for the three load resistances of 120 k Ω , 265 k Ω and 650 k Ω with the magnitude powers of 0.229 mW/m²s⁻⁴, 0.217 mW/m²s⁻⁴ and 0.233 mW/m²s⁻⁴, respectively. Figures 5.3 and 5.5 show the region of intersection of the maximum power points as shown by the three load resistances where the power amplitude remains constant.

The enlarged figure 5.6c shows the second mode power output frequency response giving lower magnitude compared with the first mode response. Figure 5.6c shows that the maximum generated power appears at the load resistance of 18 k Ω with the amplitude of 4.055 μ W/m²s⁻⁴ and resonance frequency of 214.7 Hz. Both values

represent the maximum power at the second mode. However, the appearance of maximum power from figure 5.6c does not truly present the maximum power for the second mode resonance frequency. Using simulation under excitation at short and open resonance frequencies can show the maximum power region. The shift in the resonance frequency from short to open circuit of 2.2 Hz occurs at the load resistance value above 120 k Ω .

In addition, the behaviour of reducing power with frequency is shown at the third mode power output response. Figure 5.6a shows that the third mode maximum power output emerges at the load resistance value of 6 k Ω with 0.198 nW/m²s⁻⁴ at the resonance frequency of 949.4 Hz. Again, the maximum power output in figure 5.6a at the third mode does not show the maximum power output as further investigation is required to obtain the value.

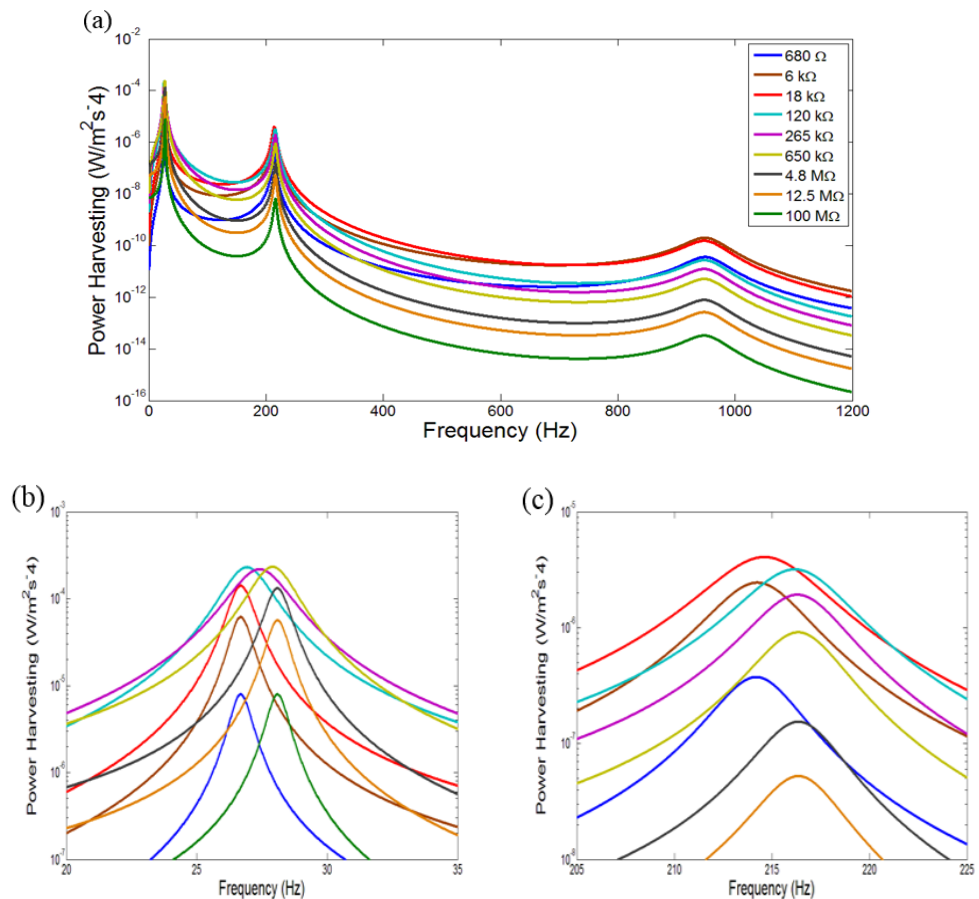


Figure 5.6 Power frequency response for unimorph beam with tip mass (a) first three modes, (b) The first mode (c) The second mode.

Figure 5.7 demonstrates the relationship of power generated for the first mode under short to open circuit resonances against varying load resistances. Previously, figure 5.3 and 5.5 showed the voltage and current magnitudes at the short circuit resonance higher than the open circuit response at lower resistance. The power response shown in figure 5.7 also shows the same behaviour. Again, varying the load resistances against power magnitude shows a crossing point when the unimorph is excited at the short and open circuit resonances. In fact, the transition point is also represented by the previous figures 5.3 and 5.5 with load resistance indicating the same value. In figure 5.7, when the unimorph beam is excited under short and open circuit resonance conditions, the power magnitude is $0.15 \text{ mW/m}^2\text{s}^{-4}$ in the region of transition point. In addition, the crossover point gives the maximum power to be generated with respect to the load resistance.

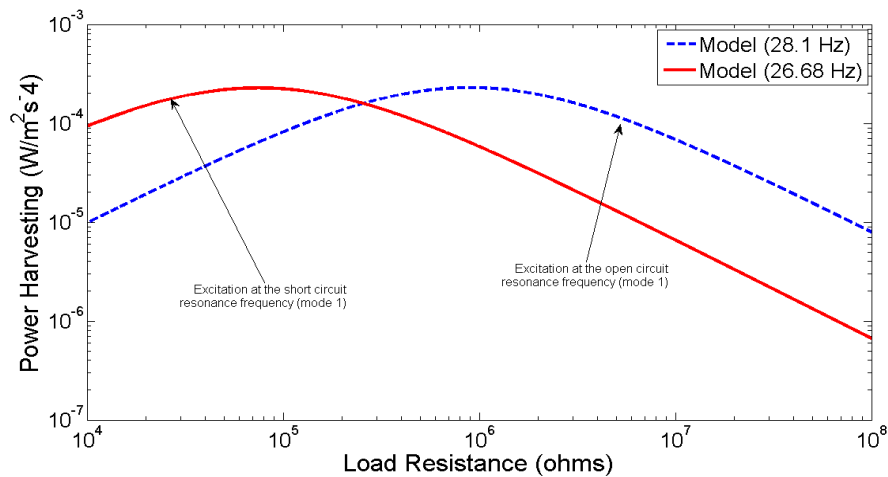


Figure 5.7 Variation of first mode power output with varying load resistance under base excitation for short and open circuit conditions.

5.3.3 The Absolute Dynamic Displacement FRFs of the Unimorph tip

Figure 5.8 shows the trend of the tip absolute dynamic displacement against frequency under varying load resistances and figure 5.9 presents the magnitude of displacement against varying load resistances under short and open circuit resonances. The absolute tip motion is represented by the ratio of amplitude with respect to the base acceleration. The simulation is set using a base acceleration of 1 m/s^2 (or 0.102 g) with absolute tip displacement units in meter per unit input base acceleration. The tip absolute displacement represents the maximum value of the transverse displacement of the tip

mass and has an important role for optimising the harvester. Figure 5.8a demonstrates the first three modes of tip transverse displacement of the unimorph beam against frequency with load resistances from 680Ω to $100 \text{ M}\Omega$. The load resistances are given by values similar with those used in the previous voltage, current and power investigation. When the load resistances of 680Ω to $120 \text{ k}\Omega$ are applied as shown in figure 5.8b for the first mode, the amplitude displacement has decreasing values with increasing resistance. However, the tip displacement amplitude behaves in opposite direction with increasing load resistances ranging from $265 \text{ k}\Omega$ to $100 \text{ M}\Omega$. Again, the same behaviours in figure 5.7c were shown for the second mode where the lowest displacement amplitude occurs at the load resistance of $18 \text{ k}\Omega$.

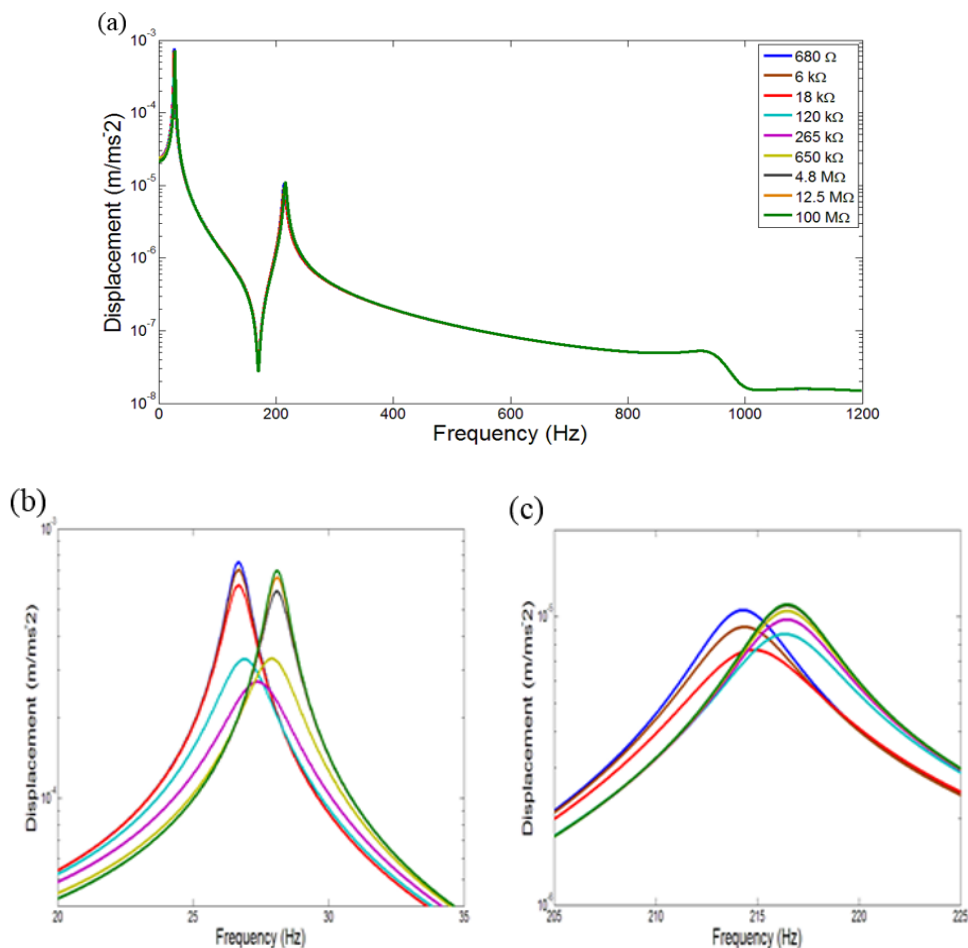


Figure 5.8 Tip displacement of the unimorph beam under varying load resistances in the range 680Ω to $100 \text{ M}\Omega$ under base excitation of 1 m/s^2 (a) The first three modes (b) The first mode (c) The second mode.

Figure 5.9 shows tip displacement under short and open circuit resonances of 26.68 Hz and 28.1 Hz respectively against load resistances. An interesting figure is shown

by the tip displacement at the short circuit resonance. High displacement amplitude occurs at low resistance values and then continuously decreases as the resistance increases using higher value. It should be noted that the higher value of the relative tip displacement for lower resistance can be seen as the coupled system behaves in a pure mechanical vibration condition.

Meanwhile, if the unimorph beam is excited at the open circuit resonance condition, lower tip displacement amplitude occurs in the region of lower resistance values. However, the tip displacement amplitude continues to increase as the resistance increases. Again, the transition point is represented in figure 5.9 and shows the transition point when the curves of tip displacement for the short and open circuit conditions intersect.

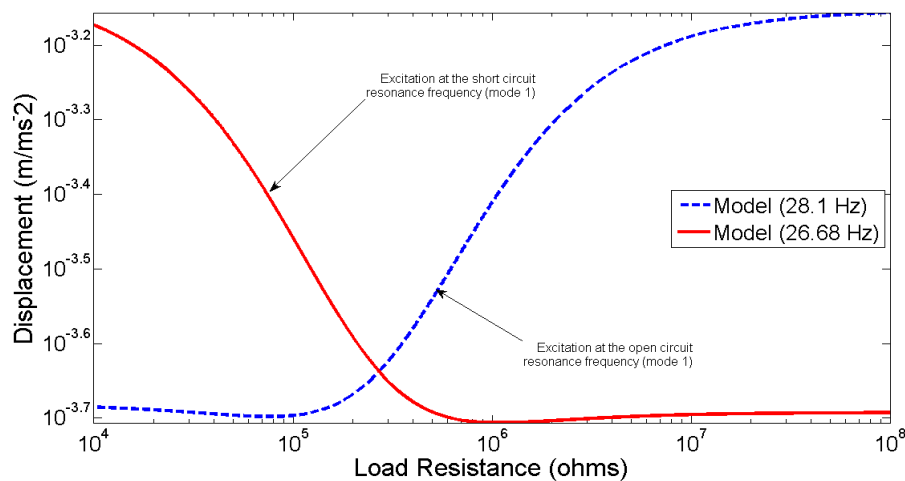


Figure 5.9 Variation of tip displacement output with varying load resistance under base excitation at the short and open circuit resonance conditions for the first mode.

5.4 Case Study of the Unimorph Beam with Tip Mass under Varying Piezoelectric Element Length

5.4.1 Electrical Voltage, Current and Power Output Frequency Response under Varying Piezoelectric Element Length

This section presents the investigation of changes to the piezoelectric element parameters focusing on the dynamic behaviour of the unimorph beam using variable length of the piezoelectric element with constant substructure dimension. In addition,

representations of electrical voltage, current and power are discussed in terms of using variable piezoelectric length. Material properties of the substructure are identical with the previous section 5.5. In table 5.1, the length of the substructure is now 50 mm without counting the length of the tip mass. For this stage as shown in figure 5.1, varying piezoelectric lengths are set to be $x_p = 10, 20, 30, 40$ and 50 mm where the base excitation was set to be 1 m/s^2 .

First, the piezoelectric element dimension was set to be $x_p = 10$ mm, width $b = 6$ mm and piezoelectric thickness $h_p = 0.190$ mm. The tip mass was set to length $l_t = 15$ mm, width $b = 6$ mm and thickness $h_t = 10$ mm. Figure 5.10 shows an illustration of the piezoelectric unimorph beam representing this case study.

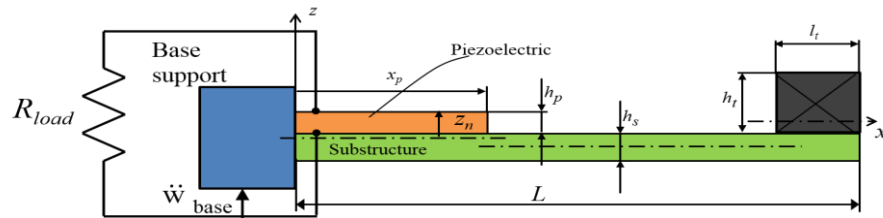


Figure 5.10 Piezoelectric unimorph beam with varying piezoelectric element length attached onto the substructure with tip mass.

Figure 5.11, 5.12 and 5.13 show the electrical voltage, current and power output frequency responses for the first two modes. The first short and open circuit resonance frequencies show 20.89 Hz and 21.07 Hz respectively and the second resonance mode gives 159.1 Hz at short circuit and 159.9 Hz at open circuit conditions. Finite element modelling of the system was performed using 50 elements for the substructure and 10 elements for the piezoelectric component.

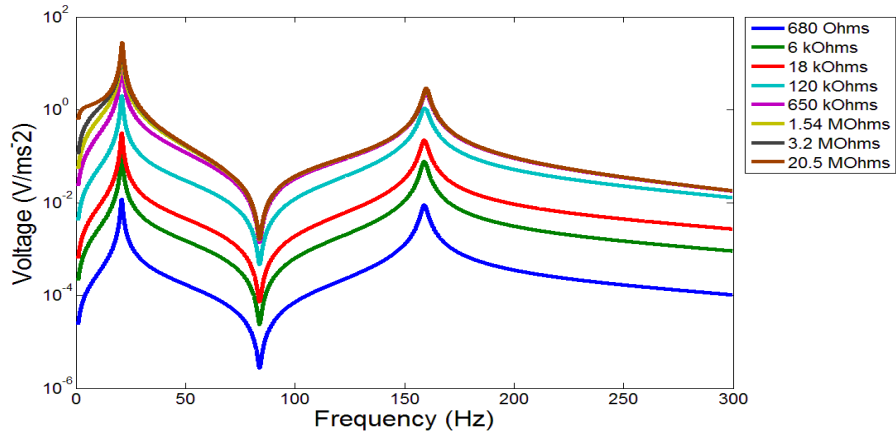


Figure 5.11 Electrical voltage FRFs using parametric piezoelectric length of 10 mm.

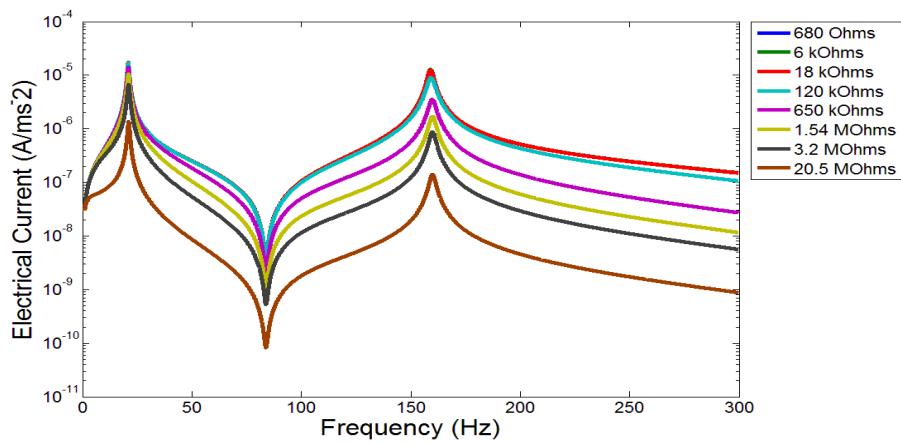


Figure 5.12 Electrical current FRF using parametric piezoelectric length 10 mm.

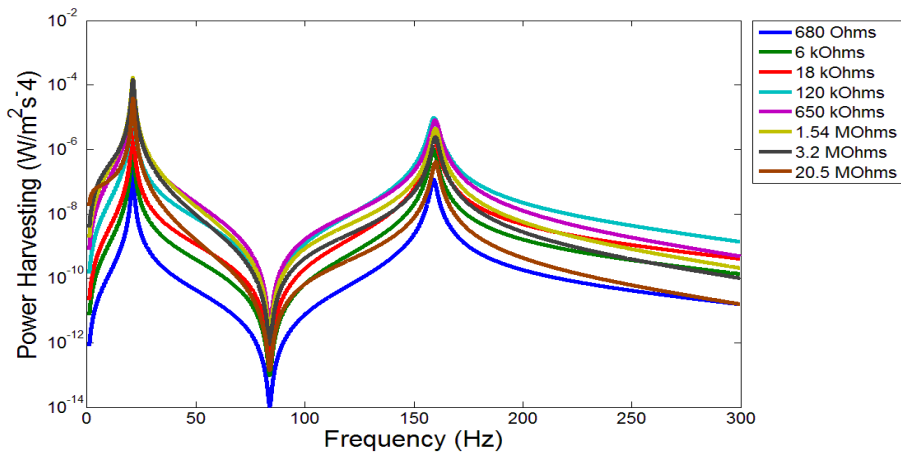


Figure 5.13 Electrical power FRF using parametric piezoelectric length 10 mm.

The results of a second investigation are given in figures 5.14-5.16 where the parametric piezoelectric length was changed to be $x_p = 20$ mm, width $b = 6$ mm and

thickness $h_p = 0.190$ mm. The substructure length remained constant at $L = 65$ mm, width $b = 6$ mm and thickness $h_s = 0.5$ mm. The tip mass has length $l_t = 15$ mm, width $b = 6$ mm and thickness $h_t = 10$ mm. The substructure system was modelled with 50 finite elements with the piezoelectric length having 20 elements. Finite element simulation results of the electrical voltage, current and power output frequency responses are shown in figures 5.14, 5.15 and 5.16. The voltage, current and power output FRFs for the first mode shows the resonance of 23.35 Hz for short circuit, followed by shift of resonance of 23.78 Hz at the open circuit resistance. The second mode resonance of electrical voltage, current and power output occurs at 161.9 Hz under short circuit and shifted to 163.1 Hz under the open circuit condition.

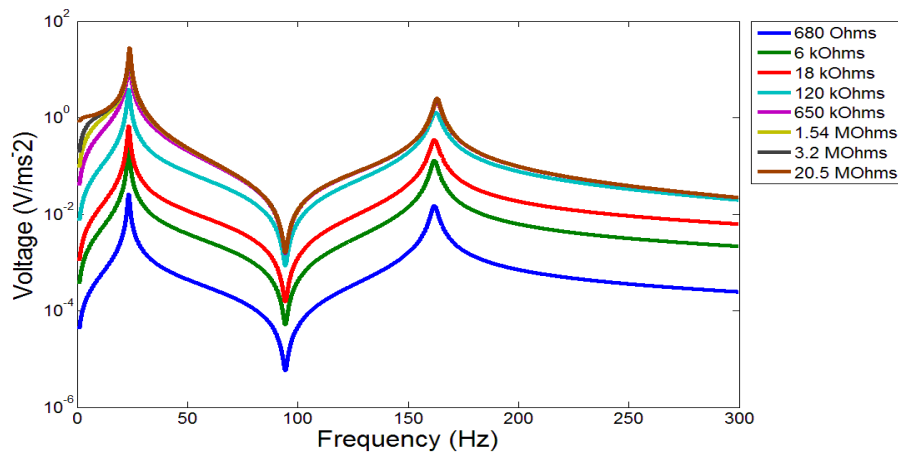


Figure 5.14 Electrical voltages FRF using parametric piezoelectric length 20 mm.

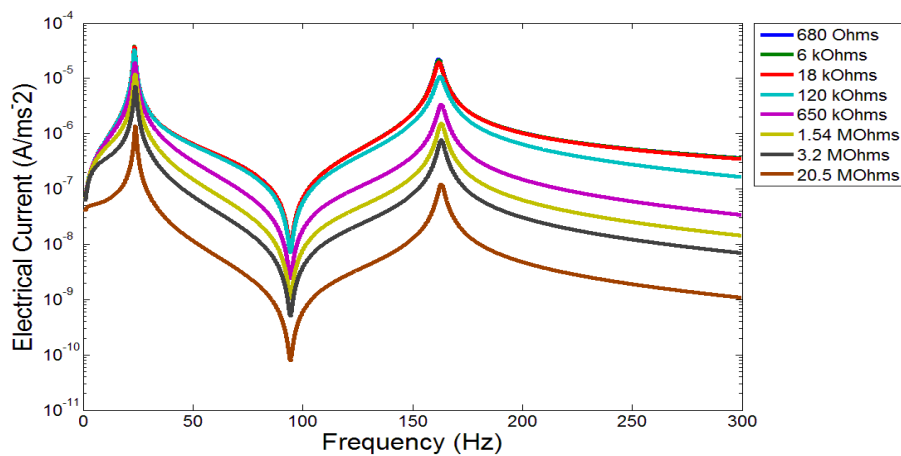


Figure 5.15 Electrical current FRF using parametric piezoelectric length 20 mm.

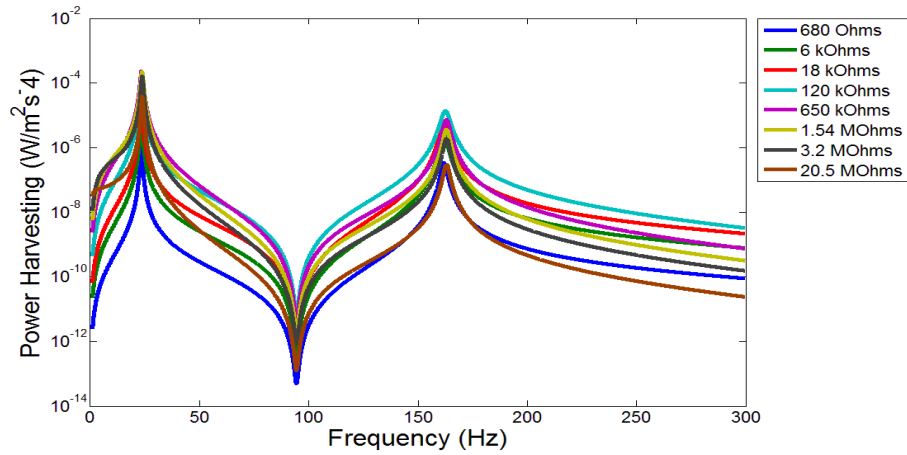


Figure 5.16 Electrical power FRF using parametric piezoelectric length 20 mm.

Figures 5.17-5.19 present the results from the finite element simulation of the piezoelectric unimorph beam with piezoelectric element length $x_p = 30$ mm, width $b = 6$ mm and thickness $h_p = 0.190$ mm. Dimension of substructure is set to have length $L = 65$ mm, width $b = 6$ mm and thickness $h_s = 0.5$ mm and dimension of tip mass is set to have length $l_t = 15$ mm, width $b = 6$ mm and thickness $h_t = 10$ mm. The finite element model uses 50 elements for the substructure and 30 elements for the piezoelectric element.

Figures 5.17, 5.18 and 5.19 show the electrical voltage, current and power output frequency responses of the unimorph beam with piezoelectric element length of 30 mm. The results show that the first mode resonance occurs at 25.27 Hz at short circuit and shifts to 25.94 Hz at the open circuit condition. In addition, the second resonance mode at the short circuit resistance occurs at 162.8 Hz and increases to 163.3 Hz at the open circuit resistance condition.

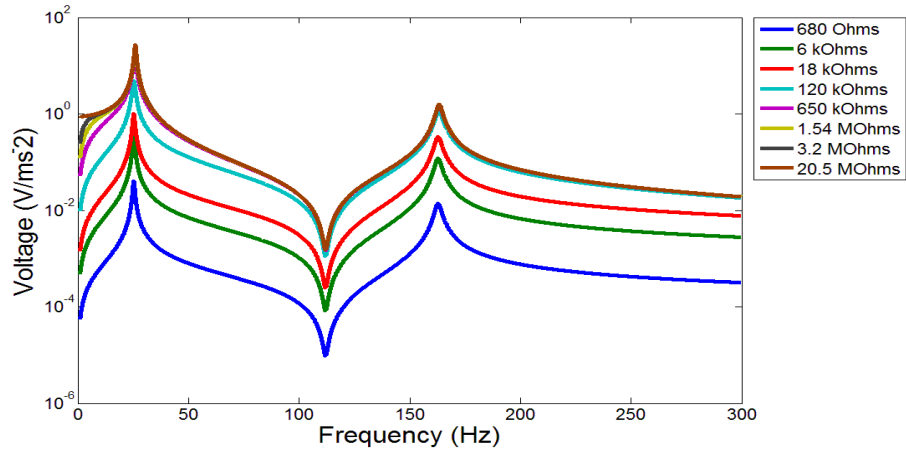


Figure 5.17 Electrical voltage FRFs with parametric piezoelectric length 30 mm.

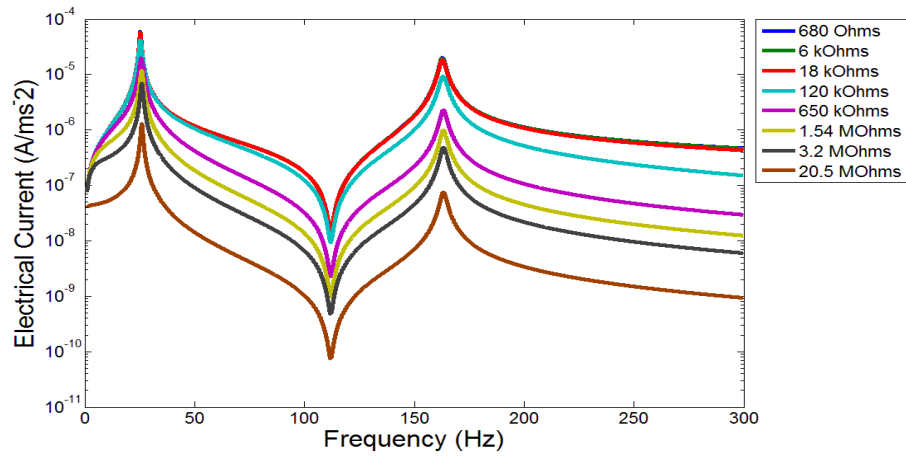


Figure 5.18 Electrical current FRF with parametric piezoelectric length 30 mm.

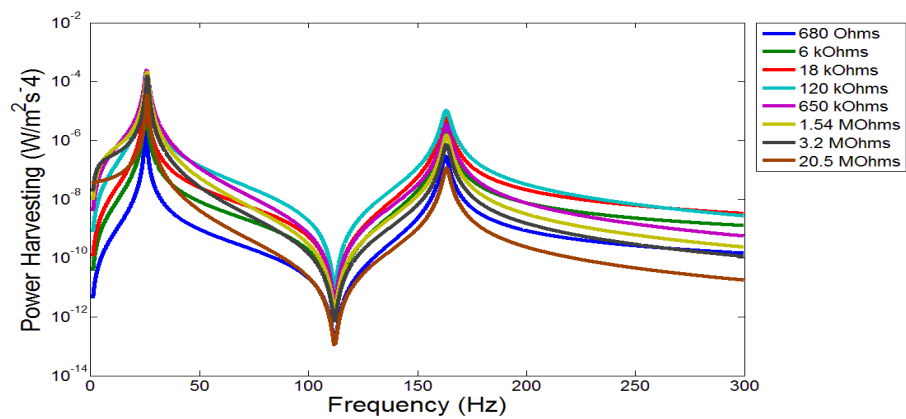


Figure 5.19 Electrical power FRF with parametric piezoelectric length 30 mm.

Investigation of frequency responses of the piezoelectric unimorph beam with length $x_p = 40$ mm, width $b = 6$ mm and thickness $h_p = 0.190$ mm are shown in figures 5.20-

5.21. The substructure dimension has a constant size with the previous investigations. Here, dimension of the substructure remains constant with length $L = 65$ mm, width $b = 6$ mm and thickness $h_s = 0.5$ mm. The tip mass dimension is again set to have length $l_t = 15$ mm, width $b = 6$ mm and the thickness $h_t = 10$ mm.

The simulated frequency responses of electrical voltage, current and power harvested are given in figures 5.20, 5.21 and 5.22. The first resonance frequency here is 26.4 Hz at short circuit and shifts to 27.21 Hz at the open circuit condition. The second mode resonance occurs at 173.7 Hz for short circuit resistance and stays constant at 173.7 Hz for the open circuit resistance.

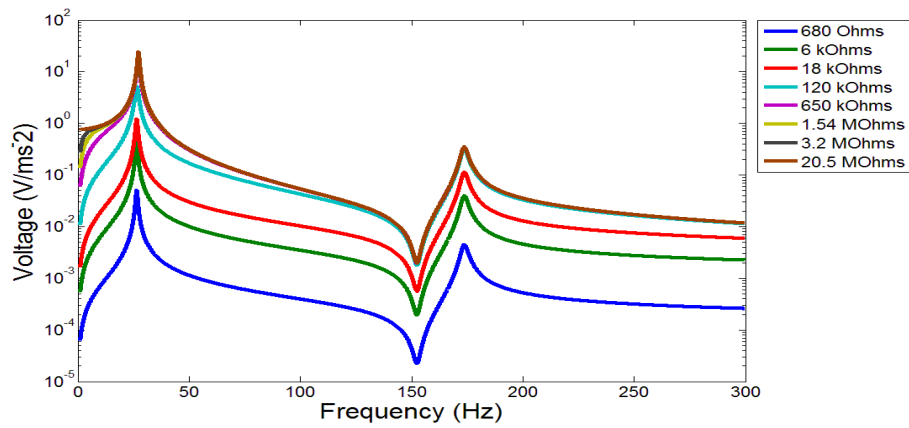


Figure 5.20 Electrical voltages FRF using parametric piezoelectric length 40 mm.

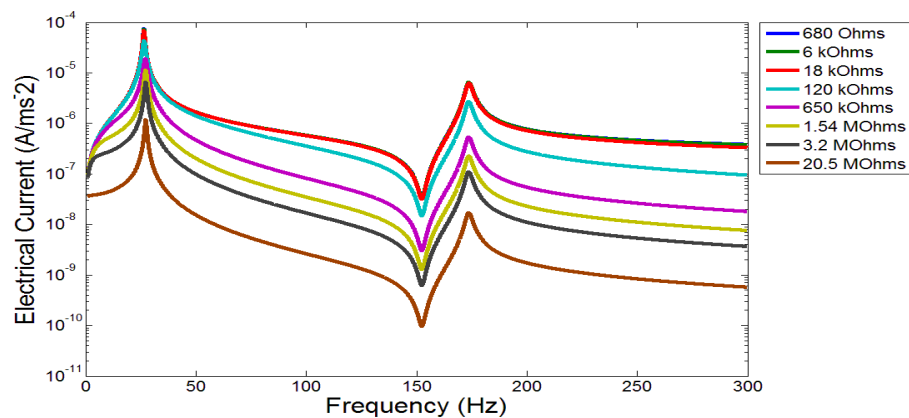


Figure 5.21 Electrical current FRF using parametric piezoelectric length 40 mm.

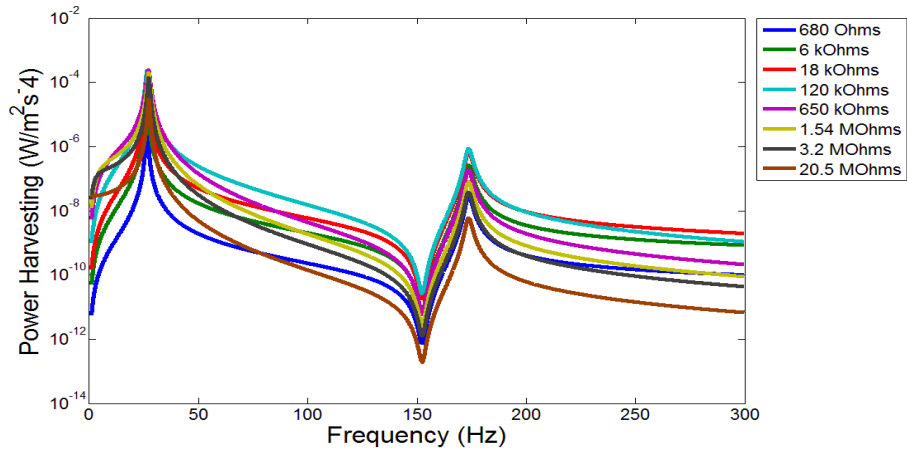


Figure 5.22 Electrical power FRF using parametric piezoelectric length 40 mm.

The frequency responses of the piezoelectric segments using 50 mm length, width $b = 6$ mm and thickness $h_p = 0.190$ mm covering over the entire substructure are shown in figures 5.23-5.25. Here, the substructure dimension remains constant with length $L = 65$ mm, width $b = 6$ mm and thickness $h_s = 0.5$ mm. The tip mass remains the same as the previous cases. The first resonance frequency here is 26.68 Hz at short circuit and shifts to 27.47 Hz at the open circuit condition. The second mode resonance occurs at 214.1 Hz for short circuit resistance and stays constant at 215.2 Hz for the open circuit resistance.

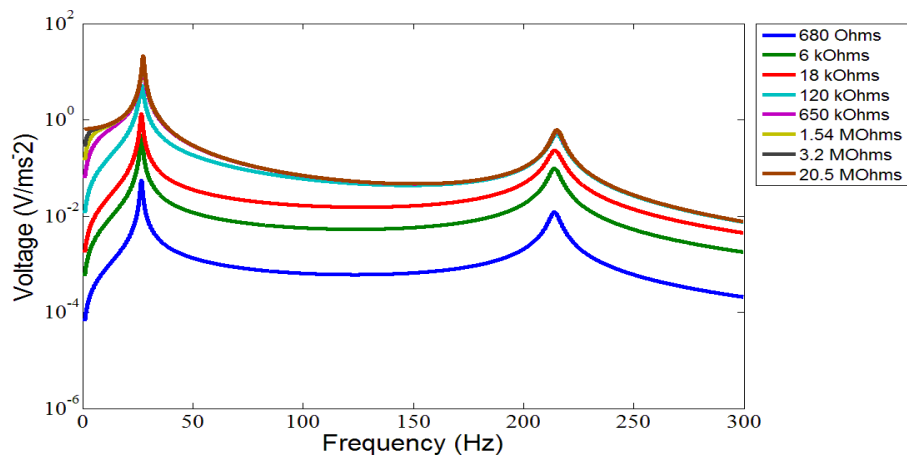


Figure 5.23 Electrical voltage FRF using parametric piezoelectric length 50 mm.

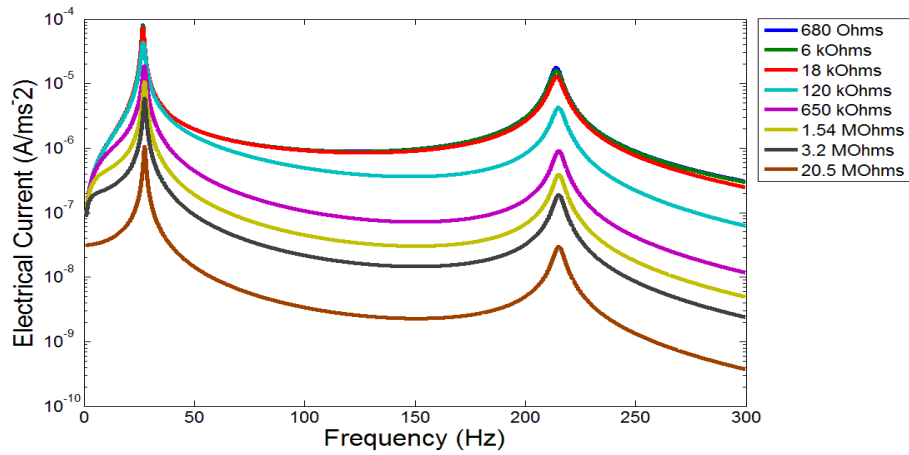


Figure 5.24 Electrical current FRF using parametric piezoelectric length 50 mm.

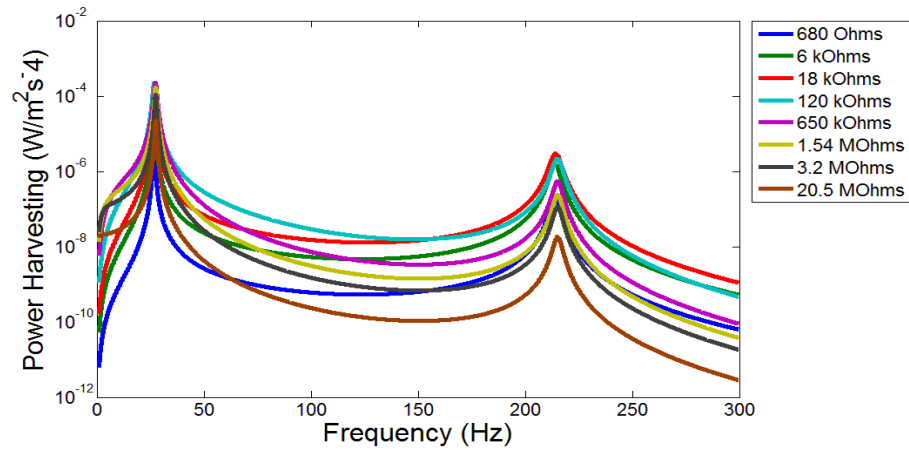


Figure 5.25 Electrical power FRF using parametric piezoelectric length 50 mm.

5.4.2 Comparison of Voltage, Current Dynamic Response of the Unimorph Beam with Varying Piezoelectric Element Length for Short and Open Circuit Resistances 680 Ω and 20.5 $M\Omega$

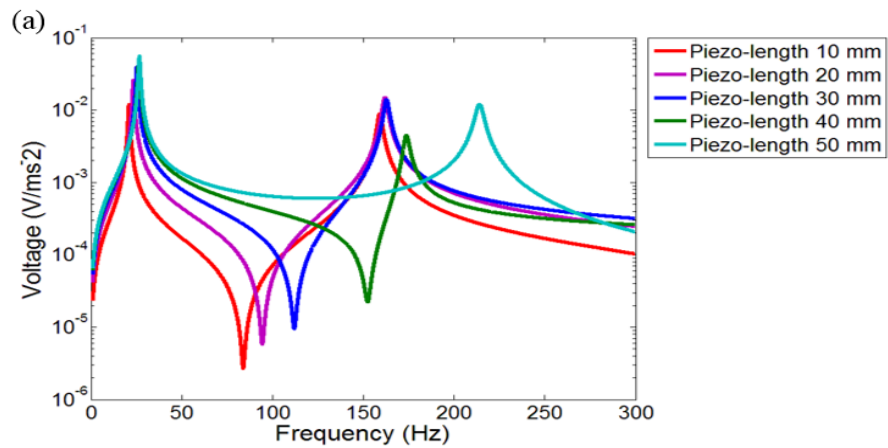
The previous section 5.4.1 showed the frequency responses of the unimorph beam with different piezoelectric element lengths from 10 mm to 50 mm using variable load resistance within the range of 680 Ω to 20.5 $M\Omega$. The previous results are discussed again in this section using the load resistances of 680 Ω and 20.5 $M\Omega$ for comparison, representing the short and open circuit conditions respectively.

Figure 5.26 shows the frequency response at short circuit resistance for the different piezoelectric element lengths. The enlarged view of the first mode response shows that the resonance frequency increases as the length of piezoelectric element increases.

However, the enlarged view of the second mode resonance indicates a different behaviour from the first mode response as shown by figure 5.26. The second mode resonance frequency with piezoelectric element of 50 mm length appears to have a significantly increasing frequency when compared with the piezoelectric element lengths from 10 mm to 40 mm. Also the voltage frequency response with piezoelectric element length of 40 mm stays at the lowest magnitude of 4.47 mV/ms^{-2} amongst the other piezoelectric lengths. Table 5.2 reports the major system responses values with load resistance of 680Ω with varying piezoelectric element length.

Table 5.2 Frequency and voltage magnitude for first two resonance modes with load resistance 680Ω and varying piezoelectric element length.

Piezoelectric length (mm)	First mode		Second mode	
	Frequency (Hz)	Voltage (mV/ms^{-2})	Frequency (Hz)	Voltage (mV/ms^{-2})
10	20.89	11.78	159.1	8.803
20	23.35	25.81	161.9	15.04
30	25.27	39.77	162.8	13.86
40	26.4	50.36	173.7	4.47
50	26.68	54.99	214.1	11.99



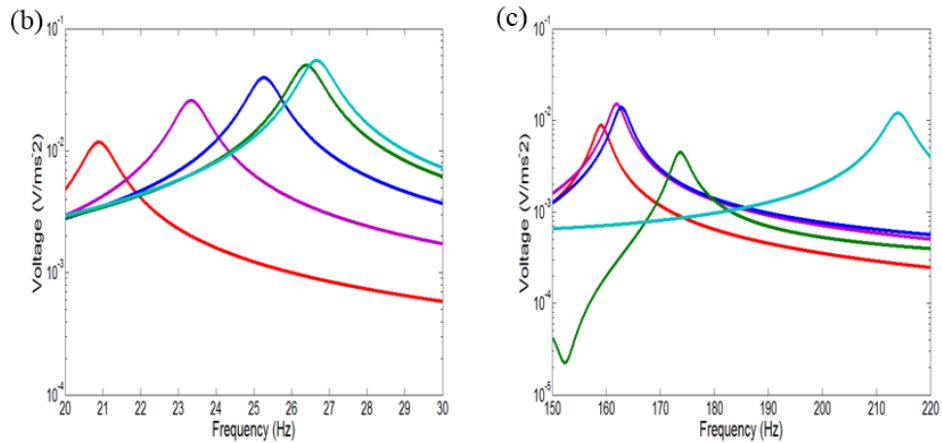


Figure 5.26 Voltage frequency responses with varying length at short circuit resistance of 680Ω : a) First two modes, b) Enlarged view for first mode, c) Enlarged view for second mode.

An electrical voltage frequency response for open circuit load resistance ($R_l = 20.5 \text{ M}\Omega$) is given in figure 5.27. It can be seen that the first mode resonance presents increasing frequencies with increasing piezoelectric element length. However, the electrical voltage amplitudes continuously reduce with increasing value of piezoelectric element length as given in table 5.3.

The second mode resonance frequency also appears to increase as the piezoelectric length increases. In terms of voltage amplitude, the shortest piezoelectric element length of 10 mm has the highest level of voltage amplitude amongst the other piezoelectric element lengths. Again, a large frequency change occurs at the second resonance between the piezoelectric element length of 50 mm length and the shorter element lengths. Table 5.3 presents the resonance frequencies and voltage amplitudes for the first two modes with load resistance of $20.5 \text{ M}\Omega$ with varying piezoelectric element length.

Table 5.3 Varying frequency and voltage magnitude for the first two modes with load resistance 20.5 MΩ and varying piezoelectric element length.

Piezoelectric length	First mode		Second mode	
(mm)	Frequency (Hz)	Voltage (V/ms ⁻²)	Frequency (Hz)	Voltage (V/ms ⁻²)
10	21.07	27.81	159.9	2.879
20	23.78	27.58	163.1	2.493
30	25.94	26.48	163.3	1.544
40	27.21	24.36	173.7	0.3481
50	27.47	21.24	215.2	0.6102

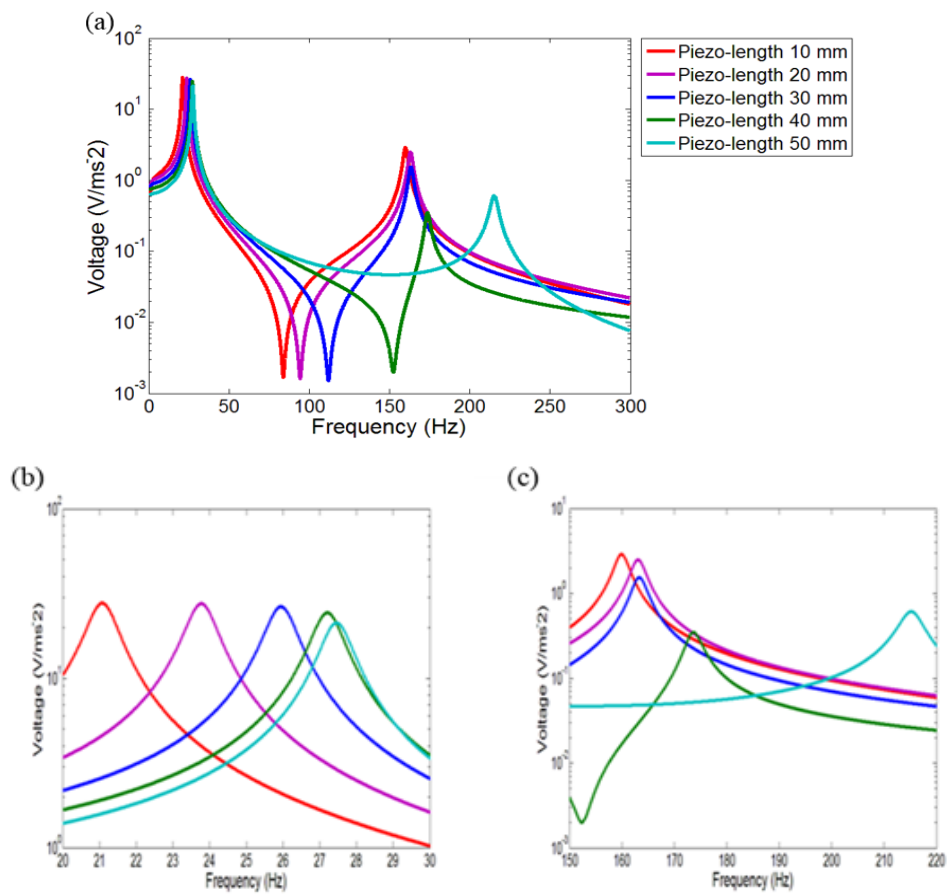


Figure 5.27 Voltage frequency responses with varying length at open circuit resistance of 20.5 MΩ: a) First two modes, b) Enlarged view for first mode, c) Enlarged view for second mode.

Investigation of the electrical current response is shown in figures 5.28 and 5.29 using short and open circuit load resistances respectively. In terms of the short circuit resistance, the electrical current frequency response behaviour has the opposite trend

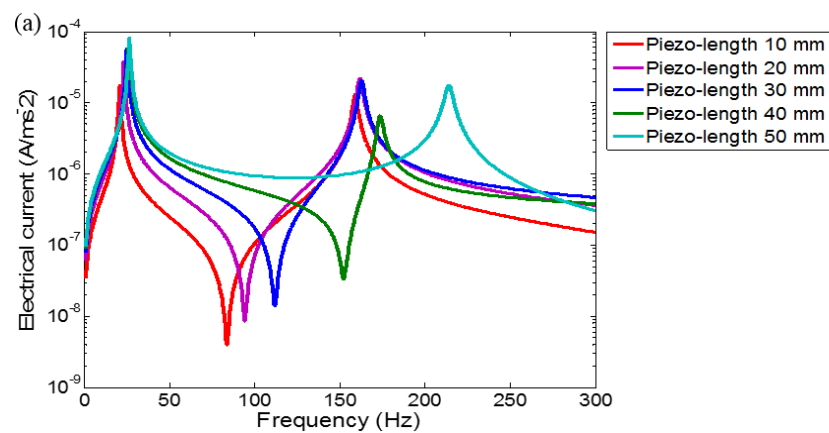
as the electrical voltage frequency response behaviour. These results can be seen in enlarge figure 5.28 for first two resonance modes.

Figure 5.28b shows increasing first mode amplitude and resonance frequency for the electrical current with increasing piezoelectric length. Detail of the changing electrical current amplitude and frequency behaviour at the first and second modes is presented in table 5.4 with piezoelectric lengths ranging from 10 mm to 50 mm.

The second mode frequency response shows similar behaviour with the second mode voltage frequency response for the short circuit condition. Again a larger resonance frequency change occurs for piezoelectric length of 50 mm compared with the other lengths ranging from 10 mm to 40 mm.

Table 5.4 Frequency and electrical current magnitude for the first two modes with load resistance 680Ω and varying piezoelectric element length.

Piezoelectric length (mm)	First mode		Second mode	
	Frequency (Hz)	Current ($\mu\text{A}/\text{ms}^{-2}$)	Frequency (Hz)	Current ($\mu\text{A}/\text{ms}^{-2}$)
10	20.89	17.32	159.1	12.95
20	23.35	37.96	161.9	22.12
30	25.27	58.48	162.8	20.38
40	26.40	74.05	173.7	6.573
50	26.68	80.87	214.0	17.64



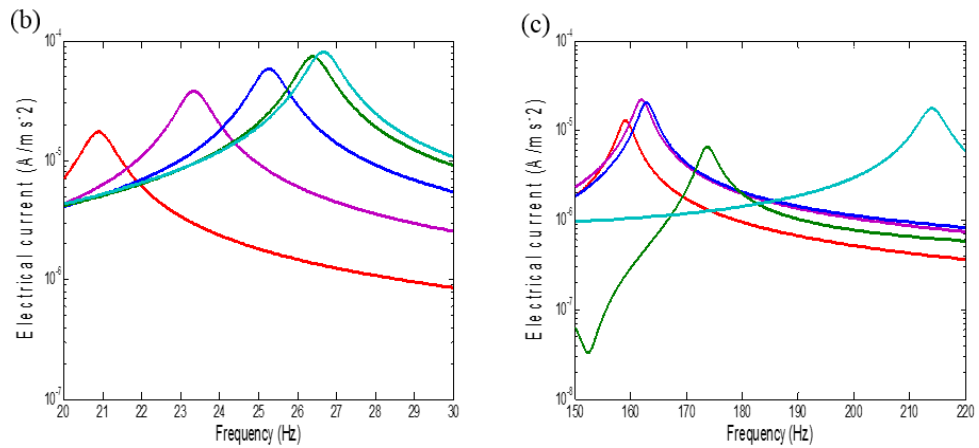


Figure 5.28 Short circuit current frequency responses with varying piezoelectric element length for 680 ohms resistance: a) First two modes, b) Enlarged view for first mode, c) Enlarged view for second mode.

Figure 5.29 shows the frequency response of electrical current with varying piezoelectric length from 10 mm to 50 mm for the open circuit load resistance condition. The first mode resonance frequency response shown in figure 5.29b gives similar behaviour to that of the previous open circuit load resistance voltage response. A similar pattern is also represented by the second mode electrical current resonance frequency with open circuit load resistance of 20.5 M Ω . Table 5.5 shows further details of the electrical current open circuit response for the first and second mode.

Figure 5.29c shows the enlarged second mode electrical current frequency response. In terms of electrical current amplitude, the value of electrical current with piezoelectric length 10 mm has the highest amplitude of 140.4 nA/ms⁻² amongst the other piezoelectric lengths. Again, the piezoelectric element with 50 mm length has a larger frequency shift over 40 Hz compared to the other piezoelectric lengths from 10 mm to 40 mm.

Table 5.5 Frequency and electrical current magnitude for the first two modes with load resistance 20.5 MΩ with varying piezoelectric element length.

Piezoelectric length	First mode		Second mode	
(mm)	Frequency (Hz)	Current (μA/ms ⁻²)	Frequency (Hz)	Current (μA/ms ⁻²)
10	21.09	1.356	160.0	0.1404
20	23.78	1.345	163.1	0.1216
30	25.96	1.291	163.3	0.0753
40	27.21	1.189	173.7	0.0169
50	27.47	1.036	215.2	0.0297

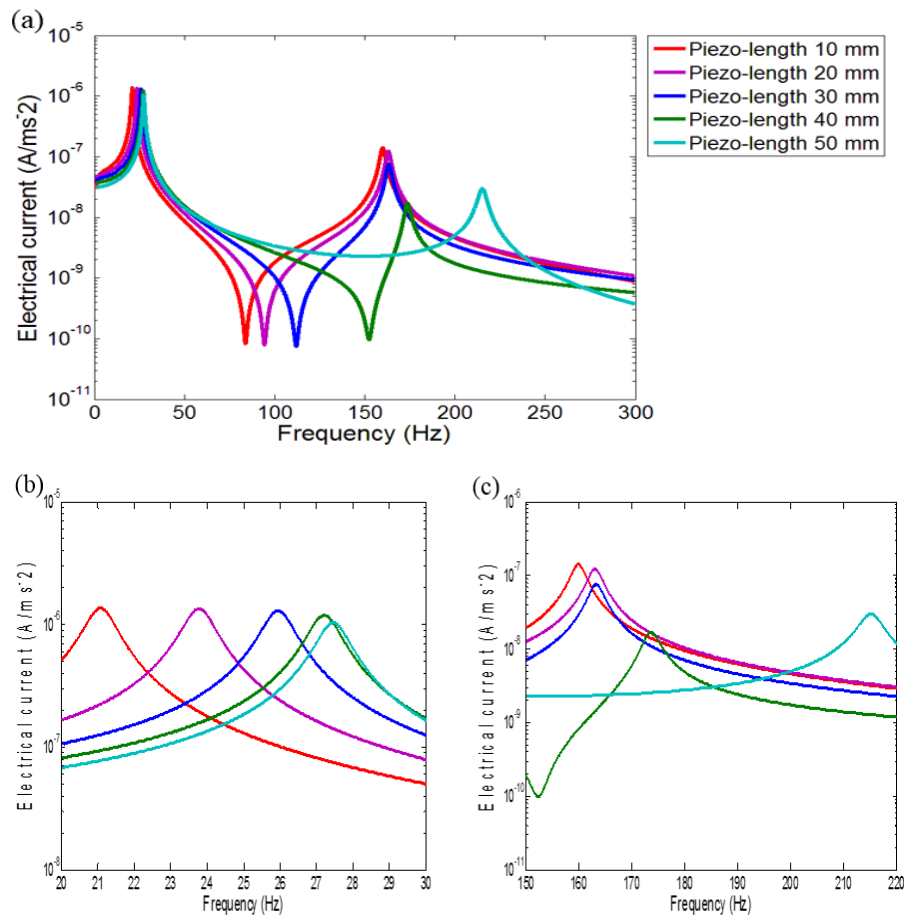


Figure 5.29 Current frequency responses with varying length at open circuit resistance 20.5 MΩ: a) First two modes, b) Enlarged view for first mode, c) Enlarged view for second mode.

5.4.3 The Unimorph Beam Power Output Dynamic Response with Varying Parametric Piezoelectric Element Length and Load Resistance

This section presents the investigation of the power harvesting response under conditions of variable piezoelectric element length and resistance ranging from 680 Ω

to 20.5 M Ω . As the power output is very important, the response of the first two modes will be discussed in detail. The behaviour will be represented using three-dimensional graphical methods. These methods have been found useful to show the dynamic changes of the peak resonances with respect to the varying piezoelectric lengths.

Figure 5.30 shows the power frequency response with varying length at load resistance of 680 ohms (or short circuit load resistance). As previously shown by the voltage and current responses, the first two mode FRFs of power output have similar patterns for short circuit conditions to those of voltage output. For example, the power output at the first mode increases as the piezoelectric length increases. The resonance frequency increases followed by increasing power output. The second mode also gives a very similar graphical pattern with the voltage and current responses as shown by the 2-D representation in figure 5.30. The peak power output starts to rise when the piezoelectric length changes from 10 mm to 20 mm. Rather than further increasing, the peak power output reduces as the piezoelectric length increases from 20 mm to 40 mm. A larger shift in the second resonance frequency then occurs as the piezoelectric length extends from 40 mm to 50 mm. Table 6.5 presents the results of the relationship between frequency, power, and piezoelectric length.

Table 5.6 Electrical power outputs for the first two resonant modes with load resistance 680 Ω and varying piezoelectric element length.

Piezoelectric length (mm)	First mode		Second mode	
	Frequency (Hz)	Power ($\mu\text{W}/\text{m}^2 \text{ s}^{-4}$)	Frequency (Hz)	Power ($\mu\text{W}/\text{m}^2 \text{ s}^{-4}$)
10	20.89	0.2039	159.1	0.1140
20	23.33	0.9796	161.9	0.3326
30	25.27	2.325	162.8	0.2824
40	26.40	3.729	173.7	0.0294
50	26.68	4.447	214.0	0.2116

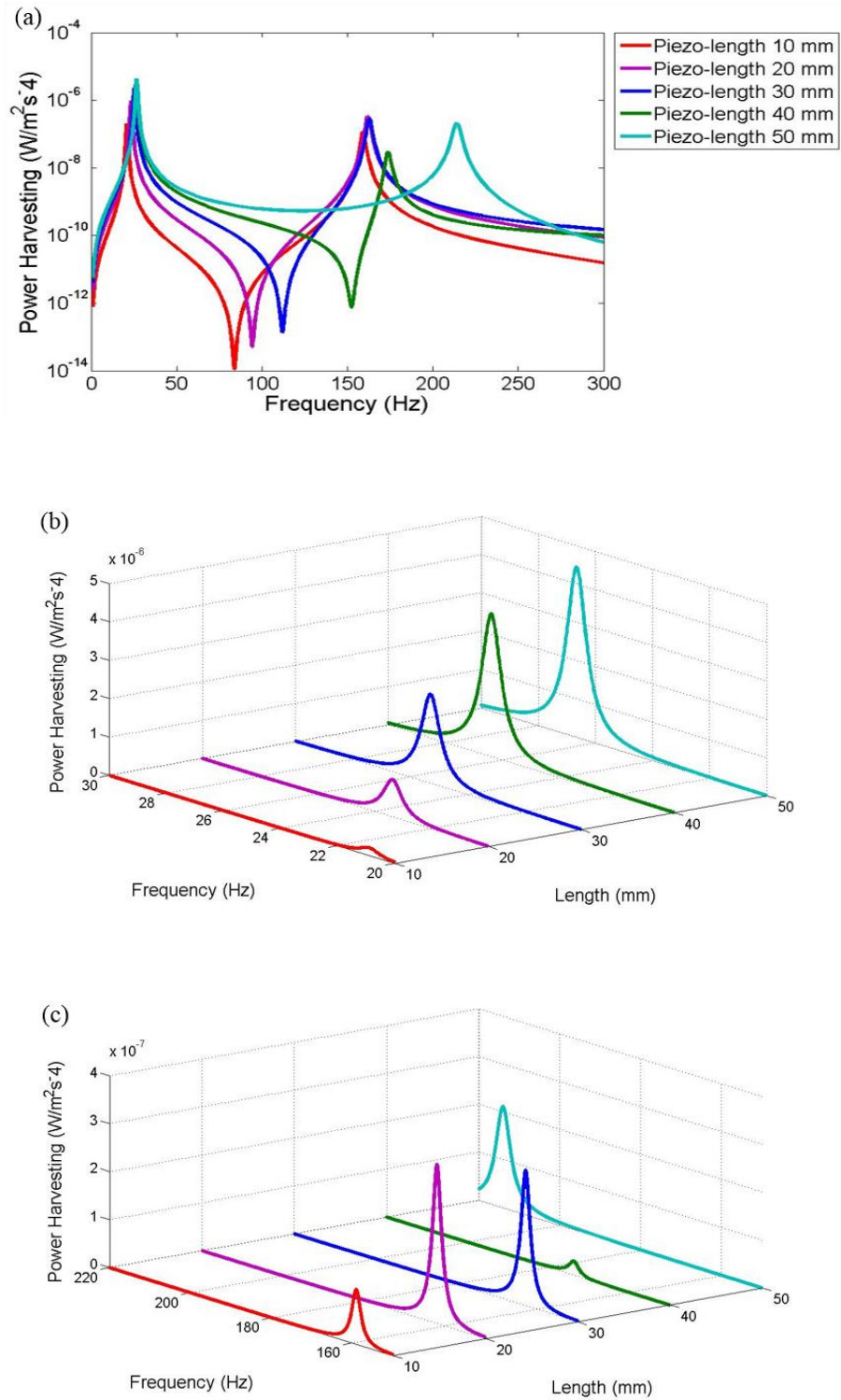


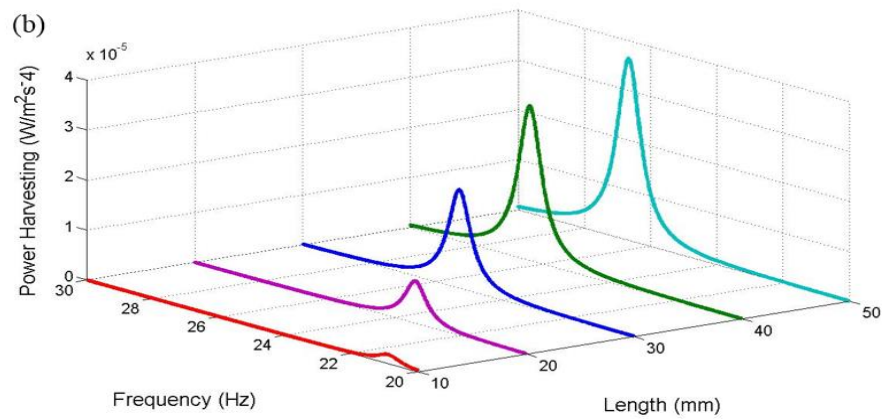
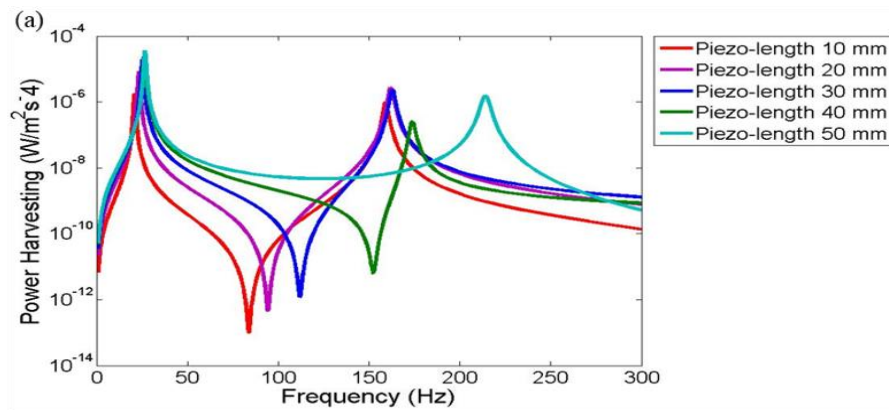
Figure 5.30 (a) Power harvesting FRF's for varying piezoelectric element length with load resistance 680 Ω . (b) First mode resonance frequency. (c) Second mode resonance frequency.

The following section presents the power response of the system as the load resistance changes from the short circuit condition to the open circuit condition. For the load resistance of 6 k Ω , a similar pattern of the power output response occurs as for the 680

Ω behaviour with respect to varying piezoelectric length as shown in figure 5.31. However, the 6 k Ω response gives higher power output compared with the 680 Ω response. The resulting power summaries are given in table 5.7 showing the relationship between frequency, power output and piezoelectric length.

Table 5.7 Detail frequency and electrical power outputs for first two resonance modes with load resistance 6 k Ω and varying piezoelectric element length.

Piezoelectric length	First mode		Second mode	
(mm)	Frequency (Hz)	Power ($\mu\text{W}/\text{m}^2 \text{ s}^{-4}$)	Frequency (Hz)	Power ($\mu\text{W}/\text{m}^2 \text{ s}^{-4}$)
10	20.89	1.794	159.1	0.9747
20	23.35	8.518	161.9	2.710
30	25.27	19.78	162.8	2.356
40	26.40	30.98	173.7	0.2576
50	26.68	36.44	214.0	1.549



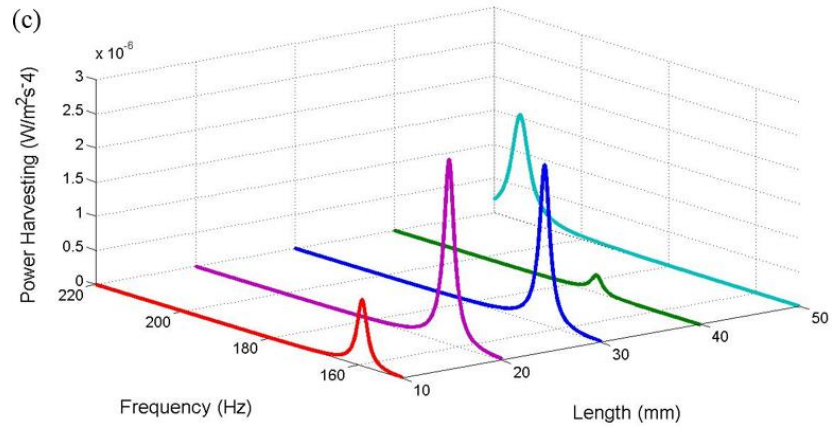


Figure 5.31 (a) Power harvesting FRF's of varying piezoelectric element length with load resistance 6 k Ω . (b) First mode resonance. (c) Second mode resonance.

Figure 5.32 shows the resulting system behaviour at the load resistance of 18 k Ω for the varying piezoelectric length. Again, the first two resonant modes have increasing frequencies as the piezoelectric length increases. The first mode increases from 20.89 Hz at the piezoelectric length 10 mm to 26.78 Hz at the piezoelectric length of 50 mm. The second mode also increases from 159 Hz to 214.3 Hz for the piezoelectric element length change from 10 mm to 50 mm.

For the power amplitude, the first resonance mode again shows increasing amplitudes with increasing piezoelectric length. The piezoelectric length of 50 mm indicates the highest power of 93.19 $\mu\text{W}/\text{m}^2 \text{s}^{-4}$ compared to the lowest power of 5.346 $\mu\text{W}/\text{m}^2 \text{s}^{-4}$. Meanwhile the second resonance mode shows that the highest power occurs using the piezoelectric length of 20 mm. Table 5.8 presents the details of the power output with respect to the varying piezoelectric length for the two modes.

Table 5.8 Detail frequencies and electrical power outputs for the first two resonance modes with load resistance 18 k Ω and varying piezoelectric element length.

Piezoelectric length (mm)	First mode		Second mode	
	Frequency (Hz)	Power ($\mu\text{W}/\text{m}^2 \text{s}^{-4}$)	Frequency (Hz)	Power ($\mu\text{W}/\text{m}^2 \text{s}^{-4}$)
10	20.89	5.346	159.0	2.720
20	23.35	24.71	161.9	6.792
30	25.27	54.70	162.8	6.085
40	26.40	81.56	173.7	0.710
50	26.78	93.19	214.3	2.984

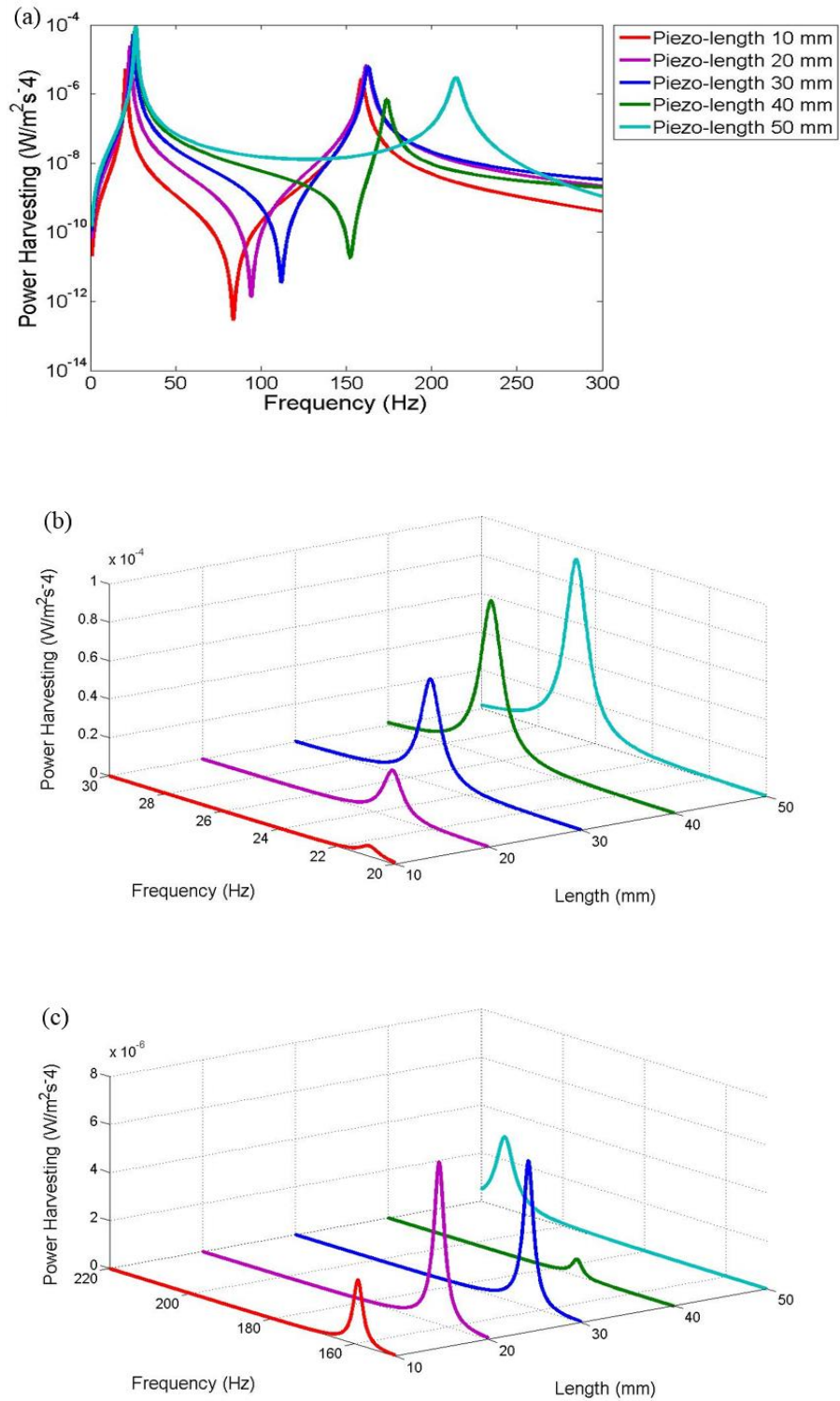


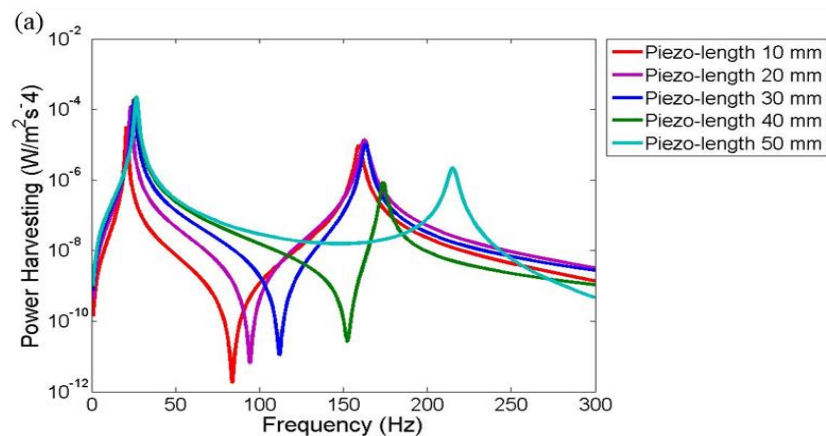
Figure 5.32 (a) Power harvesting FRF's for varying piezoelectric element length with load resistance 18 k Ω . (b) First mode resonance. (c) Second mode resonance.

The system behaviour for the increased load resistance of 120 k Ω is shown in figure 5.33, indicating that the overall power output increases with increasing load resistance. Table 5.9 shows the details of the power output response with load resistance of 120

k Ω . A similar pattern of amplitude and frequency response is shown compared with the previous result using load resistances of 680 Ω , 6 k Ω and 18 k Ω . Again, the frequencies of the first two resonance modes increase with varying piezoelectric length in the range from 10 to 50 mm. The first mode resonance is given by 20.89 Hz with piezoelectric length 10 mm and shifts to 26.80 Hz with piezoelectric length of 50 mm. In addition, the second mode resonance frequency is 159.2 Hz and rises to 215.1 Hz with piezoelectric element length ranging from 10 to 50 mm. The second mode power amplitudes reduce using different load resistances of 18 k Ω and 120 k Ω for the piezoelectric length of 50 mm giving 2.984 $\mu\text{W}/\text{m}^2 \text{ s}^{-4}$ and 2.185 $\mu\text{W}/\text{m}^2 \text{ s}^{-4}$ as shown in table 5.8 and table 5.9.

Table 5.9 Detail frequencies and electrical power outputs for the first two resonance modes with load resistance 120 k Ω and varying piezoelectric length.

Piezoelectric length (mm)	First mode		Second mode	
	Frequency (Hz)	Power ($\mu\text{W}/\text{m}^2 \text{ s}^{-4}$)	Frequency (Hz)	Power ($\mu\text{W}/\text{m}^2 \text{ s}^{-4}$)
10	20.89	33.55	159.2	9.731
20	23.36	124.5	162.6	13.92
30	25.30	199.6	163.2	10.55
40	26.48	227.1	173.7	0.865
50	26.80	226.5	215.1	2.185



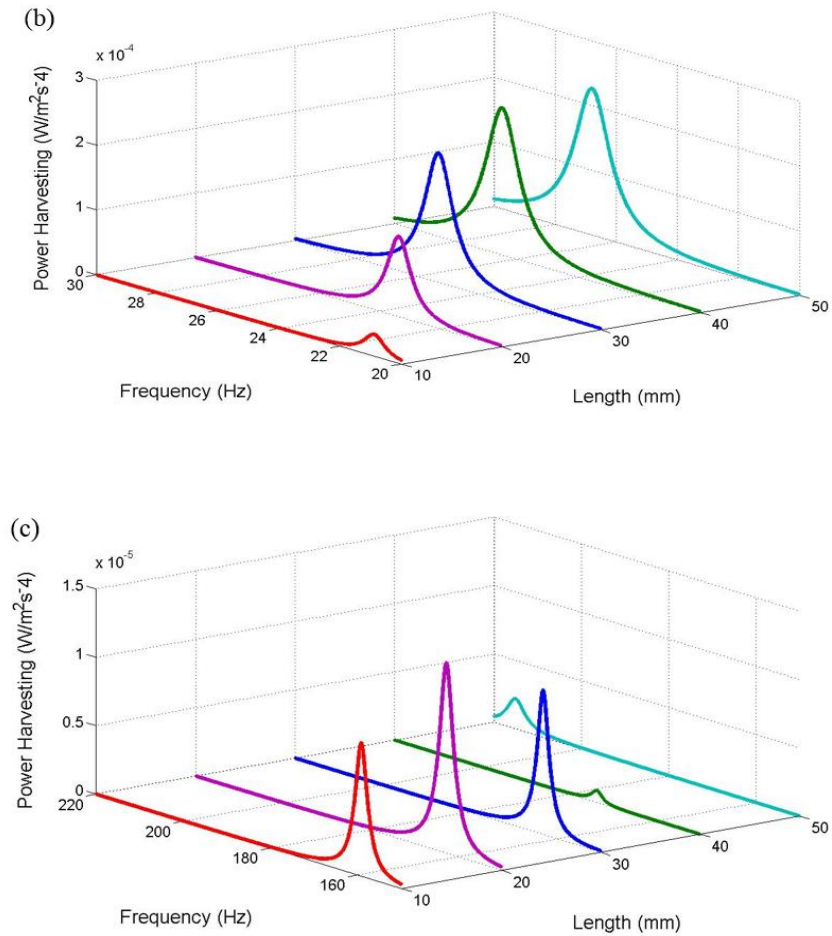


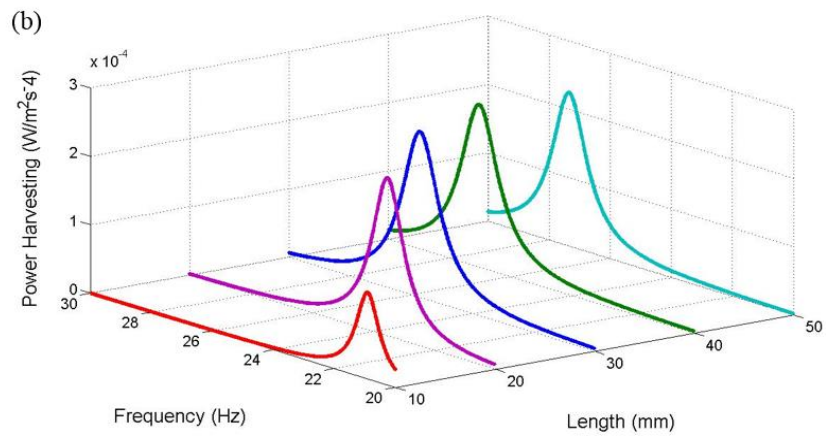
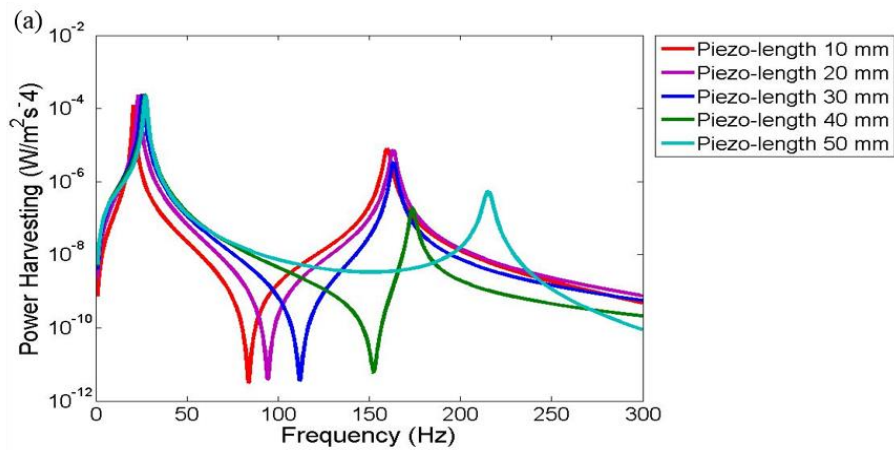
Figure 5.33 (a) Power harvesting FRF's of varying length piezoelectric element with load resistance 120 k Ω . (b) First mode resonance. (c) Second mode resonance.

Further investigation with increased load resistance of 650 k Ω as shown in figure 5.34 gives the power output FRFs with varying piezoelectric element length. Most details can be seen in table 5.10. The first mode resonance again shows increasing frequency from 20.93 Hz to 27.36 Hz as the piezoelectric length increases from 10-50 mm. The first mode power response is 126.5 $\mu\text{W}/\text{m}^2\text{s}^{-4}$ for the piezoelectric length 10 mm and then increases to the maximum power of 242.7 $\mu\text{W}/\text{m}^2\text{s}^{-4}$ for the piezoelectric length of 30 mm. As the piezoelectric length further increases, the power then reduces to give 224.4 $\mu\text{W}/\text{m}^2\text{s}^{-4}$ with piezoelectric length of 50 mm.

The second mode resonance behaviour is presented in figure 5.34c. The magnitude of electrical power for the piezoelectric length 10 mm has the highest amplitude of 8.059 $\mu\text{W}/\text{m}^2\text{s}^{-4}$ whereas the piezoelectric length of 40 mm has the lowest amplitude of 186.1 nW/m $^2\text{s}^{-4}$.

Table 5.10 Detailed frequencies and electrical power outputs for the first two resonance modes with load resistance of 650 kΩ for varying piezoelectric length.

Piezoelectric length	First mode		Second mode	
(mm)	Frequency (Hz)	Power ($\mu\text{W}/\text{m}^2 \text{s}^{-4}$)	Frequency (Hz)	Power ($\mu\text{W}/\text{m}^2 \text{s}^{-4}$)
10	20.93	126.5	159.9	8.059
20	23.52	231.6	163.1	7.225
30	25.72	242.7	163.3	3.345
40	27.05	237.7	173.7	0.186
50	27.36	224.4	215.2	0.540



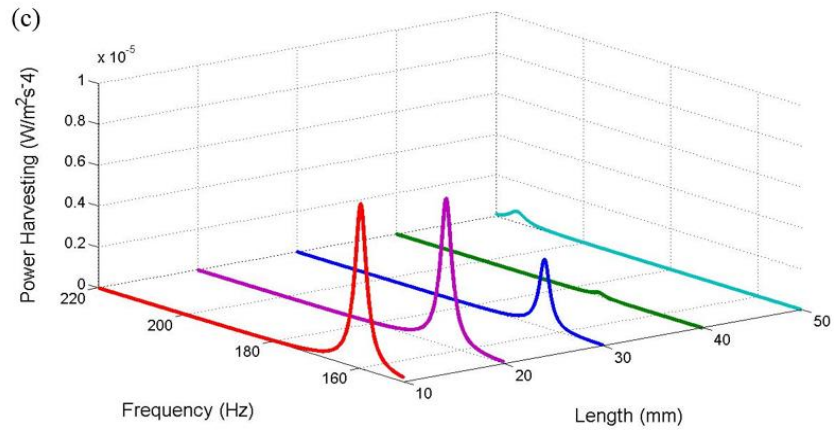


Figure 5.34 (a) Power harvesting FRF's of varying length piezoelectric element with load resistance 650 k Ω . (b) First mode resonance. (c) Second mode resonance.

The resonance of the system with increasing load resistance of 1.54 M Ω is shown in figure 5.35 with varying piezoelectric length. The first mode resonance frequency increases from 20.97 Hz to 27.44 Hz with increasing piezoelectric length from 10-50 mm as given in table 5.11. The results show that the power reduces with increasing piezoelectric length above 20 mm showing maximum power of 213.2 $\mu\text{W}/\text{m}^2\text{s}^{-4}$.

The second mode frequency rises from 159.9 Hz to 215.2 Hz with increasing piezoelectric length from 10-50 mm. Meanwhile, the power amplitude decreases from 4.475 $\mu\text{W}/\text{m}^2\text{s}^{-4}$ to 78.47 nW/m $^2\text{s}^{-4}$ with varying piezoelectric length from 10-40 mm and then rises to 235.4 nW/m $^2\text{s}^{-4}$ with piezoelectric length of 50 mm.

Table 5.11 Detailed frequencies and electrical power outputs for the first two resonance modes with load resistance of 1.54 M Ω and varying piezoelectric length.

Piezoelectric length (mm)	First mode		Second mode	
	Frequency (Hz)	Power ($\mu\text{W}/\text{m}^2\text{s}^{-4}$)	Frequency (Hz)	Power ($\mu\text{W}/\text{m}^2\text{s}^{-4}$)
10	20.97	164.9	159.9	4.475
20	23.70	213.2	163.1	3.595
30	25.89	211.8	163.3	1.490
40	27.18	197.8	173.7	0.0785
50	27.44	171.4	215.2	0.2354

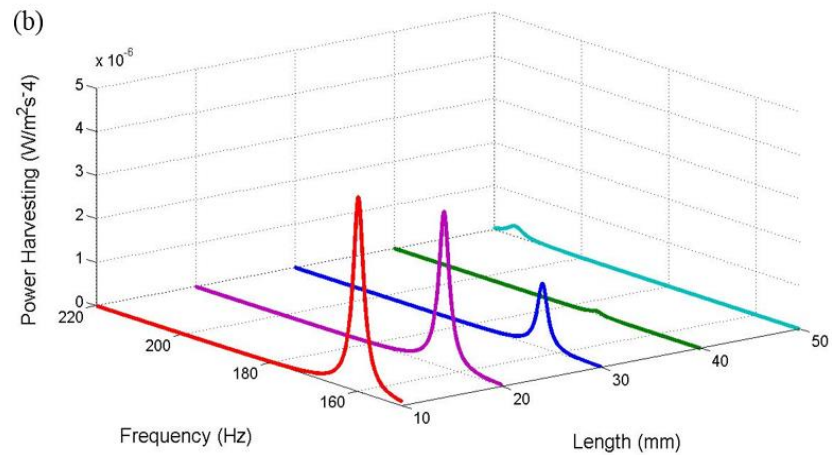
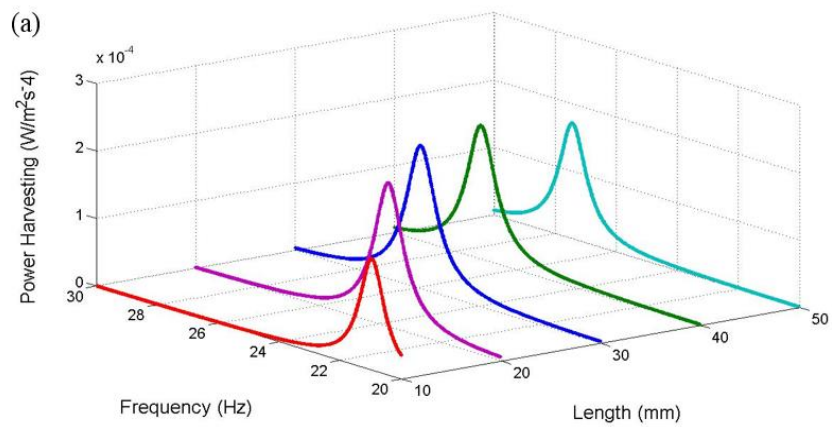
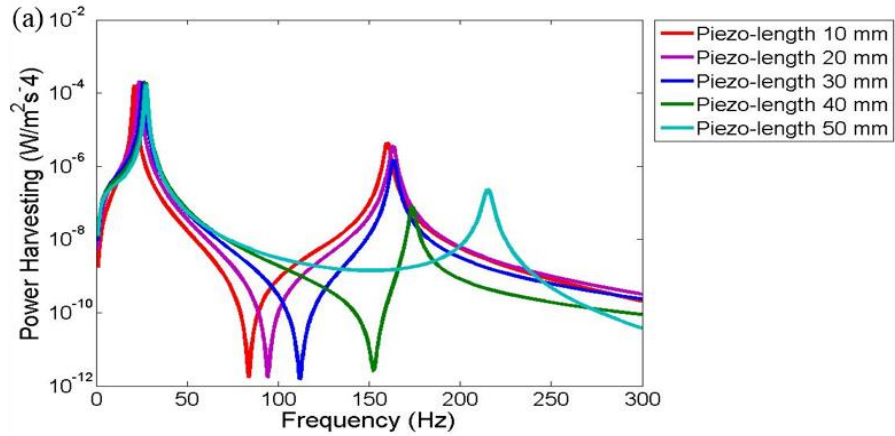


Figure 5.35 (a) Power harvesting FRF's of varying length piezoelectric element with load resistance 1.54 MΩ. (b) First mode resonance. (c) Second mode resonance.

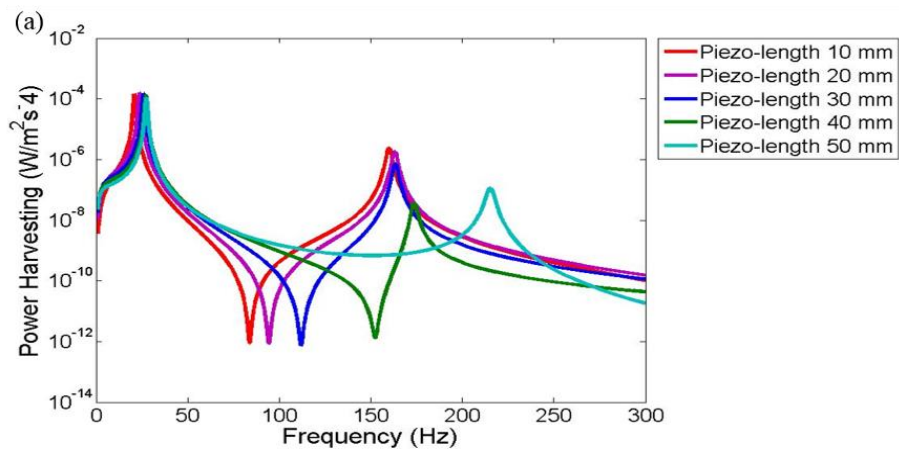
The result of the system power response for the load resistance of 3.2 MΩ are shown in figure 5.36 with varying piezoelectric element length from 10 to 50 mm. Detailed values are further provided in table 5.12 for the first two resonance modes. The first mode frequency rises from 21.04 Hz to 27.47 Hz with increasing piezoelectric length

from 10-50 mm. Again, the maximum power output occurs with a value of 158.8 $\mu\text{W}/\text{m}^2\text{s}^{-4}$ with piezoelectric length of 20 mm.

The second mode resonance frequency increases from 159.9 Hz to 215.2 Hz with increasing piezoelectric length from 10 to 50 mm. In addition, the power amplitude decreases from 2.395 $\mu\text{W}/\text{m}^2\text{s}^{-4}$ to 37.78 nW/m²s⁻⁴ with rising piezoelectric length from 10 mm to 40 mm. Then the power amplitude increases to 115.2 nW/m²s⁻⁴ with piezoelectric length of 50 mm.

Table 5.12 Detailed frequencies and electrical power outputs for first two resonance modes with load resistance 3.2 M Ω and varying piezoelectric length.

Piezoelectric length	First mode		Second mode	
(mm)	Frequency (Hz)	Power ($\mu\text{W}/\text{m}^2\text{s}^{-4}$)	Frequency (Hz)	Power ($\mu\text{W}/\text{m}^2\text{s}^{-4}$)
10	21.04	145.2	159.9	2.395
20	23.76	158.8	163.1	1.849
30	25.94	151.6	163.3	0.734
40	27.20	135.1	173.7	0.0378
50	27.47	109.8	215.2	0.1152



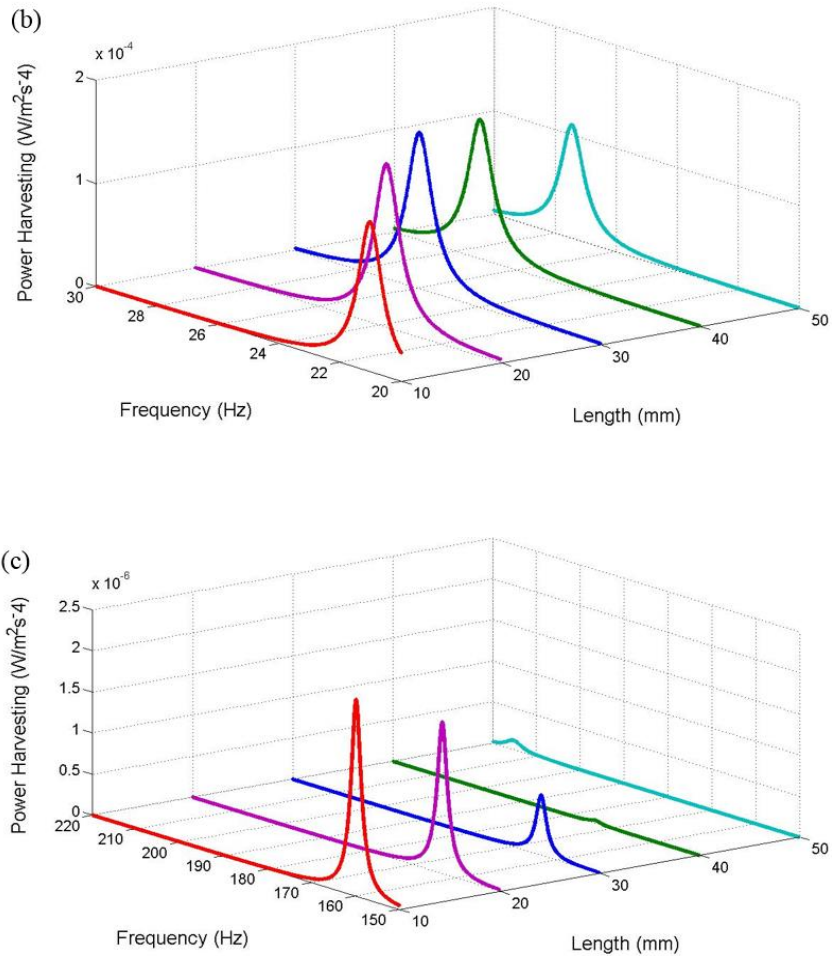


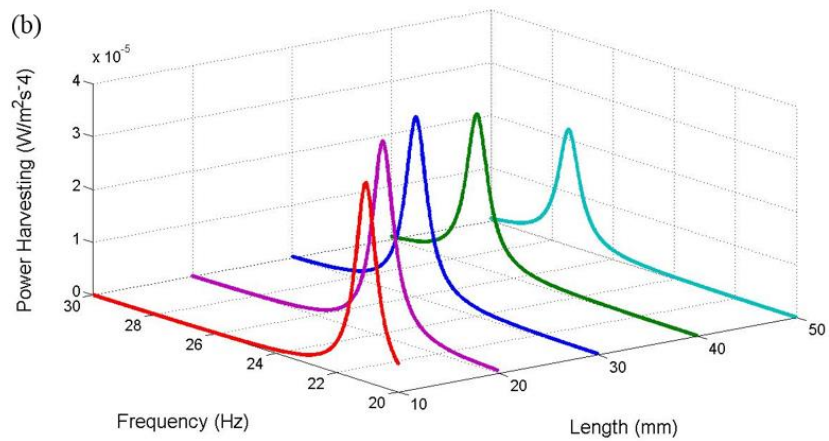
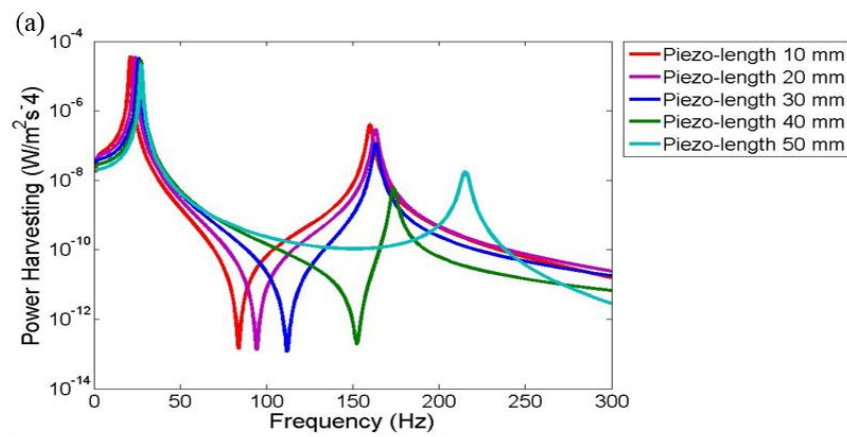
Figure 5.36 (a) Power harvesting FRF's of varying length piezoelectric element with load resistance 3.2 MΩ. (b) First mode resonance. (c) Second mode resonance.

The system response for load resistance approaching open circuit conditions of 20.5 MΩ is shown in figure 5.37 with increasing piezoelectric element length from 10 to 50 mm. The detailed values for the first two modes are provided in table 5.13. The first mode resonance increases from 21.07 Hz to 27.47 Hz with variation in piezoelectric length from 10-50 mm. However, the power amplitude continuously decreases from 37.71 μW/m²s⁻⁴ to 22.02 μW/m²s⁻⁴ with increasing piezoelectric element lengths.

The frequency of the second mode resonance is 159.9 Hz for the piezoelectric length of 10 mm and rises to 215.2 Hz for the piezoelectric length of 50 mm. The power amplitude for the second mode reduces from 404.3 nW/m²s⁻⁴ to 5.909 nW/m²s⁻⁴ with varying piezoelectric length from 10-40 mm and rises slightly to 18.16 nW/m²s⁻⁴ with piezoelectric length of 50 mm.

Table 5.13 Detailed frequencies and electrical power outputs for first two resonance modes with load resistance 20.5 MΩ and varying piezoelectric length.

Piezoelectric length	First mode		Second mode	
(mm)	Frequency (Hz)	Power ($\mu\text{W}/\text{m}^2 \text{s}^{-4}$)	Frequency (Hz)	Power ($\text{nW}/\text{m}^2 \text{s}^{-4}$)
10	21.07	37.71	159.9	404.3
20	23.78	37.11	163.1	303.2
30	25.94	34.19	163.3	116.2
40	27.21	28.96	173.7	5.909
50	27.47	22.02	215.2	18.16



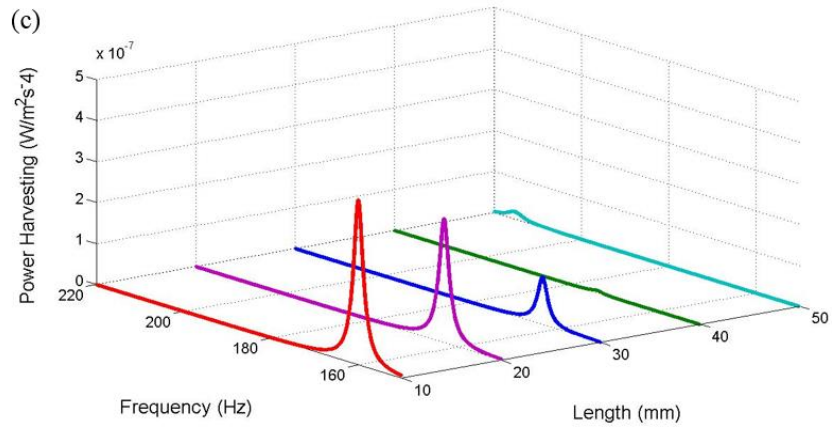


Figure 5.37 (a) Power harvesting FRF's of varying length piezoelectric element with load resistance 3.2 MΩ. (b) First mode resonance. (c) Second mode resonance.

Figure 5.38 and 5.39 show the changing response of frequency and power output with respect to the changing piezoelectric length for the first mode. Here, the load impedance at short circuit is chosen as 680 Ω because this resistance is enough to give a much better frequency response for the experimental test. However, it should be noted that in the experiment even 1 Ω resistance value shows coarse frequency response due to the dominating noise response. The power output frequency responses for different load impedances from 680 Ω to 20.5 MΩ present quite a different response curve for the first and second modes where the summary for power response from tables 6.5-13.5 are shown in figure 5.38-5.39 and 5.40-5.41, respectively.

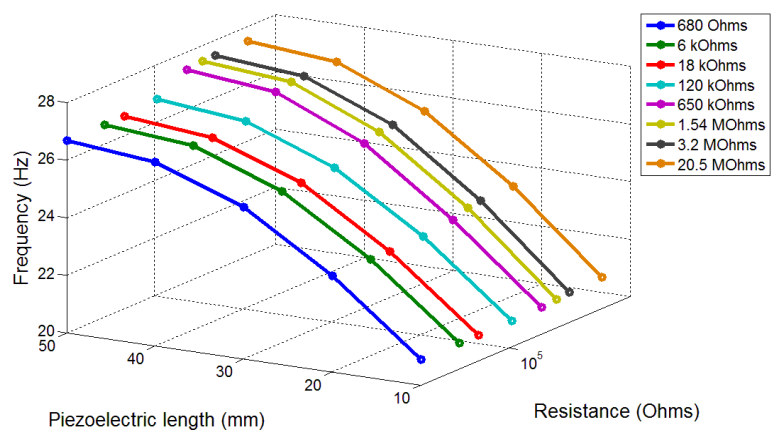


Figure 5.38 Result of changing resonance frequency under varying load impedances as a function of varying piezoelectric length for first mode.

The resonance frequency patterns with respect to changing piezoelectric element length can be seen from the short and open circuit load resistances for the first mode. It appears that both resonance frequencies have similar increasing frequency behaviour. The resonance frequency for short and open circuit load resistances tend to increase with increasing piezoelectric length.

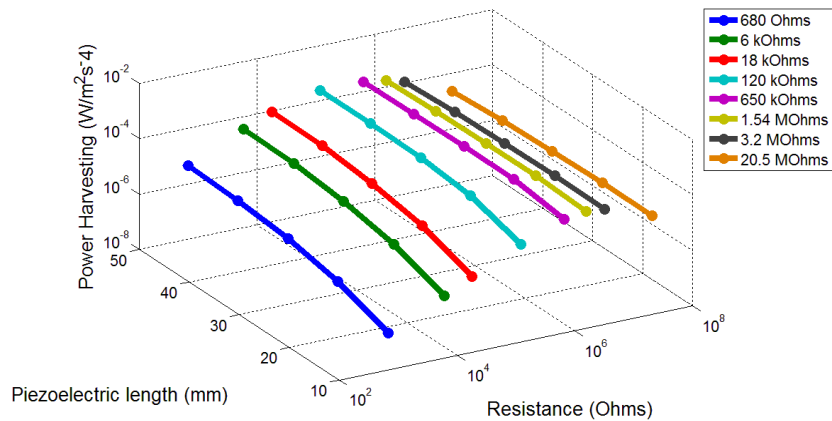


Figure 5.39 Result of changing electrical power output under varying load impedances as a function of varying piezoelectric length for first mode.

Therefore for summarising the pattern of power amplitude behaviour given from the short and open circuit load resistances at the first mode, it appears that both amplitudes have opposite behaviour. The power amplitude for short circuit resistance tends to increase with increasing piezoelectric length whereas the power amplitude at the open circuit resistance tends to decrease with increasing values piezoelectric length. Moreover, figure 5.40 and 5.41 present the resulting power output frequency response with respect to the changing piezoelectric length for the second mode.

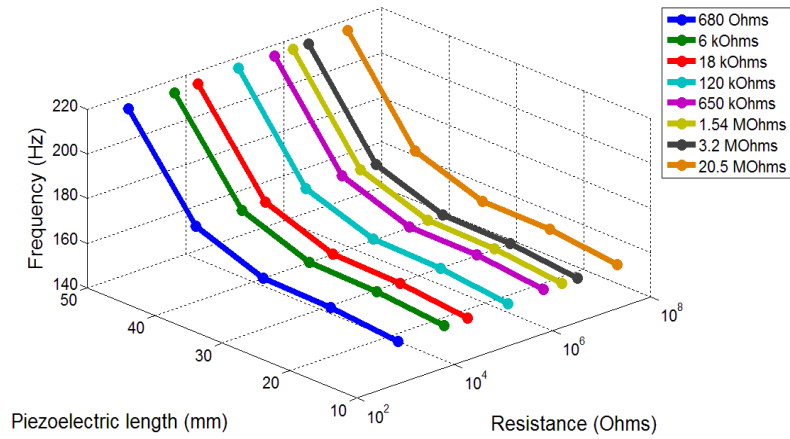


Figure 5.40 Result of changing resonance frequency under varying load impedances as a function of varying piezoelectric length for second mode.

For summarising the frequency response the trend for the short and open circuit load impedances, it appears that the resonance frequency increases with increasing piezoelectric length. However, the increasing resonance frequency seems to represent a half concave shape for the second mode whereas the first mode tends to increase with half convex form.

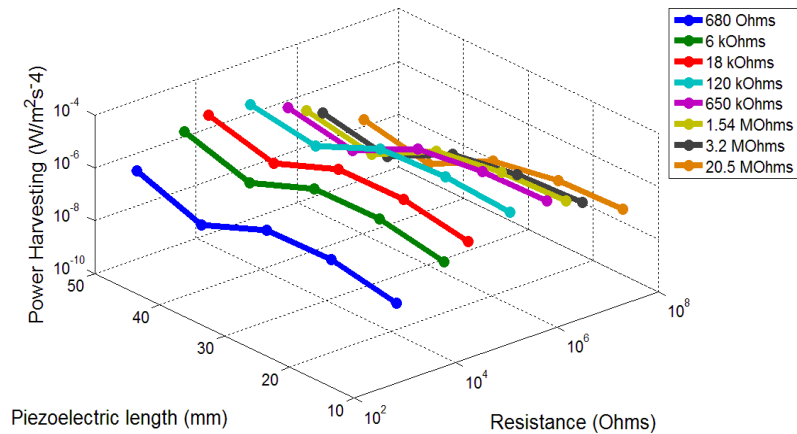


Figure 5.41 Result of changing electrical power output under varying load impedances as a function of varying piezoelectric length for the second mode.

Moreover, the power amplitude patterns for the second mode are summarised in figure 5.41, where it shows that for the short circuit resonance frequency, the power amplitude with 20 mm piezoelectric length has the highest power output whereas the piezoelectric length of 40 mm has the lowest power amplitude. Moreover, for the open

circuit resonance frequency, the piezoelectric length of 10 mm has the highest power whereas the piezoelectric length of 40 mm still has the lowest power range.

5.5 Summary

This chapter has presented the study of the unimorph power harvesting beam with tip mass offset and variable piezoelectric segment. The advantage of placing the tip mass onto the small structure is that it reduces the natural frequency value and also increases the power output. Both factors have benefit for practical engineering applications. Besides the analysis of the addition of the tip mass, this chapter has also investigated the effect of changing the length of the piezoelectric element. The analysis of parametric changes to the length, width and thickness of the piezoelectric element is very useful in developing an optimised design of the unimorph beam structure for particular applications. However, only the variation of piezoelectric element length has been explored at this stage. It should be noted that varying the dimensions of common parameters can result in very significant changes to the system resonances and power responses of the smart structure. The resulting power frequency responses using parametric piezoelectric length for the first mode has been summarised in figure 5.38 and 5.39. Here, the power resonance frequency patterns have shown a similar behaviour at short and open circuit load impedances with respect to the changing piezoelectric length, showing that the resonances frequency increases with increasing piezoelectric length. Moreover, the patterns of power amplitude seem to have opposite behaviours between load resistance at short and open circuits, where it appears that the power amplitude at short circuit tends to increase with increasing piezoelectric length whereas the power amplitude at the open circuit resistance tends to decrease with increasing piezoelectric length. For the second mode, the highest power amplitude for short circuit resistance region occurs using the piezoelectric length of 20 mm whereas the highest power for open circuit resistance occurs using piezoelectric length of 10 mm. The behaviour of the resonance frequency for the first and second modes has similar increasing resonances but has opposite behaviours. It appears that the formation of increasing resonance for the first mode shows a half convex shape whereas the second mode shows a half concave form.

Chapter 6

Unimorph Beam Power Harvester with Different Orientations

In the previous chapters 3-5, the investigation of the piezoelectric unimorph beam finite element modelling for single, multi-element and tip mass and segmentation has been explored in detail. The theoretical finite element derivations showed the basic steps for formulating the mathematical equations of the electromechanical piezoelectric energy harvester. However, this chapter considers the piezoelectric unimorph under transverse and rotational motion deformation associated with electromechanical coupling. The previous method is further extended to derive the governing finite element equations of the piezoelectric system with varying angles of orientation by including the additional effect of axial deformation and axial electromechanical coupling. Comparison between power harvesting response using axial and without axial deformation as well as electromechanical coupling will be explored. The piezoelectric unimorph beam with symmetrical length and asymmetrical thickness is bent in the middle of the total length of the piezoelectric beam. Two piezoelectric elements with the same length were glued onto the surface of the substructure where both of them were connected separately in parallel connection by adding external load resistance. This chapter focuses on formulating the finite element equations and the frequency responses of voltage, current and power output of the unimorph beam as a function of the varying orientation.

6.1 Electromechanical Finite Element for Unimorph Beam with Different Orientation with Three Degrees of Freedom per Node

6.1.1 Finite Element Modelling with Different Orientation

Modelling of the unimorph piezoelectric beam with different orientation requires the use of three degrees of freedom per node which subsequently changes the previous matrix formation. In this chapter, this particular condition is derived and discussed in detail. The investigation of the unimorph finite element model presented here considers the axial, transverse and rotation representing six degrees of freedom for

each element as shown in figure 6.1 where derivation of the matrix equations can be further developed in the forthcoming section.

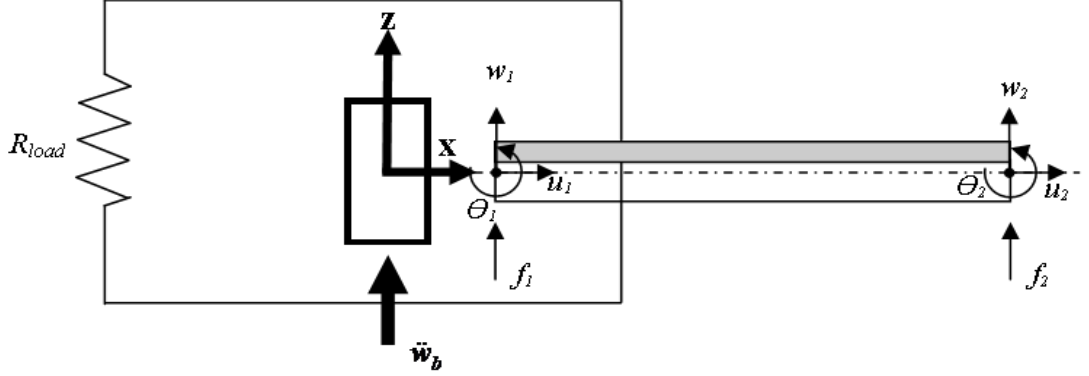


Figure 6.1 Piezoelectric unimorph beam with 6 degrees of freedom.

The displacement field for the moving beam relative to the moving base can be given as,

$$\underline{u}(x, z, t) = \underline{u}^0(x, t) - z \frac{\partial \underline{w}^0(x, t)}{\partial x} = \underline{\Phi}_u(x) \underline{u}(t) - z \underline{\Phi}_w'(x) \underline{w}(t), \quad (6.1)$$

$$\underline{v}(x, z, t) = 0, \quad (6.2)$$

$$\underline{w}(x, z, t) = \underline{w}^0(x, t) = \underline{\Phi}_w(x) \underline{w}(t), \quad (6.3)$$

where $\underline{\Phi}_u(x)$ and $\underline{\Phi}_w(x)$ indicate longitudinal and transverse shape functions, respectively. The formation of the total relative displacement vector is given by,

$$\underline{\mathbf{R}}(x, t) = \left[\underline{u}^0(x, t) - z \frac{\partial \underline{w}^0(x, t)}{\partial x} + \underline{w}^0(x, t) \right]^T. \quad (6.4)$$

The elemental strain field due to transverse and initial axial displacement can be formulated based on the Euler-Bernoulli theory as,

$$\underline{\mathbf{S}}_1(x, z, t) = \frac{\partial \underline{u}(x, z, t)}{\partial x} = \frac{\partial \underline{u}^0(x, t)}{\partial x} - z \frac{\partial^2 \underline{w}^0(x, t)}{\partial x^2}. \quad (6.5)$$

Modifying equation (6.5) in terms of the shape function gives,

$$\underline{S}_1(x, z, t) = \frac{\partial \underline{u}(x, z, t)}{\partial x} = \frac{d\underline{\Phi}_u(x)}{dx} \underline{u}(t) - z \frac{d^2 \underline{\Phi}_w(x)}{dx^2} \underline{w}(t) = \underline{\Phi}_u'(x) \underline{u}(t) - z \underline{\Phi}_w''(x) \underline{w}(t). \quad (6.6)$$

6.1.2 Piezoelectric Coupled Field Mechanical and Electrical Equations

The resulting coupled equations of mechanical and electrical fields can be developed using the constitutive equations for the substructure and piezoelectric elements as presented in the previous chapter from equations (3.11) and (3.12). The coupled field equations of the mechanical substructure and the piezoceramic elements can be presented as,

$$\begin{aligned} \underline{T}_{-1}^{(1)} &= c_{11}^{(1)} \left(\underline{\Phi}_u^{(1)'}(x) \underline{u}(t) - z \underline{\Phi}_w^{(1)''}(x) \underline{w}(t) \right), \\ \underline{T}_{-1}^{(2)} &= c_{11}^{(2)} \left(\underline{\Phi}_u^{(2)'}(x) \underline{u}(t) - z \underline{\Phi}_w^{(2)''}(x) \underline{w}(t) \right) + e_{31} \left(\underline{\Omega}(z) \underline{v}_p(t) \right). \end{aligned} \quad (6.7)$$

In addition the electric displacement vector of the piezoelectric component can be formulated by substituting equations (6.6) and the electric field equation (3.14) into the constitutive equation (3.10) to give,

$$\underline{D}_{-3} = e_{31} \left(\underline{\Phi}_u^{(2)'}(x) \underline{u}(t) - z \underline{\Phi}_w^{(2)''}(x) \underline{w}(t) \right) + \varepsilon_{33}^S \underline{\Omega}(z) \underline{v}_p(t). \quad (6.8)$$

The extended Hamilton's principle defined as energy functional forms of the potential energy, kinetic energy and work done due to the base excitation and electrical energy can be used to formulate the general electromechanical dynamic equations. The Hamilton's principle equation is written as,

$$\int_{t_1}^{t_2} [\delta(KE - PE + WE) + \delta WF] dt = 0, \quad (6.9)$$

where the parameters KE , PE , WF and WE represent kinetic energy, potential energy and non-conservative work and electrical energy. Each functional energy form can be formulated as,

$$KE = \frac{1}{2} \int_{V^{(1)}} \rho^{(1)} (\underline{\dot{\mathbf{R}}}^T \underline{\dot{\mathbf{R}}}) dV^{(1)} + \frac{1}{2} \int_{V^{(2)}} \rho^{(2)} (\underline{\dot{\mathbf{R}}}^T \underline{\dot{\mathbf{R}}}) dV^{(2)}, \quad (6.10)$$

$$PE = \frac{1}{2} \int_{V^{(1)}} (\underline{\mathbf{S}}^{(1)T} \underline{\mathbf{T}}^{(1)}) dV^{(1)} + \frac{1}{2} \int_{V^{(2)}} (\underline{\mathbf{S}}^{(2)T} \underline{\mathbf{T}}^{(2)}) dV^{(2)}, \quad (6.11)$$

$$WE = \frac{1}{2} \int_{V^{(2)}} (\underline{\mathbf{E}}^T \underline{\mathbf{D}}) dV^{(2)}$$

$$WF = -\underline{\mathbf{w}}(x) \underline{\mathbf{f}}(x) + \underline{\mathbf{v}}_p \underline{\mathbf{q}}_p. \quad (6.12)$$

The parameters ρ and V indicate the mass density and volume, respectively. Superscript $(.)^T$ denotes the transpose matrix and the over dot represents differentiation with respect to time. Equation (6.10) and (6.11) can then be written for the unimorph beam element as,

$$\delta KE = \int_{V^{(1)}} \rho^{(1)} \delta \underline{\dot{\mathbf{R}}}^T \underline{\dot{\mathbf{R}}} dV^{(1)} + \int_{V^{(2)}} \rho^{(2)} \delta \underline{\dot{\mathbf{R}}}^T \underline{\dot{\mathbf{R}}} dV^{(2)}, \quad (6.13)$$

$$\delta PE = \int_{V^{(1)}} \delta \underline{\mathbf{S}}_1^{(1)T} c_{11}^{(1)} \underline{\mathbf{S}}_1^{(1)} dV^{(1)} + \int_{V^{(2)}} \left[\left(\delta \underline{\mathbf{S}}_1^{(2)T} c_{11}^{(2)} \underline{\mathbf{S}}_1^{(2)} \right) - \left(\delta \underline{\mathbf{S}}_1^{(2)T} e_{31} \underline{\mathbf{E}}_3 \right) \right] dV^{(2)}, \quad (6.14)$$

$$\delta WE = \int_{V^{(2)}} \left[\left(\delta \underline{\mathbf{E}}_3^T e_{31} \underline{\mathbf{S}}_1^{(2)} \right) - \left(\delta \underline{\mathbf{E}}_3^T \varepsilon_{33}^S \underline{\mathbf{E}}_3 \right) \right] dV^{(2)}$$

$$\delta WF = \delta \underline{\mathbf{w}}(x) \underline{\mathbf{f}}(x) + \delta \underline{\mathbf{v}}_p \underline{\mathbf{q}}_p. \quad (6.15)$$

This further section explains the internal expression for each term in equation (6.13), (6.14) and (6.15). Expression of the mechanical coupled potential energy for equation (6.14) based on the constitutive equation (6.7) can be given as,

$$\begin{aligned}
\delta PE = & \int_{V^{(1)}} c_{11}^{(1)} \left(\begin{aligned} & \delta \underline{u}(t)^T \underline{\Phi}_u'(x)^T \underline{\Phi}_u'(x) \underline{u}(t) + z^2 \delta \underline{w}(t)^T \underline{\Phi}_w''(x)^T \underline{\Phi}_w''(x) \underline{w}(t) \\ & - z \underline{\Phi}_u'(x) \delta \underline{u}(t) \underline{\Phi}_w''(x) \underline{w}(t) - z \underline{\Phi}_u'(x) \underline{u}(t) \underline{\Phi}_w''(x) \delta \underline{w}(t) \end{aligned} \right) dV^{(1)} \\
& + \int_{V^{(2)}} c_{11}^{(2)} \left(\begin{aligned} & \delta \underline{u}(t)^T \underline{\Phi}_u'(x)^T \underline{\Phi}_u'(x) \underline{u}(t) + z^2 \delta \underline{w}(t)^T \underline{\Phi}_w''(x)^T \underline{\Phi}_w''(x) \underline{w}(t) \\ & - z \underline{\Phi}_u'(x) \underline{u}(t) \underline{\Phi}_w''(x) \underline{w}(t) - z \underline{\Phi}_u'(x) \underline{u}(t) \underline{\Phi}_w''(x) \delta \underline{w}(t) \end{aligned} \right) dV^{(2)} \quad . (6.16) \\
& + \int_{V^{(2)}} e_{31} \left(\delta \underline{u}(t)^T \underline{\Phi}_u'(x)^T \underline{\Omega}(z) \underline{v}_{-p}(t) - z \delta \underline{w}(t)^T \underline{\Phi}_w''(x)^T \underline{\Omega}(z) \underline{v}_{-p}(t) \right) dV^{(2)}
\end{aligned}$$

Here, the expression of the elastic stiffness coefficient for the unimorph beam can be expressed into three coefficient terms which are extensional stiffness in axial, extensional-bending stiffness and transverse bending (M. F. Lumentut, 2010) for each layer of the piezoelectric unimorph beam. Based on developing the equation (6.14), the internal electrical energy piezoelectric layer can be given as,

$$\delta WE = \int_{V^{(2)}} \left[\left(\delta \underline{E}_3^T e_{31} \underline{S}_1^{(2)} \right) + \left(\delta \underline{E}_3^T \varepsilon_{33}^S \underline{E}_3 \right) \right] dV^{(2)}. \quad (6.17)$$

Reformulating the internal energy term based on equation (6.14) and the constitutive equation (6.8), it can be given as,

$$\begin{aligned}
\delta WE = & \int_{V^{(2)}} \left[e_{31} \left(-\delta \underline{v}_{-p}(t)^T \underline{\Omega}(z)^T \underline{\Phi}_u'(x) \underline{u}(t) + z \delta \underline{v}_{-p}(t)^T \underline{\Omega}(z)^T \underline{\Phi}_w''(x) \underline{w}(t) \right) \right. \\
& \left. + \left(\delta \underline{v}_{-p}(t)^T \underline{\Omega}(z)^T \varepsilon_{33}^S \underline{\Omega}(z) \underline{v}_{-p}(t) \right) \right] dV^{(2)} \quad . (6.18)
\end{aligned}$$

Furthermore, the kinetic energy equation can be modified according to the change of rate of vector displacement from equation (6.4) with respect to time and modification of the energy equation (6.14) based on the vector displacement field and the density of the piezoelectric unimorph beam. The piezoelectric unimorph under base excitation undergoes relative displacement in the axial, transverse and rotation field. Corresponding to equation (6.14) and (6.4), the kinetic energy equation can be formulated based on the mass density of piezoelectric unimorph beam as,

$$\begin{aligned}
\delta KE = & \int_{V^{(1)}} \rho^{(1)} \left[\left(\delta \underline{\dot{u}}(t)^T \underline{\Phi}_u(x)^T \underline{\Phi}_u(x) \underline{\dot{u}}(t) \right) + \left(\delta \underline{\dot{w}}(t)^T \underline{\Phi}_w(x)^T \underline{\Phi}_w(x) \underline{\dot{w}}(t) \right) \right. \\
& - z \left(\delta \underline{\dot{u}}(t) \underline{\Phi}_u(x) \underline{\Phi}_w'(x) \underline{\dot{w}}(t) + \underline{\dot{u}}(t) \underline{\Phi}_u(x) \underline{\Phi}_w'(x) \delta \underline{\dot{w}}(t) \right) + z^2 \left(\delta \underline{\dot{w}}(t)^T \underline{\Phi}_w'(x)^T \underline{\Phi}_w'(x) \underline{\dot{w}}(t) \right) \left. \right] dV^{(1)} \\
& + \int_{V^{(2)}} \rho^{(2)} \left[\left(\delta \underline{\dot{u}}(t)^T \underline{\Phi}_u(x)^T \underline{\Phi}_u(x) \underline{\dot{u}}(t) \right) + \left(\delta \underline{\dot{w}}(t)^T \underline{\Phi}_w(x)^T \underline{\Phi}_w(x) \underline{\dot{w}}(t) \right) \right. \\
& - z \left(\delta \underline{\dot{u}}(t) \underline{\Phi}_u(x) \underline{\Phi}_w'(x) \delta \underline{\dot{w}}(t) + \underline{\dot{u}}(t) \underline{\Phi}_u(x) \underline{\Phi}_w'(x) \delta \underline{\dot{w}}(t) \right) + z^2 \left(\delta \underline{\dot{w}}(t)^T \underline{\Phi}_w'(x)^T \underline{\Phi}_w'(x) \underline{\dot{w}}(t) \right) \left. \right] dV^{(2)}
\end{aligned} \tag{6.19}$$

In addition, contribution of the inertial coupling between the axial and transverse displacement are only taken into consideration in the system using the asymmetrical neutral axis. The kinetic energy can be further formulated as,

$$\begin{aligned}
\delta KE = & \int_{V^{(1)}} \rho^{(1)} \left[\left(\delta \underline{\dot{u}}(t)^T \underline{\Phi}_u(x)^T \underline{\Phi}_u(x) \underline{\dot{u}}(t) \right) + \left(\delta \underline{\dot{w}}(t)^T \underline{\Phi}_w(x)^T \underline{\Phi}_w(x) \underline{\dot{w}}(t) \right) \right] dV^{(1)} \\
& \int_{V^{(2)}} \rho^{(2)} \left[\left(\delta \underline{\dot{u}}(t)^T \underline{\Phi}_u(x)^T \underline{\Phi}_u(x) \underline{\dot{u}}(t) \right) + \left(\delta \underline{\dot{w}}(t)^T \underline{\Phi}_w(x)^T \underline{\Phi}_w(x) \underline{\dot{w}}(t) \right) \right] dV^{(2)} .
\end{aligned} \tag{6.20}$$

Here, the non-conservative work is due to base acceleration of the cantilevered piezoelectric unimorph beam. The external force for the non-conservative work due to input base excitation and the applied charge can be written as,

$$WF = -\delta \underline{w}(t)^T \underline{f} + \delta \underline{v}_{-p}(t)^T \underline{q}_{-p}(t). \tag{6.21}$$

The constitutive electromechanical dynamic equation can be simplified in the form of volume integration based on equations (6.13), (6.14) and (6.15). The Hamilton's equation for energy harvesting can then be written as,

$$\left(\int_{t_1}^{t_2} \left[\int_{V^{(1)}} \rho^{(1)} \left(\delta \underline{\dot{\mathbf{u}}}(t)^T \underline{\Phi}_u(x)^T \underline{\Phi}_u(x) \underline{\dot{\mathbf{u}}}(t) + \delta \underline{\dot{\mathbf{w}}}(t)^T \underline{\Phi}_w(x)^T \underline{\Phi}_w(x) \underline{\dot{\mathbf{w}}}(t) \right) dV^{(1)} \right. \right. \\
+ \int_{V^{(2)}} \rho^{(2)} \left(\delta \underline{\dot{\mathbf{u}}}(t)^T \underline{\Phi}_u(x)^T \underline{\Phi}_u(x) \underline{\dot{\mathbf{u}}}(t) + \delta \underline{\dot{\mathbf{w}}}(t)^T \underline{\Phi}_w(x)^T \underline{\Phi}_w(x) \underline{\dot{\mathbf{w}}}(t) \right) dV^{(2)} \\
- \int_{V^{(1)}} c_{11}^{(1)} \left(\delta \underline{\mathbf{u}}(t)^T \underline{\Phi}_u'(x)^T \underline{\Phi}_u'(x) \underline{\mathbf{u}}(t) + z^2 \delta \underline{\mathbf{w}}(t)^T \underline{\Phi}_w''(x)^T \underline{\Phi}_w''(x) \underline{\mathbf{w}}(t) \right) dV^{(1)} \\
- \int_{V^{(2)}} c_{11}^{(2)} \left(\delta \underline{\mathbf{u}}(t)^T \underline{\Phi}_u'(x)^T \underline{\Phi}_u'(x) \underline{\mathbf{u}}(t) + z^2 \delta \underline{\mathbf{w}}(t)^T \underline{\Phi}_w''(x)^T \underline{\Phi}_w''(x) \underline{\mathbf{w}}(t) \right) dV^{(2)} \\
- \int_{V^{(1)}} e_{31} \left(\delta \underline{\mathbf{u}}(t)^T \underline{\Phi}_u'(x)^T \underline{\Omega}(z) \underline{\mathbf{v}}_p(t) - z \delta \underline{\mathbf{w}}(t)^T \underline{\Phi}_w''(x)^T \underline{\Omega}(z) \underline{\mathbf{v}}_p(t) \right) dV^{(1)} \\
- \int_{V^{(2)}} e_{31} \left(\delta \underline{\mathbf{v}}_p(t)^T \underline{\Omega}(z)^T \underline{\Phi}_u'(x) \underline{\mathbf{u}}(t) - z \delta \underline{\mathbf{v}}_p(t)^T \underline{\Omega}(z)^T \underline{\Phi}_w''(x) \underline{\mathbf{w}}(t) \right) dV^{(2)} \\
+ \int_{V^{(2)}} \delta \underline{\mathbf{v}}_p(t)^T \underline{\Omega}(z)^T \varepsilon_{33}^s \underline{\Omega}(z) \underline{\mathbf{v}}_p(t) dV^{(2)} \\
\left. \left. - \delta \underline{\mathbf{w}}(t)^T \underline{\Phi}_w(x) \underline{\mathbf{f}} + \delta \underline{\mathbf{v}}_p(t)^T \underline{\mathbf{q}}_p(t) \right) dt = 0. \right. \tag{6.22}$$

The foregoing equation (6.22) can be modified by applying the variational principle and separating the equations in terms of the displacements in the axial and transverse mechanical motions and the electrical form. Firstly the dynamic equation can be presented as the electromechanical coupling equation under longitudinal extension, which gives,

$$\begin{aligned}
& \int_{V^{(1)}} \rho^{(1)} \underline{\Phi}_u(x)^T \underline{\Phi}_u(x) \underline{\ddot{\mathbf{u}}}(t) dV^{(1)} + \int_{V^{(2)}} \rho^{(2)} \underline{\Phi}_u(x)^T \underline{\Phi}_u(x) \underline{\ddot{\mathbf{u}}}(t) dV^{(2)} \\
& + \int_{V^{(1)}} c_{11}^{(1)} \underline{\Phi}_u'(x)^T \underline{\Phi}_u'(x) \underline{\mathbf{u}}(t) dV^{(1)} + \int_{V^{(2)}} c_{11}^{(2)} \underline{\Phi}_u'(x)^T \underline{\Phi}_u'(x) \underline{\mathbf{u}}(t) dV^{(2)}. \tag{6.23} \\
& + \int_{V^{(1)}} e_{31} \underline{\Phi}_u'(x)^T \underline{\Omega}(z) \underline{\mathbf{v}}_p(t) dV^{(1)} = 0
\end{aligned}$$

Secondly the dynamic equation can be given in terms of the electromechanical coupling equation under transverse bending form as,

$$\begin{aligned}
& \int_{V^{(1)}} \rho^{(1)} \underline{\Phi}_w(x)^T \underline{\Phi}_w(x) \underline{\ddot{\mathbf{w}}}(t) dV^{(1)} + \int_{V^{(2)}} \rho^{(2)} \underline{\Phi}_w(x)^T \underline{\Phi}_w(x) \underline{\ddot{\mathbf{w}}}(t) dV^{(2)} \\
& + \int_{V^{(1)}} c_{11}^{(1)} z^2 \underline{\Phi}_w''(x)^T \underline{\Phi}_w''(x) \underline{\mathbf{w}}(t) dV^{(1)} + \int_{V^{(2)}} c_{11}^{(2)} z^2 \underline{\Phi}_w''(x)^T \underline{\Phi}_w''(x) \underline{\mathbf{w}}(t) dV^{(2)}. \tag{6.24} \\
& + \int_{V^{(1)}} e_{31} z \underline{\Phi}_w''(x)^T \underline{\Omega}(z) \underline{\mathbf{v}}_p(t) dV^{(1)} + \underline{\Phi}_w(x)^T \underline{\mathbf{f}} = 0
\end{aligned}$$

Thirdly the dynamic equation representing the electrical behaviour of the electromechanical piezoelectric unimorph can be written as,

$$\int_{V^{(2)}} e_{31} \left(\underline{\underline{\Omega}}(z)^T \underline{\underline{\Phi}}_u'(x) \underline{\underline{u}}(t) - z \underline{\underline{\Omega}}(z)^T \underline{\underline{\Phi}}_w''(x) \underline{\underline{w}}(t) \right) dV^{(2)} - \int_{V^{(2)}} \underline{\underline{\Omega}}(z)^T \varepsilon_{33}^S \underline{\underline{\Omega}}(z) \underline{\underline{y}}_p(t) dV^{(2)} - \underline{\underline{q}}_p = 0 \quad (6.25)$$

Altering the electrical charge function by differentiate it with respect to time obtains the electrical current across an external resistance as,

$$\int_{V^{(2)}} e_{31} \left(\underline{\underline{\Omega}}(z)^T \underline{\underline{\Phi}}_u'(x) \underline{\underline{\dot{u}}}(t) - z \underline{\underline{\Omega}}(z)^T \underline{\underline{\Phi}}_w''(x) \underline{\underline{\dot{w}}}(t) \right) dV^{(2)} - \int_{V^{(2)}} \underline{\underline{\Omega}}(z)^T \varepsilon_{33}^S \underline{\underline{\Omega}}(z) \underline{\underline{\dot{y}}}_p(t) dV^{(2)} - \underline{\underline{i}}_p(t) = 0 \quad (6.26)$$

Further modification of equations (6.23), (6.24), and (6.26) can be proceeded by simplifying all terms using matrix notation. Substituting the Rayleigh damping function through the electromechanical equation into the formation of the coupled electromechanical piezoelectric unimorph differential equation gives,

$$\begin{bmatrix} \mathbf{M}_{rn}^{(u)} & 0 & 0 \\ 0 & \mathbf{M}_{rn}^{(w)} & 0 \\ 0 & 0 & 0 \end{bmatrix} \begin{Bmatrix} \ddot{\mathbf{u}} \\ \ddot{\mathbf{w}} \\ \ddot{\mathbf{v}}_p \end{Bmatrix} + \begin{bmatrix} \mathbf{C}_{rn}^{(u)} & 0 & 0 \\ 0 & \mathbf{C}_{rn}^{(w)} & 0 \\ \mathbf{P}_{sn}^{(u)} & \mathbf{P}_{sn}^{(w)} & \mathbf{P}_D \end{bmatrix} \begin{Bmatrix} \dot{\mathbf{u}} \\ \dot{\mathbf{w}} \\ \dot{\mathbf{v}}_p \end{Bmatrix} + \begin{bmatrix} \mathbf{K}_{rn}^{(u)} & 0 & \mathbf{P}_{rs}^{(u)} \\ 0 & \mathbf{K}_{rn}^{(w)} & \mathbf{P}_{rs}^{(w)} \\ 0 & 0 & 0 \end{bmatrix} \begin{Bmatrix} \mathbf{u} \\ \mathbf{w} \\ \mathbf{v}_p \end{Bmatrix} = \begin{Bmatrix} 0 & 0 & 0 \\ 0 & \mathbf{F}_r^{(w)} & 0 \\ 0 & 0 & \mathbf{i}_p \end{Bmatrix} \quad (6.27)$$

where,

$$\begin{aligned} \mathbf{M}_{rn}^{(u)} &= \int_{V^{(1)}} \rho^{(1)} \underline{\underline{\Phi}}_u(x)^T \underline{\underline{\Phi}}_u(x) dV^{(1)} + \int_{V^{(2)}} \rho^{(2)} \underline{\underline{\Phi}}_u(x)^T \underline{\underline{\Phi}}_u(x) dV^{(2)} \\ \mathbf{M}_{rn}^{(w)} &= \int_{V^{(1)}} \rho^{(1)} \underline{\underline{\Phi}}_w(x)^T \underline{\underline{\Phi}}_w(x) dV^{(1)} + \int_{V^{(2)}} \rho^{(2)} \underline{\underline{\Phi}}_w(x)^T \underline{\underline{\Phi}}_w(x) dV^{(2)}, \\ \mathbf{K}_{rn}^{(u)} &= \int_{V^{(1)}} c_{11}^{(1)} \underline{\underline{\Phi}}_u'(x)^T \underline{\underline{\Phi}}_u'(x) dV^{(1)} + \int_{V^{(2)}} c_{11}^{(2)} \underline{\underline{\Phi}}_u'(x)^T \underline{\underline{\Phi}}_u'(x) dV^{(2)} \\ \mathbf{K}_{rn}^{(w)} &= \int_{V^{(1)}} c_{11}^{(1)} z^2 \underline{\underline{\Phi}}_w''(x)^T \underline{\underline{\Phi}}_w''(x) dV^{(1)} + \int_{V^{(2)}} c_{11}^{(2)} z^2 \underline{\underline{\Phi}}_w''(x)^T \underline{\underline{\Phi}}_w''(x) dV^{(2)}, \end{aligned}$$

$$\begin{aligned}
\mathbf{P}_{rs}^{(u)} &= \int_{V^{(1)}} e_{31} \underline{\Phi}_u'(x)^T \underline{\Omega}(z) dV^{(2)}, \mathbf{P}_{rs}^{(w)} = -\int_{V^{(1)}} e_{31} z \underline{\Phi}_w''(x)^T \underline{\Omega}(z) dV^{(2)}, \\
\mathbf{P}_{sn}^{(u)} &= \int_{V^{(2)}} e_{31} \underline{\Omega}(z)^T \underline{\Phi}_u'(x) dV^{(2)}, \mathbf{P}_{sn}^{(w)} = -\int_{V^{(2)}} e_{31} z \underline{\Omega}(z)^T \underline{\Phi}_w''(x) dV^{(2)}, \\
\mathbf{P}_D &= -\int_{V^{(2)}} \underline{\Omega}(z)^T \varepsilon_{33}^s \underline{\Omega}(z) dV^{(2)}, \mathbf{F}_r^{(w)} = -\underline{\Phi}_w(x)^T \underline{f} = -\mathbf{Q}_r \ddot{\mathbf{w}}_{base}(t). \tag{6.28}
\end{aligned}$$

where \mathbf{M}_m , \mathbf{K}_m are the local mass matrix and the local stiffness matrix. \mathbf{P}_{rs} , \mathbf{P}_{sn} represent the local electromechanical coupling terms and \mathbf{P}_D is the local capacitance matrix, \mathbf{F}_r is the force base excitation, \mathbf{z} is the displacement in the axial, transverse and rotational direction and \mathbf{v}_p is the voltage output direction. In the expression equation (6.28), the consistent local mass matrix can be represented as,

$$\begin{aligned}
\mathbf{M}_m^{(u)} &\equiv \frac{(\rho^{(1)} A^{(1)} + \rho^{(2)} A^{(2)})L}{6} \begin{bmatrix} u_1 & w_1 & \theta_1 & u_2 & w_2 & \theta_2 \\ 2 & 0 & 0 & 1 & 0 & 0 \\ 0 & 0 & 0 & 0 & 0 & 0 \\ 0 & 0 & 0 & 0 & 0 & 0 \\ 1 & 0 & 0 & 2 & 0 & 0 \\ 0 & 0 & 0 & 0 & 0 & 0 \\ 0 & 0 & 0 & 0 & 0 & 0 \end{bmatrix} \begin{matrix} u_1 \\ w_1 \\ \theta_1 \\ u_1 \\ w_2 \\ \theta_2 \end{matrix}, \\
\mathbf{M}_m^{(w)} &= \frac{(\rho^{(1)} A^{(1)} + \rho^{(2)} A^{(2)})L}{420} \begin{bmatrix} u_1 & w_1 & \theta_1 & u_2 & w_2 & \theta_2 \\ 0 & 0 & 0 & 0 & 0 & 0 \\ 0 & 156 & 22L & 0 & 54 & -13L \\ 0 & 22L & 4L^2 & 0 & 13L & -3L^2 \\ 0 & 0 & 0 & 0 & 0 & 0 \\ 0 & 54 & 13L & 0 & 156 & -22L \\ 0 & -13L & -3L^2 & 0 & -22L & 4L^2 \end{bmatrix} \begin{matrix} u_1 \\ w_1 \\ \theta_1 \\ u_1 \\ w_2 \\ \theta_2 \end{matrix}, \tag{6.29}
\end{aligned}$$

and the stiffness matrix form will be given by,

$$\begin{aligned}
\mathbf{K}_m^{(u)} &= \frac{c_{11}^{(1)} A^{(1)} + c_{11}^{(2)} A^{(2)}}{L} \begin{bmatrix} u_1 & w_1 & \theta_1 & u_2 & w_2 & \theta_2 \\ 1 & 0 & 0 & -1 & 0 & 0 \\ 0 & 0 & 0 & 0 & 0 & 0 \\ 0 & 0 & 0 & 0 & 0 & 0 \\ -1 & 0 & 0 & 1 & 0 & 0 \\ 0 & 0 & 0 & 0 & 0 & 0 \\ 0 & 0 & 0 & 0 & 0 & 0 \end{bmatrix} \begin{matrix} u_1 \\ w_1 \\ \theta_1 \\ u_1 \\ w_2 \\ \theta_2 \end{matrix}, \\
\mathbf{K}_m^{(w)} &= \frac{c_{11}^{(1)} I^{(1)} + c_{11}^{(2)} I^{(2)}}{L} \begin{bmatrix} u_1 & w_1 & \theta_1 & u_2 & w_2 & \theta_2 \\ 0 & 0 & 0 & 0 & 0 & 0 \\ 0 & 12 & 6L & 0 & -12 & 6L \\ 0 & 6L & 4L^2 & 0 & -6L & 2L^2 \\ 0 & 0 & 0 & 0 & 0 & 0 \\ 0 & -12 & -6L & 0 & 12 & -6L \\ 0 & 6L & 2L^2 & 0 & -6L & 4L^2 \end{bmatrix} \begin{matrix} u_1 \\ w_1 \\ \theta_1 \\ u_2 \\ w_2 \\ \theta_2 \end{matrix}, \quad (6.30)
\end{aligned}$$

where A , I represent the cross-sectional area and the second moment of area. The electromechanical coupling vector is given by,

$$\mathbf{P}_{sn}^{(u)} = -e_{31} b \begin{bmatrix} u_1 & w_1 & \theta_1 & u_2 & w_2 & \theta_2 \\ 1 & 0 & 0 & 1 & 0 & 0 \end{bmatrix}, \quad \mathbf{P}_{sn}^{(w)} = \frac{-e_{31} b (2z_n h_p - h_p^2)}{2h_p} \begin{bmatrix} u_1 & w_1 & \theta_1 & u_2 & w_2 & \theta_2 \\ 0 & -1 & 0 & 0 & 1 & 0 \end{bmatrix}. \quad (6.31)$$

The capacitance is shown by the following form,

$$\mathbf{P}_D = -\frac{Lb\epsilon^s}{h_p}. \quad (6.32)$$

Finally, the form of the force vector can be written as,

$$\mathbf{Q}_r = \frac{\rho^{(1)} A^{(1)} L}{2} \begin{bmatrix} u_1 & w_1 & \theta_1 & u_2 & w_2 & \theta_2 \\ 0 & 1 & \frac{L}{6} & 0 & 1 & -\frac{L}{6} \end{bmatrix}^T + \frac{\rho^{(2)} A^{(2)} L}{2} \begin{bmatrix} u_1 & w_1 & \theta_1 & u_2 & w_2 & \theta_2 \\ 0 & 1 & \frac{L}{6} & 0 & 1 & -\frac{L}{6} \end{bmatrix}^T. \quad (6.33)$$

6.2 Global Electromechanical Finite Element Equation for the Distributed Piezoelectric Unimorph Beam with Different Orientations

The formation of the global matrix electromechanical dynamic equations of motion can be written from equation (6.27) as,

$$\begin{aligned} \underbrace{\mathbf{M}}_{(n_m \times n_m)(n_m \times 1)} \ddot{\mathbf{z}}(t) + \underbrace{\mathbf{C}}_{(n_m \times n_m)(n_m \times 1)} \dot{\mathbf{z}}(t) + \underbrace{\mathbf{K}}_{(n_m \times n_m)(n_m \times 1)} \mathbf{z}(t) + \underbrace{\mathbf{P}_{rs}}_{(n_m \times n_e)(n_e \times 1)} \mathbf{v}_p = \underbrace{\mathbf{F}_r}_{(n_m \times 1)}(t) \\ \underbrace{\mathbf{P}_{sn}}_{(n_e \times n_m)(n_m \times 1)} \dot{\mathbf{z}}(t) + \underbrace{\mathbf{P}_D}_{(n_e \times n_e)(n_e \times 1)} \dot{\mathbf{v}}_p = \underbrace{\mathbf{i}_p}_{(n_e \times 1)}(t) \end{aligned} \quad (6.34)$$

Since the piezoelectric element is attached to the substructure as two segmented components as shown in figure 6.2, the electrical discretised element can be further formulated using the parallel connection of Kirchhoff's Law for the electrical voltage and current. As previously explained in chapter 3-5 the electrode layers are connected using two wires resulting in only a single voltage output. Therefore, the segments of piezoelectric material gives the same voltage output. In this case, the two piezoelectric segments are set to be in parallel connection because the connection appears to give the full voltage to each components resistances such as piezoelectric element and resistors. Based on Kirchhoff's voltage law (KVL), the multi-output electrical voltage for each segmented piezoelectric element can be given by,

$$\begin{aligned} \overbrace{(v_1 = v_2 = \dots = v_{n_e} = v_{s1})}^{\text{Piezo segment1}}, \quad \overbrace{(v_1 = v_2 = \dots = v_{n_e} = v_{s2})}^{\text{Piezo segment2}}, \\ \overbrace{\mathbf{v}_{p1} = \{1 \quad 1 \quad \dots \quad 1\}^T v_{s1}}^{\text{Piezo segment1}}, \quad \overbrace{\mathbf{v}_{p2} = \{1 \quad 1 \quad \dots \quad 1\}^T v_{s2}}^{\text{Piezo segment2}}, \\ \overbrace{\mathbf{v}_{p1} = \mathfrak{G}^T v_{s2}}^{\text{Piezo segment1}} = \overbrace{\mathbf{v}_{p2} = \mathfrak{G}^T v_{s2}}^{\text{Piezo segment2}} = v(t), \end{aligned} \quad (6.35)$$

and the electrical current using Kirchhoff current law (KCL) where the term of global current \mathbf{i}_p can be shown as,

$$\overbrace{(i_{p1} + i_{p2} + \dots + i_{p_{n_e}} = i_{ps1})}^{\text{Piezo segment1}}, \quad \overbrace{(i_{p1} + i_{p2} + \dots + i_{p_{n_e}} = i_{ps2})}^{\text{Piezo segment2}},$$

$$\begin{aligned}
& \overbrace{i_{p_1} + i_{p_2} + \dots + i_{p_{n_e}}}^{\text{Piezo segment1}} = i_{ps1} = \mathfrak{G} \mathbf{i}_{ps1} \quad , \quad \overbrace{i_{p_1} + i_{p_2} + \dots + i_{p_{n_e}}}^{\text{Piezo segment2}} = i_{ps2} = \mathfrak{G} \mathbf{i}_{ps2} \quad , \\
& \overbrace{i_{ps1} + i_{ps2}}^{\text{Piezo segment1,2}} = \overbrace{\mathfrak{G} \mathbf{i}_{ps1} + \mathfrak{G} \mathbf{i}_{ps2}}^{\text{Piezo segment1,2}} = \mathbf{i}_p(t) .
\end{aligned} \tag{6.36}$$

As previously explained for the case of the discretised piezoelectric unimorph beam, equation (6.34) for voltage and current needs to be modified using the electromechanical transformation \mathfrak{G} from equation (6.35). Therefore, the electromechanical coupling matrices from the fourth term of the first expression in equation (6.34) can be modified by substituting (6.35) of the third term to give,

$$\begin{pmatrix} \mathbf{P}_{rs} \\ n_m \times n_e \end{pmatrix} \begin{pmatrix} \mathfrak{G}^T \\ n_e \times 1 \end{pmatrix} v_{s1} = \begin{pmatrix} \mathbf{\Theta} \\ n_m \times 1 \end{pmatrix} v_{s1} \quad , \quad \begin{pmatrix} \mathbf{P}_{rs} \\ n_m \times n_e \end{pmatrix} \begin{pmatrix} \mathfrak{G}^T \\ n_e \times 1 \end{pmatrix} v_{s2} = \begin{pmatrix} \mathbf{\Theta} \\ n_m \times 1 \end{pmatrix} v_{s2} , \tag{6.37}$$

where given that the voltage in parallel form provides $v_{s1} = v_{s2} = v$, therefore equation (6.37) becomes,

$$\begin{pmatrix} \mathbf{P}_{rs} \\ n_m \times n_e \end{pmatrix} \begin{pmatrix} \mathfrak{G}^T \\ n_e \times 1 \end{pmatrix} v_{s1} = \begin{pmatrix} \mathbf{\Theta} \\ n_m \times 1 \end{pmatrix} v \quad , \quad \begin{pmatrix} \mathbf{P}_{rs} \\ n_m \times n_e \end{pmatrix} \begin{pmatrix} \mathfrak{G}^T \\ n_e \times 1 \end{pmatrix} v_{s2} = \begin{pmatrix} \mathbf{\Theta} \\ n_m \times 1 \end{pmatrix} v . \tag{6.38}$$

The second expression of the global matrices in equation (6.34) can be modified by multiplying the electromechanical vector transformation \mathfrak{G} on both sides. Additional transformation of the current function for piezoelectric segments are given by equation (6.36). Introducing the electrical vector transformation for the second term of equation (6.34) for each segmented piezoelectric element gives,

$$\begin{aligned}
& \begin{pmatrix} \mathfrak{G} \\ 1 \times n_e \end{pmatrix} \begin{pmatrix} \mathbf{P}_{sn1} \\ n_e \times n_m \end{pmatrix} \dot{\mathbf{z}} + \begin{pmatrix} \mathfrak{G} \\ 1 \times n_e \end{pmatrix} \begin{pmatrix} \mathbf{P}_{Ds1} \\ n_e \times n_e \end{pmatrix} \begin{pmatrix} \mathfrak{G}^T \\ n_e \times 1 \end{pmatrix} \dot{v}_{s1} = \begin{pmatrix} \mathfrak{G} \\ 1 \times n_e \end{pmatrix} \mathbf{i}_{ps1} \quad , \\
& \begin{pmatrix} \mathfrak{G} \\ 1 \times n_e \end{pmatrix} \begin{pmatrix} \mathbf{P}_{sn2} \\ n_e \times n_m \end{pmatrix} \dot{\mathbf{z}} + \begin{pmatrix} \mathfrak{G} \\ 1 \times n_e \end{pmatrix} \begin{pmatrix} \mathbf{P}_{Ds2} \\ n_e \times n_e \end{pmatrix} \begin{pmatrix} \mathfrak{G}^T \\ n_e \times 1 \end{pmatrix} \dot{v}_{s2} = \begin{pmatrix} \mathfrak{G} \\ 1 \times n_e \end{pmatrix} \mathbf{i}_{ps2} .
\end{aligned} \tag{6.39}$$

In terms of the third part of equation (6.35), combination between the first and second parts of equation (6.39) can be formulated as,

$$\begin{pmatrix} \mathcal{G} \\ (1 \times n_e) \end{pmatrix} \begin{pmatrix} \mathbf{P}_{sn1} + \mathbf{P}_{sn2} \\ (n_e \times n_m) \end{pmatrix} \dot{\mathbf{z}} + \begin{pmatrix} \mathcal{G} \\ (1 \times n_e) \end{pmatrix} \begin{pmatrix} \mathbf{P}_{Ds1} + \mathbf{P}_{Ds2} \\ (n_e \times n_e) \end{pmatrix} \begin{pmatrix} \mathcal{G}^T \\ (n_e \times 1) \end{pmatrix} \dot{v}_{s1} = \begin{pmatrix} \mathcal{G} \\ (1 \times n_e) \end{pmatrix} \mathbf{i}_p(t). \quad (6.40)$$

The matrices of the segmented piezoelectric system need to be transformed for different orientation angles for the global coordinate system as seen in figure 6.2b. The fundamental transformation matrix equations can be found in many textbooks (Reddy, 1993) and (Moaveni, 2003) and the transformation matrix can be applied to each discretised element to obtain the final global matrix equation including the elements having different angles of orientation. In addition, equation (6.34a) can be reformulated by incorporating equation (6.38) and altering equation (6.34b) using equation (6.40) and the current expression as $\mathbf{i} = \mathbf{v}(t)/R_{load}$. The new formation of the electromechanical finite element equation using equations (6.34) and (6.40) can then be written as,

$$\begin{aligned} \left(\mathbf{T}^T \begin{pmatrix} \mathbf{M}_{rn} \\ (n_m \times n_m) \end{pmatrix} \mathbf{T} \right) \ddot{\mathbf{z}} + \begin{pmatrix} \mathbf{C}_{rn} \\ (n_m \times n_m) \end{pmatrix} \dot{\mathbf{z}} + \left(\mathbf{T}^T \begin{pmatrix} \mathbf{K}_{rn} \\ (n_m \times n_m) \end{pmatrix} \mathbf{T} \right) \mathbf{z} + \begin{pmatrix} \mathbf{T}^T \\ (n_m \times 1) \end{pmatrix} \boldsymbol{\Theta} v = - \left(\mathbf{T}^T \begin{pmatrix} \mathbf{Q}_r \\ (n_m \times 1) \end{pmatrix} \right) \ddot{\mathbf{w}}_{base}, \\ \begin{pmatrix} \boldsymbol{\Theta}^T \\ (n_e \times n_m) \end{pmatrix} \dot{\mathbf{z}} - \frac{v}{R_{load}} + \begin{pmatrix} \mathbf{C}_p \\ (n_e \times n_e) \end{pmatrix} \dot{v} = 0. \end{aligned} \quad (6.41)$$

where the transformation matrix term is \mathbf{T} , the global mass matrix notation is $\mathbf{M} = \mathbf{T}^T \mathbf{M}_{rn} \mathbf{T}$, the global stiffness matrix is $\mathbf{K} = \mathbf{T}^T \mathbf{K}_{rn} \mathbf{T}$ and the global force matrix is $\mathbf{Q} = \mathbf{T}^T \mathbf{Q}_r$. The global modified electromechanical coupling indicates $\boldsymbol{\Theta}^T \mathbf{T} = \mathcal{G}(\mathbf{P}_{sn1} + \mathbf{P}_{sn2})$ and the global capacitance matrix gives $\mathbf{C}_p = \mathcal{G}(\mathbf{P}_{Ds1} + \mathbf{P}_{Ds2}) \mathcal{G}^T$. Each of the operational matrices can be seen in appendix C. Therefore, equation (6.41) can be rewritten as,

$$\begin{aligned} \begin{pmatrix} \mathbf{M} \\ (n_m \times n_m) \end{pmatrix} \ddot{\mathbf{z}} + \begin{pmatrix} \mathbf{C} \\ (n_m \times n_m) \end{pmatrix} \dot{\mathbf{z}} + \begin{pmatrix} \mathbf{K} \\ (n_m \times n_m) \end{pmatrix} \mathbf{z} + \begin{pmatrix} \mathbf{T}^T \\ (n_m \times 1) \end{pmatrix} \boldsymbol{\Theta} v = - \begin{pmatrix} \mathbf{Q} \\ (n_m \times 1) \end{pmatrix} \ddot{\mathbf{w}}_{base}, \\ \begin{pmatrix} \boldsymbol{\Theta}^T \\ (1 \times n_m) \end{pmatrix} \dot{\mathbf{z}} - \frac{v}{R_{load}} + \begin{pmatrix} \mathbf{C}_p \\ (1 \times 1) \end{pmatrix} \dot{v} = 0. \end{aligned} \quad (6.42)$$

The piezoelectric unimorph beam dynamic equations given by equation (6.42) can be solved for different angles of rotation by assuming linear harmonic base input acceleration motion. Therefore, the solutions of the mechanical displacement can be formulated as $\mathbf{u} = \mathbf{a} e^{i\omega t}$ and the electrical voltage as $v = b e^{i\omega t}$, where \mathbf{a} is the amplitude of the base translation, b is the amplitude of the voltage across the resistive load and ω is the driving frequency. The assumed solution can be substituted into equation (6.42) to formulate the electromechanical frequency response functions, (FRFs). The multi-mode voltage FRFs can be formulated after simplifying the derivation to give,

$$\frac{v(t)}{-\omega^2 w_{base} e^{i\omega t}} = \left[i\omega \underset{(1 \times 1)}{C_p} + \underset{(1 \times 1)}{R_l} - i\omega \underset{(1 \times n_m)}{\boldsymbol{\Theta}^T} \mathbf{T} \left(\underset{(n_m \times n_m)}{\mathbf{K}} - \underset{(n_m \times n_m)}{\omega^2 \mathbf{M}} + \underset{(n_m \times n_m)}{i\omega \mathbf{C}} \right)^{-1} \mathbf{T}^T \underset{(n_m \times 1)}{\boldsymbol{\Theta}} \right]^{-1} \times i\omega \underset{(1 \times n_m)}{\mathbf{T}^T} \underset{(1 \times n_m)}{\boldsymbol{\Theta}^T} \left[\underset{(n_m \times n_m)}{\mathbf{K}} - \underset{(n_m \times n_m)}{\omega^2 \mathbf{M}} + \underset{(n_m \times n_m)}{\mathbf{C} i\omega} \right]^{-1} \underset{(n_m \times 1)}{\mathbf{Q}} \quad (6.43)$$

The multi-mode FRFs of electric current can be formulated in terms of Kirchhoff's Current Law where the current is the fractional voltage over the load resistance value or $i = v/R_{load}$. The current frequency response function can be presented as,

$$\frac{i(t)}{-\omega^2 w_{base} e^{i\omega t}} = \frac{1}{\underset{(1 \times 1)}{R_{load}}} \left\{ \left[i\omega \underset{(1 \times 1)}{C_p} + \underset{(1 \times 1)}{R_l} - i\omega \underset{(1 \times n_m)}{\boldsymbol{\Theta}^T} \mathbf{T} \left(\underset{(n_m \times n_m)}{\mathbf{K}} - \underset{(n_m \times n_m)}{\omega^2 \mathbf{M}} + \underset{(n_m \times n_m)}{i\omega \mathbf{C}} \right)^{-1} \mathbf{T}^T \underset{(n_m \times 1)}{\boldsymbol{\Theta}} \right]^{-1} \right\} \times i\omega \underset{(1 \times n_m)}{\boldsymbol{\Theta}^T} \mathbf{T} \left[\underset{(n_m \times n_m)}{\mathbf{K}} - \underset{(n_m \times n_m)}{\omega^2 \mathbf{M}} + \underset{(n_m \times n_m)}{\mathbf{C} i\omega} \right]^{-1} \underset{(n_m \times 1)}{\mathbf{Q}} \quad (6.44)$$

The multi-mode FRFs of power output can be formulated by using the correlation of the voltage squared divided by the load resistance value or $P = v^2/R_{load}$. The frequency response function can then be written as,

$$\frac{P(t)}{\left(-\omega^2 w_{base} e^{i\omega t}\right)^2} = \frac{1}{R_{load}} \left\{ \begin{array}{l} \left[\begin{array}{l} i\omega C_p + R_l - i\omega \boldsymbol{\Theta}^T \mathbf{T} \left(\begin{array}{l} \mathbf{K} \\ (n_m \times n_m) \end{array} \right) - \omega^2 \mathbf{M} + i\omega \mathbf{C} \end{array} \right]^{-1} \mathbf{T}^T \boldsymbol{\Theta} \\ \times i\omega \boldsymbol{\Theta}^T \mathbf{T} \left[\begin{array}{l} \mathbf{K} \\ (n_m \times n_m) \end{array} \right]^{-1} \mathbf{Q} \end{array} \right\}^2. \quad (6.45)$$

6.2.1 Case Study without Tip Mass

The schematic diagram of the piezoelectric unimorph beam is shown in figure 6.2 without tip mass. Figure 6.2a presents a construction of the segmented piezoelectric system under parallel connection where 6.2b shows the discretised piezoelectric element modelled using different angles of orientation.

Two segments of piezoelectric material are glued onto the substructure. Practically, the piezoelectric segment 1 ($L_p 1$) and segment 2 ($L_p 2$) are connected in parallel using electrical cables. Since both piezoelectric segments are connected as shown in figure 6.2a, the two wires are also connected to the load resistance. The physical dimensions of the piezoelectric segments are set to be the same size with length 20 mm, width 6 mm and thickness 0.127 mm. In addition, the dimensions of the substructure have length 50 mm, width 6 mm and thickness 0.5 mm where the substructure is bent in the mid-point at a distance of 25 mm. The angle of orientations of the segmented piezoelectric unimorph beam are 0° , 10° , 20° , 30° , 40° , 50° , 60° , 70° , 80° and 90° . The simulation test of the piezoelectric unimorph was run using MATLAB software. Excitation of the structure uses base support motion in the transverse direction as shown in figure 6.2.

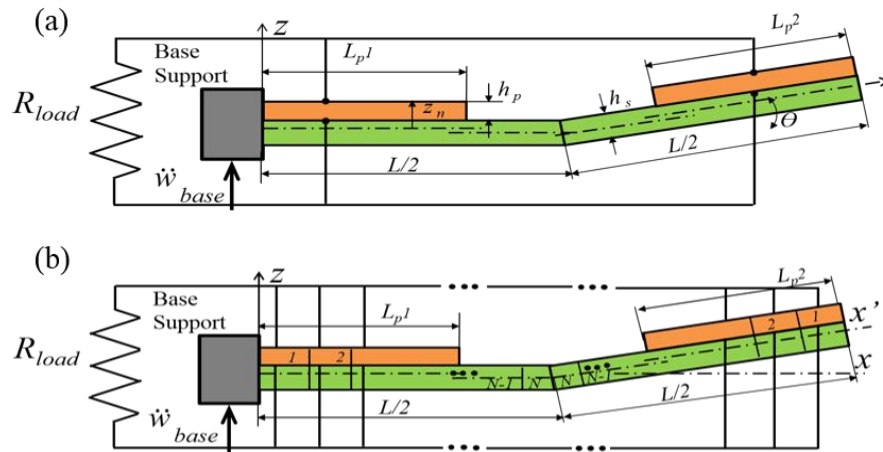


Figure 6.2 Bent segmented piezoelectric unimorph beam.

6.2.2 Displacement Frequency Response with $\theta = 0^\circ$ Angle of orientation

Figure 6.3 shows the simulated tip displacement response of the segmented piezoelectric system under base acceleration of 1 m/s^2 . In this simulation, the segmented piezoelectric element was situated on the horizontal axis or 0° angle of orientation with load resistances ranging from 100Ω to $1 \text{ M}\Omega$.

The resonance frequency response at the short and open circuit situations shifts around 1.7 Hz at the first mode as seen on the enlarged figure. Based on figure 6.3, the first mode of short and open circuit resonance frequencies gives 125.8 Hz and 127.5 Hz , respectively. The tip displacement at the short circuit resonance condition gives 0.136 mm/ms^{-2} whereas at the open circuit resonance condition is 0.118 mm/ms^{-2} .

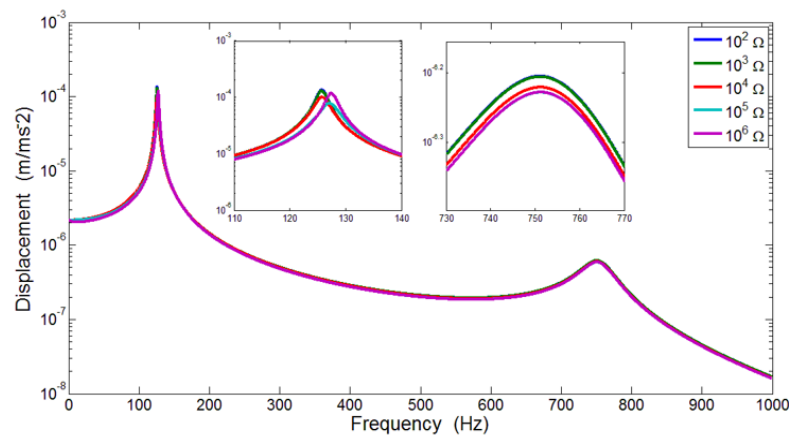


Figure 6.3 Segmented piezoelectric beam tip displacement frequency response of with 0° angle of orientation.

6.2.3 Voltage, Current and Power Output Frequency Response with $\theta = 0^\circ$ Angle of orientation

The frequency response functions of segmented piezoelectric unimorph beam using equations (6.60)-(6.62) can be used for 0° angle of orientation with the load resistance ranging from 100Ω to $1 \text{ M}\Omega$. The resulting voltage, current and power output frequency response results are presented in figures 6.4, 6.5 and 6.6, respectively.

Results shown in figure 6.4 indicate the voltage magnitude increases as the load resistance increases. The short circuit resonance for the first mode occurs at 125.8 Hz and further increases to 127.5 Hz for open circuit resistance showing similar previous tip displacement result. The voltage magnitudes at short and open circuit resistance values increase from 4.61 mV/ms^{-2} to 1.98 V/ms^{-2} . The short and open circuit resonances for the second mode occur at 751.9 Hz and 751.3 Hz , respectively. The voltage magnitude at the second resonance gives $94.25 \mu\text{V/ms}^{-2}$ at short circuit load resistance and increases to 7.39 mV/ms^{-2} at open circuit load resistance.

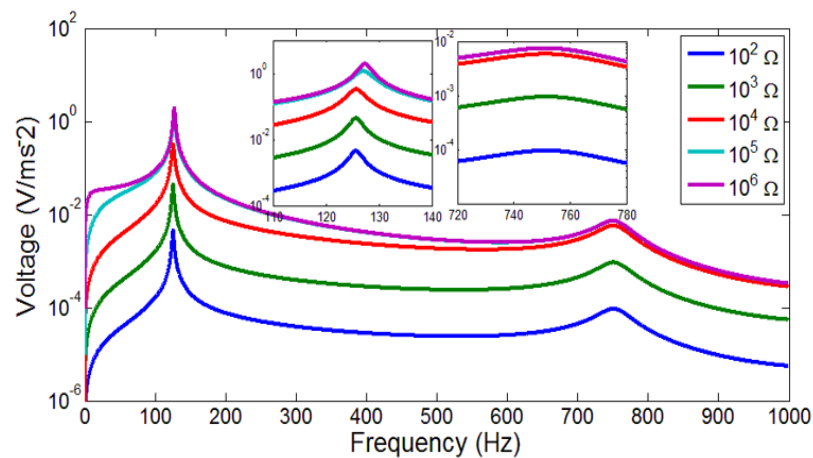


Figure 6.4 Segmented piezoelectric voltage frequency response of 0° angle of orientation.

Figure 6.5 shows current frequency response for the first mode having short and open circuit resonances of 125.8 Hz and 127.5 Hz , respectively. As given from the previous result, the monotonic current magnitude behaves in the opposite direction with the voltage. The current magnitude value at short circuit resistance gives $46.1 \mu\text{A/ms}^{-2}$ and reduces to $1.98 \mu\text{A/ms}^{-2}$ at the open circuit resistance. The short circuit resonance for the second mode occurs at 751.9 Hz with current magnitude of $94.25 \mu\text{A/ms}^{-2}$, while

the open circuit resistance resonance occurs at 751.3 Hz with current magnitude of 7.39 nA/ms⁻².

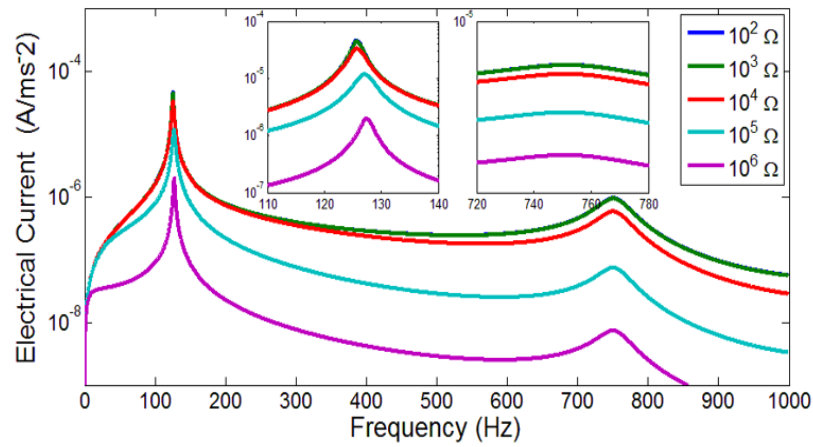


Figure 6.5 Segmented piezoelectric current frequency response with 0° angle of orientation.

The power output frequency response is given in figure 6.6. The resonance frequency at short circuit resistance again occurs at 125.8 Hz with magnitude of 0.212 $\mu\text{W}/\text{m}^2\text{s}^{-4}$. In addition, the open circuit resistance occurs at 127.5 Hz with magnitude of 3.92 $\mu\text{W}/\text{m}^2\text{s}^{-4}$. Figure 6.6a also shows the zoomed appearance of the shifting resonance frequency with the load resistance ranging from 100 Ω to 1 M Ω . The second mode of the short circuit resonance again occurs at 751.9 Hz while the open circuit resonance gives 751.3 Hz. The short circuit power output magnitude was 88.82 nW/m²s⁻⁴ and the open circuit power magnitude was 54.56 nW/m²s⁻⁴ as shown in the enlarged section of figure 6.6b.

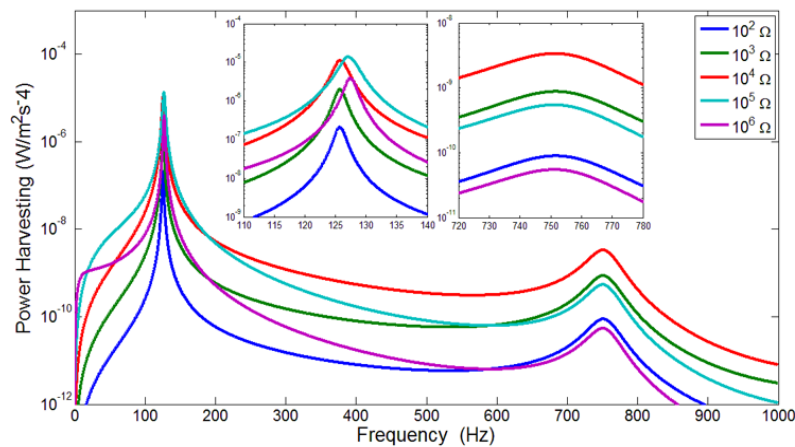


Figure 6.6 Segmented piezoelectric power output frequency response with 0° angle of orientation.

6.2.4 Comparison of Voltage and Current Response as a Function of Angle of Orientation

Detailed voltage and current frequency responses with different angles of orientation are shown in figure 6.7 and 6.8. The segmented piezoelectric system was simulated as the angle of orientation changed from 0° to 90° with base input acceleration of 1 ms^{-2} . The voltage and current dynamic responses presented here use the resistance of 100Ω . It was found that most of the responses for different angles of orientation give a similar trend response with other resistances but show the expected change of resonance frequency and magnitude. Equation (6.43) and (6.44) were used to find the voltage and current frequency response of the segmented piezoelectric unimorph beam with different angles of orientation.

Figure 6.7a presents the voltage frequency response for the first and second modes. For the first mode, the resonance frequency increases as the angle of orientation increases. However, voltage magnitude reduces as the angle of orientation changes. This phenomenon can be caused by the effective reduction in transverse length of the segmented piezoelectric unimorph beam using different angles.

The opposite frequency response behavior appears at the second mode, where the resonance frequency reduces with increasing angle of orientation, followed by reducing voltage magnitude. The enlarged view of figure 6.7b shows that the resonance frequency shifts with changes of orientation angles. The results of the unimorph beam for the first mode resonance frequencies using angles from 0° to 90° can be summarised in table 6.1 below.

Comparison of the second mode frequency response is given in the enlarged figure 6.7c with load resistance of 100Ω . As previously mentioned, the opposite resonance frequency behavior occurs for the short circuit resistance as the orientation angle increases from 0° to 90° . Increasing the angle of orientation for the second mode appears to significantly reduce the peak resonance. For increasing angles of orientation from 60° to 90° , the second mode reduces in visibility. The electrical voltage frequency response for the second mode as a function of angle of orientation can be summarised in table 6.1.

Table 6.1 Comparison of first two modes electrical voltage responses with resistance 100 Ω.

Angle (°)	Frequency (Hz)		Voltage (V/ms ⁻²)	
	First Mode (Hz)	Second Mode (Hz)	First Mode (mV/ms ⁻²)	Second Mode (μV/ms ⁻²)
0°	125.8	751.9	4.61	94.25
10°	126.2	739.4	4.52	88.42
20°	127.5	704.9	4.39	72.23
30°	129.6	656.4	4.24	52.53
40°	132.8	603.0	4.06	36.06
50°	137.0	550.9	3.85	26.32
60°	142.4	N/A	3.61	N/A
70°	149.2	N/A	3.36	N/A
80°	157.7	N/A	3.08	N/A
90°	168.1	N/A	2.79	N/A

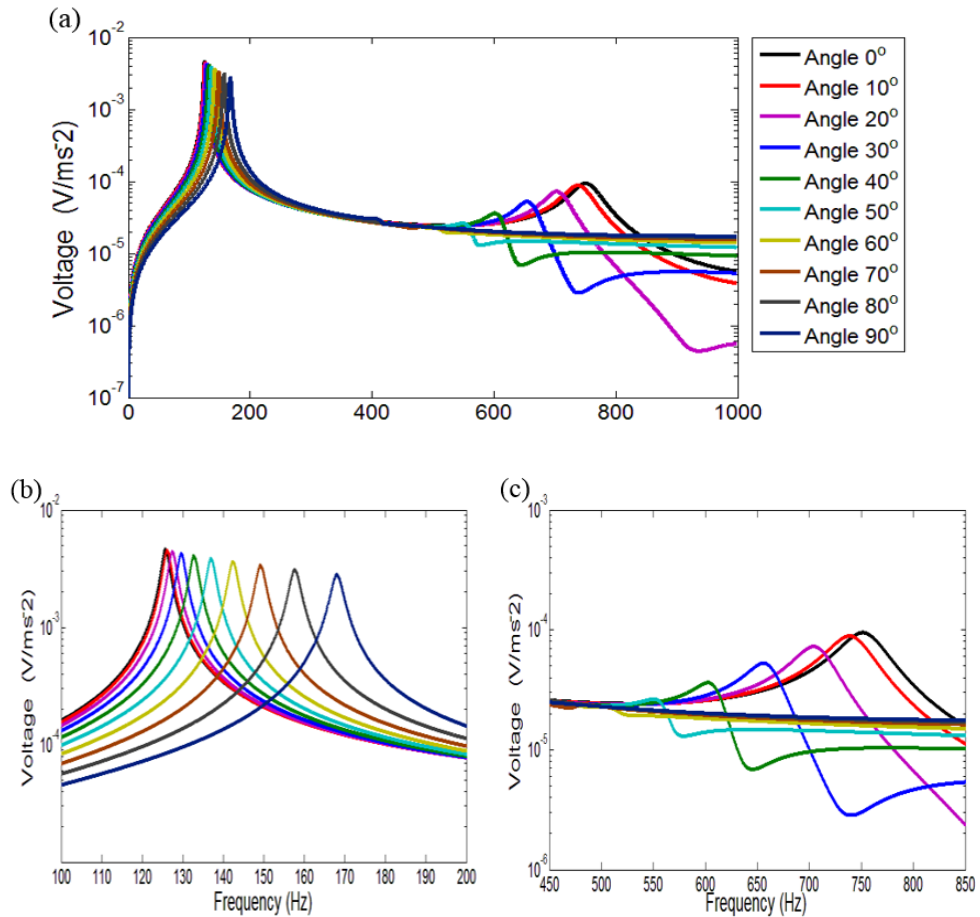


Figure 6.7 (a) Segmented FRFs voltage comparison for orientation angles from 0° to 90° (b) The first mode (c) The second mode.

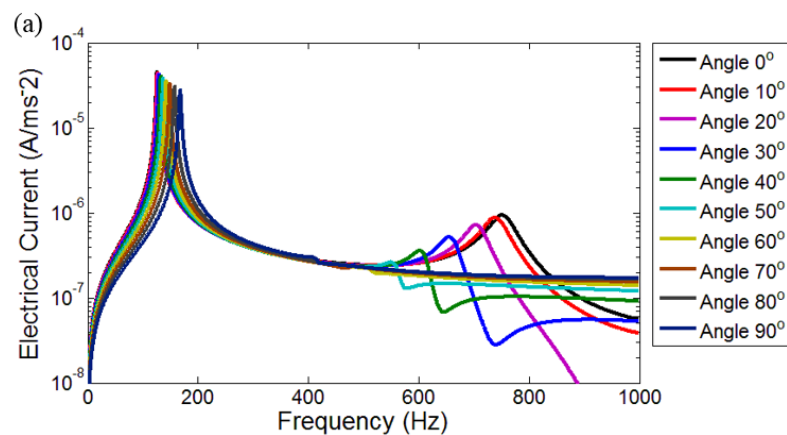
The previous investigations provided in chapters 3, 4 and 5 showed that the electrical current magnitude behaved opposite to the electrical voltage magnitude as the load resistance increased but both had similar monotonic appearance. Here, the monotonic

electrical voltage response also increases with increasing load resistance whereas the electrical current reduces from the short to open circuit resistances.

In case of different angles of orientation, figure 6.8 presents the trend of dynamic behavior of the current frequency response with load resistance of 100 Ω . The enlarged figures 6.8a and 6.8b show a clear peak in the resonance frequencies at the first and second modes. Similar to the trend presented by the dynamic voltage response, the first mode current resonance frequency increases with decreasing magnitude of electrical current with increasing angle of orientation. However, the second mode shows a decreasing resonance frequency followed by decreasing magnitudes of electrical current. Figure 6.8 shows the peaks of electrical current responses for the first and second modes. Table 6.2 presents the summary of the electrical current responses for the first and second modes.

Table 6.2 Comparison of first two modes electrical current responses with resistance 100 Ω .

Angle ($^{\circ}$)	Frequency		Current	
	First Mode (Hz)	Second Mode (Hz)	First Mode ($\mu\text{A}/\text{ms}^{-2}$)	Second Mode ($\mu\text{A}/\text{ms}^{-2}$)
0 $^{\circ}$	125.8	751.9	46.08	942.5
10 $^{\circ}$	126.2	739.4	45.18	884.2
20 $^{\circ}$	127.5	704.9	43.96	722.3
30 $^{\circ}$	129.6	656.4	42.42	525.3
40 $^{\circ}$	132.8	603.0	40.60	360.6
50 $^{\circ}$	137.0	550.9	38.50	263.2
60 $^{\circ}$	142.4	N/A	36.14	N/A
70 $^{\circ}$	149.2	N/A	33.57	N/A
80 $^{\circ}$	157.7	N/A	30.83	N/A
90 $^{\circ}$	168.1	N/A	27.98	N/A



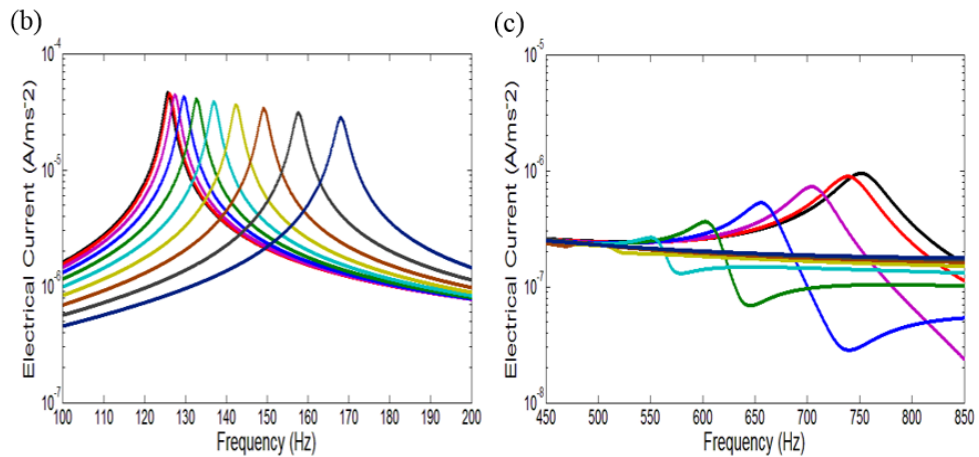


Figure 6.8 (a) Segmented current FRFs comparison as a function of orientation angle (b) The first mode (c) The second mode.

6.2.5 Power Output Frequency Response Comparison with Varying Orientation Angle

This section shows the resulting power harvesting dynamic response under base excitation for different angles of orientation. The load resistance values of $100\ \Omega$, $1\ \text{k}\Omega$, $10\ \text{k}\Omega$, $100\ \text{k}\Omega$ and $1\ \text{M}\Omega$ were used for the analysis. The resulting power output response for load resistance of $100\ \Omega$ are given in figures 6.9 as a function of varying angle of orientation. It should be noted that curves of power frequency responses with load impedances from $1\ \text{k}\Omega$ - $1\ \text{M}\Omega$ appear to show similar behaviors with the first and second mode resonances. Therefore, the power frequency responses are summarized in tables 6.3-6.7 for each load resistance of $100\ \Omega$ - $1\ \text{M}\Omega$. The electrical power output frequency responses for the first and second mode using load resistance $100\ \Omega$ are expressed using table 6.3 based on figure 6.9. Again, the appearances of resonance frequencies have similar behavior with the electrical voltage and current frequency responses.

Table 6.3 Comparison of modes one and two electrical power responses with resistance 100Ω .

Angle ($^{\circ}$)	Frequency		Power	
	First Mode (Hz)	Second Mode (Hz)	First Mode ($\text{nW/m}^2\text{s}^{-4}$)	Second Mode ($\text{pW/m}^2\text{s}^{-4}$)
0°	125.8	751.9	212.4	88.83
10°	126.2	739.2	204.1	78.18
20°	127.5	704.6	193.2	52.18
30°	129.7	656.4	179.9	27.60
40°	132.8	603.0	164.8	12.99
50°	137.0	550.9	148.2	6.929
60°	142.4	500.4	130.6	5.088
70°	149.2	483.7	112.7	5.666
80°	157.7	449.3	95.02	6.613
90°	168.1	405.4	78.27	9.074

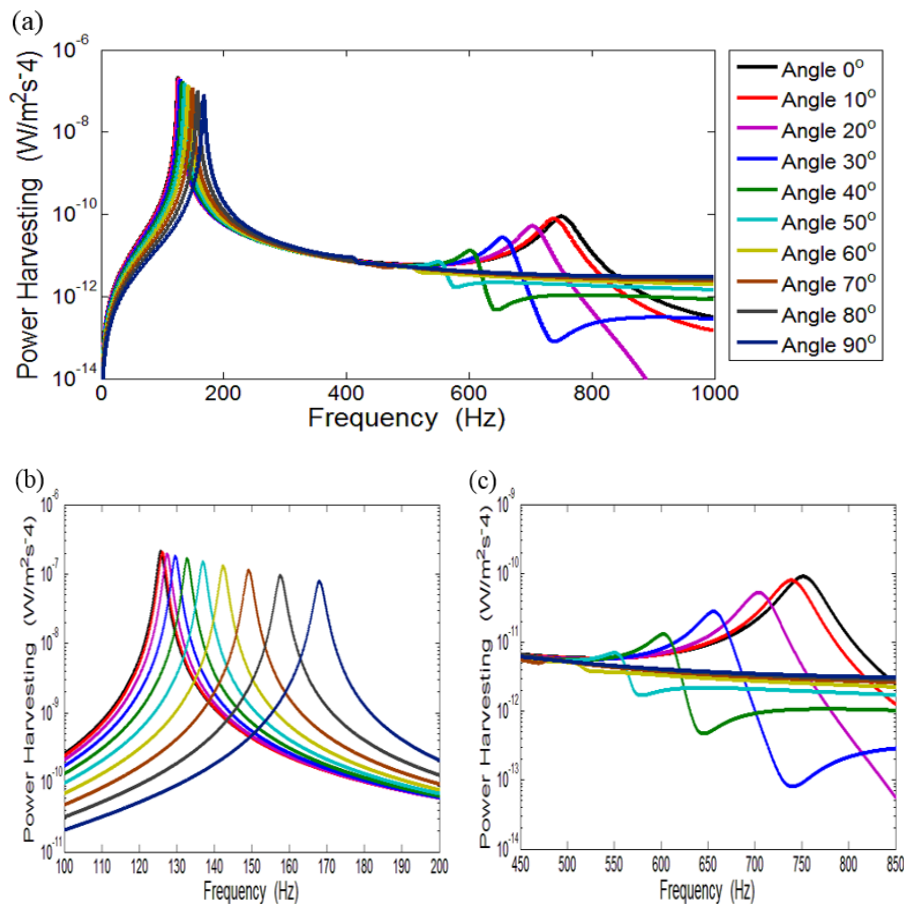


Figure 6.9 (a) Segmented power output FRFs comparison as a function of orientation angle (b) The first mode (c) Second mode.

Tables 6.4-6.7 show the power output response with load resistance. Figure 6.10 shows the power output frequency responses for each resistance where they are summarised in tables 6.4-6.7.

Table 6.4 Comparison of modes one and two electrical power responses with resistance 1 k Ω .

Angle (°)	Frequency		Power	
	First Mode (Hz)	Second Mode (Hz)	First Mode (nW/m ² s ⁻⁴)	Second Mode (pW/m ² s ⁻⁴)
0°	125.8	751.9	1989	872.3
10°	126.2	739.2	1911	768.4
20°	127.5	704.6	1809	513.7
30°	129.6	656.4	1683	272.4
40°	132.8	603.0	1540	128.6
50°	137.0	550.9	1382	68.67
60°	142.4	500.4	1216	50.49
70°	149.2	483.7	1047	56.27
80°	157.7	449.2	880.4	65.73
90°	168.1	405.4	723.1	90.29

Table 6.5 Comparison of modes one and two electrical power responses with resistance 10 k Ω .

Angle (°)	Frequency		Power	
	First Mode (Hz)	Second Mode (Hz)	First Mode (μ W/m ² s ⁻⁴)	Second Mode (pW/m ² s ⁻⁴)
0°	125.9	751.9	11.19	3349
10°	126.3	738.7	10.74	3013
20°	127.6	704.3	10.12	2134
30°	129.7	656.1	9.357	1226
40°	132.9	602.7	8.479	633.5
50°	137.1	550.4	7.523	369.4
60°	142.5	500.4	6.523	295.5
70°	149.4	482.9	5.519	338.8
80°	157.8	448.7	4.552	418.7
90°	168.3	405.4	3.658	616.7

Table 6.6 Comparison of modes one and two electrical power responses with resistance 100 k Ω .

Angle (°)	Frequency		Power	
	First Mode (Hz)	Second Mode (Hz)	First Mode (μ W/m ² s ⁻⁴)	Second Mode (pW/m ² s ⁻⁴)
0°	127.2	751.3	13.86	541.7
10°	127.6	738.7	13.28	493.1
20°	128.9	704.7	12.45	362.0
30°	131.2	655.9	11.41	220.6
40°	134.3	602.4	10.22	123.1
50°	138.6	549.7	8.918	786.7
60°	144.1	500.4	7.576	69.84
70°	150.9	482.0	6.252	83.54
80°	159.6	447.7	5.001	113.0
90°	170.1	405.4	3.872	189.3

Table 6.7 Comparison of modes one and two electrical power responses with resistance
1 M Ω .

Angle ($^{\circ}$)	Frequency		Power	
	First Mode (Hz)	Second Mode (Hz)	First Mode ($\mu\text{W}/\text{m}^2\text{s}^{-4}$)	Second Mode ($\text{pW}/\text{m}^2\text{s}^{-4}$)
0 $^{\circ}$	127.5	751.3	3.196	54.57
10 $^{\circ}$	127.9	738.7	3.741	49.68
20 $^{\circ}$	129.2	704.1	3.477	36.49
30 $^{\circ}$	131.4	655.9	3.141	22.25
40 $^{\circ}$	134.6	602.4	2.754	12.44
50 $^{\circ}$	138.9	549.7	2.339	7.960
60 $^{\circ}$	144.4	500.4	1.921	7.082
70 $^{\circ}$	151.3	482.0	1.522	8.482
80 $^{\circ}$	159.8	447.7	1.161	11.50
90 $^{\circ}$	170.4	405.4	0.8502	19.36

The resonance frequency as a function of angle of orientation given in figure 6.10 using short to open circuit load resistances shows the major trend of the first mode.

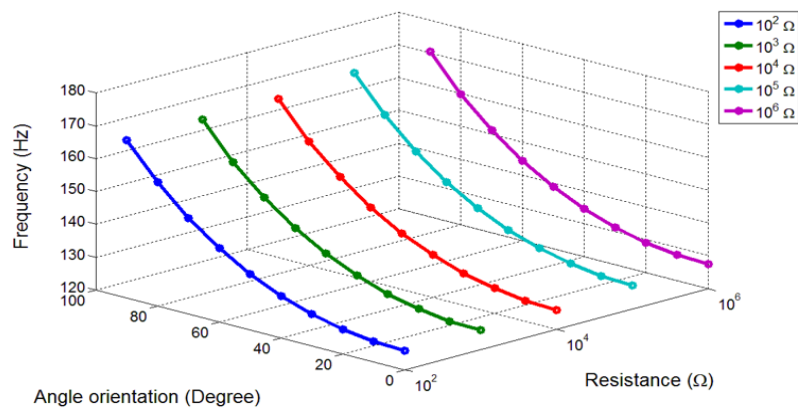


Figure 6.10 First mode FRF variation of the segmented piezoelectric system as a function of orientation angle from 0 $^{\circ}$ to 90 $^{\circ}$ with load resistances.

In addition, the patterns of power amplitude behavior with respect to variable load resistance from short to open circuit given in figure 6.11 appears to give similar behavior when the angles of orientation of the unimorph beam are increased from 0 $^{\circ}$ to 90 $^{\circ}$. Here, the patterns of power amplitude from short to open circuit load resistances reduce with increasing angle of the segmented unimorph beam from 0 $^{\circ}$ to 90 $^{\circ}$.

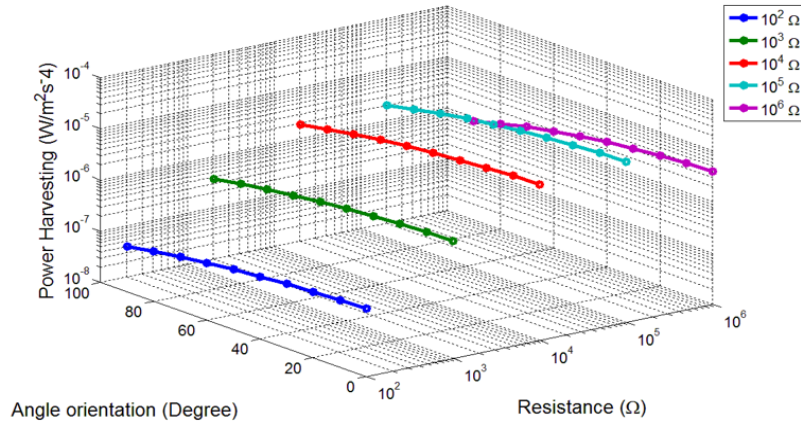


Figure 6.11 First mode comparison of power output FRFs of the segmented piezoelectric for varying angle of orientation from 0° to 90° with load resistance.

Figure 6.12 shows the magnitude of electrical power output with respect to load resistances when the segmented piezoelectric unimorph beam is excited under short and open circuit resonance frequencies for the first mode. It can be seen from the separated result of the electrical power output with the load resistance under short and open circuits as shown in figures 6.12, that the maximum electrical power magnitude reduces with the changes of the load resistance. The downward pointing arrows direction illustrate the changes of the maximum electrical power with short and open circuit load resistances when the angle of orientations of segmented piezoelectric unimorph increase.

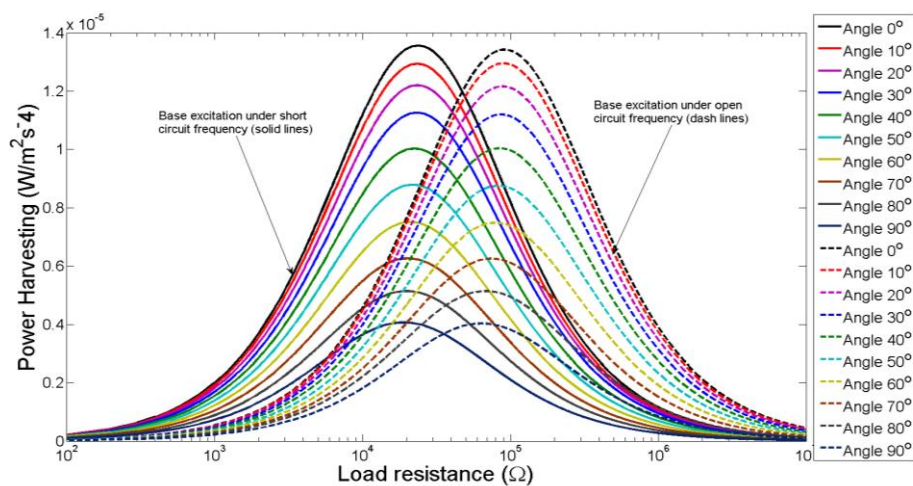


Figure 6.12 Power output at short and open circuit conditions for varying angles of orientation.

As shown in figure 6.12, when the segmented unimorph beam was excited under the first mode resonance condition, the power amplitudes versus load resistance results are presented in tables 6.8 and 6.9.

Table 6.8 Maximum power output and resistances under base excitation for short and open circuit resonances conditions.

Angle (°)	Short circuit resonance		Open circuit resonance	
	Resistances (kΩ)	Power (μW/m ² s ⁻⁴)	Resistances (kΩ)	Power (μW/m ² s ⁻⁴)
0°	23.8	13.56	91.4	13.42
10°	23.5	12.93	89.9	12.96
20°	23.4	12.19	88.9	12.16
30°	23.4	11.26	86.8	11.20
40°	22.5	10.03	84.9	10.04
50°	21.8	8.787	82.7	8.753
60°	21.1	7.507	79.2	7.485
70°	20.3	6.261	74.7	6.253
80°	19.9	5.140	68.2	5.141
90°	19.1	4.064	63.8	4.031

Table 6.9 Maximum power output and crossover resistances under base excitation for the first mode.

Angle (°)	Crossover points	
	Resistances (kΩ)	Power (μW/m ² s ⁻⁴)
0°	47.39	11.98
10°	45.85	11.50
20°	45.91	10.85
30°	45.45	10.03
40°	43.61	8.937
50°	42.80	7.805
60°	41.09	6.678
70°	39.06	5.595
80°	36.83	4.563
90°	35.36	3.673

The schematic representation of the electrical power outputs versus modifying angles of orientation for the segmented piezoelectric unimorph beam are given in figure 6.13 based on the results in tables 6.8 and 6.9.

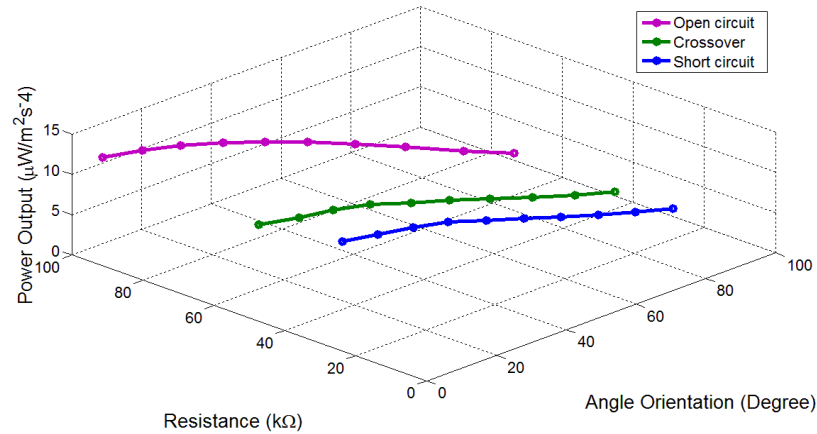


Figure 6.13 Power output of the segmented piezoelectric system with different angle of orientation at the first mode resonance.

Therefore the electrical power as a function of angles orientation for three maximum points under short and open circuit resonances shows that all points give similar behavior. First, it can be seen that the power amplitudes with the load resistances at short and open circuit resonances reduce with angle of orientations increases.

6.3 Comparison between Axial Deformation and Non-Axial Deformation

This section discusses the comparative study when the axial deformation and the axial electromechanical coupling are ignored from the piezoelectric structure using different orientation. The comparative study is based on the electrical voltage and power output frequency responses at short and open circuit resistances. Figure 6.14 shows the comparison study for the electrical voltage frequency response of the piezoelectric unimorph with and without axial deformation and electromechanical coupling using 0° orientation. Figure 6.14 shows that the contribution of the axial deformation and the axial electromechanical coupling gives very similar value of voltage magnitude at short circuit load resistance where the resonant frequency is shown to be at 125.8 Hz. The voltage magnitude with axial deformation at open circuit load resistance shows 2 % less magnitude than the voltage response without axial contribution with a resonance frequency of 127.5 Hz. Based on figure 6.14, the electrical voltage magnitude for axial contribution gives 5.341 mV/ms^{-2} for short circuit and 2.292 V/ms^{-2} for open circuit resistance. Meanwhile, the electrical voltage without axial

contribution gives 5.341 mV/ms^{-2} for short circuit resistance and shifts to 2.338 V/ms^{-2} for open circuit resistance.

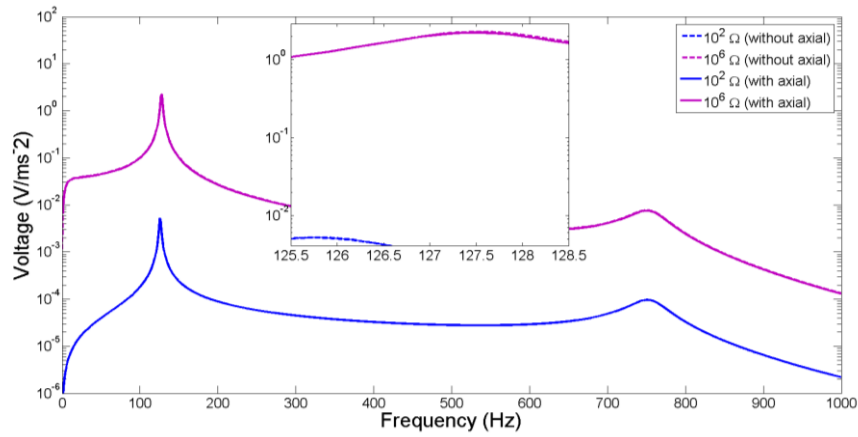


Figure 6.14 Influence of axial deformation and axial electromechanical coupling with 0° angle of orientation for electrical voltage.

The power output frequency response for 0° angle of orientation is given in figure 6.15. Again, the power shows a similar behavior with the previous voltage response. Here, the magnitude of power output response under axial contribution presents the same behavior as previous voltage response with similar frequency at short and open circuit load resistances. The electrical power output with axial contribution gives $285.3 \text{ nW/m}^2\text{s}^{-4}$ for short circuit resistance and shifts to $5.251 \text{ } \mu\text{W/m}^2\text{s}^{-4}$ for open circuit resistance. Meanwhile, the electrical power output without axial contribution gives $285.3 \text{ nW/m}^2\text{s}^{-4}$ for short circuit and shifts to $5.465 \text{ } \mu\text{W/m}^2\text{s}^{-4}$ for open circuit resistance.

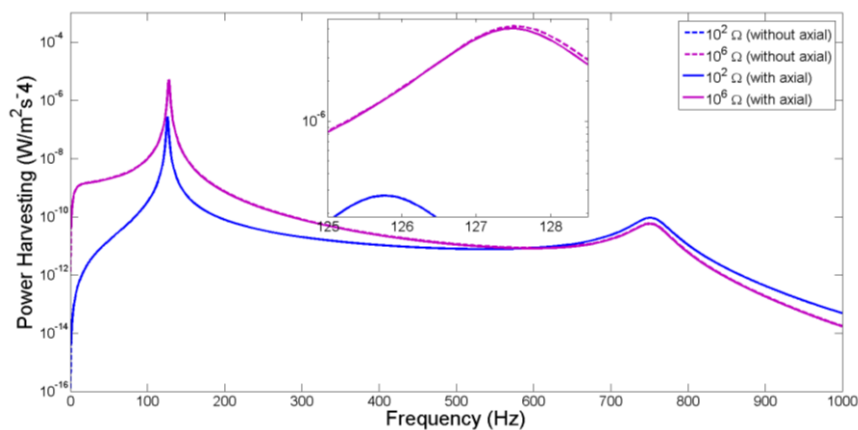


Figure 6.15 Influence of axial deformation and axial electromechanical coupling with 0° angle of orientation for power harvesting.

Another comparison study of the axial contribution is given in figure 6.16 with 45° angle. Here, the study shows that the contribution of changing angle of orientation affects the frequency value for short and open circuit resistances, it seems that the resonance frequency at short and open circuits using axial contribution shows lower value than without axial contribution. The range of resonant frequencies for axial contribution gives 134.7 Hz for short circuit and shifts to 136.6 Hz for open circuit resistances whereas without axial contribution it results in 143.1 Hz for short circuit and 145.1 Hz for open circuit resistance. In addition, the magnitude of electrical voltage under axial consideration was shown to be lower than the electrical voltage without axial consideration. The axial contribution shows the voltage magnitude of 4.795 mV/ms^{-2} for short circuit and 1.938 V/ms^{-2} for open circuit resistances whereas without axial contribution the electrical voltage was 5.28 mV/ms^{-2} for short circuit and 2.06 V/ms^{-2} for open circuit resistances.

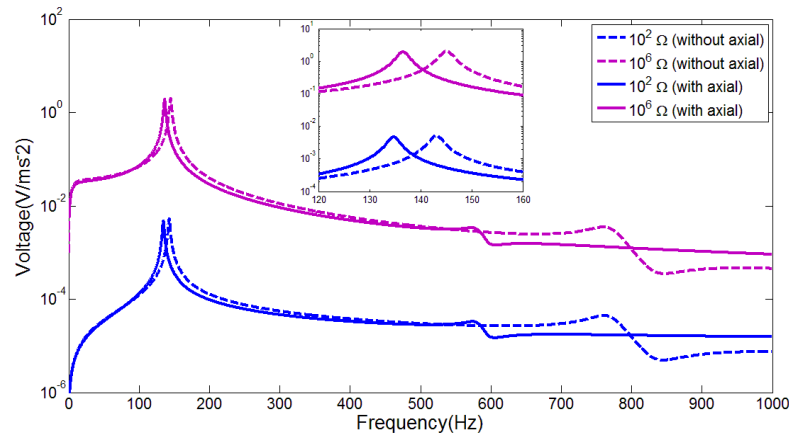


Figure 6.16 Influence of axial deformation and axial electromechanical coupling with 45° angle of orientation for electrical voltage.

The power output frequency response for 45° angle of orientation is given by figure 6.17. Again, the resonance frequency with axial contribution have shown lower value than without axial contribution for the short and open circuit resistances. This phenomenon is also followed by less amount of power output for axial contribution. Here, the electrical power output for axial contribution gives $229.9 \text{ nW/m}^2\text{s}^{-4}$ for short circuit resistance and shifts to $3.755 \text{ } \mu\text{W/m}^2\text{s}^{-4}$ for open circuit resistance whereas the power output without axial contribution gives $278.8 \text{ nW/m}^2\text{s}^{-4}$ for short circuit and shifts to $4.244 \text{ } \mu\text{W/m}^2\text{s}^{-4}$ for open circuit resistance. Therefore, it seems that the contribution of axial deformation and axial electromechanical coupling show very

important aspects to be considered when the piezoelectric configuration has different orientation.

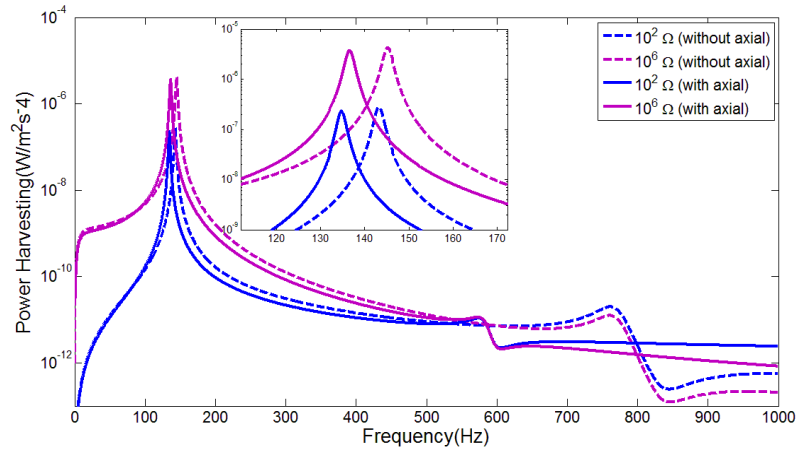


Figure 6.17 Influence of axial deformation and axial electromechanical coupling with 45° angle of orientation for electrical power.

6.4 Comparison Study Considering the Shifting Neutral Axis

This section presents the comparison study of using the generalized neutral axis and shifting neutral axis of the piezoelectric unimorph beam with different orientation. Here, the generalized neutral axis means that the line of the neutral axis remains at the same location along the length of piezoelectric unimorph, even when the piezoelectric segment is removed while the shifting neutral axis means that the neutral axis line is adjusted when the piezoelectric segment is removed. The configuration of the generalized neutral axis and the shifting neutral axis can be seen in figure 6.18.

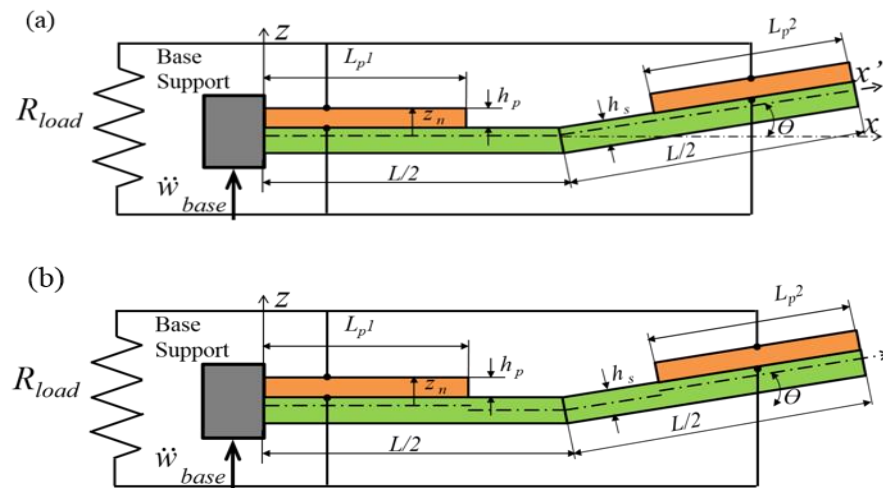


Figure 6.18 (a) Generalized neutral axis (b) Shifting neutral axis.

The comparison study of generalized neutral axis and shifting neutral axis is presented with 0° and 45° orientations. The study is very useful to see the behavior of the resonant frequency and magnitude with respect to the changing location of neutral axis since this frequently was ignored for some of the previous MEMS power harvesting study. The reason for ignoring shifting neutral axis is possibly due to the small distance change of the shifting axis. The comparison study for 0° angle of orientation is given in figure 6.19 for electrical voltage frequency response. Based on the response trend, it seems that the magnitude of electrical voltage for the generalized neutral axis and shifting neutral axis has shown quite similar peaks whereas the resonance frequency for shifting neutral axis shows lower value than for the generalized neutral axis. Based on figure 6.19, the resonance frequency at short circuit resistance shifted from 126.6 Hz to 125.8 Hz using the generalized neutral axis and the shifting neutral axis, respectively. In addition, with the open circuit resistance, the resonance frequency of 128.3 Hz for the generalized neutral axis shifts to 127.5 Hz for the shifting neutral axis.

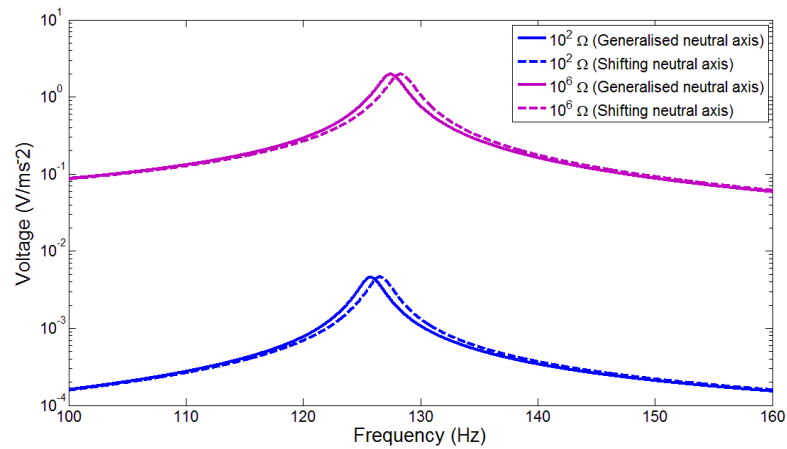


Figure 6.19 Electrical voltage frequency response comparison for generalized neutral axis and shifting neutral axis for 0° angle of orientation.

Figure 6.20 shows the power output for the generalized neutral axis and shifting neutral axis. The resulting power output also has a similar power magnitude whereas the resonance frequency for shifting neutral axis is lower in value than for the generalized neutral axis.

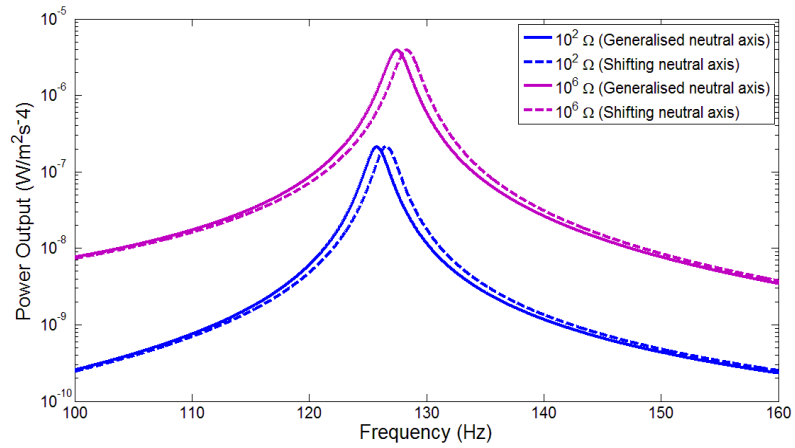


Figure 6.20 Electrical power output frequency response comparison for generalized neutral axis and shifting neutral axis 0° angle of orientation.

Figure 6.21 and 6.22 show the comparison study of electrical voltage and power output for the generalized neutral axis and shifting neutral axis with 45° angle of orientation. Based on the result from the electrical voltage frequency response for the piezoelectric unimorph for 45° orientation, the electrical magnitudes show very similar values with the short and open circuit resistances. Again, the resonance frequency for the short and open circuit resistances using the generalized neutral axis show higher value than the shifting neutral axis. Here, the resonance for the generalized neutral axis case gives 135.6 Hz and shifts to 134.8 Hz for the shifting neutral axis at short circuit resistance. Meanwhile, the open circuit resistance gives the resonance of 137.5 Hz for the generalized neutral axis and reduces to 136.6 Hz for the shifting neutral axis.

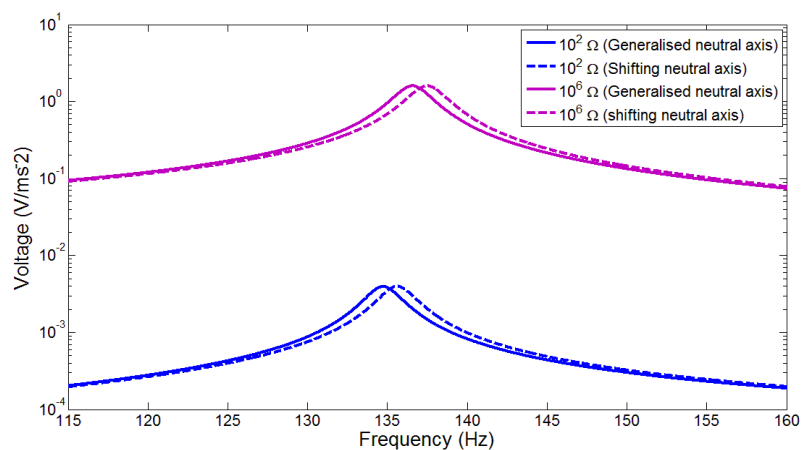


Figure 6.21 Electrical voltage frequency response comparison for generalized neutral axis and shifting neutral for axis 45° angle of orientation.

In addition, the comparison study of power output for generalized neutral axis and shifting neutral is given by figure 6.22. The study shows similar behavior with the previous study for 0° angle of orientation. Here, the power outputs for short and open circuit resistances shows very similar response for both neutral axis models whereas the resonance frequency for the shifting neutral axis shows lower value than the generalized neutral axis response.

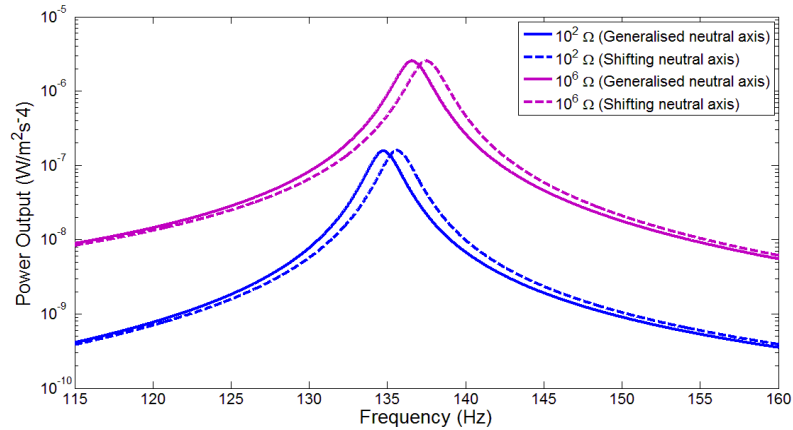


Figure 6.22 Comparison electrical power output frequency response for generalized neutral axis and shifting neutral axis of 45° angle of orientation.

For summarising the influence of the shifting neutral axis, it seems to show only small effect to the magnitude of the electrical voltage and power output. However, the results show that it affects the resonance frequency for different angles of orientation with frequency change of less than 1 Hz. The shift in the frequency due to the generalized and the shifting neutral axis for 0° angle of orientation was 0.8 Hz for the short and open circuit resistance.

6.5 Summary

This chapter presents an investigation of the dynamic responses of the segmented piezoelectric unimorph beam using different angles of orientation. The overall results for dynamic responses of tip displacement, parallel voltage, current and power have been simulated. The mathematical models for the segmented piezoelectric element for varying angles of orientation have been discussed in detail.

Each segmented finite element was modelled using six degrees of freedom where the system input was under base excitation in the transverse direction. The mathematical finite element model was derived from the equations of motion in section 6.1.

In addition, the development of the electromechanical coupling equations for piezoelectric segments was given by considering only the parallel connection. The piezoelectric element equations emphasized not only the two segments connected to each other but also the connection with load resistances.

Since the piezoelectric unimorph beams considered different angles of orientation, the proposed technique for matrix transformation was introduced by multiplying the transformation matrix equation by the discretisation matrix to obtain the global form of the system matrices. More detailed explanation of this technique is provided in appendix C.

The direct non-orthonormalised method has been used to derive the frequency response functions. A MATLAB program was developed to show the frequency response of voltage, current and power output for different angles of orientation.

A case study has been used to illustrate the behavior of the piezoelectric unimorph beam with tip mass and different orientations. According to the results obtained in section 6.2.1 for a flat unimorph beam, the first resonance frequency occurs at 125.8 Hz at short circuit and 127.5 at open circuit load resistances. In addition, the second mode of resonance frequency occurs at 751.9 Hz and 751.3 Hz for short and open circuit load resistance. It should be noted that the load resistance values for short and open circuit conditions used are 100 Ω and 1 M Ω , respectively.

The voltage and current responses with varying angle of orientation from 0° to 90° showed increasing resonance frequencies and decreasing magnitudes of electrical voltage and current for the first mode. The increase of the first mode resonance frequencies with orientation changes from 0°-90° went from 125.8 Hz to 168.1 Hz. The second mode resonance frequency showed the opposite behavior, where changing of the angle of orientation from 0° to 90° gave decreasing resonance frequency values and the magnitude of electrical voltage and current.

The electrical power frequency response is given by section 6.2.5 with the load resistances ranging from 100Ω to $1 \text{ M}\Omega$. The frequency responses are described in figures 6.7-6.12 showing the changes of resonance peak as the angle of orientation increased. Similar behavior of the resonance frequencies gave the dynamic power response compared to the voltage and current response for the first and second modes, where the resonance frequency increased with the increase in angle. As load resistances changed from short to open circuit resonance frequency shifted from 125.8 Hz to 168.1 Hz .

In addition, the investigation of the electrical power output with load resistance was given by figure 6.12. The maximum electrical power response was obtained at the short circuit load resistance of $23.8 \text{ k}\Omega$ for the flat unimorph and $19.1 \text{ k}\Omega$ for the 90° orientation. The corresponding maximum open circuit results were $91.4 \text{ k}\Omega$ for the flat unimorph beam and $63.8 \text{ k}\Omega$ for the 90° orientation. Figure 6.13 showed the relationship between angle of orientation, resistance and power amplitude for the maximum values of short circuit, open circuit and crossover point for the resonance frequency excitation examples. Obviously, the first mode response of the segmented piezoelectric unimorph gave an increasing resonance frequency value but a reducing amount of electrical power when the angle of orientation increased.

Furthermore, the contribution of axial deformation and axial electromechanical coupling into the piezoelectric unimorph beam with different orientation has shown very important aspect. The results of section 6.3 showed that the resonance frequencies changed very significantly when the piezoelectric orientation changed. The axial deformation and axial electromechanical coupling showed only minor change in frequency and response magnitude comparing to that without axial consideration.

Chapter 7

Experimental Power Harvesting of the Piezoelectric Unimorph Beam with Different Angle of orientation

In this chapter, comparison between finite element and experimental studies of the piezoelectric unimorph beam with varying angle of orientations of 0° , 30° and 90° are presented in detail. In chapter 6, the equations of the finite element method with different angles of orientation were derived to formulate frequency response functions which can be used for validation against the experimental result for electrical voltage, current and power output with variable load resistances ranging from 1500Ω to $4 \text{ M}\Omega$. The piezoelectric unimorph beam for both numerical and experimental tests was excited under base motion in the transverse direction with an acceleration value of 1 m/s^2 .

7.1 Material Properties of the Unimorph Beam and Experimental Set up

Properties and geometries of the piezoelectric unimorph beam are given in table 7.1. The piezoelectric unimorph beam consists of two materials which are brass and piezoelectric. The piezoelectric material was made of PZT PSI-5A4E (Piezo System Inc., Woburn, MA). The piezoelectric unimorph structure as shown in figure 7.1 was set up with varying angle of orientation. The geometrical substructure of the unimorph beam had an overall substructure length of 50 mm with horizontal segment length of 25 mm and an oriented segment length of 25 mm. The width of the substructure was 6.3 mm and the thickness was 0.5 mm. The piezoelectric unimorph material had a set length of 20 mm, width 6.3 mm and thickness 0.190 mm. It should be noted that the thickness of piezoelectric element was not the same as the previous simulation study since only a limited thickness of material was available in the laboratory. The locations of the piezoelectric elements 1 and 2 were set with a gap of 10 mm and covered each end of the substructure. Since the simulation and experimental work used the parallel electrical connection, a wire was soldered onto the positive point of the electrode surface of the piezoelectric element 1 connected to the piezoelectric element 2. As the brass component is a conductive material, the negative point of the piezoelectric elements 1 and 2 were assumed to be connected in parallel where both piezoelectric

elements were glued together to the top surface of the substructure. For configuration of the parallel electrical connection of the unimorph beam with the resistive load, a wire was soldered onto the top surface of piezoelectric element 1 as the positive output wire and another wire was soldered onto the surface of the substructure as the negative output. These two wires were used to connect with the load resistances. For setting the load resistances, an electronic board was used for arranging resistive impedance values of 1.5 k Ω , 2.5 k Ω , 10 k Ω , 120 k Ω , 200 k Ω , 300 k Ω , 2 M Ω and 4 M Ω . The short circuit resistance value of 1.5e3 Ω was chosen for the experimental test as it was found that this low value of resistance gave defined resonant peaks for the first two resonant modes when using the swept sine excitation. Testing using lower resistance values was performed by using 100 Ω , 500 Ω and 1 k Ω . However it was found that these lower resistances resulted in significant electrical noise in the FFT responses and it was very difficult to see the first two resonance modes.

The main experimental tools consisted of a desktop computer unit with Bruel & Kjaer 3650B digital signal analyser and used a Core 2 duo processor with 2 Gigabyte RAM memory and PulseShop 13.1 B&K software. The digital signal analyser B&K 3560B-B020 with 5 channels was connected through the computer using a LAN cable connection. Three channels of dynamic data were recorded using the analyser including the B&K accelerometer type 4507B with frequency measurement range from 3-25 kHz, the polytec laser vibrometer PDV 100 and the voltage across the load resistances was measured from the resistor board using a BNC connector. A signal generator (Agilent) was connected to the B&K 2706 amplifier and the resulting amplified signal was sent to the B&K 4809 exciter. A stud connector was used for connecting the base support. The base support was used to clamp the piezoelectric unimorph beam with fixed-free boundary condition.

The frequency analysis for the testing data was set with a bandwidth of 2 kHz, using 6400 lines giving a window resolution of 0.3125 Hz. The accelerometer sensitivity of 9.633 mV/ms⁻² was used for the Pulse software to obtain the measurement results in engineering units. It should be noted that the accelerometer was used to measure the base input excitation. Dynamic tip velocity measurements on the piezoelectric unimorph was carried out using the Polytec laser vibrometer with a measurement range scale of 500 mm/s and low pass filter setting of 22 kHz. The sensitivity of the laser

vibrometer was given as 125 mm/s.V which converted to the scale inputted to the Pulse software of 8 V/m.s⁻¹. The sensitivity scale of the voltage output measured across the load resistance was set to be 1 V/V for the Pulse software. Since the acceleration is given per-unit acceleration in m/s⁻², the results of the frequency responses are presented by experiment and numerical analysis as per-unit acceleration in m/s⁻².

Table 7.1 Properties and geometries of the piezoelectric unimorph beam.

	Piezoceramic (PSI-5A4E)	Substructure (Brass)
Length, L (mm)	20	50
Width, b (mm)	6.3	6.3
Thickness, h_p and h_s (mm)	0.190	0.5
Young's Modulus, c_{11} (GPa)	66	105
Density, ρ (kg/m ³)	7800	9000
Piezoelectric constant, d_{31} (pm/V)	-190	-
Permittivity, ϵ_{33}^T (F/m)	$1800 \epsilon_0$	-
Permittivity free space, ϵ_0 (pF/m)	8.854	-

Figure 7.1 shows the sketch configuration of segmented piezoelectric unimorph beam with different angle of orientation. The setup of apparatus and sample of the experimental piezoelectric unimorph beam with different orientation is shown in figure 7.2.

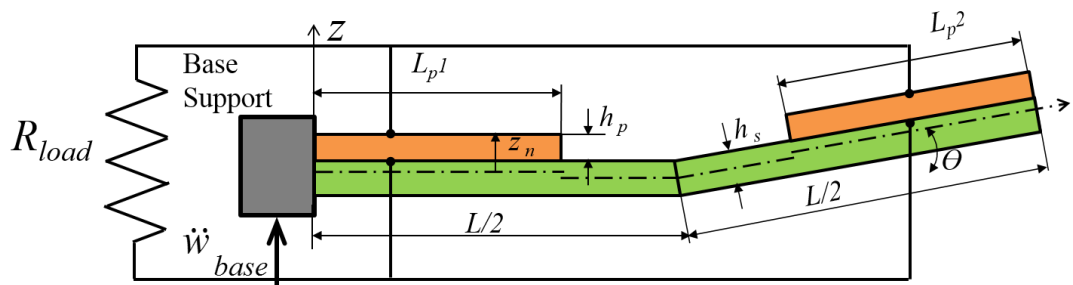


Figure 7.1 Segmented unimorph beam configuration with varying angle of orientation.

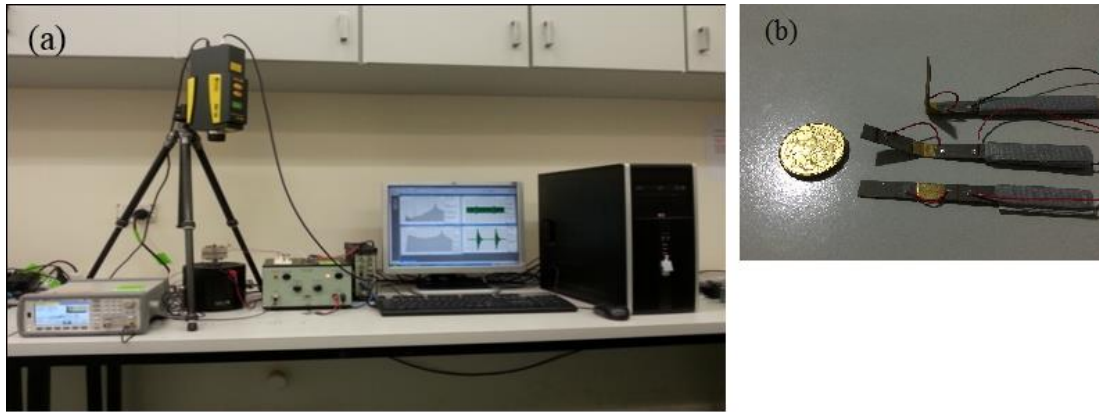


Figure 7.2 (a) Experimental test set up (b) piezoelectric unimorph samples with 0°, 30° and 90° orientations.

7.2 Unimorph Frequency Response with 0° Angle of orientation

7.2.1 Validation of First Mode Electrical Voltage Frequency Response

This section presents the detail of the electrical frequency response of the unimorph beam. Figures 7.3-7.5 show illustration of the electrical voltage, current and power output frequency response with variable load resistance from 1.5 k Ω to 4 M Ω . Since the resulting frequency responses are based on the variation of load resistances in a range which acts as resistive shunt damping, identification of mechanical damping ratio for the numerical analysis can be performed by matching the amplitude of the tip velocity and voltage response amplitude between the numerical analysis and the experimental work under the short circuit load resistance. It should be noted that even damping ratio effect is due to the mechanical system structural response and electromechanical coupling and external resistive load contribution to the electromechanical damping. For that reason, identification of damping ratio must be under short circuit load resistance conditions in order to reduce the electrical effect to the structure. In the process of matching the resonance peak amplitudes for both the numerical and experiment results, the half power factor bandwidth method was used to measure damping ratios and Rayleigh damping values. Matching the numerical peak frequency response at the first resonance mode obtained the Rayleigh damping constant for Alpha (α) = 6.0 1/s and Beta (β) = 2.5x10⁻⁵ s at the load resistance value of 1.5 k Ω . The damping ratio (ζ) using Rayleigh damping constant can be formulated using the following method (Clough & Penzien, 1993),

$$\begin{Bmatrix} \alpha \\ \beta \end{Bmatrix} = \frac{2\omega_1\omega_2}{\omega_2^2 - \omega_1^2} \begin{bmatrix} \omega_2 & -\omega_1 \\ -1/\omega_2 & 1/\omega_1 \end{bmatrix} \begin{Bmatrix} \zeta_1 \\ \zeta_2 \end{Bmatrix}. \quad (7.1)$$

Figure 7.3a-c shows the resulting numerical and experimental voltage frequency responses with varying load resistances. Generally, the voltage resonance frequency increases as the load resistance values increase. In addition, a monotonic increase of the peak voltage magnitude clearly occurs as the load resistances changes. The numerical voltage frequency responses are given by the solid lines and are confirmed using the experimental tests as given with the round dots of the same colour. Although the experimental results (round dots) do not coincide precisely with the numerical results (solid lines), they are a very close match. There may be boundary constraint problems with the experimental tests, as having a real fixed boundary condition is difficult to achieve in the experimental test.

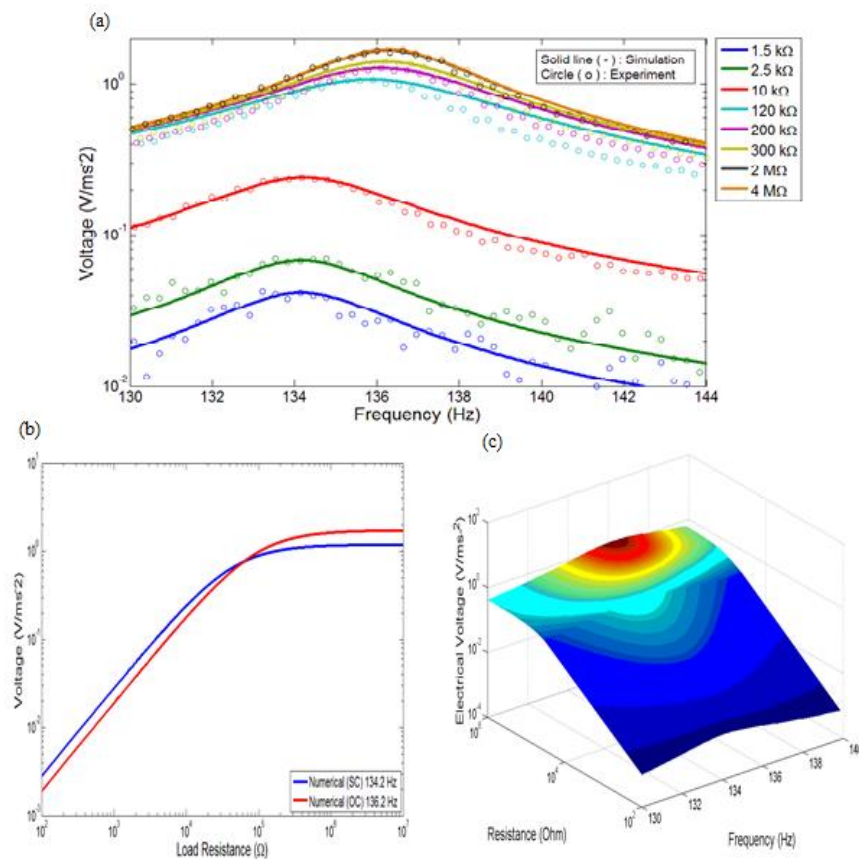
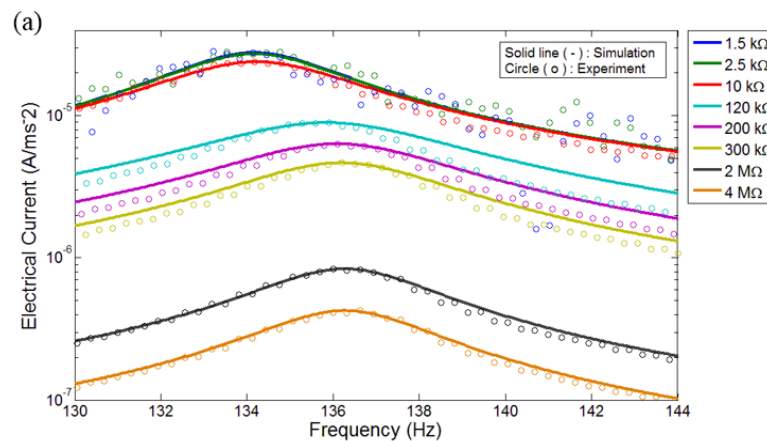


Figure 7.3 (a) Voltage frequency response comparison between numerical (solid line) and experimental analysis (round dot) for 0° angle (flat) orientation (b) The first mode resonant voltage peak amplitude under the base excitation with the short circuit and open circuit resistances (c) 3-D plot.

7.2.2 Validation of First Mode Electrical Current Frequency Response

Figure 7.4 shows the comparison of the electrical current frequency responses between the numerical and experimental analysis at the first mode resonance. Figure 7.4a shows the trend of decreasing peak electrical current amplitudes followed by shifting resonance frequency when load resistances increase from 1.5 k Ω to 4 M Ω . The shift of resonances frequency from 134.2 Hz to 136.3 Hz gives the electrical current amplitude reductions from 27.76 $\mu\text{A}/\text{ms}^{-2}$ to 0.425 $\mu\text{A}/\text{ms}^{-2}$. It should be noted that the experimental data collections for electrical currents were calculated using the measured voltage data based on the load resistances. Again, the resulting figure 7.4a gives good agreement between the numerical and experimental analysis for the piezoelectric unimorph with zero angle of orientation. The simulated behaviour of electrical current amplitude against varying load resistance is given in figure 7.4b showing the short and open circuits. The electrical current shows higher amplitude under the short circuit resonance excitation than that for the open circuit resonance excitation. However, the aforementioned behaviour in figure 7.4b changes after passing an overlapping point. The simulated 3-D analysis is shown in Figure 7.4c against varying load resistance. Here, the highest electrical current for a given resonance frequency is presented by the dark red colour and the decreasing electrical current amplitude with shifting frequency is presented by the blue colour.



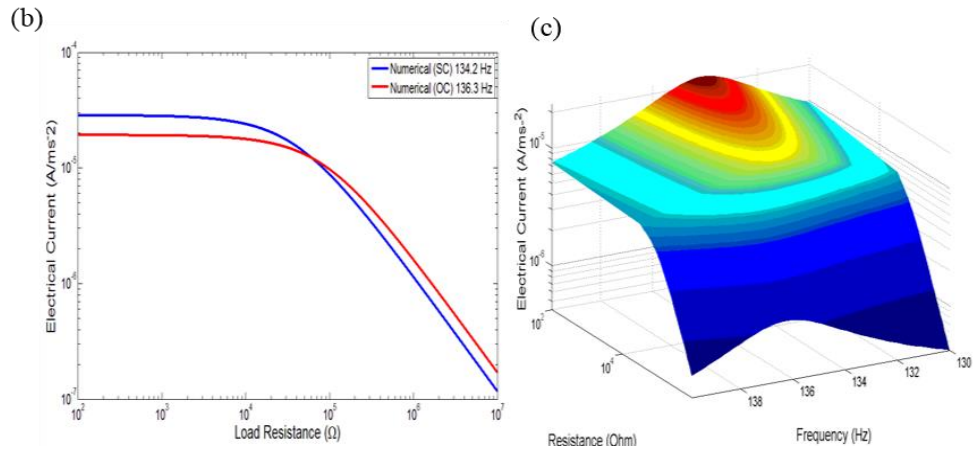


Figure 7.4 (a) Electrical current frequency response comparison between numerical (solid line) and experimental analysis (round dot) for 0° angle (flat) orientation (b) Current under base excitation at short and open circuit (c) 3-D plot.

7.2.3 Validation of First Mode Electrical Power Output Frequency Response

Figure 7.5a shows the power output frequency response comparison between the experimental and numerical tests with varying load resistance at the first mode resonance. Validation of the numerical power output frequency responses shows the same behaviour as the experimental power frequency responses. Again, the shift in resonance frequency is clearly shown for both the short circuit and open circuit frequency responses. The power output amplitude reaches a maximum midway between the short circuit and open circuit load resistance as shown clearly in figure 7.5b when the piezoelectric unimorph beam is excited under short and open circuit resonance frequency. The maximum power amplitude for short and open circuit is clearly given in the range of load resistances from 10 kΩ to 1 MΩ. Based on the simulation result in figure 7.5b, the maximum load resistance of 62.72 kΩ gives maximum power amplitude of 9.191 μW/m²s⁻⁴. The simulated 3D analysis given in figure 7.5c also shows the region of maximum power output with shifting resonance frequency.

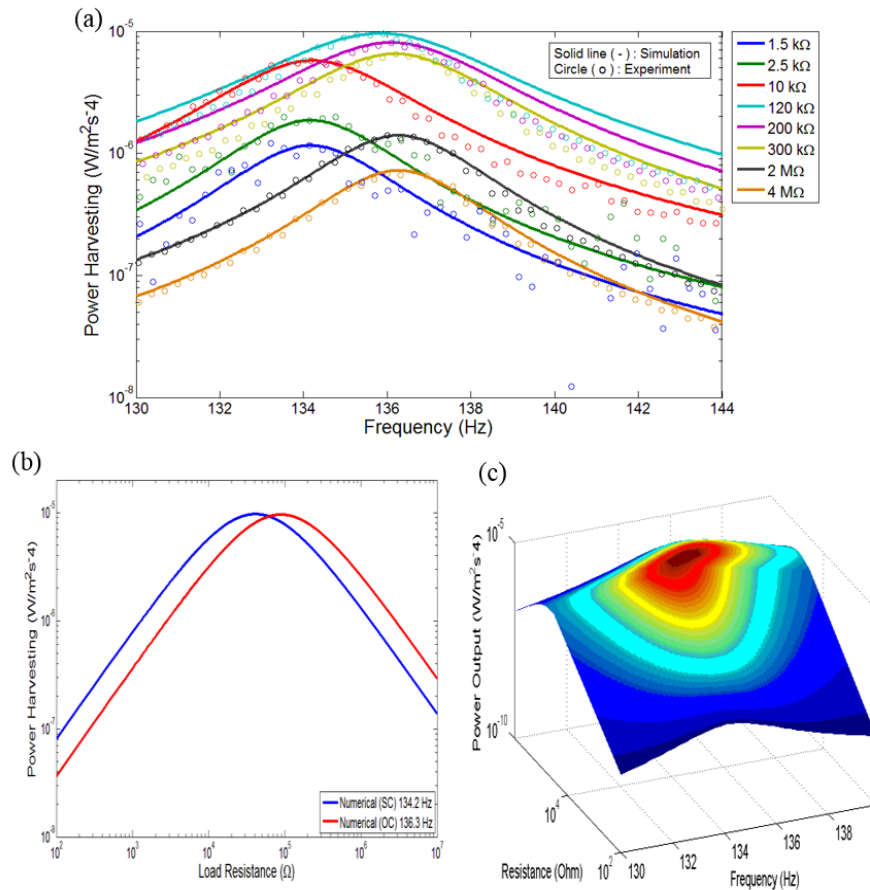


Figure 7.5 (a) Power output frequency response comparison between numerical (solid line) and experimental analysis (round dot) for 0° angle (flat) orientation (b) Variable power under base excitation at short and open circuit resonance (c) 3-D plot.

7.3 Piezoelectric Unimorph Frequency Response with 30° Angle of orientation

7.3.1 Validation of First Mode Electrical Voltage Frequency Response

Figure 7.6 is given to validate the numerical simulation result with the experimental test study for the piezoelectric unimorph with 30° angle of orientation. Based on the numerical simulation analysis, the first mode resonance frequency is 138.3 Hz under short circuit resistance and shifts to 140.5 Hz under open circuit load resistance (solid lines). The resulting experimental test analysis gives good agreement as represented by the round dots in figure 7.6a. Increasing voltage amplitude and shifting frequencies are clearly shown by both data results. Matching the frequency response of the numerical and the experimental work gave the Rayleigh damping constant of Alpha (α) = 6.5 1/s and Beta (β) = 2.6x10⁻⁵ s. Figure 7.6b shows the investigation of the first modal voltage amplitude against variable load resistance. A similar behaviour in the

voltage amplitudes at lower resistances was shown in figure 7.6b compared with figure 7.3b. Even the high load resistance responses has similar behaviour, where this formation occurs after passing the overlapping point from short to open circuit conditions. The simulated 3D analysis clearly shows the resulting frequency responses against varying load resistance where the highest voltage amplitude with shifting resonance frequency are presented in dark red colour.

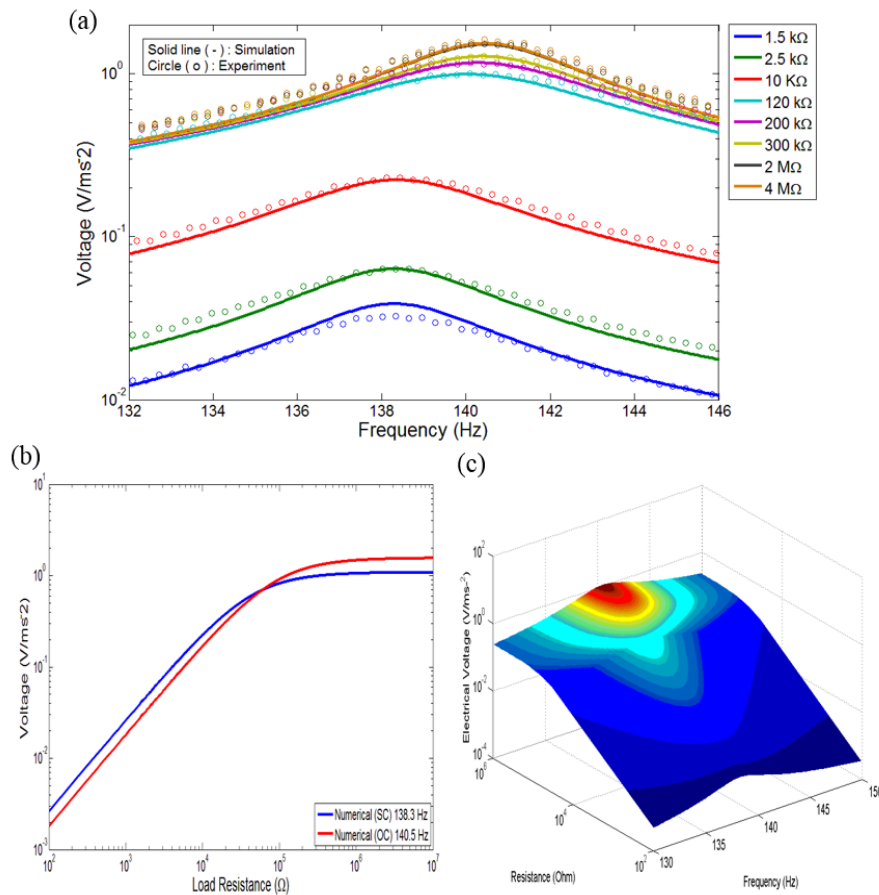


Figure 7.6 (a) FRFs voltage comparison between numerical (solid line) and experimental analysis (round dot) for 30° angle of orientation (b) Voltage and load resistance under short and open circuit frequency excitation (c) 3-D plot.

7.3.2 Validation of First Mode Electrical Current Frequency Response

Figure 7.7a presents a validation of the electrical current frequency response for the numerical analysis with the experimental test analysis showing good agreement between the numerical and the experimental work. The shift in the resonance frequency followed by decreasing electrical current amplitude occurred when the load resistance increased from 1.5 kΩ to 4 MΩ. Figure 7.7b confirms this behaviour by

exciting the piezoelectric unimorph under short and open circuit resonance frequency. Again, similar behaviour was also presented in figures 7.7b and 7.4b. 3D simulation analysis as shown in figure 7.7c shows the shift in frequency response behaviour of electrical current as the load resistance changes. The highest electrical current amplitude value is shown in a dark red colour region for lower resistance and then the colour changes to dark blue at higher resistance.

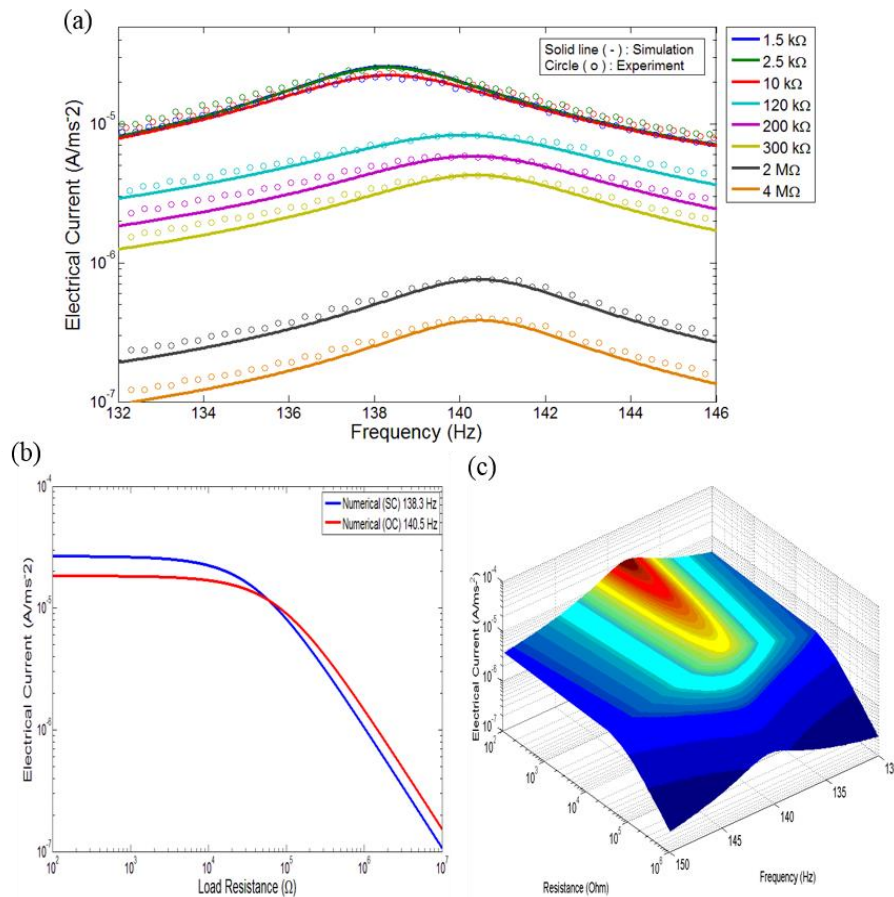


Figure 7.7 (a) FRFs current comparison between numerical (solid line) and experimental analysis (round dot) for 30° angle of orientation (b) Current and load resistance under base short and open circuit frequency excitation (c) 3-D plot.

7.3.3 Validation of First Mode Electrical Power Output Frequency Response

Validation of the numerical power output response for the unimorph with 30° angle of orientation given in figure 7.8a shows close agreement between the numerical and the experimental test using changes of load resistance. The result of figure 7.8a shows the shift in resonance frequency from short to open circuit load resistances. As previously shown for the voltage and current responses, the resonance frequency of 138.3 Hz at

the short circuit load resistance using numerical simulation shifts to 140.5 Hz at the open circuit load resistance. In addition, the experimental resonance frequency also shifts from 138.3 Hz for the short circuit load resistance to 140.4 Hz for the open circuit load resistance. Comparison between the numerical and the experimental power amplitudes shows $999 \text{ nW/m}^2\text{s}^{-4}$ and $711.2 \text{ nW/m}^2\text{s}^{-4}$ at short circuit load resistance and $588.7 \text{ nW/m}^2\text{s}^{-4}$ and $651.6 \text{ nW/m}^2\text{s}^{-4}$ at the open circuit load resistance, respectively. The corresponding peak power amplitude at the open circuit load resistance $120 \text{ k}\Omega$ shows $8.172 \text{ }\mu\text{W/m}^2\text{s}^{-4}$ for the numerical test in comparison with $8.354 \text{ }\mu\text{W/m}^2\text{s}^{-4}$ for the experimental test. Investigation of the maximum power for short and open circuit resonance conditions can be seen in figure 7.8b with the load resistances of $41 \text{ k}\Omega$ and $85.4 \text{ k}\Omega$, respectively. The overlapping point from the short and open circuit resonance frequency excitations in figure 7.8b gives $60.17 \text{ k}\Omega$ with maximum power off-resonance of $7.969 \text{ }\mu\text{W/m}^2\text{s}^{-4}$ as presented in the simulation. Moreover, figure 7.8c shows the simulated 3-D analysis of the relationship between frequency and power amplitude against variable load resistance.

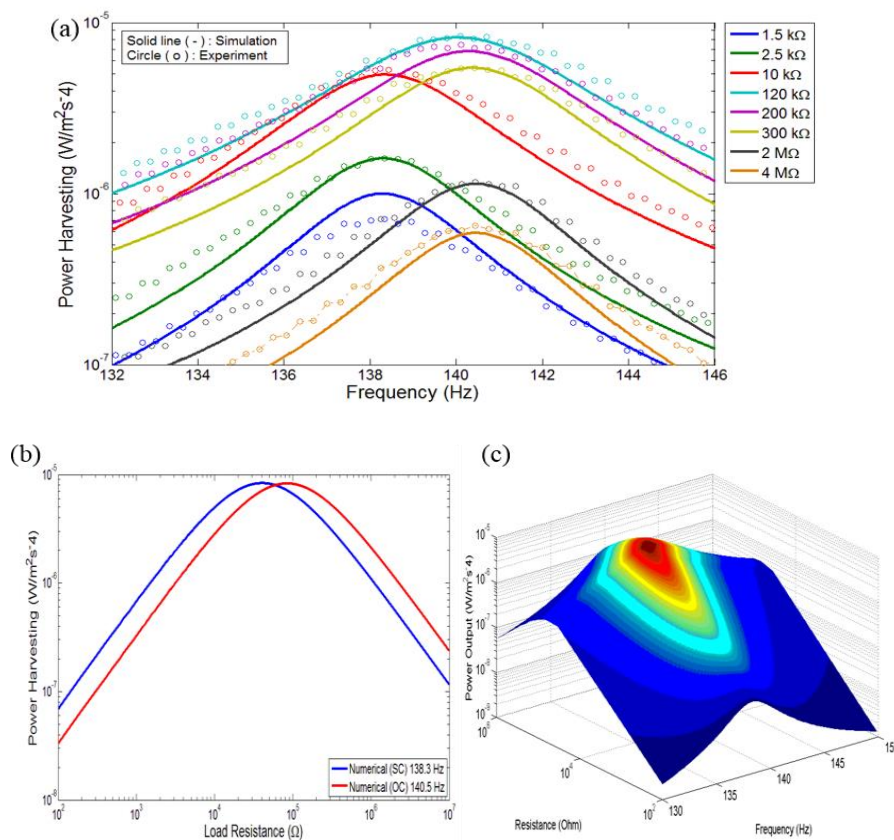


Figure 7.8 FRFs of power output comparison between numerical (solid line) and experimental analysis (round dot) for 30° angle of orientation (b) current and load resistance under short and open circuit base excitation (c) 3-D plot.

7.4 Piezoelectric Unimorph Frequency Response with 90° Angle of orientations

7.4.1 Validation of First Mode Electrical Voltage Frequency Response

Figure 7.9a shows the electrical voltage response against frequency for varying load resistance with 90° angle of orientation. It shows that the resonance frequency shifts with increasing voltage amplitudes as the load resistance increases. The numerical voltage FRFs was given by using Rayleigh damping constant values with Alpha (α) = 5.5 1/s and Beta (β) = 1.1×10^{-5} s. Moreover, validations of numerical simulation for voltage frequency responses in figure 7.9a show close agreement with the experimental results. Based on the numerical investigation with short and open circuit load resistances, the resonance frequency shifts from 179 Hz to 181.8 Hz and the voltage magnitude increases from 51.25 mV/ms⁻² to 1.613 V/ms⁻².

Investigation of the variable voltage under resonance frequency excitation is given by figure 7.9b showing that the voltage amplitude under short circuit resonance frequency excitation (blue line) at low resistances is higher than that under the open circuit resonance frequency excitation (red line). However, both lines overlap at the resistance of 44.56 k Ω with voltage amplitude of 546.8 mV/ms⁻². Therefore, at higher resistances, the open circuit resonance frequency excitation shows higher voltage magnitude than the short circuit resonance frequency excitation.

In addition, the simulated 3-D analyses as shown by figure 7.9c confirms the occurrence of the shift in resonance frequency with increasing voltage amplitude by increasing the load resistances. It can be seen in figures 7.9a and 7.9c that the peak of the resonance frequency shifts about 2.8 Hz from low to high load resistances. The voltage at higher resistances gives higher amplitude than that at the lower load resistance values.

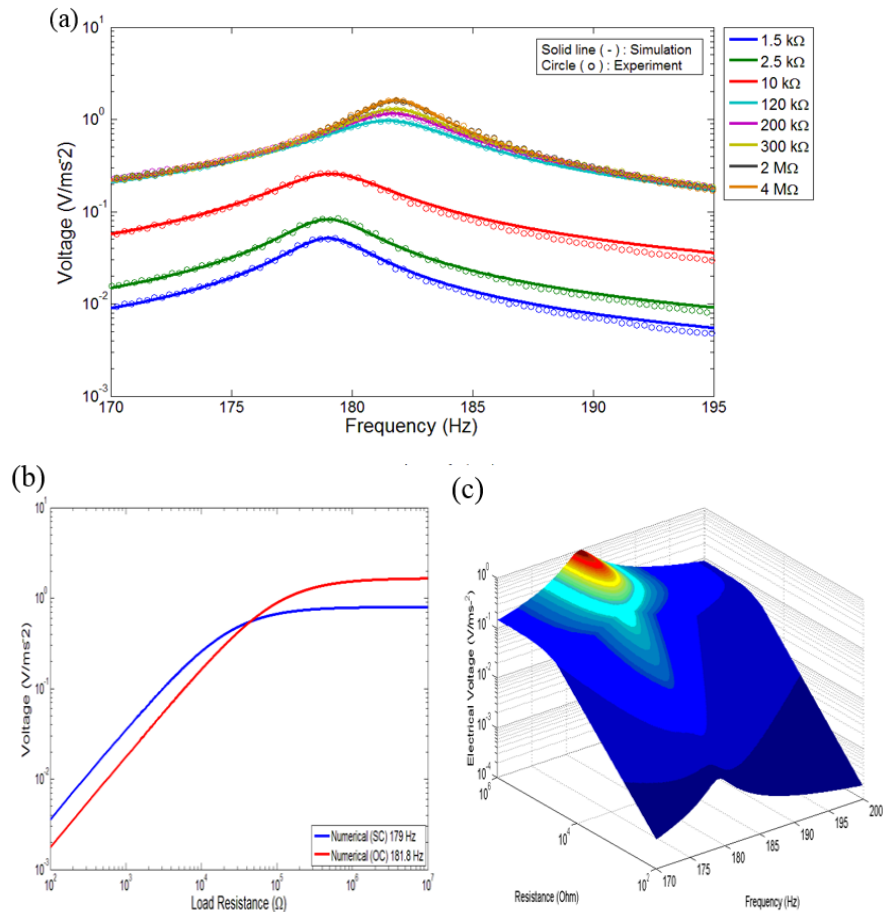


Figure 7.9 (a) Voltage frequency response comparison between numerical (solid line) and experimental analysis (round dot) for 90° angle of orientation (b) Voltage and load resistance under short and open circuit base excitation (c) 3-D plot.

7.4.2 Validation of First Mode Electrical Current Frequency Response

The behaviour of the electrical current FRFs for 90° angle of orientation can be seen in figure 7.10a-c with variable load resistances. Based on figure 7.10a, the electrical current configuration shows the shift in frequency followed by decrease of amplitudes under increasing load resistances. Close agreement between the numerical and experimental results can also be obtained. The clear transition between the short circuit resonance response (1.5 kΩ to 10 kΩ) and the open circuit resonance response (120 kΩ to 4 MΩ) is also obvious as shown in figure 7.10b. The results show that the electrical current at lower resistances under short circuit resonance excitation gives higher amplitude than that at higher resistances under the open circuit resonance excitation. Although the electrical current amplitude reduces as the load resistance increases, the electrical current at the higher load resistances for the open circuit

resonance excitation gives higher amplitude than the short circuit resonance excitation. This event occurs after both lines overlap at the load resistance of 44.56 k Ω .

The three dimensional numerical result shows the corresponding frequency and electrical current response under varying load resistances as shown in figure 7.10c. The dark red colour shows the peak current response for the short circuit load resistance.

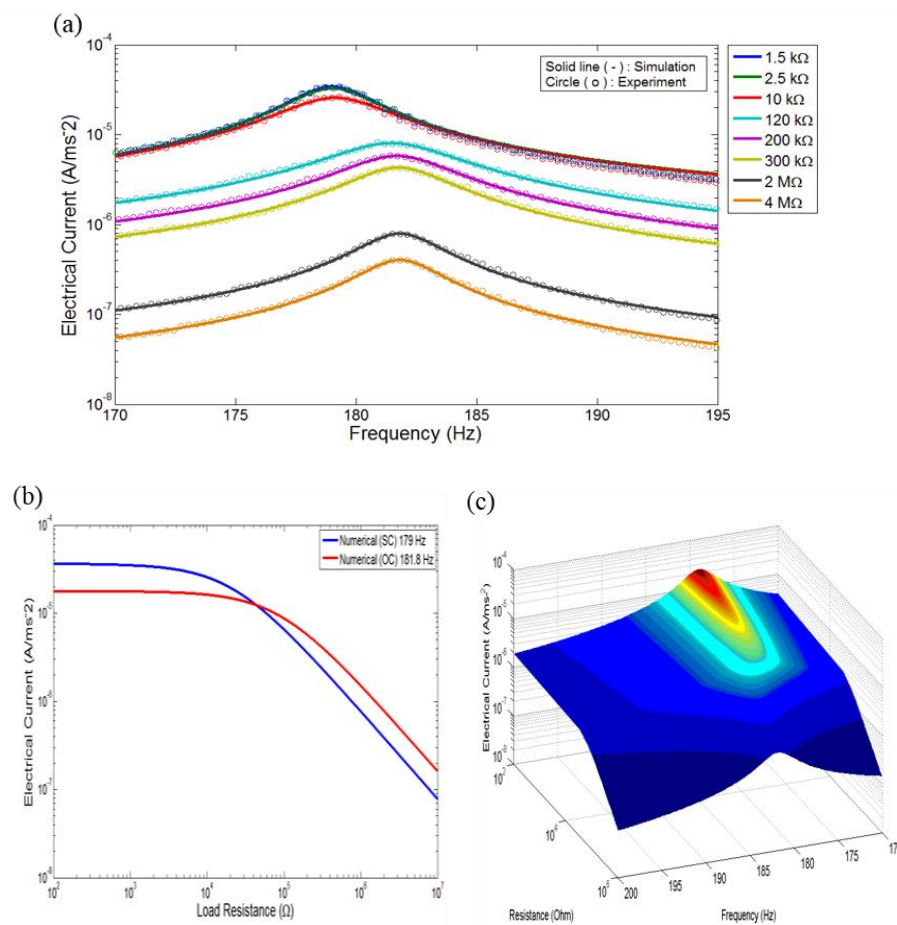


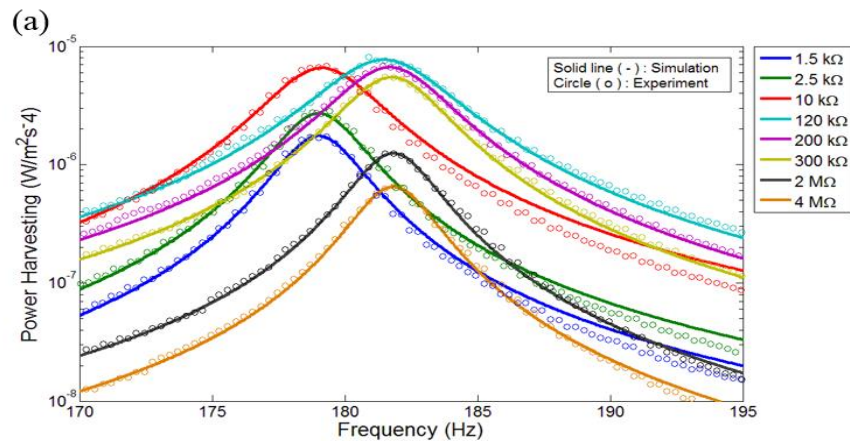
Figure 7.10 Electrical current frequency response comparison between numerical (solid line) and experimental analysis (round dot) for piezoelectric with 90° angle of orientation (b) Current and load resistance response under short and open circuit base excitation (c) 3-D plot.

7.4.3 Validation of First Mode Electrical Power Output Frequency Response

Figure 7.11 presents the power output frequency response with orientation angle of 90° under varying load resistances. The result shows close agreement between

numerical and experimental tests. The resonance frequency shifts from 179 Hz under the short circuit resistance to 181.8 Hz for the open circuit resistance. The corresponding power output amplitudes give $1.751 \mu\text{W}/\text{m}^2\text{s}^4$ and $0.6505 \mu\text{W}/\text{m}^2\text{s}^4$ for the short and open circuit resistances, respectively. Based on the results shown in figure 7.11a, the power output increases from the short circuit resistance with increasing load resistance but then reduces after reaching the open circuit resistance. Further investigation of the maximum power for the short and open circuit resistance can be clearly seen in figure 7.11b when the piezoelectric unimorph is excited under short and open circuit resonances. The maximum power and maximum load resistance values can be taken from the result overlapping lines between the short and open circuit resonances. Based on figure 7.11b, the maximum load resistance value was given by $44.56 \text{ k}\Omega$ with resulting power amplitude of $6.709 \mu\text{W}/\text{m}^2\text{s}^4$.

Figure 7.11c gives the simulated 3-D plot with frequency response behaviour under varying load resistances. The peak resonance frequency shifts until reaching the dark red region with power amplitude shifting from short to open circuit load resistances. The maximum power range can be seen in the load resistance range from $10 \text{ k}\Omega$ to $1 \text{ M}\Omega$.



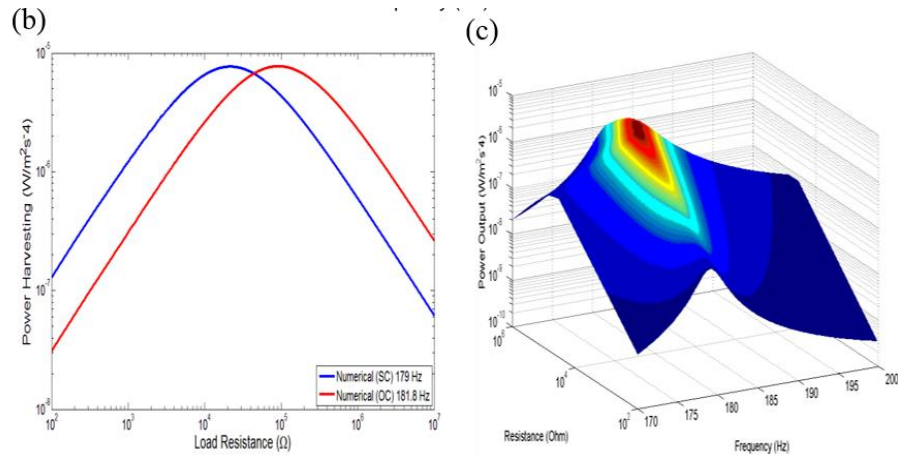


Figure 7.11 Power output frequency response comparison between numerical (solid line) and experimental analysis (round dot) for 90° angle of orientation (b) Power output and load resistance under short and open circuit base excitation (c) 3-D plot.

7.5 Summary

This chapter presents the validation between the numerical simulation and experimental tests of the segmented unimorph beam with different angles of orientation from 0° to 90°. Detailed investigation was undertaken by using the piezoelectric unimorph for orientations from 0°, 30° and 90° angles. Each angle of orientation unimorph model presented the electrical voltage, current and power output FRFs for the first mode resonance. The frequency responses were validated by matching the numerical frequency response with the experimental test under varying load resistances. Based on the results of the investigation, the first mode resonance behaviour gave close agreement result for the voltage, current and power output for each angle of orientation. Investigation of the voltage, current and power amplitude relationship with respect to variable load resistances was also presented by exciting the piezoelectric unimorph at the short and open circuit resonance frequency. The resulting variable voltage, current and power output versus load resistances were very useful to explore the maximum load resistance values and corresponding maximum voltage, current and power output for each angle of orientation. The 3-D simulation analysis was then used to show the important frequency response behaviour with respect to the varying load resistances for each angle of orientation.

Numerical simulation shows that the resonance for angle of orientation with 0° occurs from 134.2 Hz to 136.3 Hz whereas the experimental test for the short and open circuit

load shows 134.2 Hz to 136.3 Hz, respectively. Moreover, for the 30° unimorph angle of orientation, the resonance frequency shifts from 138.3 Hz for short circuit resistance to 140.5 Hz for the open circuit resistance. The resulting resonance frequency for the experimental result with 30° orientation gave 138.3 Hz for short circuit and shifted to 140.4 Hz for open circuit load resistance. Finally, the piezoelectric unimorph with 90° angle of orientation showed the resonance frequencies of 179 Hz and 181.8 Hz for the short and open circuit load resistances whereas the experimental work gave 178.7 Hz for short circuit resistance and shifted to 181.8 Hz for open circuit load resistance, respectively.

The maximum power output for the 0° angle of orientation unimorph gave 9.191 $\mu\text{W}/\text{m}^2\text{s}^{-4}$ with maximum load resistance of 62.72 k Ω . The 30° angle of orientation unimorph gave the maximum load resistance of 60.17 k Ω with maximum power of 7.969 $\mu\text{W}/\text{m}^2\text{s}^{-4}$. Finally, the 90° angle of orientation gave the maximum load resistance of 44.56 k Ω with power amplitude value of 6.709 $\mu\text{W}/\text{m}^2\text{s}^{-4}$.

Chapter 8

Summary, Conclusion and Future Work

This thesis presented the numerical analysis of the electromechanical dynamic formulation of a piezoelectric unimorph beam power harvester. The energy harvesting approach using piezoelectricity can be applicable for micro-scale design with compact size, high energy and sensitivity which can be promising technology for self-powered smart sensor devices in health condition monitoring applications. This research focuses on the development of the finite element method for modelling several designs of the piezoelectric unimorph beam energy harvester. The research showed the development and derivation of the fundamental electromechanical dynamic equations using a simplification model of a single element to resolve the multi-element design such as the segmented unimorph beam. Research background and literature review were presented in chapter 1 and 2, respectively. Chapter 3 developed a single element unimorph beam and showed the fundamental concept of derivation of the electromechanical dynamic equations using finite element methods. The single element was initially associated with four degrees of freedom coupled with the piezoelectric element. The electromechanical coupled equation was formulated based on linear constitutive equations of the substructure and the piezoelectric structure. The electromechanical dynamic equation was derived based on Hamilton's principle in terms of the mechanical and electrical energy with extended non-conservative work equation. The extended Hamilton's principle obtained the form of the local electromechanical dynamic matrix equation that can be extended into the global matrices to form the general electromechanical dynamic equation. The solution for FRFs of the electromechanical dynamic equation was developed using a novel non-orthonormalised direct method since this solution can remove the normalisation process for the eigenfunction and generalisation of eigenvector functions.

Chapter 4 showed the development of the extended single element model into the multi-element model as the single element solution gave less than the required accuracy in calculations. It should be noted that chapter 4 also introduced the derivation of the electromechanical discretisation multi-element using the electromechanical transformation vector. The solution of the FRFs using direct non-

orthonormalised methods for multi elements were compared against the analytical results from the orthonormalised method in (Alper Erturk & Inman, 2008a) and finite element methods using the orthonormalised method in (M. Lumentut & Howard, 2014) as presented in a comparison study (Warman et al., 2014). The frequency response for voltage, current and power was obtained based on the convergence study for the eigenfunction series related to the number elements used. The result showed the FRFs of voltage, current and power having good agreement between the direct non-orthonormalised method and orthonormalised method as introduced by the previous papers.

Further, modelling the piezoelectric unimorph beam using tip mass and varying length of the piezoelectric element were discussed in chapter 5. The tip mass offset method was incorporated into the fundamental formulas in order to show the frequency responses of the electrical voltage, current and power for asymmetrical cross-sections of the piezoelectric unimorph beam. In addition, a parametric study using varying length of the piezoelectric element was presented showing the multimode responses. The power outputs for the multi-mode responses with varying piezoelectric element lengths and load resistances were explored for the first and second mode responses. It was found that the pattern of the power amplitude at short and open circuit resistance for the first mode gave both amplitude with opposite behaviour. The power amplitude for short circuit resistance tends to increase with increasing piezoelectric length whereas the power amplitude at the open circuit resistance tends to decrease with increasing values of piezoelectric length. For the second mode, the pattern of power amplitude at short circuit resistance with 20 mm piezoelectric length has the highest generated power whereas the piezoelectric of length 40 mm has the lowest power amplitude. The open circuit resistance with piezoelectric length of 10 mm has the highest generated power, while the piezoelectric length of 40 mm still gave the lowest power range.

Chapter 6 simulated the segmented piezoelectric unimorph beam with different angle of orientations under varying load resistances of 100 Ω to 1 M Ω where the segmented piezoelectric element are connected in parallel. The set of two piezoelectric elements had symmetrical size attached at each end and the piezoelectric unimorph was bent in the middle of the total piezoelectric unimorph length. The varying angle of orientation

was taken from 0° to 90° angle of orientations with the increasing increment angle of 10° under base excitation in transverse direction. The comparison of multi-mode frequency responses of voltage, current and power showed that the resonances increased with increasing angle of orientation followed by decreasing voltage, current and power output for the first mode. However, the second mode showed the resonances behave in opposite direction with the first mode resonances as the voltage, current and power amplitude decreased with the angle of orientation increase and the amplitude decreased as the angle of orientation increased.

Finally, chapter 7 presented the comparison study between the simulation and experimental tests of the piezoelectric unimorph beam response with different orientation using angles of 0° , 30° , 90° . The resulting research showed that the FRFs of voltage, current and power output were presented having good agreement in behaviour with varying load resistances. Using the 0° angle of orientation, the first modal frequencies for the simulation and experimental work for voltage, current and power output at the short circuit resistance resonance gave 134.2 Hz for the simulation and in the experiment, and at the open circuit resistance resonance, gave 136.3 Hz in the simulation and in the experimental test, respectively. Investigation for the 30° angle of orientation showed that the simulation and experimental work at short circuit resonance gave similar results of 138.3 Hz, where for open circuit resistance, resonance frequencies of 140.5 Hz were found in the simulation and 140.4 Hz in the experimental test, respectively. Investigation for 90° angle of orientations gave the simulation and experimental work at short circuit resistance resonance with resonance frequencies of 179 Hz in the simulation and 178.7 Hz in the experiment and at the open circuit resistance resonance with resonance frequencies of 181.8 Hz in the simulation and experiment test, respectively.

The coupled single finite element model with four degrees of freedom was used to formulate the frequency response function using the direct non-orthonormalised method. Verification of the 4-DOF single element model was given by comparison of the results with previously published research. The transformation of the electromechanical coupling of the single element to the multi element model was formulated using the electromechanical vector transformation. The convergence study showed that a low number of elements gave coarse results whereas increasing the

number of elements gave much improved results as shown with the comparison study using the published research. Extension of the study using six degrees of freedom was explored with the segmented unimorph beam with different angles of orientation and the resulting model was verified using the experimental test to provide confidence in the model and again the results were shown to give good agreement. The development of the finite element analysis using the multi element models has been demonstrated to be very effective for the analysis of different system designs, for example in varying the length of the piezoelectric element and for modelling segmented designs with different angles of orientation.

Research using piezoelectric material for energy harvesting has grown in wide range of applications. Self-power using micro-electromechanical design can be the best solution to avoid the replacement of the limited battery power supply. Condition monitoring in rare or remote areas can be a possible new area to apply the technology. Research contribution especially for optimisation of design is important to broaden the application of the electromechanical dynamic power harvester. The finite element solution of the electromechanical frequency response functions equations can now be possible and can be applied into different novel designs with parallel electrical connections.

Future work suggestion;

1. Power harvesting of the piezoelectric unimorph beam with different angle of orientation using single and double tip mass.
2. Power harvesting of the piezoelectric unimorph beam with different angle of orientation with variation in piezoelectric geometry.
3. Effect of power harvesting under serial connection.

References

- Abdelkefi, A., & Barsallo, N. (2014). Comparative modeling of low-frequency piezomagnetoelastic energy harvesters. *Journal of Intelligent Material Systems and Structures*, 25(14), 1771-1785.
- Abdelkefi, A., Barsallo, N., Tang, L., Yang, Y., & Hajj, M. R. (2014). Modeling, validation, and performance of low-frequency piezoelectric energy harvesters. *Journal of Intelligent Material Systems and Structures*, 25(12), 1429-1444.
- Abdelkefi, A., Hajj, M., & Nayfeh, A. (2012). Piezoelectric energy harvesting from transverse galloping of bluff bodies. *Smart Materials and Structures*, 22(1), 015014.
- Abdelkefi, A., Yan, Z., & Hajj, M. R. (2013). Modeling and nonlinear analysis of piezoelectric energy harvesting from transverse galloping. *Smart Materials and Structures*, 22(2), 025016.
- Ajitsaria, J., Choe, S.-Y., Shen, D., & Kim, D. (2007). Modeling and analysis of a bimorph piezoelectric cantilever beam for voltage generation. *Smart Materials and Structures*, 16(2), 447.
- Akaydin, H. D., Elvin, N., & Andreopoulos, Y. (2010). Energy harvesting from highly unsteady fluid flows using piezoelectric materials. *Journal of Intelligent Material Systems and Structures*, 21(13), 1263-1278.
- Allen, J., & Smits, A. (2001). Energy harvesting eel. *Journal of fluids and structures*, 15(3), 629-640.
- Allik, H., & Hughes, T. J. (1970). Finite element method for piezoelectric vibration. *International journal for numerical methods in engineering*, 2(2), 151-157.
- Anton, S. R., & Sodano, H. A. (2007). A review of power harvesting using piezoelectric materials (2003–2006). *Smart Materials and Structures*, 16(3), R1.
- Arms, S. W., Townsend, C., Churchill, D., Galbreath, J., & Mundell, S. (2005). *Power management for energy harvesting wireless sensors*. Paper presented at the Smart Structures and Materials.

- Ayed, S. B., Abdelkefi, A., Najar, F., & Hajj, M. R. (2013). Design and performance of variable-shaped piezoelectric energy harvesters. *Journal of Intelligent Material Systems and Structures*, 1045389X13489365.
- Beeby, S. P., Tudor, M. J., & White, N. M. (2006). Energy harvesting vibration sources for microsystems applications. *Measurement Science and Technology*, 17(12), R175.
- Bibo, A., Li, G., & Daqaq, M. F. (2011). Electromechanical modeling and normal form analysis of an aeroelastic micro-power generator. *Journal of Intelligent Material Systems and Structures*, 22(6), 577-592.
- Chen, S.-N., Wang, G.-J., & Chien, M.-C. (2006). Analytical modeling of piezoelectric vibration-induced micro power generator. *Mechatronics*, 16(7), 379-387.
- Clough, R. W., & Penzien, J. (1993). *Dynamic of Structures*. New York: Wiley.
- Curie, J., & Curie, P. (1880). On electric polarization in hemihedral crystals with inclined faces. *Comptes Rendus*, 91, 383-386.
- Dayou, J., Kim, J., Im, J., Zhai, L., How, A. T. C., & Liew, W. Y. (2015). The effects of width reduction on the damping of a cantilever beam and its application in increasing the harvesting power of piezoelectric energy harvester. *Smart Materials and Structures*, 24(4), 045006.
- Deng, L., Wen, Q., Jiang, S., Zhao, X., & She, Y. (2015). On the optimization of piezoelectric vibration energy harvester. *Journal of Intelligent Material Systems and Structures*, 26(18), 2489-2499.
- Dutoit, N. E., & Wardle, B. L. (2006). Performance of microfabricated piezoelectric vibration energy harvesters. *Integrated Ferroelectrics*, 83(1), 13-32.
- Dutoit, N. E., Wardle, B. L., & Kim, S.-G. (2005). Design considerations for MEMS-scale piezoelectric mechanical vibration energy harvesters. *Integrated Ferroelectrics*, 71(1), 121-160.

- Elvin, N. G., & Elvin, A. A. (2009a). A coupled finite element—circuit simulation model for analyzing piezoelectric energy generators. *Journal of Intelligent Material Systems and Structures*, 20(5), 587-595.
- Elvin, N. G., & Elvin, A. A. (2009b). A general equivalent circuit model for piezoelectric generators. *Journal of Intelligent Material Systems and Structures*, 20(1), 3-9.
- Erturk, A., & Inman, D. J. (2008a). A distributed parameter electromechanical model for cantilevered piezoelectric energy harvesters. *Journal of Vibration and Acoustics*, 130(4), 041002.
- Erturk, A., & Inman, D. J. (2008b). On mechanical modeling of cantilevered piezoelectric vibration energy harvesters. *Journal of Intelligent Material Systems and Structures*.
- Erturk, A., & Inman, D. J. (2009). An experimentally validated bimorph cantilever model for piezoelectric energy harvesting from base excitations. *Smart Materials and Structures*, 18(2), 025009.
- Erturk, A., Tarazaga, P. A., Farmer, J. R., & Inman, D. J. (2009). Effect of strain nodes and electrode configuration on piezoelectric energy harvesting from cantilevered beams. *Journal of Vibration and Acoustics*, 131(1), 011010.
- Fang, H.-B., Liu, J.-Q., Xu, Z.-Y., Dong, L., Chen, D., Cai, B.-C., & Liu, Y. (2006). A MEMS-based piezoelectric power generator for low frequency vibration energy harvesting. *Chinese Physics Letters*, 23, 732-734.
- Fang, H.-B., Liu, J.-Q., Xu, Z.-Y., Dong, L., Wang, L., Chen, D., . . . Liu, Y. (2006). Fabrication and performance of MEMS-based piezoelectric power generator for vibration energy harvesting. *Microelectronics Journal*, 37(11), 1280-1284.
- Feenstra, J., Granstrom, J., & Sodano, H. (2008). Energy harvesting through a backpack employing a mechanically amplified piezoelectric stack. *Mechanical Systems and Signal Processing*, 22(3), 721-734.

- Ferrari, M., Ferrari, V., Marioli, D., & Taroni, A. (2006). Modeling, fabrication and performance measurements of a piezoelectric energy converter for power harvesting in autonomous microsystems. *IEEE Transactions on Instrumentation and Measurement*, 55(6), 2096-2101.
- Goldschmidtboeing, F., & Woias, P. (2008). Characterization of different beam shapes for piezoelectric energy harvesting. *Journal of Micromechanics and Microengineering*, 18(10), 104013.
- González, J. L., Rubio, A., & Moll, F. (2002). Human powered piezoelectric batteries to supply power to wearable electronic devices. *International journal of the Society of Materials Engineering for Resources*, 10(1), 34-40.
- Granstrom, J., Feenstra, J., Sodano, H. A., & Farinholt, K. (2007). Energy harvesting from a backpack instrumented with piezoelectric shoulder straps. *Smart Materials and Structures*, 16(5), 1810.
- Guan, Q. C., Ju, B., Xu, J. W., Liu, Y. B., & Feng, Z. H. (2013). Improved strain distribution of cantilever piezoelectric energy harvesting devices using H-shaped proof masses. *Journal of Intelligent Material Systems and Structures*, 1045389X13476150.
- Hagood, N. W., Chung, W. H., & Von Flotow, A. (1990). Modelling of piezoelectric actuator dynamics for active structural control. *Journal of Intelligent Material Systems and Structures*, 1(3), 327-354.
- Häsler, E., Stein, L., & Harbauer, G. (1984). Implantable physiological power supply with PVDF film. *Ferroelectrics*, 60(1), 277-282.
- Hobeck, J., & Inman, D. (2012). Artificial piezoelectric grass for energy harvesting from turbulence-induced vibration. *Smart Materials and Structures*, 21(10), 105024.
- Jeon, Y., Sood, R., Jeong, J.-H., & Kim, S.-G. (2005). MEMS power generator with transverse mode thin film PZT. *Sensors and Actuators A: Physical*, 122(1), 16-22.
- Junior, C. D. M., Erturk, A., & Inman, D. J. (2009). An electromechanical finite element model for piezoelectric energy harvester plates. *Journal of Sound and Vibration*, 327(1), 9-25.

- Kim, H., Lee, S., Cho, C., Kim, J. E., Youn, B. D., & Kim, Y. Y. (2015). An experimental method to design piezoelectric energy harvesting skin using operating deflection shapes and its application for self-powered operation of a wireless sensor network. *Journal of Intelligent Material Systems and Structures*, 26(9), 1128-1137.
- Kim, M., Dugundji, J., & Wardle, B. L. (2015). Efficiency of piezoelectric mechanical vibration energy harvesting. *Smart Materials and Structures*, 24(5), 055006.
- Kymissis, J., Kendall, C., Paradiso, J., & Gershenfeld, N. (1998). *Parasitic power harvesting in shoes*. Paper presented at the Wearable Computers, 1998. Digest of Papers. Second International Symposium on.
- Liao, Y., & Sodano, H. A. (2012). Optimal placement of piezoelectric material on a cantilever beam for maximum piezoelectric damping and power harvesting efficiency. *Smart Materials and Structures*, 21(10), 105014.
- Lien, I., & Shu, Y. (2012). Array of piezoelectric energy harvesting by the equivalent impedance approach. *Smart Materials and Structures*, 21(8), 082001.
- Lippmann, G. (1881). Principe de la conservation de l'électricité. *Annales de chimie et de physique (Elsevier)*, 24, 145.
- Liu, J.-Q., Fang, H.-B., Xu, Z.-Y., Mao, X.-H., Shen, X.-C., Chen, D., . . . Cai, B.-C. (2008). A MEMS-based piezoelectric power generator array for vibration energy harvesting. *Microelectronics Journal*, 39(5), 802-806. doi: <http://dx.doi.org/10.1016/j.mejo.2007.12.017>
- Lu, F., Lee, H., & Lim, S. (2003). Modeling and analysis of micro piezoelectric power generators for micro-electromechanical-systems applications. *Smart Materials and Structures*, 13(1), 57.
- Lumentut, M., & Howard, I. (2010). *The analysis of a piezoelectric bimorph beam with two input base motions for power harvesting*. Paper presented at the IOP Conference Series: Materials Science and Engineering.

Lumentut, M., & Howard, I. (2011). Analytical modeling of self-powered electromechanical piezoelectric bimorph beams with multidirectional excitation. *International Journal of Smart and Nano Materials*, 2(3), 134-175.

Lumentut, M., & Howard, I. (2014). Electromechanical finite element modelling for dynamic analysis of a cantilevered piezoelectric energy harvester with tip mass offset under base excitations. *Smart Materials and Structures*, 23(9), 095037.

Lumentut, M. F. (2010). *Mathematical dynamics of electromechanical piezoelectric energy harvesters*: Curtin University of Technology.

Lumentut, M. F., & Howard, I. M. (2009). *An analytical method for vibration modelling of a piezoelectric bimorph beam for power harvesting*. Paper presented at the ASME 2009 Conference on Smart Materials, Adaptive Structures and Intelligent Systems.

Lumentut, M. F., Teh, K., & Howard, I. (2008). Computational FEA model of a coupled piezoelectric sensor and plate structure for energy harvesting. *Australian Journal of Mechanical Engineering*, 5(2), 199-208.

Mateu, L., & Moll, F. (2005). Optimum piezoelectric bending beam structures for energy harvesting using shoe inserts. *Journal of Intelligent Material Systems and Structures*, 16(10), 835-845.

Meitzler, A., Tiersten, H., Warner, A., Berlincourt, D., Couqin, G., & Welsh III, F. (1988). IEEE standard on piezoelectricity: Society.

Mitcheson, P. D., Yeatman, E. M., Rao, G. K., Holmes, A. S., & Green, T. C. (2008). Energy harvesting from human and machine motion for wireless electronic devices. *Proceedings of the IEEE*, 96(9), 1457-1486.

Moaveni, S. (2003). *Finite element analysis: theory and application with ANSYS*: Pearson Education India.

Muthalif, A. G., & Nordin, N. D. (2015). Optimal piezoelectric beam shape for single and broadband vibration energy harvesting: Modeling, simulation and experimental results. *Mechanical Systems and Signal Processing*, 54, 417-426.

- Ou, Q., Chen, X., Gutschmidt, S., Wood, A., Leigh, N., & Arrieta, A. F. (2012). An experimentally validated double-mass piezoelectric cantilever model for broadband vibration-based energy harvesting. *Journal of Intelligent Material Systems and Structures*, 23(2), 117-126.
- Paradiso, J. A., & Starner, T. (2005). Energy scavenging for mobile and wireless electronics. *Pervasive Computing, IEEE*, 4(1), 18-27.
- Park, J. C., & Park, J. Y. (2013). Asymmetric PZT bimorph cantilever for multi-dimensional ambient vibration harvesting. *Ceramics International*, 39, S653-S657.
- Patel, R., McWilliam, S., & Popov, A. A. (2011). A geometric parameter study of piezoelectric coverage on a rectangular cantilever energy harvester. *Smart Materials and Structures*, 20(8), 085004.
- Platt, S. R., Farritor, S., & Haider, H. (2005). On low-frequency electric power generation with PZT ceramics. *Mechatronics, IEEE/ASME Transactions on*, 10(2), 240-252.
- Priya, S. (2005). Modeling of electric energy harvesting using piezoelectric windmill. *Applied Physics Letters*, 87(18), 184101. doi: <http://dx.doi.org/10.1063/1.2119410>
- Priya, S. (2007a). Advances in Energy Harvesting Using Low Profile Piezoelectric Transducers. *Electroceram*, 19, 165-182.
- Priya, S. (2007b). Advances in energy harvesting using low profile piezoelectric transducers. *Journal of electroceramics*, 19(1), 167-184.
- Reddy, J. N. (1993). *An introduction to the finite element method* (Vol. 2): McGraw-Hill New York.
- Richards, C. D., Anderson, M. J., Bahr, D. F., & Richards, R. F. (2004). Efficiency of energy conversion for devices containing a piezoelectric component. *Journal of Micromechanics and Microengineering*, 14(5), 717.
- Roundy, S., & Wright, P. K. (2004). A piezoelectric vibration based generator for wireless electronics. *Smart Materials and Structures*, 13(5), 1131.

- Roundy, S., Wright, P. K., & Rabaey, J. (2003). A study of low level vibrations as a power source for wireless sensor nodes. *Computer communications*, 26(11), 1131-1144.
- Sang, C. M., Dayou, J., & Liew, W. Y. (2013). Increasing the output from piezoelectric energy harvester using width-split method with verification. *International Journal of Precision Engineering and Manufacturing*, 14(12), 2149-2155.
- Schmidt, V. H. (1992). *Piezoelectric energy conversion in windmills*. Paper presented at the IEEE Ultrason. Symp.
- Sirohi, J., & Mahadik, R. (2011). Piezoelectric wind energy harvester for low-power sensors. *Journal of Intelligent Material Systems and Structures*, 1045389X11428366.
- Sodano, H. A., Inman, D. J., & Park, G. (2004). A review of power harvesting from vibration using piezoelectric materials. *Shock and Vibration Digest*, 36(3), 197-206.
- Sodano, H. A., Inman, D. J., & Park, G. (2005a). Comparison of piezoelectric energy harvesting devices for recharging batteries. *Journal of Intelligent Material Systems and Structures*, 16(10), 799-807.
- Sodano, H. A., Inman, D. J., & Park, G. (2005b). Generation and storage of electricity from power harvesting devices. *Journal of Intelligent Material Systems and Structures*, 16(1), 67-75.
- Sodano, H. A., Lloyd, J., & Inman, D. J. (2006). An experimental comparison between several active composite actuators for power generation. *Smart Materials and Structures*, 15(5), 1211.
- Sodano, H. A., Park, G., & Inman, D. J. (2004). Estimation of Electric Charge output for piezoelectric energy harvesting. *Strain*, 40, 49-58. doi: 10.1111/j.1475-1305.2004.00120.x
- Starner, T. (1996). Human-powered wearable computing. *IBM Systems Journal*, 35(3.4), 618-629.

Starner, T., & Paradiso, J. A. (2004). Human generated power for mobile electronics (pp. 1-35): CRC Press.

Tang, L., Yang, Y., & Soh, C.-K. (2012). Improving functionality of vibration energy harvesters using magnets. *Journal of Intelligent Material Systems and Structures*, 1045389X12443016.

Taylor, G. W., Burns, J. R., Kammann, S. M., Powers, W. B., & Wel, T. R. (2001). The energy harvesting eel: a small subsurface ocean/river power generator. *Oceanic Engineering, IEEE Journal of*, 26(4), 539-547.

Voigt, W. (1908). *Lehrbuch der Kristallphysik* (Teubner, Leipzig, 1928). *There is no corresponding record for this reference.*

Wang, X., Ehlers, C., & Neitzel, M. (1997). An analytical investigation of static models of piezoelectric patches attached to beams and plates. *Smart Materials and Structures*, 6(2), 204.

Warman, E., Lumentut, M. F., & Howard, I. M. (2014). *Comparative numerical studies of electromechanical finite element vibration power harvester approaches of a piezoelectric unimorph*. Paper presented at the Advanced Intelligent Mechatronics (AIM), 2014 IEEE/ASME International Conference on.

Xiong, X., & Oyadiji, S. O. (2013). Modal electromechanical optimization of cantilevered piezoelectric vibration energy harvesters by geometric variation. *Journal of Intelligent Material Systems and Structures*, 1045389X13502872.

Yang, Y., & Tang, L. (2009). Equivalent circuit modeling of piezoelectric energy harvesters. *Journal of Intelligent Material Systems and Structures*.

Yoon, H.-S., Washington, G., & Danak, A. (2005). Modeling, optimization, and design of efficient initially curved piezoceramic unimorphs for energy harvesting applications. *Journal of Intelligent Material Systems and Structures*, 16(10), 877-888.

Zhao, L., Tang, L., Yang, Y., & Asme. (2012). *Small Wind Energy Harvesting from Galloping using Piezoelectric Materials*.

Zhao, S., & Erturk, A. (2012). Electroelastic modeling and experimental validations of piezoelectric energy harvesting from broadband random vibrations of cantilevered bimorphs. *Smart Materials and Structures*, 22(1), 015002.

Zhu, M., Worthington, E., & Tiwari, A. (2010). Design study of piezoelectric energy-harvesting devices for generation of higher electrical power using a coupled piezoelectric-circuit finite element method. *IEEE Transactions on Ultrasonics, Ferroelectrics and Frequency Control*, 57(2), 427-437.

Zhu, Q. (2011). Optimal frequency for flow energy harvesting of a flapping foil. *Journal of Fluid Mechanics*, 675(20), 495-517.

"Every reasonable effort has been made to acknowledge the owners of copyright material. I would be pleased to hear from any copyright owner who has been omitted or incorrectly acknowledged."

Appendixes

Appendix A

A.1 Modelling Neutral Axis for Composite Material

The combined neutral axis for two composite materials can be formulated by using force balance summation in the x direction.

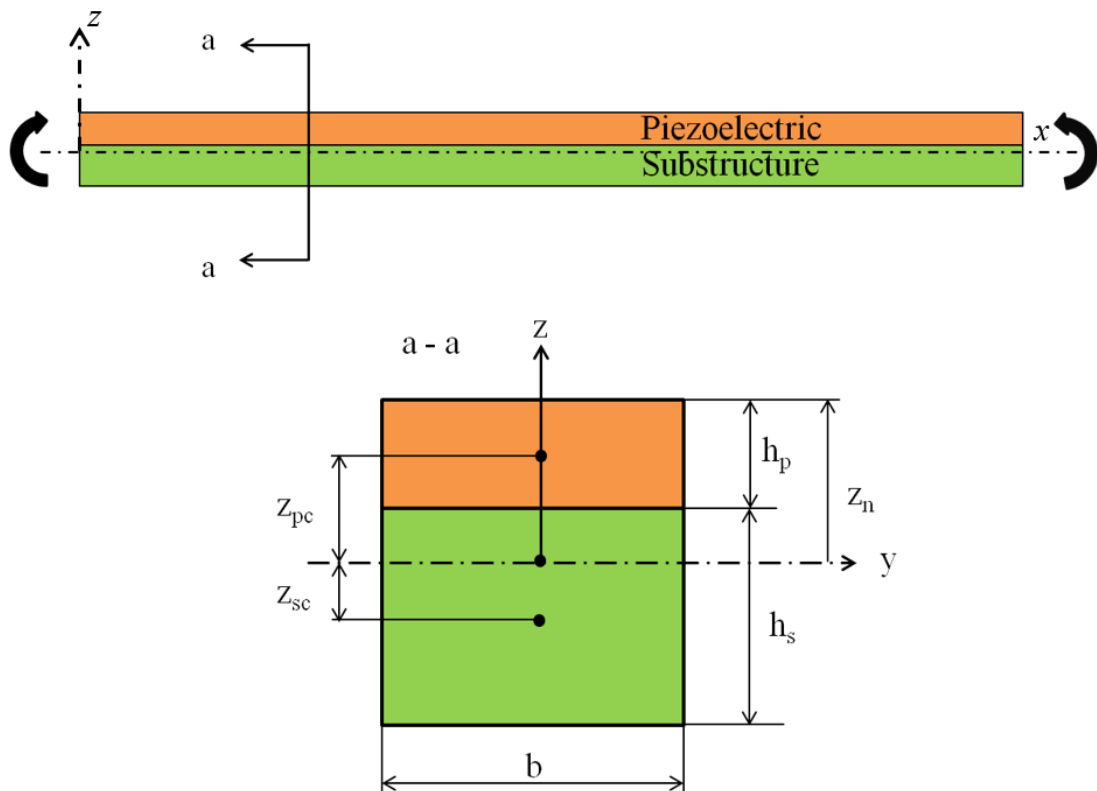


Figure A.1 Unimorph beam with section a-a view

A.2 Uniform Composite Materials Method

Summing forces in the x direction gives,

$$\sum F = 0 \rightarrow \int \sigma dA = 0,$$

which becomes,

$$0 = \int_{A^{(1)}} \sigma_s dA + \int_{A^{(2)}} \sigma_p dA. \quad (\text{A.1})$$

Assume a radius of curvature, ρ , the stress can be written as $\sigma = \frac{c_{11}z}{\rho}$,

Therefore the summation of force balance equation can be represented as,

$$0 = \int_{A^{(1)}} c_{11}^{(1)} \frac{z_{sc}}{\rho} dA + \int_{A^{(2)}} c_{11}^{(2)} \frac{z_{pc}}{\rho} dA. \quad (\text{A.2})$$

Since the curvatures can be assumed to be the same at all locations of the given cross-section, equation (A.2) can be simplified to,

$$0 = \int_{A^{(1)}} c_{11}^{(1)} z_{sc} dA + \int_{A^{(2)}} c_{11}^{(2)} z_{pc} dA. \quad (\text{A.3})$$

Equation (A.3) is not solved by using the integral form since the centroid of each material area will be known. The solution can be done by composing the material into a uniform or homogenous region that will affect the width of material with a constant height. The width of material depends on the ratio of the elastic material modulus where it can be formulated as $b^{(1)}c_{11}^{(1)} = b^{(2)}c_{11}^{(2)}$. The neutral axis can be formulated using summation of the moment for the system.

A.3 Integration Method

Determining the asymmetric neutral axis can also be found by using direct integration of the cross-section shown in figure A.1. This can be written as,

$$\sum F = 0 \rightarrow \int_{-h_s+(z_n-h_p)}^{z_n-h_p} c_{11}^{(1)} z dy dz + \int_{z_n-h_p}^{z_n} c_{11}^{(2)} z dy dz = 0. \quad (\text{A.4})$$

Manipulating equation (A.4), the neutral axis can be formulated as,

$$z_n = \frac{c_{11}^{(1)}h_s^2 + c_{11}^{(2)}h_p^2 + 2c_{11}^{(1)}h_s h_p}{2(c_{11}^{(1)}h_s + c_{11}^{(2)}h_p)}, \quad (\text{A.5})$$

where coefficients $c_{11}^{(1)}$ and $c_{11}^{(2)}$ represent substructure elastic stiffness and piezoelectric elastic stiffness at constant electric field, respectively.

Appendix B

B.1 Parameter Local Elemental Matrices

The local element matrix for the unimorph beam with tip mass is presented by the equations below with the total of four degrees of freedom per element. In case the unimorph beam is without a tip mass, the tip mass term can be ignored in the calculation. It should be noted that the tip mass is only allowable when the tip was attached at the top of the substructure. The local matrices of the unimorph beam can be given as,

$$\begin{aligned} \mathbf{M}^{(e)} = & \frac{\rho^{(1)} A^{(1)} L}{420} \begin{bmatrix} 156 & 22L & 54 & -13L \\ 22L & 4L^2 & 13L & -3L^2 \\ 54 & 13L & 156 & -22L \\ -13L & -3L^2 & -22L & 4L^2 \end{bmatrix} + \frac{\rho^{(2)} A^{(2)} L}{420} \begin{bmatrix} 156 & 22L & 54 & -13L \\ 22L & 4L^2 & 13L & -3L^2 \\ 54 & 13L & 156 & -22L \\ -13L & -3L^2 & -22L & 4L^2 \end{bmatrix} \\ & + 2I_0^{tip} x_c \begin{bmatrix} 0 & 0 & 0 & 0 \\ 0 & 0 & 0 & 0 \\ 0 & 0 & 0 & 1 \\ 0 & 0 & 0 & 0 \end{bmatrix} + I_0^{tip} \begin{bmatrix} 0 & 0 & 0 & 0 \\ 0 & 0 & 0 & 0 \\ 0 & 0 & 1 & 0 \\ 0 & 0 & 0 & 0 \end{bmatrix} + I_2^{tip} \begin{bmatrix} 0 & 0 & 0 & 0 \\ 0 & 0 & 0 & 0 \\ 0 & 0 & 0 & 0 \\ 0 & 0 & 0 & 1 \end{bmatrix} \end{aligned} \quad , \text{(B.1)}$$

$$\mathbf{K}^{(e)} = \frac{c_{11}^{(1)} I^{(1)}}{L^3} \begin{bmatrix} 12 & 6L & -12 & 6L \\ 6L & 4L^2 & -6L & 2L^2 \\ -12 & -6L & 12 & -6L \\ 6L & 2L^2 & -6L & 4L^2 \end{bmatrix} + \frac{c_{11}^{(2)} I^{(2)}}{L^3} \begin{bmatrix} 12 & 6L & -12 & 6L \\ 6L & 4L^2 & -6L & 2L^2 \\ -12 & -6L & 12 & -6L \\ 6L & 2L^2 & -6L & 4L^2 \end{bmatrix} \quad , \text{(B.2)}$$

$$\mathbf{P}_{rs} = \frac{-e_{31} b (2z_n h_p - h_p^2)}{2h_p} [0 \quad -1 \quad 0 \quad 1] \quad , \quad \mathbf{P}_D = -\frac{Lb\varepsilon^s}{h_p} \quad , \quad \text{(B.3)}$$

$$\begin{aligned} \mathbf{Q} = & \frac{\rho^{(1)} A^{(1)} L}{2} \begin{bmatrix} L & 1 & -L \\ 1 & \frac{L}{6} & 1 & -\frac{L}{6} \end{bmatrix} + \frac{\rho^{(2)} A^{(2)} L}{2} \begin{bmatrix} L & 1 & -L \\ 1 & \frac{L}{6} & 1 & -\frac{L}{6} \end{bmatrix} \\ & + I_0^{tip} x_c [0 \quad 0 \quad 0 \quad 1] + I_0^{tip} [0 \quad 0 \quad 1 \quad 0] \quad . \end{aligned} \quad \text{(B.4)}$$

Appendix C

C.1 Determining Transformation Parameter of the Local Element Matrix

In this section, the matrix transformation for the unimorph beam with total of six degrees of freedom per element can be formulated by multiplying the local elemental matrix with the transformation matrix as,

$$\begin{aligned}
 \mathbf{M}_m = & \begin{bmatrix} \cos \theta & \sin \theta & 0 & 0 & 0 & 0 \\ -\sin \theta & \cos \theta & 0 & 0 & 0 & 0 \\ 0 & 0 & 1 & 0 & 0 & 0 \\ 0 & 0 & 0 & \cos \theta & \sin \theta & 0 \\ 0 & 0 & 0 & -\sin \theta & \cos \theta & 0 \\ 0 & 0 & 0 & 0 & 0 & 1 \end{bmatrix}^T \times \frac{\rho A^{(1)} L}{420} \begin{bmatrix} 140 & 0 & 0 & 70 & 0 & 0 \\ 0 & 156 & 22L & 0 & 54 & -13L \\ 0 & 22L & 4L^2 & 0 & 13L & -3L^2 \\ 70 & 0 & 0 & 140 & 0 & 0 \\ 0 & 54 & 13L & 0 & 156 & -22L \\ 0 & -13L & -3L^2 & 0 & -22L & 4L^2 \end{bmatrix} \\
 & \times \begin{bmatrix} \cos \theta & \sin \theta & 0 & 0 & 0 & 0 \\ -\sin \theta & \cos \theta & 0 & 0 & 0 & 0 \\ 0 & 0 & 1 & 0 & 0 & 0 \\ 0 & 0 & 0 & \cos \theta & \sin \theta & 0 \\ 0 & 0 & 0 & -\sin \theta & \cos \theta & 0 \\ 0 & 0 & 0 & 0 & 0 & 1 \end{bmatrix} + \begin{bmatrix} \cos \theta & \sin \theta & 0 & 0 & 0 & 0 \\ -\sin \theta & \cos \theta & 0 & 0 & 0 & 0 \\ 0 & 0 & 1 & 0 & 0 & 0 \\ 0 & 0 & 0 & \cos \theta & \sin \theta & 0 \\ 0 & 0 & 0 & -\sin \theta & \cos \theta & 0 \\ 0 & 0 & 0 & 0 & 0 & 1 \end{bmatrix}^T \\
 & \times \frac{\rho A^{(2)} L}{420} \begin{bmatrix} 140 & 0 & 0 & 70 & 0 & 0 \\ 0 & 156 & 22L & 0 & 54 & -13L \\ 0 & 22L & 4L^2 & 0 & 13L & -3L^2 \\ 70 & 0 & 0 & 140 & 0 & 0 \\ 0 & 54 & 13L & 0 & 156 & -22L \\ 0 & -13L & -3L^2 & 0 & -22L & 4L^2 \end{bmatrix} \times \begin{bmatrix} \cos \theta & \sin \theta & 0 & 0 & 0 & 0 \\ -\sin \theta & \cos \theta & 0 & 0 & 0 & 0 \\ 0 & 0 & 1 & 0 & 0 & 0 \\ 0 & 0 & 0 & \cos \theta & \sin \theta & 0 \\ 0 & 0 & 0 & -\sin \theta & \cos \theta & 0 \\ 0 & 0 & 0 & 0 & 0 & 1 \end{bmatrix}, \tag{C.1}
 \end{aligned}$$

$$\begin{aligned}
& \mathbf{K}_m = \begin{bmatrix} \cos \theta & \sin \theta & 0 & 0 & 0 & 0 \\ -\sin \theta & \cos \theta & 0 & 0 & 0 & 0 \\ 0 & 0 & 1 & 0 & 0 & 0 \\ 0 & 0 & 0 & \cos \theta & \sin \theta & 0 \\ 0 & 0 & 0 & -\sin \theta & \cos \theta & 0 \\ 0 & 0 & 0 & 0 & 0 & 1 \end{bmatrix}^T \\
& \times \begin{bmatrix} \frac{A^{(1)}c_{11}^{(1)}}{L} & 0 & 0 & -\frac{A^{(1)}c_{11}^{(1)}}{L} & 0 & 0 \\ 0 & \frac{12c_{11}^{(1)}I^{(1)}}{L^3} & \frac{6c_{11}^{(1)}I^{(1)}}{L^2} & 0 & -\frac{12c_{11}^{(1)}I^{(1)}}{L^3} & \frac{6c_{11}^{(1)}I^{(1)}}{L^2} \\ 0 & \frac{6c_{11}^{(1)}I^{(1)}}{L^2} & \frac{4c_{11}^{(1)}I^{(1)}}{L} & 0 & -\frac{6c_{11}^{(1)}I^{(1)}}{L^2} & \frac{2c_{11}^{(1)}I^{(1)}}{L} \\ -\frac{A^{(1)}c_{11}^{(1)}}{L} & 0 & 0 & \frac{A^{(1)}c_{11}^{(1)}}{L} & 0 & 0 \\ 0 & -\frac{12c_{11}^{(1)}I^{(1)}}{L^3} & -\frac{6c_{11}^{(1)}I^{(1)}}{L^2} & 0 & \frac{12c_{11}^{(1)}I^{(1)}}{L^3} & -\frac{6c_{11}^{(1)}I^{(1)}}{L^2} \\ 0 & \frac{6c_{11}^{(1)}I^{(1)}}{L^2} & \frac{2c_{11}^{(1)}I^{(1)}}{L} & 0 & -\frac{6c_{11}^{(1)}I^{(1)}}{L^2} & \frac{4c_{11}^{(1)}I^{(1)}}{L} \end{bmatrix} \\
& \times \begin{bmatrix} \cos \theta & \sin \theta & 0 & 0 & 0 & 0 \\ -\sin \theta & \cos \theta & 0 & 0 & 0 & 0 \\ 0 & 0 & 1 & 0 & 0 & 0 \\ 0 & 0 & 0 & \cos \theta & \sin \theta & 0 \\ 0 & 0 & 0 & -\sin \theta & \cos \theta & 0 \\ 0 & 0 & 0 & 0 & 0 & 1 \end{bmatrix} + \begin{bmatrix} \cos \theta & \sin \theta & 0 & 0 & 0 & 0 \\ -\sin \theta & \cos \theta & 0 & 0 & 0 & 0 \\ 0 & 0 & 1 & 0 & 0 & 0 \\ 0 & 0 & 0 & \cos \theta & \sin \theta & 0 \\ 0 & 0 & 0 & -\sin \theta & \cos \theta & 0 \\ 0 & 0 & 0 & 0 & 0 & 1 \end{bmatrix}^T \\
& \times \begin{bmatrix} \frac{A^{(2)}c_{11}^{(2)}}{L} & 0 & 0 & -\frac{A^{(2)}c_{11}^{(2)}}{L} & 0 & 0 \\ 0 & \frac{12c_{11}^{(2)}I^{(2)}}{L^3} & \frac{6c_{11}^{(2)}I^{(2)}}{L^2} & 0 & -\frac{12c_{11}^{(2)}I^{(2)}}{L^3} & \frac{6c_{11}^{(2)}I^{(2)}}{L^2} \\ 0 & \frac{6c_{11}^{(2)}I^{(2)}}{L^2} & \frac{4c_{11}^{(2)}I^{(2)}}{L} & 0 & -\frac{6c_{11}^{(2)}I^{(2)}}{L^2} & \frac{2c_{11}^{(2)}I^{(2)}}{L} \\ -\frac{A^{(2)}c_{11}^{(2)}}{L} & 0 & 0 & \frac{A^{(2)}c_{11}^{(2)}}{L} & 0 & 0 \\ 0 & -\frac{12c_{11}^{(2)}I^{(2)}}{L^3} & -\frac{6c_{11}^{(2)}I^{(2)}}{L^2} & 0 & \frac{12c_{11}^{(2)}I^{(2)}}{L^3} & -\frac{6c_{11}^{(2)}I^{(2)}}{L^2} \\ 0 & \frac{6c_{11}^{(2)}I^{(2)}}{L^2} & \frac{2c_{11}^{(2)}I^{(2)}}{L} & 0 & -\frac{6c_{11}^{(2)}I^{(2)}}{L^2} & \frac{4c_{11}^{(2)}I^{(2)}}{L} \end{bmatrix} \\
& \times \begin{bmatrix} \cos \theta & \sin \theta & 0 & 0 & 0 & 0 \\ -\sin \theta & \cos \theta & 0 & 0 & 0 & 0 \\ 0 & 0 & 1 & 0 & 0 & 0 \\ 0 & 0 & 0 & \cos \theta & \sin \theta & 0 \\ 0 & 0 & 0 & -\sin \theta & \cos \theta & 0 \\ 0 & 0 & 0 & 0 & 0 & 1 \end{bmatrix} , \quad (\text{C.2})
\end{aligned}$$

$$\mathbf{P}_{sn} \equiv \begin{bmatrix} \cos \theta & \sin \theta & 0 & 0 & 0 & 0 \\ -\sin \theta & \cos \theta & 0 & 0 & 0 & 0 \\ 0 & 0 & 1 & 0 & 0 & 0 \\ 0 & 0 & 0 & \cos \theta & \sin \theta & 0 \\ 0 & 0 & 0 & -\sin \theta & \cos \theta & 0 \\ 0 & 0 & 0 & 0 & 0 & 1 \end{bmatrix}^T \times \left\{ \frac{-e_{31}b(2z_n h_p - h_p^2)}{2h_p} \times [0 \ 0 \ -1 \ 0 \ 0 \ 1] \right\} , \quad (\text{C.3})$$

$$\mathbf{P}_D = -\frac{Lb\varepsilon^s}{h_p}, \quad (\text{C.4})$$

$$\mathbf{Q}_r = \begin{bmatrix} \cos\theta & \sin\theta & 0 & 0 & 0 & 0 \\ -\sin\theta & \cos\theta & 0 & 0 & 0 & 0 \\ 0 & 0 & 1 & 0 & 0 & 0 \\ 0 & 0 & 0 & \cos\theta & \sin\theta & 0 \\ 0 & 0 & 0 & -\sin\theta & \cos\theta & 0 \\ 0 & 0 & 0 & 0 & 0 & 1 \end{bmatrix}^T \times \left\{ \frac{\rho^{(1)} A^{(1)} L}{2} \times \left[0 \quad 1 \quad \frac{L}{6} \quad 0 \quad 1 \quad \frac{L}{6} \right] \right\} \\ + \begin{bmatrix} \cos\theta & \sin\theta & 0 & 0 & 0 & 0 \\ -\sin\theta & \cos\theta & 0 & 0 & 0 & 0 \\ 0 & 0 & 1 & 0 & 0 & 0 \\ 0 & 0 & 0 & \cos\theta & \sin\theta & 0 \\ 0 & 0 & 0 & -\sin\theta & \cos\theta & 0 \\ 0 & 0 & 0 & 0 & 0 & 1 \end{bmatrix}^T \times \left\{ \frac{\rho^{(2)} A^{(2)} L}{2} \times \left[0 \quad 1 \quad \frac{L}{6} \quad 0 \quad 1 \quad \frac{L}{6} \right] \right\} \quad . (\text{C.5})$$

Appendix D

D.1 Piezoelectric Constitutive Equation

The standard form of the piezoelectric constitutive equation can be given as,

$$S_{ij} = s_{ijkl}^E T_{kl} + d_{kij} E_k, \quad (D.1)$$

$$D_i = d_{ikl} T_{kl} + \varepsilon_{ik}^T E_k. \quad (D.2)$$

The formation equation (D.1) and (D.2) can also be reformed into the following form,

$$T_{ij} = c_{ijkl}^E S_{kl} - e_{kij} E_k, \quad (D.3)$$

$$D_i = e_{ikl} S_{kl} + \varepsilon_{ik}^S E_k. \quad (D.4)$$

Equation (D.3) and (D.4) can be presented in matrix form as,

$$\begin{Bmatrix} \mathbf{T} \\ \mathbf{D} \end{Bmatrix} = \begin{bmatrix} \mathbf{c}^E & -\mathbf{e} \\ \mathbf{e} & \boldsymbol{\varepsilon}^S \end{bmatrix} \begin{Bmatrix} \mathbf{S} \\ \mathbf{E} \end{Bmatrix}, \quad (D.5)$$

where \mathbf{T} , \mathbf{D} , \mathbf{S} and \mathbf{E} represent as stress, electric displacement, strain and electric field. The superscript E and S represent that the constants are evaluated at constant electric field and constant strain, respectively. Equation (D.3) can be expanded into 3D formation as,

$$\begin{Bmatrix} T_1 \\ T_2 \\ T_3 \\ T_4 \\ T_5 \\ T_6 \\ D_1 \\ D_2 \\ D_3 \end{Bmatrix} = \begin{bmatrix} c_{11}^E & c_{12}^E & c_{13}^E & 0 & 0 & 0 & 0 & 0 & 0 & e_{31} \\ c_{12}^E & c_{11}^E & c_{13}^E & 0 & 0 & 0 & 0 & 0 & 0 & e_{31} \\ c_{13}^E & c_{13}^E & c_{33}^E & 0 & 0 & 0 & 0 & 0 & 0 & e_{33} \\ 0 & 0 & 0 & c_{44}^E & 0 & 0 & 0 & e_{15} & 0 & 0 \\ 0 & 0 & 0 & 0 & c_{44}^E & 0 & e_{15} & 0 & 0 & 0 \\ 0 & 0 & 0 & 0 & 0 & c_{66}^E & 0 & 0 & 0 & 0 \\ 0 & 0 & 0 & 0 & e_{15} & 0 & \varepsilon_{11}^S & 0 & 0 & 0 \\ 0 & 0 & 0 & e_{15} & 0 & 0 & 0 & \varepsilon_{22}^S & 0 & 0 \\ e_{31} & e_{31} & e_{33} & 0 & 0 & 0 & 0 & 0 & 0 & \varepsilon_{33}^S \end{bmatrix} \begin{Bmatrix} S_1 \\ S_2 \\ S_3 \\ S_4 \\ S_5 \\ S_6 \\ E_1 \\ E_1 \\ E_1 \end{Bmatrix}. \quad (D.6)$$

where the contracted notation based on Voigt's notation gives $11 \rightarrow 1$, $22 \rightarrow 2$, $33 \rightarrow 3$, $23 \rightarrow 4$, $13 \rightarrow 5$, $12 \rightarrow 6$, it was used so that the vectors of stress and strain components are

$$\begin{Bmatrix} T_1 \\ T_2 \\ T_3 \\ T_4 \\ T_5 \\ T_6 \end{Bmatrix} = \begin{Bmatrix} T_{11} \\ T_{22} \\ T_{33} \\ T_{23} \\ T_{13} \\ T_{12} \end{Bmatrix}, \begin{Bmatrix} S_1 \\ S_2 \\ S_3 \\ S_4 \\ S_5 \\ S_6 \end{Bmatrix} = \begin{Bmatrix} S_{11} \\ S_{22} \\ S_{33} \\ 2S_{23} \\ 2S_{13} \\ 2S_{12} \end{Bmatrix}. \quad (\text{D.7})$$

D.2 Reduced Equation for Thin Beam

If the thin piezoelectric element is modelled based on the Euler-Bernoulli beam theory or Rayleigh beam theory, zero-stress components will happen in terms of,

$$T_2 = T_3 = T_4 = T_5 = T_6 = 0. \quad (\text{D.8})$$

Therefore the stress-electric displacement form of the reduced constitutive equation can be given as,

$$\begin{Bmatrix} T_1 \\ D_1 \end{Bmatrix} = \begin{bmatrix} c_{11}^E & -e_{31} \\ e_{31} & \epsilon_{33}^S \end{bmatrix} \begin{Bmatrix} S_1 \\ E_3 \end{Bmatrix}. \quad (\text{D.9})$$

The component of elastic modulus, piezoelectric constant and permittivity can be reduced from the three-dimensional form to the plane-stress condition, giving,

$$c_{11}^E = \frac{1}{s_{11}^E}, \quad e_{31} = \frac{d_{31}}{s_{11}^E}, \quad \epsilon_{33}^S = \epsilon_{33}^T - \frac{d_{31}^2}{s_{11}^E}. \quad (\text{D.10})$$

Appendix E

E.1 Three-dimensional Form of the Constitutive for Isotropic Material

The tensor representation of the three-dimensional situation for isotropic material can be given as,

$$\begin{Bmatrix} T_1 \\ T_2 \\ T_3 \\ T_4 \\ T_5 \\ T_6 \end{Bmatrix} = \frac{c_{11}}{(1+\nu)+(1-2\nu)} \begin{bmatrix} 1-\nu & \nu & \nu & 0 & 0 & 0 \\ \nu & 1-\nu & \nu & 0 & 0 & 0 \\ \nu & \nu & 1-\nu & 0 & 0 & 0 \\ 0 & 0 & 0 & (1-2\nu)/2 & 0 & 0 \\ 0 & 0 & 0 & 0 & (1-2\nu)/2 & 0 \\ 0 & 0 & 0 & 0 & 0 & (1-2\nu)/2 \end{bmatrix} \begin{Bmatrix} S_1 \\ S_2 \\ S_3 \\ S_4 \\ S_5 \\ S_6 \end{Bmatrix}, \quad (\text{E.1})$$

E.2 Reduced for Thin Beam

If the thin piezoelectric element is modelled based on the Euler-Bernoulli beam theory or Rayleigh beam theory, zero-stress components occurs in terms of,

$$T_2 = T_3 = T_4 = T_5 = T_6 = 0. \quad (\text{E.2})$$

Therefore, equation (E.1) can be reduced to,

$$T_1 = c_{11}^E S_1. \quad (\text{E.3})$$

Appendix F

```

% =====
% MATLAB FEA Piezoelectric unimorph power Harvesting
% USING SINGLE ELEMENT
% Written by Eziwarman
% Department Mechanical Engineering Curtin University Australia
% =====
clear all
clc
n=1; % number of elements
% =====
% Beam parameters
% =====
len=100e-3; % total length of beam
b=20e-3; % width of structure and PZT
hs=.5e-3; % thickness of structure
hp=.4e-3; % thickness of PZT
a=b*(hs); % area of structure
a_p=b*(hp); % area of PZT
le=len/n; % length of finite element
% =====
% Properties of the beam
% =====
Es=100e9; % Young's modulus [steel]
Ep=66e9; % Young's Modulus [PZT]
rho_s=7165; % density structure in [kg/m^3]
rho_p=7800; % density PZT in [kg/m^3]
e31=-12.54; % Piezoelectric constant (C/m^2)
eps33=1.3555e-008; % Permittivity of constant strain
i_s=(b*(hs.^3))/12; % second area of moment inertia of
%cross section structure
i_p=(b*(hp.^3))/12; % second area of moment inertia of
%cross section PZT
% =====
% Finding the neutral axis from top PZT to neutral axis
% =====
zn=centroid(Es,Ep,hp,hs); % neutral axis
% =====
% Finding the neutral axis from bottom structure to neutral axis
% =====
nr=Es/Ep; % Ratio of Young Modulus
hs_1=((hp.^2)+(2*hp*hs)+(nr*(hs.^2))); % Numerator finding
neutral axis
hs_2=2*(hp+(nr*hs)); % Denominator finding
neutral axis
hsa_1=hs_1/hs_2; % Distance neutral axis
from bottom
hpa=(hs+hp)-hsa_1; % confirm neutral axis
% =====
% Finding the inertia of the substructure and piezoelectric
% =====
d_s=hsa_1-(hs/2); % Distance neutral axis to centroid structure
d_p=zn-(hp/2); % Distance neutral axis to centroid piezoelectric
ad=a*(d_s.^2); % Distance to neutral axis
% =====
% Inertia structure and Piezoelectric
% =====
in_s=i_s+(a*(d_s.^2)); % Inertia structure
in_p=i_p+(a_p*(d_p.^2)); % Inertia Piezoelectric

```

```

% =====
% element mass matrix
% =====
me=[156 22*le 54 -13*le;...
    22*le 4*le.^2 13*le -3*le.^2;...
    54 13*le 156 -22*le;...
    -13*le -3*le.^2 -22*le 4*le.^2];
ms=((rho_s*a*le)/420)*me; % mass structure
mp=((rho_p*a_p*le)/420)*me; % mass piezoelectric
% =====
% element stiffness matrix
% =====
ke=[12 6*le -12 6*le;...
    6*le 4*le.^2 -6*le 2*le.^2;...
    -12 -6*le 12 -6*le;...
    6*le 2*le.^2 -6*le 4*le.^2];
ks=((Es*in_s)/(le.^3))*ke; % stiffness structure
kp=((Ep*in_p)/(le.^3))*ke; % stiffness piezoelectric
% =====
% electromechanical coupling
% =====
const=-e31*b*(2*zn*hp-(hp^2))/(hp^2);
cstru=const*[0 -1 0 1]; % coupling matrices
ksp=cstru;
% =====
% force matrix
% =====
fs=(rho_s*a*le)/2;
Qs=fs*[1 le/6 1 -le/6]';
fp=(rho_p*a_p*le)/2;
Qp=fp*[1 le/6 1 -le/6]';
Q1=Qs+Qp; % force matrices
% =====
% capacitance
% =====
kpp=(le*b*-eps33)/hp;
% =====
% Assemble global each mass and stiffness matrix
% =====
M=ms+mp; % Global mass matrices struc and PZT
K=ks+kp; % Global Stiffness matrices struc and PZT and couple
% =====
% Global Mechanical damping matrix
% =====
alpha=4.886;
beta=1.2433e-5;
C=(alpha*M)+(beta*K);
% =====
% Applying boundary condition
% =====
bc=[1 2]; % zero boundary transverse and rotation
M(bc,:)=[];
M(:,bc)=[];
Mc=M;
K(bc,:)=[];
K(:,bc)=[];
Kc=K;
C(bc,:)=[];
C(:,bc)=[];
Cc=C;
ksp(:,bc)=[];

```

```

ksp1=ksp';
Q1(bc,:)=[];
Q=Q1;
% =====
% Vector transformation
% =====
pshi=ones(1,n); % Function transforming coupling to scalar matrix
kspc=ksp1*pshi';
% =====
% Finding natural frequency
% =====
invm=inv(Mc);
kmod=invm*(Kc);
[d,v]=eig(kmod);
freq_nat=sqrt(eig(kmod));
f_nat=sort(freq_nat/(2*pi));
% =====
% iterating input frequency range
% =====
freq_end=1000; % input last frequency
hrqf=freq_end*2*pi;
hrqi=2*pi*10; % input initial frequency
deltahrq=1;
nhrq=fix((hrqf-hrqi)/deltahrq)+1;%the number of the generated freq
% =====
% iterating the electrical voltage, current and power
% =====
freq=zeros(5,nhrq);
nl=0;
s2=0;
% =====
% iterating input load resistance
% =====
for Rdd=[1e2 1e3 1e4 1e5 1e6];
nl=nl+1;
for r=hrqi:deltahrq:hrqf; % iterating input frequency
Rl=-1/Rdd;
s2=s2+1;
freq(nl,s2)=freq(nl,s2)+(inv((kpp*i*r+Rl)-kspc'*i*r*(inv(Kc-
Mc*r.^2+Cc*i*r)*kspc))*kspc'*i*r*(inv(Kc-Mc*r.^2+Cc*i*r)*Q));
end
s2=0;
end
figure(1)
nqr=hrqi:deltahrq:hrqf;
semilogy(nqr/(2*pi),(abs(freq)));
xlabel('Frequency(Hz)');
ylabel('Voltage(V/ms^-2)');
legend('10^2 Ohms','10^3 Ohms','10^4 Ohms','10^5 Ohms','10^6
Ohms',1);
% =====
% Iterating electrical current
% =====
cur=zeros(5,nhrq);
nl=0;
s2=0;
% iterating input load resistance
for Rdd=[1e2 1e3 1e4 1e5 1e6];
nl=nl+1;
for r=hrqi:deltahrq:hrqf;% iterating input frequency
Rl=(-1/Rdd);

```

```

s2=s2+1;
cur(n1,s2)=cur(n1,s2)+(-Rl)*(inv((kpp*i*r+Rl)-kspc'*i*r*(inv(Kc-
Mc*r^2+Cc*i*r)*kspc))*(kspc'*i*r*(inv(Kc-Mc*r^2+Cc*i*r)*Q)));
end
s2=0;
end
figure(2)
nqr=hrqi:deltahrq:hrqf;
semilogy(nqr/(2*pi),(abs(cur)));
xlabel('Frequency(Hz)');
ylabel('Electrical Current(A/ms^-2)');
legend('10^2 Ohms','10^3 Ohms','10^4 Ohms','10^5 Ohms','10^6
Ohms',1);
% =====
% Iterating electrical power
% =====
Pow=zeros(5,nhrq);
n1=0;
s2=0;
% iterating input load resistance
for Rdd=[1e2 1e3 1e4 1e5 1e6];
n1=n1+1;
for r=hrqi:deltahrq:hrqf; % iterating input frequency
Rl=-1/Rdd;
s2=s2+1;
Pow(n1,s2)=Pow(n1,s2)+(-Rl)*(inv((kpp*i*r+Rl)-kspc'*i*r*(inv(Kc-
Mc*r.^2+Cc*i*r)*kspc))*(kspc'*i*r*(inv(Kc-Mc*r.^2+Cc*i*r)*Q))).^2;
end
s2=0;
end
figure(3)
nqr=hrqi:deltahrq:hrqf;
semilogy(nqr/(2*pi),(abs(Pow)));
xlabel('Frequency(Hz)');
ylabel('Power Harvesting(W/m^2s^-4)');
legend('10^2 Ohms','10^3 Ohms','10^4 Ohms','10^5 Ohms','10^6
Ohms',1);

% =====
%           MATLAB Piezoelectric Unimorph beam Power Harvesting
%           Multi elements using non-orthonormalised Method
%           Validation with published research A. Erturk and D.J. Inman
%           Written by Eziwarman
% =====
clear all
clc
n=20; % number of elements
% =====
% Beam parameters
% =====
len=100e-3; % total length of beam
b=20e-3; % width of structure and PZT
hs=.5e-3; % thickness of structure
hp=.4e-3; % thickness of PZT
a=b*(hs); % area of structure
a_p=b*(hp); % area of PZT
le=len/n; % length of finite element
% =====
% Properties of the beam
% =====
Es=100e9; % Young's modulus [steel]

```

```

Ep=66e9; % Young's Modulus [PZT]
rho_s=7165; % density structure in [kg/m^3]
rho_p=7800; % density PZT in [kg/m^3]
e31=-12.54; % Piezoelectric constant (C/m^2)
eps33=1.3555e-008; % Permittivity of constant strain
i_s=(b*(hs.^3))/12; % second area of moment inertia of
cross % section structure

i_p=(b*(hp.^3))/12; % second area of moment inertia of
cross % section PZT

% =====
% Finding the neutral axis from top PZT to neutral axis
% =====
zn=centroid(Es,Ep,hp,hs); % neutral axis
% =====
% Finding the neutral axis from bottom structure to neutral axis
% =====
nr=Es/Ep; % Ratio of Young Modulus
hs_1=((hp.^2)+(2*hp*hs)+(nr*(hs.^2))); % Numerator finding
neutral axis
hs_2=2*(hp+(nr*hs)); % Denominator for finding
neutral axis
hsa_1=hs_1/hs_2; % Distance neutral axis
from bottom
hpa=(hs+hp)-hsa_1; % confirm neutral axis
% =====
% Finding the inertia structure and piezo
% =====
d_s=hsa_1-(hs/2); % Distance neutral axis to centroid structure
d_p=zn-(hp/2); % Distance neutral axis to centroid piezoelectric
ad=a*(d_s.^2); % Distance to neutral axis
% =====
% Inertia structure and Piezo electric
% =====
in_s=i_s+(a*(d_s.^2)); % Inertia structure
in_p=i_p+(a_p*(d_p.^2)); % Inertia Piezoelectric
% =====
% element mass matrix
% =====
ms=mstruc(rho_s,a,le); % mass structure
mp=mpiezo(rho_p,a_p,le); % mass piezoelectric
% =====
% element stiffness matrix
% =====
ks=sstruc(Es,in_s,le); % stiffness structure
kp=spiezo(Ep,in_p,le); % stiffness piezoelectric
cstru=cpl(b,hp,e31,zn); % electromechanical coupling
fto=force(le,a,rho_s,a_p,rho_p); % force
cp=(le*b*-eps33)/hp; % capacitance each element
% =====
% Arrangement of global matrix
% =====
[msg,mpg]=mglobal(n,ms,mp); % Global matrices structure
[ksg,kpg]=kglobal(n,ks,kp); % Global matrices piezoelectric
[ksp,cstrug]=cplse(n,cstru); % Global piezo coupling matrix
[Q1]=gforce(n,fto);
[kpp]=capt(n,cp);
sum=trace(kpp);
% =====
% Total global Matrix

```

```

% =====
M=msg+mpg;      % Global mass matrices struc and PZT
K=ksg+kpg;      % Global Stiffness matrices struc and PZT and couple
% =====
% Global Mechanical damping matrix
% =====
alpha=4.886;
beta=1.2433e-5;
C=(alpha*M)+(beta*K);
% =====
% Applying boundary condition
% =====
bc=[1 2];      % zero boundary transverse and rotation
M(bc,:)=[];
M(:,bc)=[];
Mc=M;
K(bc,:)=[];
K(:,bc)=[];
Kc=K;
C(bc,:)=[];
C(:,bc)=[];
Cc=C;
ksp(:,bc)=[];
ksp1=ksp';
Q1(bc,:)=[];
Q=Q1;
% =====
% Transformation coupling
% =====
pshi=ones(1,n); % Function transforming coupling to scalar matrix
kspc=ksp1*pshi';
% =====
% Finding Undamped natural fix-free
% =====
% Finding eigenvalue and eigenvector
% =====
invm=inv(Mc);
kmmod=invm*Kc;
[d,v]=eig(kmmod);
freq_nat=sqrt(eig(kmmod));
f_nat=sort(freq_nat/(2*pi));
% =====
% Finding Voltage response
% =====
% Iterating input frequency range
% =====
freq_end=1000;      % input last frequency
hrqf=freq_end*2*pi;
hrqi=2*pi*0;      % input initial frequency
deltahrq=1;
nhrq=fix((hrqf-hrqi)/deltahrq)+1; % the number of the generated
                                frequency
% =====
% Iterating the electrical voltage, current and power
% =====
freq=zeros(5,nhrq);
nl=0;
s2=0;
% =====
% Iterating input load resistance
% =====

```

```

for Rdd=[1e2 1e3 1e4 1e5 1e6];
nl=nl+1;
for r=hrqi:deltahrq:hrqf; % iterating input frequency
Rl=-1/Rdd;
s2=s2+1;
freq(nl,s2)=freq(nl,s2)+(inv((sum*i*r+Rl)-kspc'*i*r*(inv(Kc-
Mc*r.^2+Cc*i*r)*kspc)))*(kspc'*i*r*(inv(Kc-Mc*r.^2+Cc*i*r)*Q)));
end
s2=0;
end
figure(1)
nqr=hrqi:deltahrq:hrqf;
semilogy(nqr/(2*pi),(abs(freq)));
xlabel('Frequency(Hz)');
ylabel('Voltage(V/ms^-2)');
legend('10^2 Ohms','10^3 Ohms','10^4 Ohms','10^5 Ohms','10^6
Ohms',1);
hold on
% Iterating electrical current
cur=zeros(5,nhrq);
nl=0;
s2=0;
% iterating input load resistance
for Rdd=[1e2 1e3 1e4 1e5 1e6];
nl=nl+1;
for r=hrqi:deltahrq:hrqf;% iterating input frequency
Rl=(-1/Rdd);
s2=s2+1;
cur(nl,s2)=cur(nl,s2)+(-Rl)*(inv((sum*i*r+Rl)-kspc'*i*r*(inv(Kc-
Mc*r.^2+Cc*i*r)*kspc)))*(kspc'*i*r*(inv(Kc-Mc*r.^2+Cc*i*r)*Q)));
end
s2=0;
end
figure(2)
nqr=hrqi:deltahrq:hrqf;
semilogy(nqr/(2*pi),(abs(cur)));
xlabel('Frequency(Hz)');
ylabel('Electrical Current(A/ms^-2)');
legend('10^2 Ohms','10^3 Ohms','10^4 Ohms','10^5 Ohms','10^6
Ohms',1);
hold on
% Iterating electrical power
Pow=zeros(5,nhrq);
nl=0;
s2=0;
% iterating input load resistance
for Rdd=[1e2 1e3 1e4 1e5 1e6];
nl=nl+1;
for r=hrqi:deltahrq:hrqf; % iterating input frequency
Rl=-1/Rdd;
s2=s2+1;
Pow(nl,s2)=Pow(nl,s2)+(-Rl)*(inv((sum*i*r+Rl)-kspc'*i*r*(inv(Kc-
Mc*r.^2+Cc*i*r)*kspc)))*(kspc'*i*r*(inv(Kc-Mc*r.^2+Cc*i*r)*Q))).^2;
end
s2=0;
end
figure(3)
nqr=hrqi:deltahrq:hrqf;
semilogy(nqr/(2*pi),(abs(Pow)));
xlabel('Frequency(Hz)');
ylabel('Power Harvesting(W/m^2s^-4)');

```

```

legend('10^2 Ohms','10^3 Ohms','10^4 Ohms','10^5 Ohms','10^6
Ohms',1);
hold on

% =====
% Function Command
% =====

function [capg]=capt(n,cp);
cap=eye(n,n);
capg=(cp*cap);

function zn=centroid(Es,Ep,hp,hs)
% Finding the neutral axis
zn_1=(Es*(hs.^2))+ (Ep*(hp.^2))+2*(Es*hs*hp);
zn_2=2*( (Es*hs)+(Ep*hp));
zn=zn_1/zn_2;

function [cp]=cap(le,b,eps,hp);
cp=-(le*b*eps)/hp;

function cstru=cpl(b,hp,e31,zn);
const=-(e31*b*(2*zn*hp)-(hp^2))/hp^2;
cstru=const*[0 -1 0 1];

function [ksp,cstrug]=cplse(n,cstru);
u=cstru;
m=n;
h=n*2+2;
cstrug=zeros(m,h);
offset = 1;
for i=1:m;
    cstrug(i,offset:offset+length(u)-1)=u;
    offset = offset+2;
end
ksp=cstrug;

function [fto]=force(le,a,rho_s,a_p,rho_p);
fs=(rho_s*a*le)/2;
Qs=fs*[1 le/6 1 -le/6]';
fp=(rho_p*a_p*le)/2;
Qp=fp*[1 le/6 1 -le/6]';
fto1=Qs+Qp;
fto=(fto1);

function [Q1]=gforce(n,fto);
u=fto';
m=n;
h=n*2+2;
Q2=zeros(m,h);
offset=1;
for i=1:m
    Q2(i,offset:offset+length(u)-1)=u;
    offset = offset+2;
end
Q3=Q2';
y=zeros(h,1);
for j=1:h
    y(j)=sum(Q3(j,:));
end
Q1=y;

```

```

function mp=mpiezo(rho_p,a_p,le)
% element mass matrix
% length of each element
me=[156 22*le 54 -13*le;...
    22*le 4*le.^2 13*le -3*le.^2;...
    54 13*le 156 -22*le;...
    -13*le -3*le.^2 -22*le 4*le.^2];
mp=(rho_p*a_p*le)/420)*me;

function ms=mstruc(rho_s,a,le)
% element mass substructure matrix
me=[156 22*le 54 -13*le;...
    22*le 4*le.^2 13*le -3*le.^2;...
    54 13*le 156 -22*le;...
    -13*le -3*le.^2 -22*le 4*le.^2];
ms=(rho_s*a*le)/420)*me;

function [msg,mpg]=mglobal(n,ms,mp);
msg=zeros(n*2+2,n*2+2);
mpg=zeros(n*2+2,n*2+2);
for i = 1:n,
msg((i-1)*2+1:(i-1)*2+4, (i-1)*2+1:(i-1)*2+4) = msg((i-1)*2+1:(i-1)*2+4, (i-1)*2+1:(i-1)*2+4)+ms;
mpg((i-1)*2+1:(i-1)*2+4, (i-1)*2+1:(i-1)*2+4) = mpg((i-1)*2+1:(i-1)*2+4, (i-1)*2+1:(i-1)*2+4)+mp;
end

function kp=spiezo(Ep,in_p,le)
% element stiffness piezoelectric matrix
ke= [12 6*le -12 6*le;...
    6*le 4*le.^2 -6*le 2*le.^2;...
    -12 -6*le 12 -6*le;...
    6*le 2*le.^2 -6*le 4*le.^2];
kp=((Ep*in_p)/(le.^3))*ke;

function ks=sstruc(Es,in_s,le)
% element stiffness substructure matrix
ke=[12 6*le -12 6*le;...
    6*le 4*le.^2 -6*le 2*le.^2;...
    -12 -6*le 12 -6*le;...
    6*le 2*le.^2 -6*le 4*le.^2];
ks=((Es*in_s)/(le.^3))*ke;

function [ksg,kpg]=kglobal(n,ks,kp)
ksg=zeros(n*2+2,n*2+2);
kpg=zeros(n*2+2,n*2+2);
for i = 1:n,
ksg((i-1)*2+1:(i-1)*2+4, (i-1)*2+1:(i-1)*2+4) = ksg((i-1)*2+1:(i-1)*2+4, (i-1)*2+1:(i-1)*2+4)+ks;
kpg((i-1)*2+1:(i-1)*2+4, (i-1)*2+1:(i-1)*2+4) = kpg((i-1)*2+1:(i-1)*2+4, (i-1)*2+1:(i-1)*2+4)+kp;
end

```

```

% =====
%           MATLAB Piezoelectric Unimorph beam Power Harvesting
%           Multi elements using non-orthonormalised Method
%           Comparison with published research M.Lumentut and I.M. Howard
%           Written by Eziwarman
% =====
clear all
clc
n=50; % number of elements
% =====
% Beam parameters
% =====
len=50e-3; % total length of beam
b=6e-3; % width of structure and PZT
hs=.5e-3; % thickness of structure
hp=0.190e-3; % thickness of PZT
a=b*(hs); % area of structure
a_p=b*(hp); % area of PZT
le=len/n; % length of finite element
% =====
% Properties of the beam
% =====
Es=105e9; % Young's modulus [Brass]
Ep=66e9; % Young's Modulus [PZT]
rho_s=9000; % density structure in [kg/m^3]
rho_p=7800; % density PZT in [kg/m^3]
e31=-12.54; % Piezoelectric constant (C/m^2)
eps33=1.3555e-008; % Permittivity of constant strain
i_s=(b*(hs.^3))/12; % second area of moment inertia of
%cross section structure
i_p=(b*(hp.^3))/12; % second area of moment inertia of
%cross section PZT

% Tip mass properties
rho_t=7800;
lt=15e-3;
ht=10e-3;
% =====
% Finding the neutral axis from top PZT to neutral axis
% =====
zn=centroid(Es,Ep, hp, hs); % neutral axis
% =====
% Finding the neutral axis from bottom structure to neutral axis
% =====
nr=Es/Ep; % Ratio Young Modulus
hs_1=((hp.^2)+(2*hp*hs)+(nr*(hs.^2))); % Numerator finding neutral
axis
hs_2=2*(hp+(nr*hs)); % Denominator finding neutral axis
hsa_1=hs_1/hs_2; % Distance neutral axis from bottom
hpa=(hs+hp)-hsa_1; % confirm neutral axis
% =====
% Finding the inertia structure and piezo
% =====
d_s=hsa_1-(hs/2); % Distance neutral axis to
%centroid structure
d_p=zn-(hp/2); % Distance neutral axis to
%centroid piezoelectric
ad=a*(d_s.^2); % Distance to neutral axis
% =====
% Inertia structure and Piezo electric
% =====
in_s=i_s+(a*(d_s.^2)); % Inertia structure

```

```

in_p=i_p+(a_p*(d_p.^2)); % Inertia Piezoelectric
% =====
% element mass matrix
% =====
ms=mstruc(rho_s,a,le); % mass structure
mp=mpiezo(rho_p,a_p,le); % mass piezoelectric
mtip=tipmas(rho_t,rho_s,lt,b,ht,hs,hp,zn);
% =====
% element stiffnes matrix
% =====
[ks]=sstruc(Es,in_s,le); % stiffness structure
[kp]=spiezo(Ep,in_p,le); % stiffness piezoelectric
[cstru]=cpl(b,hp,e31,zn); % mechanical coupling
[fto]=force(le,a,rho_s,a_p,rho_p); % force
[ftip]=tipf(rho_t,rho_s,rho_p,b,lt,ht,hs); % tip mass
[cp]=cap(le,b,eps33,hp); % capacitance
% =====
% Arrangement of global matrix
% =====
[msg,mpg]=mglobal(n,ms,mp); % Global matrices structure
[tip]=mgtip(n,mtip); % Global tip mass
[ksg,kpg]=kglobal(n,ks,kp); % Global matrices
%piezoelectric
[ksp,cstrug]=cplse(n,cstru); % Global piezoelectric
%coupling matrix
[Q1]=gforce(n,fto); % Global Force
[Qtip]=gftip(n,ftip); % Global tip mass
[capg]=capt(n,cp); % Global capacitance
sum=trace(capg);
% =====
% Total global Matrix
% =====
M=msg+mpg+tip; % Global mass matrices struc and PZT
K=ksg+kpg; % Global stiffness matrices struc
%and PZT
Qto=Q1+Qtip;
% =====
% Global Mechanical damping matrix
% =====
alpha=4.886;
beta=1.2433e-5;
C=(alpha*M)+(beta*K);
% =====
% Applying boundary condition
% =====
bc=[1 2]; % zero boundary transverse and rotation
M(bc,:)=[];
M(:,bc)=[];
Mc=M;
K(bc,:)=[];
K(:,bc)=[];
Kc=K;
C(bc,:)=[];
C(:,bc)=[];
Cc=C;
ksp(:,bc)=[];
ksp1=ksp';
Qto(bc,:)=[];
Q=Qto;
% =====
% Transformation coupling

```

```

% =====
pshi=ones(1,n);          % Function transforming coupling to scalar
%matrix
kspc=ksp1*pshi';
% =====
% Finding Undamped natural fix-free
% =====
% Finding eigenvalue and eigenvector
% =====
invm=inv(Mc);
kmmod=invm*Kc;
[d,v]=eig(kmmod);
freq_nat=sqrt(eig(kmmod));
f_nat=sort(freq_nat/(2*pi));
% =====
% Finding Voltage response
% =====
% iterating input frequency range
% =====
freq_end=300;           % input last frequency
hrqf=freq_end*2*pi;
hrqi=2*pi*1;           % input initial frequency
deltahrq=0.1;
nhrq=fix((hrqf-hrqi)/deltahrq)+1; % the number of the generated
%frequency
% =====
% iterating the electrical voltage
% =====
freq=zeros(10,nhrq);
nl=0;
s2=0;
% =====
% iterating input load resistance
% =====
for Rdd=[680 6e3 18e3 12e4 6.5e5 1.545e6 3.2e6 20.5e6 120e6 355e6];
nl=nl+1;
for r=hrqi:deltahrq:hrqf; % iterating input frequency
Rl=-1/Rdd;
s2=s2+1;
freq(nl,s2)=freq(nl,s2)+(inv((sum*i*r+Rl)-kspc'*i*r*(inv(Kc-
Mc*r.^2+Cc*i*r)*kspc))*(kspc'*i*r*(inv(Kc-Mc*r.^2+Cc*i*r)*Q)));
end
s2=0;
end
figure(1)
nqr=hrqi:deltahrq:hrqf;
semilogy(nqr/(2*pi),(abs(freq)),'LineWidth',3);
xlabel('Frequency (Hz)','FontSize',24);
ylabel('Voltage (V/ms^-2)','FontSize',24);
legend('680 Ohms','6 kOhms','18 kOhms','120 kOhms','265 kOhms','650
kOhms','4.8 MOhms','12.5 MOhms','100 MOhms',1);
hold on
% =====
% iterating electrical current
% =====
cur=zeros(10,nhrq);
nl=0;
s2=0;
%iterating input load resistance
for Rdd=[680 6e3 18e3 12e4 6.5e5 1.545e6 3.2e6 20.5e6 120e6 355e6];
nl=nl+1;

```

```

for r=hrqi:deltahrq:hrqf;% iterating input frequency
Rl=(-1/Rdd);
s2=s2+1;
cur(nl,s2)=cur(nl,s2)+(-Rl)*(inv((sum*i*r+Rl)-kspc'*i*r*(inv(Kc-
Mc*r^2+Cc*i*r)*kspc))*(kspc'*i*r*(inv(Kc-Mc*r^2+Cc*i*r)*Q)));
end
s2=0;
end

figure(2)
nqr=hrqi:deltahrq:hrqf;
semilogy(nqr/(2*pi),(abs(cur)),'LineWidth',3);
xlabel('Frequency (Hz)','FontSize',24);
ylabel('Electrical Current (A/ms^-2)','FontSize',24);
legend('680 Ohms','6 kOhms','18 kOhms','120 kOhms','265 kOhms','650
kOhms','4.8 MOhms','12.5 MOhms','100 MOhms',1);
hold on
% =====
% iterating electrical power
% =====
Pow=zeros(10,nhrq);
nl=0;
s2=0;
%iterating input load resistance
%for Rdd=[680 6e3 18e3 120e3 265e3 65e4 4.2e6 12.5e6 100e6];
    for Rdd=[680 6e3 18e3 12e4 6.5e5 1.545e6 3.2e6 20.5e6 120e6
355e6];
        %for Rdd=[3.2e4 4.45e4 6.3e4];
            nl=nl+1;
            for r=hrqi:deltahrq:hrqf; % iterating input frequency
                Rl=-1/Rdd;
                s2=s2+1;
                Pow(nl,s2)=Pow(nl,s2)+(-Rl)*(inv((sum*i*r+Rl)-kspc'*i*r*(inv(Kc-
                Mc*r.^2+Cc*i*r)*kspc))*(kspc'*i*r*(inv(Kc-Mc*r.^2+Cc*i*r)*Q))).^2;
            end
            s2=0;
        end
    end

figure(3)
nqr=hrqi:deltahrq:hrqf;
semilogy(nqr/(2*pi),(abs(Pow)),'LineWidth',3);
xlabel('Frequency (Hz)','FontSize',24);
ylabel('Power Harvesting (W/m^2s^-4)','FontSize',24);
legend('680 Ohms','6 kOhms','18 kOhms','120 kOhms','265 kOhms','650
kOhms','4.8 MOhms','12.5 MOhms','100 MOhms',1);
hold on
% =====
% iterating displacement
% =====
dis=zeros(10,nhrq);
nl=0;
s2=0;
%iterating input load resistance
%for Rdd=[680 6e3 18e3 120e3 265e3 65e4 4.2e6 12.5e6 100e6];
    for Rdd=[680 6e3 18e3 12e4 6.5e5 1.545e6 3.2e6 20.5e6 120e6
355e6];
        nl=nl+1;
        dl=0;
        for r=hrqi:deltahrq:hrqf; % iterating input frequency
            Rl=-1/Rdd;
            s2=s2+1;

```

```

dl=dl+1;
dd=((inv(Kc-Mc*r.^2+Cc*i*r))*((inv(sum*i*r+Rl-(kspc'*i*r*(inv(Kc-
Mc*r.^2+Cc*i*r)*kspc))))*(Q*(sum*i*r+Rl)))));
dvect(nl,dl) = dd(length(dd)-1,1);
end
s2=0;
end
figure(4)
nqr=hrqi:deltahrq:hrqf;
semilogy(nqr/(2*pi),(abs(dvect)),'LineWidth',3);
xlabel('Frequency (Hz)','FontSize',24);
ylabel('Displacement (m/ms^-2)','FontSize',24);
legend('680 Ohms','6 kOhms','18 kOhms','120 kOhms','265 kOhms','650
kOhms','4.8 MOhms','12.5 MOhms','100 MOhms',1);
hold on

% =====
% Additional Function Command (for tip mass)
% =====
function [tip]=mgtip(n,mtip);
tip=zeros(n*2+2,n*2+2);
for i=n
tip((i-1)*2+1:(i-1)*2+4,(i-1)*2+1:(i-1)*2+4) = tip((i-1)*2+1:(i-
1)*2+4,(i-1)*2+1:(i-1)*2+4)+mtip;
end
function ftip=tipf(rho_t,rho_s,rho_p,b,lt,ht,hs)
io=rho_t*b*lt*ht+rho_p*b*lt*hs;
xc=(rho_t*b*(lt^2)*ht+rho_p*b*(lt^2)*hs)/2*(rho_t*b*lt*ht+rho_p*b*lt
*hs);
f=[0 0 0 1];
f1=[0 0 1 0];
f2=io*xc*f';
f3=io*f1';
ftip=f2+f3

function [mtip]=tipmas(rho_t,rho_s,lt,b,ht,hs,hp,zn);
io=rho_t*b*lt*ht+rho_s*b*lt*hs;
xc=((rho_t*b*(lt.^2)*ht)+(rho_s*b*(lt.^2)*hs))/(2*((rho_t*b*lt*ht)+(
rho_s*b*lt*hs)));
i2=(rho_t*b*lt*ht*(((lt^2)+(ht^2))/12)+(zn-
hp+(ht/2))^2+(lt/2)^2)+(rho_s*b*lt*hs*(((lt^2)+(ht^2))/12)+(lt/2)^
2+(hs/2-(zn-hp))^2));
mt1=[0 0 0 0;
      0 0 0 0;
      0 0 0 1;
      0 0 0 0];
mtip1=2*io*xc*mt1;

mt2=[0 0 0 0;
      0 0 0 0;
      0 0 1 0;
      0 0 0 0];
mtip2=io*mt2;

mt3=[0 0 0 0;
      0 0 0 0;
      0 0 0 0;
      0 0 0 1];
mtip3=i2*mt3;
mtip=mtip1+mtip2+mtip3;

```

```

% =====
% Additional Function Command (for varying piezoelectric length)
% =====
function [ksp,cstrug]=cplse(n,cstru)
u=cstru;
m=n;
h=n*2+2;
cstrug=zeros(m,h);
offset = 1;
%for i=1:10;
    %for i=1:20
        %for i=1:30
            for i=1:40
                cstrug(i,offset:offset+length(u)-1)=u;
                offset = offset+2;
            end
        end
    end
ksp=cstrug;

function [Q1]=gforce(n,fto,Qs);
u=fto';
m=n;
h=n*2+2;
Q2=zeros(m,h);
offset=1;
%for i=1:10
    %for i=1:20
        %for i=1:30
            for i=1:40
                Q2(i,offset:offset+length(u)-1)=u;
                offset = offset+2;
            end
        end
    end
Q3=Q2';
y=zeros(h,1);
for j=1:h
    y(j)=sum(Q3(j,:));
end
Q1a=y;
u2=Qs';
Q4=zeros(m,h);
%offset=11;
    %offset=21;
        %offset=31;
            offset=41;
%for i=11:h
    %for i=21:h
        %for i=31:h
            for i=41:h
                Q4(i,offset:offset+length(u2)-1)=u2;
                offset = offset+2;
            end
        end
    end
Q5=Q4';
y1=zeros(h,1);
%for j=23:h
    %for j=43:h
        %for j=63:h
            for j=83:h
                y1(j)=sum(Q5(j,:));
            end
        end
    end
Q1b=y1;
Q1=Q1a+Q1b;

```

```

function [Qtip]=gftip(n,ftip);
Qtip=zeros(n*2+2,1);
for i=n
    Qtip((i-1)*2+1:(i-1)*2+4,1) = Qtip((i-1)*2+1:(i-1)*2+4,1)+ftip;
end

function [ksg,kpg]=kglobal(n,ks,kp,ks1)

ksga=zeros(n*2+2,n*2+2);
ksgb=zeros(n*2+2,n*2+2);
kpg=zeros(n*2+2,n*2+2);

%for i=1:10
    %for i=1:20
        %for i=1:30
            for i=1:40
ksga((i-1)*2+1:(i-1)*2+4,(i-1)*2+1:(i-1)*2+4) = ksga((i-1)*2+1:(i-1)*2+4,(i-1)*2+1:(i-1)*2+4)+ks;
            end
%for ii=10+1:n
    %for ii=20+1:n
        %for ii=30+1:n
            for ii=40+1:n
ksgb((ii-1)*2+1:(ii-1)*2+4,(ii-1)*2+1:(ii-1)*2+4) = ksgb((ii-1)*2+1:(ii-1)*2+4,(ii-1)*2+1:(ii-1)*2+4)+ks1;
            end
%for j=1:10
    %for j=1:20
        %for j=1:30
            for j=1:40
kpg((j-1)*2+1:(j-1)*2+4,(j-1)*2+1:(j-1)*2+4) = kpg((j-1)*2+1:(j-1)*2+4,(j-1)*2+1:(j-1)*2+4)+kp;
            end
ksg=ksga+ksgb;

function [msg,mpg]=mglobal(n,ms,mp);

msg=zeros(n*2+2,n*2+2);
mpg=zeros(n*2+2,n*2+2);

for i = 1:n
msg((i-1)*2+1:(i-1)*2+4,(i-1)*2+1:(i-1)*2+4) = msg((i-1)*2+1:(i-1)*2+4,(i-1)*2+1:(i-1)*2+4)+ms;
end
%for j = 1:10
    %for j=1:20
        %for j=1:30
            for j=1:40
mpg((j-1)*2+1:(j-1)*2+4,(j-1)*2+1:(j-1)*2+4) = mpg((j-1)*2+1:(j-1)*2+4,(j-1)*2+1:(j-1)*2+4)+mp;
            end
end

```

```

% =====
%           MATLAB Piezoelectric Unimorph beam Power Harvesting
%           Piezoelectric unimorph with different orientation
%           using non-orthonormalised Method
%           Written by Eziwarman
% =====
clear all
clc
n=50; % number of elements
=====
% Beam parameters
%
=====
len=50e-3; % total length of beam
b=6e-3; % width of structure and PZT
hs=.5e-3; % thickness of structure
hp=.127e-3; % thickness of PZT
a=b*(hs); % area of structure
a_p=b*(hp); % area of PZT
le=len/(n); % length of finite element
=====
% Properties of the beam
%
=====
Es=105e9; % Young's modulus [Brass]
Ep=66e9; % Young's Modulus [PZT]
rho_s=9000; % density structure in [kg/m^3]
rho_p=7800; % density PZT in [kg/m^3]
e31=-12.54; % Piezoelectric constant (C/m^2)
eps33=1.3555e-008; % Permittivity of constant strain
i_s=(b*(hs.^3))/12; % second area of moment inertia of
cross section structure
i_p=(b*(hp.^3))/12; % second area of moment inertia of
cross section PZT
=====
% Finding the neutral axis from top PZT to neutral axis
%
=====
zn=centroid(Es,Ep,hp,hs); % neutral axis
%
=====
% Finding the neutral axis from bottom structure to neutral axis
%
=====
nr=Es/Ep; % Ratio Young Modulus
hs_1=((hp.^2)+(2*hp*hs)+(nr*(hs.^2))); % Numerator finding neutral
axis
hs_2=2*(hp+(nr*hs)); % Denominator finding
neutral axis
hsa_1=hs_1/hs_2; % Distance neutral axis
from bottom
hpa=(hs+hp)-hsa_1; % confirm neutral axis
%
=====
% Finding the inertia structure and piezo
%
=====
d_s=hsa_1-(hs/2); % Distance neutral axis to
centroid structure
d_p=zn-(hp/2); % Distance neutral axis to
centroid piezoelectric

```

```

ad=a*(d_s.^2); % Distance to neutral axis
%
=====
% Inertia structure and Piezo electric
%
=====
in_s=i_s+(a*(d_s.^2)); % Inertia structure
in_p=i_p+(a_p*(d_p.^2)); % Inertia Piezoelectric
%
=====
% transformation matrix
%
=====
=====
theta=90;
T=[cosd(theta) sind(theta) 0 0 0 0;...
   -sind(theta) cosd(theta) 0 0 0 0;...
   0 0 1 0 0 0;...
   0 0 0 cosd(theta) sind(theta) 0;...
   0 0 0 -sind(theta) cosd(theta) 0;
   0 0 0 0 0 1];
%
=====
% element mass matrix element 1
%
=====
ms=mstruc(rho_s,a,le); % mass structure
mp=mpiezo(rho_p,a_p,le); % mass piezoelectric
%
=====
% Mass transformation element 2
%
=====
mms=T'*ms*T; % mass structure
mmp=T'*mp*T; % mass piezoelectric
%
=====
% element stiffness matrix element 1
%
=====
[ks,ks1]=sstruc(Es,in_s,le,a,i_s); % stiffness structure
kp=spiezo(Ep,in_p,le,a_p); % stiffness piezoelectric
%
=====
% Stiffness transformation element 2
%
=====
kks=T'*ks*T; % stiffness structure
kks1=T'*ks1*T;
kkp=T'*kp*T; % stiffness piezoelectric
[cstru]=cpl(b,hp,e31,zn);
[cstru1]=cpl1(b,hp,e31,zn); % electromechanical coupling
[fto,Qs,Qp]=force(le,a,rho_s,a_p,rho_p); % force
[cp]=cap(le,b,eps33,hp); % capacitance each element
%
=====
% Assembly matrix
%
=====
% iterasi for horizontal and transformation structural mass matrix

```

```

%
=====
[msg,mpg]=msglobal(n,ms,mp);
[msgt,mpgt]=mpglobal(n,mms,mmp);
%
=====
% iterate for horizontal stiffness and transformation structural
matrix
%
=====
[ksg,kpg]=ksglobal(n,ks,ks1,kp);
[ksgt,kpgt]=kpglobal(n,kks,kks1,kkp);
%
=====
% The global electromechanical coupling
%
=====
[ksp]=cplse(n,cstru);
[ksp2]=cplset(n,cstru1,T);
%
=====
% the global force coupling
%
=====
[Q1]=gforce(n,Qs,Qp);
[Q2]=gforcet(n,Qs,Qp,T);
[capg]=capt(n,cp);
sum=trace(capg);
%
=====
% Summation global matrix
%
=====
M=(msg+mpg)+(msgt+mpgt);
K=(ksg+kpg)+(ksgt+kpgt);
ksp3=ksp+ksp2;
Q10=Q1+Q2;
%
=====
% Global Mechanical damping matrix
%
=====
alpha=4.886;
beta=1.2433e-05;
C=(alpha*M)+(beta*K);
%
=====
% Applying boundary condition
%
=====
bc=[1 2 3]; % zero boundary transverse and rotation
M(bc,:)=[];
M(:,bc)=[];
Mc=M;
K(bc,:)=[];
K(:,bc)=[];
Kc=K;
C(bc,:)=[];
C(:,bc)=[];
Cc=C;
ksp3(:,bc)=[];

```

```

ksp1=ksp3';
Q10(bc,:)=[];
Q=Q10;

%
=====
% Transformation coupling
%
=====

pshi=ones(1,n);
kspc=ksp1*pshi';
%
=====

% Finding eigenvalue and eigenvector
%
=====

invm=inv(Mc);
kmmod=invm*Kc;
[d,v]=eig(kmmod);
freq_nat=sqrt(eig(kmmod));
f_nat=sort(freq_nat/(2*pi));

% Finding Voltage response
% =====
% Iterating input frequency range
% =====
freq_end=200; % input last frequency
hrqf=freq_end*2*pi;
hrqi=2*pi*100; % input initial frequency
deltahrq=1;
nhrq=fix((hrqf-hrqi)/deltahrq)+1; % the number of the generated
frequency
% =====
% Iterating the electrical voltage
% =====
freq=zeros(5,nhrq);
nl=0;
s2=0;
% =====
% Iterating input load resistance
% =====
for Rdd=[1e2 1e3 1e4 1e5 1e6];
nl=nl+1;
for r=hrqi:deltahrq:hrqf; % iterating input frequency
Rl=-1/Rdd;
s2=s2+1;
freq(nl,s2)=freq(nl,s2)+(inv((sum*i*r+Rl)-kspc'*i*r*(inv(Kc-
Mc*r.^2+Cc*i*r)*kspc))*(kspc'*i*r*(inv(Kc-Mc*r.^2+Cc*i*r)*Q)));
end
s2=0;
end

figure(1)
nqr=hrqi:deltahrq:hrqf;
semilogy(nqr/(2*pi),(abs(freq)));
xlabel('Frequency(Hz)');
ylabel('Voltage(V/ms^-2)');
legend('10^2 \Omega','10^3 \Omega','10^4 \Omega','10^5 \Omega','10^6
\Omega',1);
hold on

```

```

% Iterating electrical current
cur=zeros(5,nhrq);
nl=0;
s2=0;
% iterating input load resistance
for Rdd=[1e2 1e3 1e4 1e5 1e6];
nl=nl+1;
for r=hrqi:deltahrq:hrqf;% iterating input frequency
Rl=(-1/Rdd);
s2=s2+1;
cur(nl,s2)=cur(nl,s2)+(-Rl)*(inv((sum*i*r+Rl)-kspc'*i*r*(inv(Kc-
Mc*r^2+Cc*i*r)*kspc))*(kspc'*i*r*(inv(Kc-Mc*r^2+Cc*i*r)*Q)));
end
s2=0;
end

figure(2)
nqr=hrqi:deltahrq:hrqf;
semilogy(nqr/(2*pi),(abs(cur)));
xlabel('Frequency(Hz)');
ylabel('Electrical Current(A/ms^-2)');
legend('10^2 \Omega','10^3 \Omega','10^4 \Omega','10^5 \Omega','10^6
\Omega',1);
hold on

% Iterating electrical power
Pow=zeros(5,nhrq);
nl=0;
s2=0;
% iterating input load resistance
for Rdd=[1e2 1e3 1e4 1e5 1e6];
% for Rdd=[3.2e4 4.45e4 6.3e4];
nl=nl+1;
for r=hrqi:deltahrq:hrqf; % iterating input frequency
Rl=-1/Rdd;
s2=s2+1;
Pow(nl,s2)=Pow(nl,s2)+(-Rl)*(inv((sum*i*r+Rl)-kspc'*i*r*(inv(Kc-
Mc*r.^2+Cc*i*r)*kspc))*(kspc'*i*r*(inv(Kc-Mc*r.^2+Cc*i*r)*Q))).^2;
end
s2=0;
end

figure(3)
nqr=hrqi:deltahrq:hrqf;
semilogy(nqr/(2*pi),(abs(Pow)));
xlabel('Frequency(Hz)');
ylabel('Power Harvesting(W/m^2s^-4)');
legend('10^2 \Omega','10^3 \Omega','10^4 \Omega','10^5 \Omega','10^6
\Omega',1);
hold on

dis=zeros(8,nhrq);
nl=0;
s2=0;
% iterating input load resistance
for Rdd=[1e2 1e3 1e4 1e5 1e6];
nl=nl+1;
dl=0;
for r=hrqi:deltahrq:hrqf; % iterating input frequency
Rl=-1/Rdd;
s2=s2+1;

```

```

dl=dl+1;
dd=((inv(Kc-Mc*r.^2+Cc*i*r))*((inv(sum*i*r+Rl-(kspc'*i*r*(inv(Kc-
Mc*r.^2+Cc*i*r)*kspc))))*(Q*(sum*i*r+Rl))));
dvect(nl,dl) = dd(length(dd)-1,1);
end
s2=0;
end

figure(4)
nqr=hrqi:deltahrq:hrqf;
semilogy(nqr/(2*pi), (abs(dvect)));
xlabel('Frequency(Hz)');
ylabel('Displacement(m/ms^-2)');
legend('10^2 \Omega', '10^3 \Omega', '10^4 \Omega', '10^5 \Omega', '10^6
\Omega', 1);
hold on

% =====
% Function Command for different orientation
% =====
function [cp]=cap(le,b,eps33, hp);
cp=-(le*b*eps33)/hp;

function [capg]=capt(n, cp);
A=zeros(5,n);
cap=eye(20,n);
C=cp*cap;
H=[C;A];
B=zeros(5,n);
F=zeros(20,30);
cap1=eye(20,20);
D=cp*cap1;
J=horzcat(F,D);
I=[B;J];
capg=[H;I];

function zn=centroid(Es,Ep, hp,hs) % Finding the neutral axis
zn_1=(Es*(hs.^2))+Ep*(hp.^2)+2*(Es*hs*hp);
zn_2=2*(Es*hs+Ep*hp);
zn=zn_1/zn_2;

function cstru=cpl(b, hp, e31, zn);
const=-e31*b*((2*zn*hp-(hp.^2))/(2*hp));
%cstru=const*[0 0 -1 0 0 1]; % ignoring coupling
cstru=const*[-1/((2*zn*hp-(hp.^2))/(2*hp)) 0 -1 1/((2*zn*hp-
(hp.^2))/(2*hp)) 0 1];

function cstrul=cpl1(b, hp, e31, zn);
const=-e31*b*((2*zn*hp-(hp.^2))/(hp^2));
cstrul=const*[-1/((2*zn*hp-(hp.^2))/(hp^2)) 0 -1 1/((2*zn*hp-
(hp.^2))/(hp^2)) 0 1];

function [ksp]=cplse(n, cstru);
u=cstru;
m=n;
h=n*3+3;
cstrug=zeros(m,h);
offset = 1;
for i=1:20
    cstrug(i, offset:offset+length(u)-1)=u;

```

```

        offset = offset+3;
    end
    ksp=cstrug;

function [ksp2]=cplset(n,cstrul,T);
ksp=zeros(n,n*3+3);
u1=cstrul*T;
offset=91;
for j=31:n
    ksp(j,offset:offset+length(u1)-1)=u1;
    offset=offset+3;
end
ksp2=ksp;

function [Q1]=gforce(n,Qs,Qp);
% Composing force structure matrix
u2=Qs;
Q2=zeros(n,n*3+3);
offset=1;
for i=1:25
    Q2(i,offset:offset+length(u2)-1)=u2;
    offset = offset+3;
end
Q3=Q2';
y=zeros(n*3+3,1);
for j=1:n*3+3
    y(j)=sum(Q3(j,:));
end
Q1a=y;
% Composing piezoelectric force matrix
u3=Qp;
Q4=zeros(n,n*3+3);
offset=1;
for i=1:20
    Q4(i,offset:offset+length(u3)-1)=u3;
    offset = offset+3;
end
Q5=Q4';
x=zeros(n*3+3,1);
for j=1:n*3+3
    x(j)=sum(Q5(j,:));
end
Q1b=x;
Q1=Q1a+Q1b;
function [Q2]=gforcet(n,Qs,Qp,T);
%composing structure with tranformation angle matrix
u3=T'*Qs;
Q5=zeros(n,n*3+3);
offset=76;
for i=26:n
    Q5(i,offset:offset+length(u3)-1)=u3;
    offset = offset+3;
end
Q6=Q5';
y=zeros(n*3+3,1);
for j=76:n*3+3
    y(j)=sum(Q6(j,:));
end
Q2a=y;
% Composing piezoelectric force matrix

```

```

u4=Qp;
Q7=zeros(n,n*3+3);
offset=91;
for i=31:n
    Q7(i,offset:offset+length(u4)-1)=u4;
    offset = offset+3;
end
Q8=Q7';
x=zeros(n*3+3,1);
for j=91:n*3+3
    x(j)=sum(Q8(j,:));
end
Q2b=x;
Q2=Q2a+Q2b;

function [ksgt,kpgt]=kpglobal(n,kks,kks1,kkp);
ksgta=zeros(n*3+3,n*3+3);
ksgtb=zeros(n*3+3,n*3+3);
kpgt=zeros(n*3+3,n*3+3);
for jj=(n/2)+1:30
    ksgta((jj-1)*3+1:(jj-1)*3+6,(jj-1)*3+1:(jj-1)*3+6) = ksgta((jj-1)*3+1:(jj-1)*3+6,(jj-1)*3+1:(jj-1)*3+6)+kks1;
end
for j=(30)+1:n
    ksgtb((j-1)*3+1:(j-1)*3+6,(j-1)*3+1:(j-1)*3+6) = ksgtb((j-1)*3+1:(j-1)*3+6,(j-1)*3+1:(j-1)*3+6)+kks;
end
for i=(n/2)+6:n
    kpgt((i-1)*3+1:(i-1)*3+6,(i-1)*3+1:(i-1)*3+6) = kpgt((i-1)*3+1:(i-1)*3+6,(i-1)*3+1:(i-1)*3+6)+kkp;
end
ksgt=ksgta+ksgtb;

function [ksg,kpg]=ksglobal(n,ks,ks1,kp);
ksga=zeros(n*3+3,n*3+3);
ksgb=zeros(n*3+3,n*3+3);
kpg=zeros(n*3+3,n*3+3);
for i=1:20
    ksga((i-1)*3+1:(i-1)*3+6,(i-1)*3+1:(i-1)*3+6) = ksga((i-1)*3+1:(i-1)*3+6,(i-1)*3+1:(i-1)*3+6)+ks;
end
for ii=20+1:(n/2)
    ksgb((ii-1)*3+1:(ii-1)*3+6,(ii-1)*3+1:(ii-1)*3+6) = ksgb((ii-1)*3+1:(ii-1)*3+6,(ii-1)*3+1:(ii-1)*3+6)+ks1;
end
for j=1:20
    kpg((j-1)*3+1:(j-1)*3+6,(j-1)*3+1:(j-1)*3+6) = kpg((j-1)*3+1:(j-1)*3+6,(j-1)*3+1:(j-1)*3+6)+kp;
end
ksg=ksga+ksgb;

function [msgt,mpgt]=mpglobal(n,mms,mmp)
msgt=zeros(n*3+3,n*3+3);
mpgt=zeros(n*3+3,n*3+3);
for j=(n/2)+1:n
    msgt((j-1)*3+1:(j-1)*3+6,(j-1)*3+1:(j-1)*3+6) = msgt((j-1)*3+1:(j-1)*3+6,(j-1)*3+1:(j-1)*3+6)+mms;
end
for i=(n/2)+6:n
    mpgt((i-1)*3+1:(i-1)*3+6,(i-1)*3+1:(i-1)*3+6) = mpgt((i-1)*3+1:(i-1)*3+6,(i-1)*3+1:(i-1)*3+6)+mmp;
end

```

```

end

function mp=mpiezo(rho_p,a_p,le)
% element mass matrix
% length of each element

me=[140 0 0 70 0 0;
    0 156 22*le 0 54 -13*le;...
    0 22*le 4*le.^2 0 13*le -3*le.^2;...
    70 0 0 140 0 0;
    0 54 13*le 0 156 -22*le;...
    0 -13*le -3*le.^2 0 -22*le 4*le.^2];
mp=(rho_p*a_p*le)/420)*me;

function [msg,mpg]=msglobal(n,ms,mp);
msg=zeros(n*3+3,n*3+3);
mpg=zeros(n*3+3,n*3+3);
for i=1:(n/2)
    msg((i-1)*3+1:(i-1)*3+6,(i-1)*3+1:(i-1)*3+6) = msg((i-1)*3+1:(i-1)*3+6,(i-1)*3+1:(i-1)*3+6)+ms;
end
for i=1:20
    mpg((i-1)*3+1:(i-1)*3+6,(i-1)*3+1:(i-1)*3+6) = mpg((i-1)*3+1:(i-1)*3+6,(i-1)*3+1:(i-1)*3+6)+mp;
end

function [ms]=mstruc(rho_s,a,le)
% element mass matrix
% length of each element

me=[140 0 0 70 0 0;
    0 156 22*le 0 54 -13*le;...
    0 22*le 4*le.^2 0 13*le -3*le.^2;...
    70 0 0 140 0 0;
    0 54 13*le 0 156 -22*le;...
    0 -13*le -3*le.^2 0 -22*le 4*le.^2];
ms=(rho_s*a*le)/420)*me;

function kp=spiezo(Ep,in_p,le,a_p)

ke= [a_p 0 0 -a_p 0 0;
    0 12*in_p/(le.^2) 6*in_p/(le) 0 -12*in_p/(le.^2) 6*in_p/(le);...
    0 6*in_p/(le) 4*in_p 0 -6*in_p/(le) 2*in_p;...
    -a_p 0 0 a_p 0 0;...
    0 -12*in_p/(le.^2) -6*in_p/(le) 0 12*in_p/(le.^2) -6*in_p/(le);
    0 6*in_p/(le) 2*in_p 0 -6*in_p/(le) 4*in_p];
kp=((Ep)/(le))*ke;

function [ks,ks1]=sstruc(Es,in_s,le,a,i_s)

ke=[a 0 0 -a 0 0;
    0 12*in_s/(le.^2) 6*in_s/(le) 0 -12*in_s/(le.^2) 6*in_s/(le);...
    0 6*in_s/(le) 4*in_s 0 -6*in_s/(le) 2*in_s;...
    -a 0 0 a 0 0;...
    0 -12*in_s/(le.^2) -6*in_s/(le) 0 12*in_s/(le.^2) -6*in_s/(le);
    0 6*in_s/(le) 2*in_s 0 -6*in_s/(le) 4*in_s];
ks=((Es)/(le))*ke;
ke1=[a 0 0 -a 0 0;
    0 12*i_s/(le.^2) 6*i_s/(le) 0 -12*i_s/(le.^2) 6*i_s/(le);...
    0 6*i_s/(le) 4*i_s 0 -6*i_s/(le) 2*i_s;...

```

```
-a 0 0 a 0 0;...  
0 -12*i_s/(le.^2) -6*i_s/(le) 0 12*i_s/(le.^2) -6*i_s/(le);  
0 6*i_s/(le) 2*i_s 0 -6*i_s/(le) 4*i_s];  
ks1=((Es)/(le))*kel;
```